Doctoral Dissertation
Doctoral Program in Civil and Environmental Engineering (32nd Cycle)

A new method for 2D stochastic inverse modeling in Magnetotellurics: application to the Larderello-Travale geothermal field and novel results from 3D inversion

Francesca Pace

Supervisor
Prof. A. Godio

Doctoral Dissertation
Doctoral Program in Civil and Environmental Engineering (32nd Cycle)

A new method for 2D stochastic inverse modeling in Magnetotellurics: application to the Larderello-Travale geothermal field and novel results from 3D inversion

Francesca Pace

* * * * * *

Supervisor
Prof. A. Godio, *Politecnico di Torino*

Doctoral Examination Committee:
Prof. Jean-François Girard, Referee, University of Strasbourg (France)
Dr. Adele Manzella, Referee, CNR IGG Pisa, (Italy)
Dr. Perla Piña-Varas, Referee, University of Barcelona (Spain)
Prof. Michele Pipan, Referee, University of Trieste (Italy)
Prof. Laura Valentina Socco, Referee, Politecnico di Torino (Italy)

Politecnico di Torino
2019

I hereby declare that, the contents and organisation of this dissertation constitute my own original work and does not compromise in any way the rights of third parties, including those relating to the security of personal data.

…………………………………..…

Francesca Pace

Turin, December 27, 2019

Summary

The magnetotelluric method (MT) is one of the most effective geophysical techniques for the investigation of deep geothermal systems because it can recover the electrical-resistivity distribution of the Earth from a few meters to hundreds of kilometers of depth.

The MT inverse problem is ill-posed in nature with nonlinear and equivalent solutions. The standard approach to solve the inverse problem is the iterated and linearized inversion. However, it is also possible to adopt the global search approach, which performs stochastic inverse modeling by adopting the Monte-Carlo or metaheuristic methods. Global search methods have become of major interest in geophysics because they are theoretically able to find the global minimum of a function as the final solution without being trapped in one of the several local minima. The potential advantages of metaheuristics are also to provide complete sampling of the search space of solutions and independence from the starting model.

The development of a metaheuristic method to solve the 2D MT inverse problem represents a novelty in the framework of the existing MT inversion techniques. Moreover, deploying 2D stochastic inverse modeling to interpret MT data from geothermal areas has a great potential, mostly in those cases where the geological complexity and the difficulty in retrieving reliable external constraints can negatively affect the solution of the inverse problem. One of the most extraordinary geothermal resources in the world is the Larderello-Travale geothermal area (LTGA), located in south Tuscany, Italy. The area has been the object of vast industrial and scientific research over the past century. Nonetheless, some geological, physical and chemical aspects are still a matter of research.

This thesis investigates a new method, based on particle swarm optimization (PSO), to perform stochastic inverse modeling of 2D MT data. The PSO input parameters were accurately calibrated by means of a sensitivity analysis in order to enhance the stability and convergence of the solution. The computationally demanding nature of the algorithm was overcome by parallelizing the code to be run on a High Performance Computing (HPC) cluster. PSO was applied to two examples of MT synthetic data of different complexity. The PSO was initialized both by giving a priori information and by using a random initialization. The a priori information was given to a small number of particles, i.e., selected models, as the initial position, so that the swarming behavior was only slightly influenced. We demonstrated that there is no need for the a priori initialization to obtain robust 2D models because the results were largely comparable with the results from randomly initialized PSO. After this validation, the method was applied to the MT benchmark for real-field data, the COPROD2 data set (Canada). PSO of COPROD2 data provided a resistivity model of the earth in line with results from previous interpretations. The stochastic nature of PSO and the combination of exploration and exploitation behaviors played a key role in finding the global minimum of the search space as final solution.

The PSO algorithm was also applied to two MT profiles located in the LTGA. For the first time, MT data from this geothermal area have been 2D interpreted using a metaheuristic method. The final models succeeded in imaging very complex resistivity structures similar to those presented in previous research, but with the following advantages: (i) the final models have not been initially biased by an external starting model derived from geology and (ii) the RMSEs associated to the final PSO models were lower than those associated to the models obtained by different inversion techniques.

Furthermore, 3D MT inversion is currently an area of very intensive research and no work to date has focused on 3D inversion of MT data from the Travale geothermal area. The MT data that have been acquired in Travale during the past decades were recovered and accurately analyzed to determine the geoelectrical dimensionality and directionality, strike direction and phase tensor properties. Static shift was corrected through new time-domain electromagnetic (TDEM) measurements. A number of 3D MT inversion tests were performed by changing the grid rotation, error floor and starting model in order to assess the connection between the inversion response and geology. The final 3D model was compared with other subsurface data and models. To the best of the authors' knowledge, this is the first 3D resistivity model of the Travale geothermal system derived from complete MT inversion. The outcome of this study provides new insight into the interpretation of the complex geothermal system of Travale.

Acknowledgment

Coming to the end of this doctoral experience, I wish to sincerely thank to:

My supervisor professor Godio, for his valuable support during the last three years. He has allowed my research to be enriched by attending international conferences, working at University of Barcelona in the frame of the Erasmus+ Tranineeship and carrying out the field campaigns. He also founded the extension of my scholarship in order to cover the final steps of the thesis writing.

Alessandro, who has encouraged me in exploring the attractiveness of Magnetotellurics and geothermics. He has always demonstrated full patience and collaborative approach to clarify my issues, correct my mistakes and improve my work with interesting comments. I am very proud of the work we have performed together as colleagues.

Anna, Pilar, Alex, Juanjo, Perla and the other members of the electromagnetic-geophysics group at University of Barcelona. I spent there a fantastic period, which was plenty of progress in my research work and invaluable for their warm hospitality.

Adele Manzella and IGG-CNR di Pisa, that shared the magnetotelluric data set from the geothermal area of Larderello-Travale and gave me scientific support to study this fascinating subject.

Naser Meqbel (Consulting-GEO), who kindly provided the inversion code ModEM and the software 3D-GRID Academic.

Chiara, who kindly hosted me in her quiet office during the last month of thesis writing. It has been an ideal workplace for full concentration and thinking.

Diego, who always solved the every-day or last-minute problems with the maximum availability and efficiency.

The PhD candidates of the geophysics group, Farbod, Myrto, Andrea, Bin Bin and Shufan, for the amusing moments spent together.

My friends from “Tazzetti”, the master of science degree and the group “Piemontesi per caso”, that filled my spare time with fun moments and memorable travels.

Giovanni, who strongly encouraged me during the most stressful moments of the doctorate. His advice was precious to get out of anxiety, build my personal path and pursue my objectives.

My parents and my sister, and their ability to make me feeling home despite the distance. Without knowing the details of my day-work or deadlines, they always trusted me and made me feeling a stronger person.

***

Al termine di questa esperienza di dottorato, vorrei ringraziare profondamente:

il prof. Godio, che con la sua disponibilità e comprensione mi ha sostenuta nell'attività di ricerca di questi 3 anni, permettendomi di arricchirla attraverso la partecipazione a conferenze internazionali, l'esperienza presso l'Università di Barcellona e le campagne di misura sul campo. Devo anche ringraziare per l'estensione della borsa di ricerca per poter serenamente scrivere, consegnare e revisionare la tesi.

Alessandro, che sin dai primi giorni dell'esperienza di dottorato mi ha non solo trasmesso le sue conoscenze ma anche infuso l'interesse per la Magnetotellurica, essendo entrambi accomunati dalla passione per la geotermia. In questi 3 anni grazie alla sua immancabile disponibilità e all'ottimo lavoro di squadra credo che abbiamo ottenuto quelli che, almeno per me, considero dei successi.

Anna, Pilar, Alex, Juanjo, Perla e tutto il gruppo di geofisica elettromagnetica dell'Università di Barcellona. Grazie a loro ho trascorso un favoloso periodo all'estero, fruttuoso dal punto di vista della mia ricerca, per merito della loro massima condivisione della conoscenza scientifica, e ricchissimo e indimenticabile dal punto di vista umano.

Adele Manzella e l'IGG-CNR di Pisa, che mi hanno concesso di poter lavorare sui dati magnetotellurici dell'area geotermica di Larderello-Travale.

Naser Meqbel (Consulting-GEO), che ha gentilmente concesso l'utilizzo di ModEM per l'inversione 3D dei dati magnetotellurici e di 3D-GRID Academic per la visualizzazione dei risultati.

Chiara, che negli ultimi mesi di dottorato mi ha accolta nel suo ufficio garantendomi la tranquillità e la concentrazione di un ambiente lavorativo ideale.

Diego e alla sua massima disponibilità nel risolvere i piccoli problemi quotidiani di lavoro ma anche nell'accettare la campagna di misure TDEM che a febbraio 2019 è stata organizzata all'ultimo momento.

Per i piacevoli momenti trascorsi insieme, i dottorandi geofisici Farbod, Myrto, Andrea, Bin Bin e Shufan.

I miei amici del “Tazzetti”, i “Piemontesi per caso” e i colleghi della magistrale, che hanno riempito i weekend di svago, divertimento e viaggi indimenticabili.

Giovanni, che in questi tre anni, e non solo, mi ha sostenuta e incoraggiata nel superare le difficoltà e le ansie del dottorato. Attraverso le nostre camminate in montagna ho imparato a non lavorare nel weekend e ad avere più chiari i miei obiettivi.

I miei genitori e mia sorella che, nonostante la lontananza, mi hanno fatto sentire sempre il loro calore e comprensione familiare. Pur non sapendo i dettagli del mio lavoro, mi hanno sempre supportata in ogni scelta, confidando nella mia bravura e capacità.

Ai miei genitori

Contents

List of Tables

List of Figures

List of abbreviations

Nomenclature

Symbol	Unit of measurement	Description
$\boldsymbol{E}$	V/m	Electric field
$\boldsymbol{B}$	T	Magnetic induction
$\boldsymbol{H}$	A/m	Magnetic field
$\boldsymbol{j}$	A/m^2	Current density
$\boldsymbol{D}$	C/m^2	Electric displacement
η_f	C/m^3	Electric charge density
σ	S/m	Electric conductivity
ρ	Ωm	Electric resistivity
ε	F/m	Dielectric permittivity
μ	H/m	Magnetic permeability
t	s	time
f	Hz	Frequency
ω	rad/s	Angular frequency
T	s	Period
δ	m	Skin depth
$\underline{Z}$	Ω	Impedance tensor (2x2)
$\underline{M}$	m/s	Magnetotelluric tensor (2x2)
$\rho_{a\,ij}$	Ωm	Apparent resistivity
φ_{ij}	°	phase
$\boldsymbol{T}$	-	Geomagnetic transfer function (Tipper vector)
$\boldsymbol{C}$	-	Galvanic distortion matrix
g, $\boldsymbol{T}$, $\boldsymbol{S}$, $\boldsymbol{A}$	-	gain, twist, shear, anisotropy (Groom and Bailey's decomposition)
θ	°	Arbitrary rotation angle
$\boldsymbol{X}$, $\boldsymbol{Y}$	m/s	Real and imaginary part of the Magnetotelluric tensor $\underline{M}$
$\boldsymbol{\Phi}$	-	Phase tensor
Φ_{max}, Φ_{min}		Singular values of the phase tensor
α	°	Direction of the phase tensor

β	°	Skew angle of the phase tensor

d	m	Diffusion depth for Time-Domain Electro-Magnetic (TDEM) method
L	m	Side length of the TDEM acquisition loop
R	m	Equivalent radius of the TDEM square loop with side L

Particle swarm optimization (PSO) nomenclature		
$\boldsymbol{v_i^k}$	-	Velocity of the i^{th}-particle at the k^{th}-iteration
$\boldsymbol{x_i^k}$	-	Position of the i^{th}-particle at the k^{th}-iteration
ω^k	-	Inertia weight
α_1, α_2	-	Cognitive and social accelerations
γ_1, γ_2	-	Uniformly distributed random numbers $\in [0,1]$
$\boldsymbol{P_i}$	-	Local best position of the i^{th}-particle of the swarm
$\boldsymbol{G}$	-	Global best position of the swarm
N	-	Swarm size or number of particles forming the swarm
$F(\boldsymbol{m})$	-	Objective function to be optimized to solve the inverse problem
$\boldsymbol{m}$	-	model parameter, i.e., the resistivity model
$\boldsymbol{d_{obs}}$	-	Generic observed data
$\rho_{a,o}$, $\rho_{a,p}$	Ωm	Observed and predicted apparent resistivity
$\varphi_{a,o}$, $\varphi_{a,p}$	°	Observed and predicted phase
$\lambda, \lambda_x, \lambda_z$	-	Lagrange multiplier in the general case, horizontal and vertical directions
a, b	-	Weighting coefficients for 1D PSO
M	-	Number of data in 2D MT inverse problem
$\boldsymbol{\Delta\rho_{a,o}, \Delta\varphi_o}$	%	Errors in observed apparent resistivity and phase

Multi-objective particle swarm optimization (MOPSO) nomenclature		
$\boldsymbol{f(m)}$		Vector of the multi-dimensional objective function
PF		Pareto Front
P^*		Pareto optimal set
$\boldsymbol{\sigma_\phi}$		Error of the generic observed data ϕ
RI	%	Repository index
SP		Spacing
α	°	Deviation angle between the bisector of the objective space (with slope 1) and the Theil-Sen regression line

Acronyms

AI	Artificial intelligence
CSI	Computational swarm intelligence
EC	Evolutionary computation
GA	Genetic algorithm
HPC	High performance computing

MOEA	Multi-objective evolutionary computation
MOPSO	Multi-objective particle swarm optimization
MT	Magnetotelluric
NLCG	Non-linear conjugate gradient
NRMSE	Normalized root-mean-square error
NSGA-III	Non-dominated sorting genetic algorithm-III
PSO	Particle swarm optimization
RMSE	Root-mean-square error
SI	Swarming intelligence
SVD	Singular value decomposition
TDEM	Time-domain electro-magnetic
TE	Transversal electric
TM	Transversal magnetic
VES	Vertical electric sounding
WAL	Weaver et al. (2000)
WALDIM	Martì et al. (2009)

Chapter 1

Introduction

1.1 Motivation and background

Geothermal resources represent one of the most powerful and fascinating natural renewable resources because they are based on the heat stored in the Earth's interior. The increasing number of applications of geothermal energy, from electric power generation to district heating, can play a pivotal role in addressing the Sustainable Development Goals (SDGs) listed by the United Nation General Assembly in 2015 and endorsed by the scientific community. Geothermal resources are encompassed in SDG number 7, which is to "ensure access to affordable, reliable, sustainable and modern energy for all". The global agreement of the Conference of the Parties 21 held in Paris in 2015 announced the need for global and urgent actions for the mitigation of climate change, limitation of the world-temperature growth and de-carbonization.

One of the most extraordinary geothermal resources in the world is the Larderello-Travale geothermal area (LTGA), located in south Tuscany, Italy. LTGA is traditionally said to be the place where geothermal exploration began in 1913 and represents a milestone for the exploitation of geothermal resource for electric power production. The area has been the object of vast industrial and scientific research over the past century. Nonetheless, some geological, physical and chemical aspects of LTGA are still a matter of research and debate.

One of the greatest challenges in the exploration of the deep geothermal reservoir is to provide novel drilling and investigation technologies to reach the geothermal deep fluids at supercritical conditions (high temperature and pressure) in the continental crust. The deep supercritical conditions are today under exploration in the Larderello field, in the framework of the pioneering deep-drilling project DESCRAMBLE. The first evidence of supercritical conditions resulted in 2017 from the drilling test in *Venelle-2* well, where 510 °C and 300 bar were measured at a depth of 2.9 km (DESCRAMBLE project – EU H2020;

Bertani et al. 2018). The intrinsic geological and hydrogeological complexity of the LTGA makes challenging the geoscientific characterization of the geothermal system. Geophysical exploration is of crucial importance to increase our knowledge of geothermal systems.

Seismic, gravity and magnetic surveys can provide valuable information on the shape, size, depth and interfaces of the constituting structures of the geothermal system in terms of velocity of the elastic waves, density and magnetic susceptibility. However, they are not completely accurate for the individuation of the geothermal fluids, which are the main exploration target. Electrical and electromagnetic (EM) prospections are far more suitable for detecting the occurrence and placement of hydrothermal circulation. EM methods have been recognized to best characterize the geothermal features (Pellerin et al. 1996). Specifically, the clay-cap appears to be properly detected by controlled-source audio-magnetotelluric (CSAMT) and transient EM (TEM) data. The underlying deep reservoir is effectively imaged by deploying the magnetotelluric (MT) method.

MT is one of the most effective geophysical techniques for the investigation of deep geothermal systems because it can recover the electrical-resistivity distribution of the Earth at depths ranging from a few meters to hundreds of kilometers (Pellerin et al. 1996; Muñoz 2014). The geothermal system is usually a volume of hot permeable rocks and faults and /or fractures where the conductive geothermal fluid circulates. The variation of the resistivity distribution of the subsurface can reveal the essential features of the geothermal system in order to identify and characterize the heat source, hot fluid circulation and the deep structures hosting the geothermal reservoir.

The MT inverse problem is ill-posed in nature with nonlinear and equivalent solutions, meaning that many models can equally fit the data (within a certain tolerance threshold). Various inversion algorithms have been proposed in the literature to solve the one-dimensional (1D), two-dimensional (2D) and three-dimensional (3D) MT inverse problem (Siripunvaraporn 2012). The standard approach in geophysics is iterated and linearized inversion, which deploys derivative-based local-search algorithms. However, to solve the inverse problem, it is also possible to adopt the global search approach, which performs stochastic inverse modeling by adopting the Monte-Carlo or metaheuristic methods (Sen and Stoffa 2013). Global search methods have become of major interest in geophysics because they are theoretically able to find the global minimum of a function as the final solution without being trapped in one of several local minima. Moreover, the high computational load of global search methods, which was one of the major issues of the past, is gradually being overcome thanks to the striking improvements in computer efficiency and the increasing accessibility to clusters or cloud computing.

In the MT literature so far, global search methods have received scant attention and have been applied to the 1D inverse problem (e.g., Santilano 2017).

Their application to the 2D MT problem has not yet been investigated, except for the single contribution of Everett and Schulz (1993). Therefore, the development of a metaheuristic method to solve the 2D MT inverse problem represents a novelty in the framework of the existing MT inversion techniques. Given the under-determined nature of the inverse problem and given the extreme complexity of the structures within the Earth's crust, forward and inverse modeling is not an easy task. In the past decades, a number of algorithms have been developed with their underlying assumptions and limitations. Metaheuristics represents a completely different approach to address the problem, with the potential advantages of providing complete sampling of the search space of the solutions independence from the starting model and robustness with respect to local solutions. Moreover, deploying 2D stochastic inverse modeling to interpret MT data from geothermal areas can have great potential for the characterization of the geothermal system, mostly in those cases where the geological complexity and the difficulty in retrieving reliable external constraints (e.g., from well-log or other geophysical methods) can negatively affect the solution of the inverse problem.

The last decade has seen the rapid development of 3D MT inversion codes, few of which have been made available to the electromagnetic academic community (Siripunvaraporn 2012). 3D MT inversion is nowadays of pivotal importance for the characterization of the geoelectrical structures from geothermal areas (Piña-Varas et al. 2014; Lindsey et al. 2015). The LTGA has been investigated by a number of geophysical surveys during the past decades, but no work to date has focused on the 3D inversion of MT data from the Travale geothermal area.

1.2 Thesis objectives

Considering the key role of the resistive structures inferred by MT surveys in geothermal areas, this doctoral thesis:

a) Explores the application of stochastic inverse modeling to 2D MT data and examines its effectiveness, advantages and challenges. A new methodology is proposed and is based on computational swarm intelligence. This methodology seeks to overcome the main limitations of the local search approach. The main limitations are that the final solution can easily be trapped in one of the several local minima and can also be strongly biased by the initial assumption of the starting model. These two drawbacks can potentially become of crucial importance for the interpretation of MT data from geothermal areas, such as the LTGA. The scientific challenge addressed by the proposed method is twofold: overcoming the computational load and characterizing a complex electrical-resistivity distribution in the subsurface of the LTGA.

b) Provides new insight into the deep structures of the Travale geothermal system by means of 3D MT inversion, which is the current hot topic in the

MT field. Introducing 3D MT inversion made it possible to recover the "vintage" MT data set of Travale, which so far has only been 2D interpreted. The 3D resistivity model of the Travale geothermal system offers an updated contribution to the definition of dimension and spatial orientation of the deep structures as well as of their role in the geothermal system.

1.3 Thesis outline

The structure of this thesis reflects the work of the three years of the doctorate program and takes the form of eight chapters. A schematic view of the work plan is drawn in Figure 1.1.

After this opening chapter, Chapter 2 begins by laying out the theoretical tenets of the MT method and how the electrical resistivity distribution of the subsurface can be estimated from MT data. The chapter describes the MT transfer functions, i.e., the MT complex tensors, and how their properties change depending on the underlying geoelectrical structures. Close attention is paid to the methods that retrieve the geoelectrical dimensionality and directionality from the MT tensors, since dimensionality analysis is the preliminary step to correctly interpret the data.

Chapter 3 first provides an overview of computational swarm intelligence and, more in detail, of the algorithm particle swarm optimization (PSO). As stated in Section 1.2, a main objective of this project is to demonstrate the advantages of stochastic inverse modeling in MT. Chapter 3 explains how to apply PSO to the one-dimensional (1D) MT inverse problem and to the correction of the static shift. The remaining part of the chapter presents a novel method developed for the joint optimization of multiple geophysical data sets by means of multi-objective optimization methods (MOPSO and genetic algorithm). Details of the joint-optimization results are provided in Appendix A and are extracted from Pace et al. (2019b).

The application of PSO to the 2D MT inverse problem is discussed in Chapter 4 and is based on Pace et al. (2019a). The chapter begins by presenting the main aspects adopted for a correct implementation of PSO to properly address the complexity of the 2D MT inverse problem. Particular attention is paid to a detailed sensitivity analysis of the input arguments of the algorithm. The chapter goes on to validate the optimization method on two synthetic examples of 2D MT data of different complexity. The PSO is also applied to MT field data, the COPROD2 data set, that is the benchmark to test new 2D MT inversion methods. Finally, the chapter discusses the computational aspects of PSO.

The core of the investigation of this thesis is the geothermal area of Larderello-Travale and is discussed in Chapter 5. The first sections of this chapter outline a detailed geothermal, geological and geophysical framework of the Travale geothermal system. Then, the MT data set acquired in the past is recovered and accurately analyzed in terms of geoelectrical dimensionality, phase tensor properties and strike direction. A complete overview of the MT data set is provided in Appendix B. Chapter 5 ends with the correction of the static shift occurring for some MT apparent-resistivity curves by means of time-domain electromagnetic (TDEM) data. TDEM soundings were acquired during a field survey in 2019 and are entirely supplied in Appendix C.

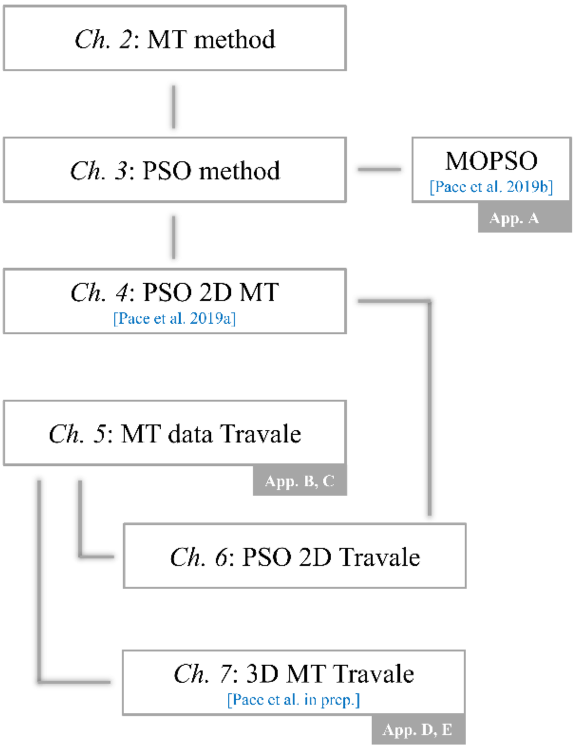

Figure 1.1 Schematic view of the thesis plan.

Chapter 6 focuses on the 2D stochastic inverse modeling of two MT profiles located in the Larderello and Travale areas, respectively. The adopted method is PSO of 2D MT data, presented in Chapter 4. As described in Chapter 5, the MT data were acquired in 1992 and 2004 as part of two different projects for exploration and research purposes, respectively (European INTAS project).

The 3D MT inversion of the data set presented in Chapter 5 is analyzed in Chapter 7. The 3D MT inversion was computed using the ModEM software, which is available for the EM research community (Kelbert et al. 2014). The inversion scheme of ModEM is based on nonlinear conjugate gradient. Both the inversion settings and the result analysis were arranged in 3D-GRID Academic, a supporting tool kindly provided by prof. N. Meqbel for research purposes. The final result can be considered the first 3D resistivity model of the Travale geothermal system derived by complete 3D MT inversion. Details on the outcome are drawn in Appendices D and E.

Chapter 2

The magnetotelluric method

This chapter presents the generalities of the magnetotelluric method. Firstly, the theoretical tenets of the method are explained together with the ruling equations. Then, the chapter describes how to process and analyze the measured data. Close attention is paid to the dimensionality analysis, the preliminary step to correctly interpret the data. The final section deals with the state of the art of the methods used for the forward and inverse modeling.

2.1. Introduction

The magnetotelluric (MT) method is a passive electromagnetic (EM) technique that measures the electrical (***E***) and magnetic (***B***) fields naturally occurring on the Earth's surface in order to determine the electrical conductivity of the Earth at depths ranging from some meters to hundreds of kilometers.

Differently from active geoelectric techniques, the MT method utilizes the natural geomagnetic variations as a passive power source for electromagnetic induction in the Earth. The origin of these low-amplitude natural fluctuations is external and lies, for the period range 1-10^5 s, in the interaction between the solar wind and magnetosphere and, for the period range 10^{-3} - 1 s, in the meteorological activity such as lightning discharges (see Figure 2.1). A portion of this external energy, or electromagnetic field, reaches the Earth's surface and penetrates it, being the Earth a conductor. This induces an electric field, or telluric currents, that produce a secondary magnetic field. The MT method simultaneously measures these ***E*** and ***B*** fields in orthogonal directions on the surface of the investigation area. The conductivity distribution of the underlying material as well as the periodicity of the source influence the depth of investigation.

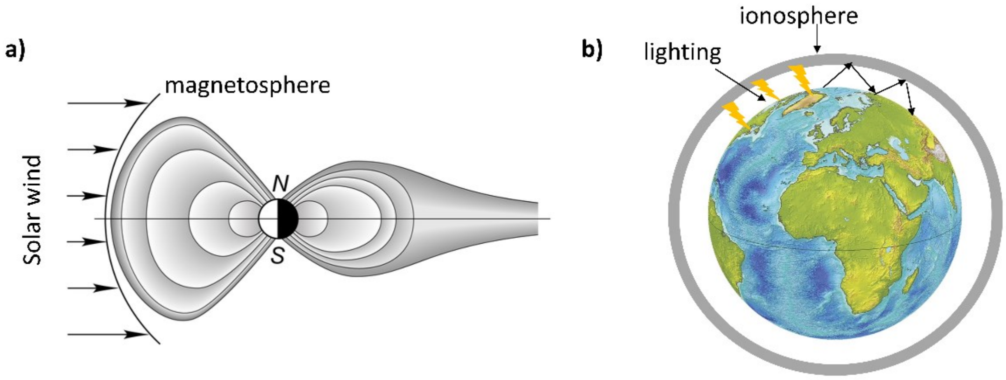

Figure 2.1 Natural sources of EM fields recorded in MT; **a) The i**nteraction between the solar wind and Earth's magnetic field creates the magnetosphere, which acts as source of fields between 1 and 10^5 s (i.e., below 1 Hz) (modified from em.geosci.xyz); **b)** the EM fields at periods below 1 s are generated by lighting activity and are plane waves bouncing between the Earth's surface and the ionosphere.

The fundamentals of magnetotellurics took place in the works of Tikhonov (1950, reprinted 1986) and Cagniard (1953). After decades of striking improvements regarding acquisition, processing and modeling techniques, an extensive explanation of the MT theory and practice can be found in Simpson and Bahr (2005), Berdichevsky and Dmitriev (2008), Zhdanov (2009) and Chave and Jones (2012). The last developments allowed MT to be placed alongside other geophysical methods such as seismology (Dupis 1997). MT has increasingly been adopted in geological applications, oil and gas reservoirs, geothermal resources, space weather as well as studies about faults, groundwater, ocean-bottom and metalliferous ores (Simpson and Bahr 2005).

2.2. Fundamentals of the MT method

The propagation of the electromagnetic field and its interaction with the Earth's interior are governed by the Maxwell's equations. For a polarizable and magnetisable medium, they can be expressed in differential form as:

$$\nabla \times \boldsymbol{E} = -\frac{\partial \boldsymbol{B}}{\partial t}, \qquad \text{Faraday's law} \qquad (2.1)$$

$$\nabla \times \boldsymbol{H} = \boldsymbol{j} + \frac{\partial \boldsymbol{D}}{\partial t}, \qquad \text{Ampere's law} \qquad (2.2)$$

$$\nabla \cdot \boldsymbol{D} = \eta_f, \qquad \text{Gauss' law for electricity} \qquad (2.3)$$

$$\nabla \cdot \boldsymbol{B} = 0, \qquad \text{Gauss' law for magnetism} \qquad (2.4)$$

where bold letters are vectors and specifically: $\boldsymbol{E}$ is the electric field (in $\mathrm{Vm^{-1}}$), $\boldsymbol{B}$ is magnetic induction (in T), $\boldsymbol{H}$ is the magnetic field (in $\mathrm{Am^{-1}}$), $\boldsymbol{D}$ is electric displacement (in $\mathrm{Cm^{-2}}$), $\boldsymbol{j}$ is the electric current density (in $\mathrm{Am^{-2}}$) and η_f is the electric charge density owing to free charges (in $\mathrm{Cm^{-3}}$). Curl ($\nabla \times$) and divergence ($\nabla \cdot$) are vector calculus expressions.

For a linear and isotropic medium, the constitutive relationships say:

$$\boldsymbol{j} = \sigma \boldsymbol{E}, \qquad \text{Ohm's law} \qquad (2.5)$$

$$\boldsymbol{B} = \mu \boldsymbol{H} \qquad (2.6)$$

$$\boldsymbol{D} = \varepsilon\boldsymbol{E} \tag{2.7}$$

where σ is the electrical conductivity of the medium (in $\mathrm{Sm^{-1}}$), μ is the magnetic permeability (in $\mathrm{Hm^{-1}}$) and ε is the dielectric permittivity (in $\mathrm{Fm^{-1}}$). All these properties are scalar. In MT, the variations of μ and ε are assumed negligible compared with variations of σ, which is the reciprocal of the electrical resistivity ρ (in Ωm).

The other main simplifying assumptions of the MT method for electromagnetic induction in the Earth are

1. The electric displacement ($\boldsymbol{D}$) is quasi-static due to the very low frequencies of MT sounding acquisitions. This means that $\partial\boldsymbol{D}/\partial t$ is negligible compared with $\boldsymbol{j}$ and that the EM induction in the Earth can be treated as a pure diffusive process.
2. The plane-wave assumption states that the natural EM field arriving on the Earth's surface can be treated as uniform and plane-polarized electromagnetic wave with an orthogonal incidence on the Earth's surface (Vozoff 1972). The reason is that the source of the EM field is the ionosphere, which is far away from the point of the MT measurement. The consequence of the assumption of time invariance of the exciting source is that the relationship between $\boldsymbol{E}$ and $\boldsymbol{B}$ should be self-similar at any given site, independently of the day they are recorded.

After these considerations, the Maxwell's equations can be rewritten in the form:

$$\nabla \times \boldsymbol{E} = -\frac{\partial \boldsymbol{B}}{\partial t} \tag{2.8}$$

$$\nabla \times \boldsymbol{B} = \mu_0\sigma\boldsymbol{E} \tag{2.9}$$

$$\nabla \cdot \boldsymbol{E} = \frac{\eta_f}{\varepsilon} \tag{2.10}$$

$$\nabla \cdot \boldsymbol{B} = 0 \tag{2.11}$$

where the magnetic permeability is assumed in free space ($\mu_0 = 4\pi\cdot 10^{-7}\ \mathrm{Hm^{-1}}$).

In order to estimate the distribution of conductivity in the subsurface, we can take the curl of equation 2.8 and 2.9, considering the harmonic form for $\boldsymbol{E}$ and $\boldsymbol{B}$, and, after some algebra, derive the diffusion equations:

$$\nabla^2\boldsymbol{E} = i\omega\mu_0\sigma\boldsymbol{E} \tag{2.12}$$

$$\nabla^2\boldsymbol{B} = i\omega\mu_0\sigma\boldsymbol{B} \tag{2.13}$$

where ω is the angular frequency ($\omega = 2\pi f = 2\pi/T$, being f the frequency and T its reciprocal, the period). Equations 2.12 and 2.13 imply that the energy that diffuses through the Earth is exponentially dissipated. This decay can be quantified by the *skin depth* or *penetration depth* δ (in m), the depth at which the EM field decays to $1/e \approx 37\%$ (Vozoff 1991):

$$\delta(T) = \sqrt{\frac{2}{\omega\mu_0\sigma}} \approx 503\sqrt{\rho T} \tag{2.14}$$

Data acquired at periods from 10^{-4} to 1 s refer to the shallow subsurface (i.e., up to some tens of meters of depth), while the penetration depth increases for periods up to 10^5 s. Although the longer the period of acquisition the higher the depth of investigation, at longer periods the data resolution decreases. Moreover, the skin depth depends on the subsurface conductivity distribution. The maximum skin depth theoretically reaches hundreds of kilometers, but it can drop if the overlying sample of Earth is highly conductive. The MT method is hence highly competitive in imaging deep conductive bodies surrounded by more resistive structures.

The electrical resistivity (ρ) of the rocks in the lithosphere and asthenosphere spans seven orders of magnitude between 10^{-2} Ωm and 10^{5} Ωm (Figure 2.2). These values result from chemical and physical processes and depend on the temperature, pressure, mineralogy, porosity and multi-phase systems (saturation, salinity of the fluid phase or partial melt fraction). A thorough analysis can be found in Jones (1992) and Evans (2012).

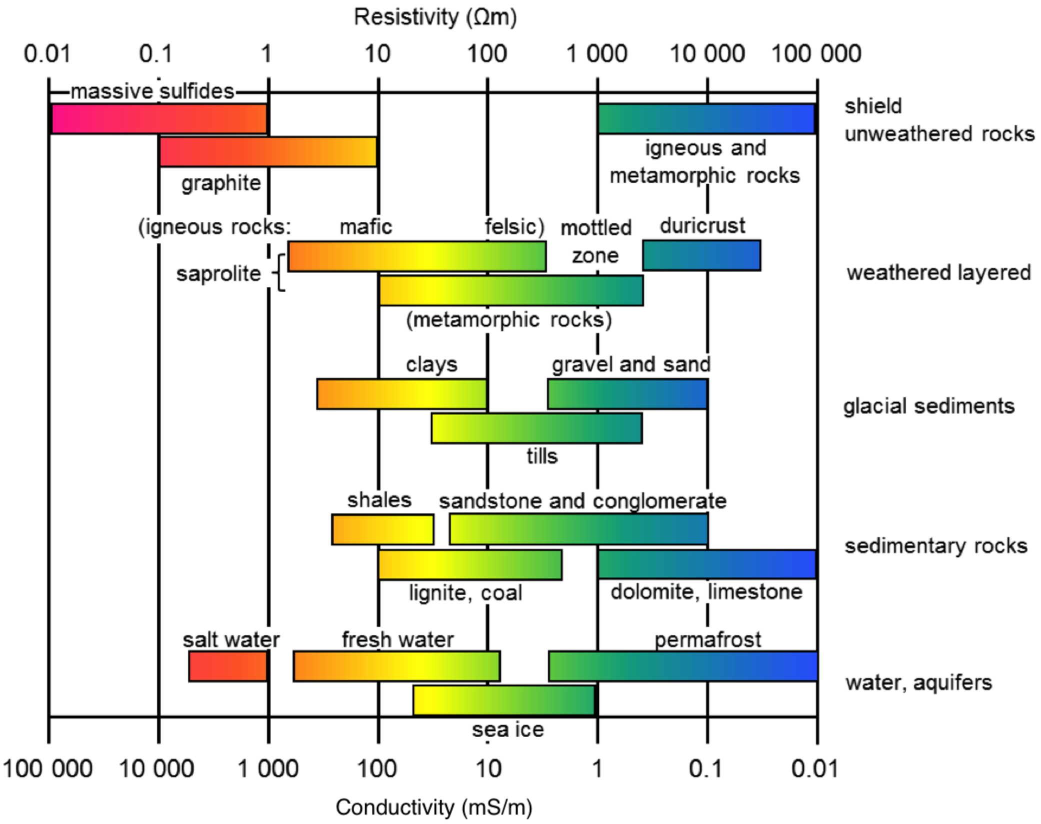

Figure 2.2 Electrical resistivity (Ωm) of the Earth's materials (source:https://em.geosci.xyz/content/physical_properties/electrical_conductivity/electrical_conductivity_values.html)

2.3. MT transfer functions

The MT method measures, at a given site, the variations with frequency of five components of the EM field. As can be seen from Figure 2.3, they are the horizontal electric components (E_x and E_y) and the horizontal (B_x, B_y) and vertical (B_z) magnetic components. The magnetotelluric transfer functions are tensor relationships between the electric- and magnetic-field orthogonal components as a function of the frequency. The fundamental MT transfer functions are the following complex tensors: the impedance tensor $\underline{Z}(\omega)$ (Ω), the magnetotelluric tensor $\underline{M}(\omega)$ (m/s) and the geomagnetic transfer function $\boldsymbol{T}(\omega)$ (dimensionless). The components of these transfer functions are complex values and allow the resistivity distribution of the subsurface to be estimated as a function of depth.

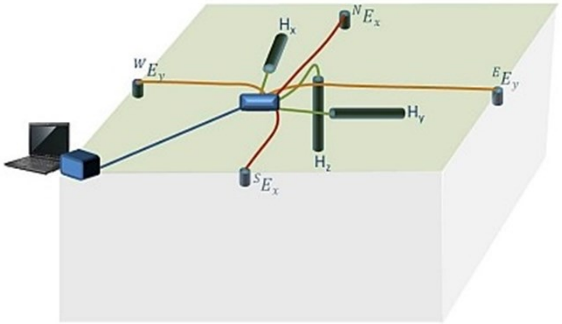

Figure 2.3 Typical setup for MT data acquisition (modified from https://www.gfz-potsdam.de). Three induction coils or magnetometers measure the orthogonal components of the magnetic field (B_x, B_y and B_z). Two pairs of electrodes measure the orthogonal components of the electric field (E_x and E_y). The reference frame is usually oriented to the geographic north.

2.3.1 The impedance and MT tensor

The impedance tensor $\underline{Z}(\omega)$ is a second rank tensor (2 x 2) that links the horizontal components of $\boldsymbol{E}$ and $\boldsymbol{H}$ (Cantwell 1960). At a given frequency, considering equation 2.6:

$$\begin{pmatrix} E_x(\omega) \\ E_y(\omega) \end{pmatrix} = \begin{pmatrix} Z_{xx} & Z_{xy} \\ Z_{yx} & Z_{yy} \end{pmatrix} \cdot \begin{pmatrix} B_x(\omega)/\mu_0 \\ B_y(\omega)/\mu_0 \end{pmatrix} \qquad (2.15)$$

The Z_{ij} components (ij = xx, xy, yx, yy) are complex values that can be decomposed into two scalar magnitudes, the modulus and the phase. The modulus is called *apparent resistivity* ρ_a (Ωm):

$$\rho_{a_{ij}}(\omega) = \frac{1}{\mu_0 \omega} \left| Z_{ij}(\omega) \right|^2 \qquad (2.16)$$

The impedance phase φ (°) is

$$\varphi_{ij}(\omega) = \tan^{-1}\left(\frac{Im(Z_{ij}(\omega))}{Re(Z_{ij}(\omega))} \right) \qquad (2.17)$$

Apparent resistivity and phase are the two fundamental MT measurements for data interpretation. The physical meaning of the apparent resistivity is not the absolute resistivity of the medium but the average resistivity of the equivalent uniform half-space. The phase changes according to the increasing or decreasing resistivity with depth, thus providing additional information about the surrounding geoelectrical structures investigated.

The magnetotelluric tensor $\underline{M}(\omega)$ relates the electric field and the magnetic induction (Weaver et al. 2000):

$$\begin{pmatrix} E_x(\omega) \\ E_y(\omega) \end{pmatrix} = \begin{pmatrix} M_{xx} & M_{xy} \\ M_{yx} & M_{yy} \end{pmatrix} \cdot \begin{pmatrix} B_x(\omega) \\ B_y(\omega) \end{pmatrix} \qquad (2.18)$$

2.3.2 The geomagnetic transfer function

The geomagnetic transfer function or, briefly, tipper vector ***T(ω)*** relates the vertical component of the magnetic field to its two horizontal components:

$$B_z(\omega) = \left(T_x(\omega), T_y(\omega)\right) \cdot \begin{pmatrix} B_x(\omega) \\ B_y(\omega) \end{pmatrix} \qquad (2.19)$$

The tipper vector can be decomposed into its real and imaginary vectors, representing the projection of B_z into the horizontal plane x-y: $\boldsymbol{T}_{re}(\omega) = \left(Re(T_x), Re(T_y)\right)$ and $\boldsymbol{T}_{im}(\omega) = \left(Im(T_x), Im(T_y)\right)$. These real vectors are graphically represented by means of the *induction arrows*, which are useful to infer the presence of lateral variations of the electrical resistivity. In the Parkinson convention, the arrows point toward the region of highest conductance, i.e., current concentrations (Parkinson 1959). Conversely, in the Weise convention, the arrows point away from conductive zones.

2.4. The MT dimensionality

The MT transfer functions can assume different shape and properties depending on the resistivity distribution of the subsurface. In fact, the tensors $\underline{Z}$ and $\underline{M}$ store information about the dimensionality and directionality of the underlying geoelectrical structures. The *geoelectrical dimensionality* can be 1D, 2D or 3D. Moreover, the presence of local (small-scale) heterogeneities in the shallow Earth's crust can generate the phenomenon of galvanic distortion, which can be removed using specific techniques.

2.4.1 Dimensionality analysis

Dimensionality analysis is fundamental to understand how to interpret the MT data and represents the preliminary step to correctly perform the MT modeling or inversion.

The case of one-dimensional (1D) Earth occurs when the resistivity changes only with depth without lateral variations. Figure 2.4 shows an example of 1D resistivity model, i.e., a horizontally-stratified Earth. The magnetotelluric tensor $\underline{M}_{1D}(\omega)$ has null components in the main diagonal and, in the secondary diagonal, equal components in modulus but opposite in sign: $M_{xx}=M_{yy}=0;\ M_{xy}=-M_{yx}$. In 1D, the Tipper vector components are both zero because there is not a net component of B_z, which does not change direction with depth (see Table 2.1).

An example of two-dimensional (2D) resistivity model is shown in Figure 2.4. The resistivity changes both with depth and along one horizontal direction (y-direction). The lateral discontinuity is directed along the x-direction and extends to infinity. The direction along with the resistivity does not change (x-direction) is called the *geoelectrical strike*. In correspondence of the vertical contact, the resistivity variation from ρ_1 to ρ_2 causes a discontinuity in E_y because of the principle of conservation of current (Ohm's law of equation 2.5). The assumption of 2D implies that all the variations of the fields parallel to the strike are zero and that the electric and magnetic fields are orthogonal, namely, polarized in parallel or perpendicular to the strike. For this reason, the two fields can be decoupled into two independent modes:

a) The transverse-electric mode (or *TE* polarization) in which the electric field (and the current flowing) is parallel to the strike
b) The transverse-magnetic mode (or *TM* polarization) in which the magnetic field is parallel to the strike and the electric currents cross the structures.

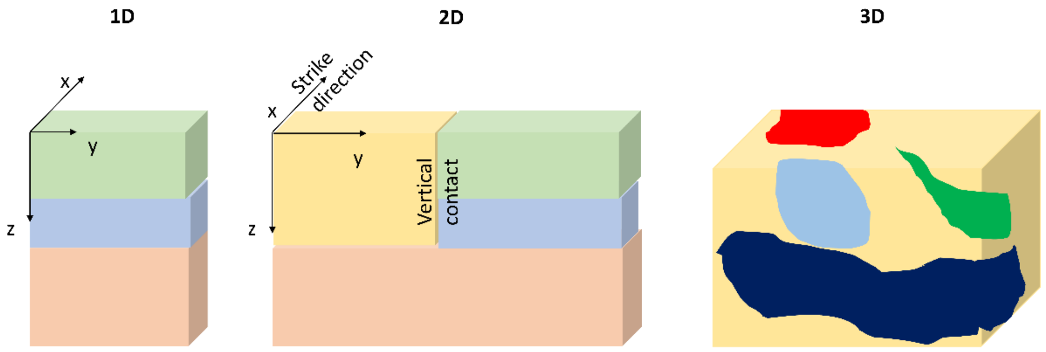

Figure 2.4 1D, 2D and 3D resistivity models as conceived in MT to infer the geoelectric dimensionality. The different colors of the blocks stand for different resistivity values. The 2D case shows the vertical contact striking in the x-direction and determining the two-mode polarizations of the electromagnetic fields (TE and TM).

If the reference frame of the MT survey coincides with the strike of the 2D structure, the magnetotelluric tensor is anti-diagonal (i.e., zero components in the main diagonal): $M_{xx}=M_{yy}=0$; $M_{xy}= M_{TE}$; $M_{yx} = M_{TM}$. The Tipper component aligned with the strike is null ($T_x = 0$), while the real and imaginary parts of the other vector component (T_x) are perpendicular to the strike (see Table 2.1) and parallel but oppositely-directed with each other. In some real 2D cases, the MT survey is not carried out following the strike direction, which can be unknown or ambiguous. As a consequence, the transfer function components are never zero. To fix that, the tensor $\underline{M}_{2D}(\omega)$ is usually rotated into a coordinate frame parallel and perpendicular to the strike $\underline{M}'_{2D}(\omega)$ so that the main diagonal components are nulled.

In a three-dimensional (3D) resistivity model there are variations along all the three directions, as illustrated in Figure 2.4. All the components of $\underline{M}(\omega)$ are independent of each other and there is no available rotation of the tensor to yield null components (see Table 2.1).

Table 2.1 The magnetotelluric tensor $\underline{M}(\omega)$ assumes different configurations according to the resistivity distribution in the subsurface (1D, 2D, 3D). $\boldsymbol{M}_{\parallel}$and $\boldsymbol{M}_{\parallel}$ refers to the components parallel and perpendicular to the strike direction, respectively.

	Dimensionality		
	1D	***2D***	***3D***

Tensor components	$M_{xx}=M_{yy}=0$	$M_{xx}=-M_{yy}$	$M_{xx}\neq -M_{yy}$
	$M_{xy}=-M_{yx}$	$M_{xy}\neq -M_{yx}$	$M_{xy}\neq M_{yx}$
MT tensor	$\begin{pmatrix} 0 & M \\ -M & 0 \end{pmatrix}$	$\begin{pmatrix} 0 & M_{\parallel} \\ M_{\perp} & 0 \end{pmatrix}$	$\begin{pmatrix} M_{xx} & M_{xy} \\ M_{yx} & M_{yy} \end{pmatrix}$
Tipper	$T_x = T_y = 0$	$T_{\parallel} = 0; T_{\perp} \neq 0$	$T_x \neq T_y \neq 0$

The geoelectrical dimensionality of a given MT data set can be recovered by means of different valid approaches. The most established methods are:

1. The Bahr's parametrization (Bahr 1991): it proposes some dimensionality parameters, such as the Swift's skew (κ), the regional 1D indicator (μ) and the regional skew (η), in order to check whether the magnetotelluric tensor could be described by a general physical model, such as 1D model or the more complex superimposition model of a regional 2D model with a local 3D structure on surface. The limitation of this method is that the threshold values indicated for κ, μ and η to classify the dimensionality have no mathematical meaning. As proved in Ledo et al. (2002b), Martì et al. (2005) and Simpson and Bahr (2005), Bahr's criteria are not sufficient to correctly characterize the dimensionality.
2. The WAL method (Weaver et al. 2000): it is based on the values assumed by seven independent plus one dependent rotational invariants, which are derived from the observed magnetotelluric tensor independently from the direction of the measuring axes. The dimensionality is inferred by the number of invariants that vanished. The main limitation of this method is that the invariants rarely vanish in case of field data, thus potentially yielding to incorrect dimensionality inferences.
3. The WALDIM approach (Martì et al. 2005; Martì et al. 2009) revised the WAL method to overcome its limitations and make the dimensionality analysis consistent. This method introduces new statistically-proved threshold values below which the invariants are regarded as nulled. By redefining the conditions, the issues of misinterpretation or undetermined dimensionality has been solved.

Other common methods for the dimensionality analysis are: the strike decomposition (McNeice and Jones 2001), the Mohr circle (Lilley and Weaver 2010) and the phase tensor (Caldwell et al. 2004), which is analyzed in Section 2.4.3.

In this thesis, the dimensionality analysis of MT data was performed following the WALDIM method, because it represents the most recent approach and overcomes the limitations of the previous ones. The WALDIM software (written in Fortran) analyzes the observed magnetotelluric tensor with the associated data errors, calculates the WAL rotational invariants and, obeying the threshold values, estimates the complete geoelectrical dimensionality at single or bands of period for each MT site (Martì et al. 2009). The output is classified into one of eight possible dimensionality types:

a) 1D
b) 2D
c) 3D/2D twist: 2D regional structure affected by galvanic distortion only in the twist parameter
d) 3D/1D2D: 1D or 2D structure affected by galvanic distortion and strike direction non-recoverable
e) 3D/1D2D diag.: 1D or 2D structure affected by galvanic distortion and diagonal MT tensor
f) 3D/2D: general case of galvanic distortion over a regional 2D structure
g) 3D affected or not by galvanic distortion
h) undetermined dimensionality.

Chapter 5 reports the result of the dimensionality analysis of the MT data set of the Travale geothermal area.

2.4.2 Galvanic distortion

The dimensionality analysis described in the previous section can be also used to understand whether the data are affected or not by galvanic distortion, which can be appropriately retrieved and corrected (Martì et al. 2009).

As previously mentioned, small-scale conductivity contrasts in the shallow subsurface can generate a distortion in the impedance tensor $\underline{Z}(\omega)$. In fact, the heterogeneities localized in the near-surface distort the EM response produced by the underlying or "regional" structure under investigation. As the period of the MT sounding increases, and the skin depth as well, the inductive effects produced by the near-surface heterogeneities decrease and become negligible compared to the inductive response produced by the regional conductivity structure. Then, as the skin depth exceeds the dimension of the near-surface heterogeneities, only their frequency-independent galvanic (non-inductive) response remains. This galvanic distortion is also called *static shift*. It is static because it is not time-dependent and it does not affect the phase of the transfer functions. It results hence in a "shift" of the apparent-resistivity curve to higher or lower values by a constant, real scaling factor, thus preserving the same shape of the recorded apparent-resistivity curve (Jones 1988; Chave and Jones 2012).

The main reason for the correction of galvanic distortion is that the main target of an MT exploration survey is the (deep) regional structure. It is hence fundamental to manage the measured magnetotelluric tensor to remove the effects of distortion and recover the regional responses. A number of established techniques have been proposed to recover the undistorted transfer functions over 1D or 2D structures (Zhang et al. 1987; Bahr 1988; Groom and Bailey 1989; Smith 1995). The decomposition technique of Groom and Bailey (1989) represents the benchmark for the analysis and removal of the galvanic distortion caused by a 2D structure on a regional scale. This decomposition separates the effects of 3D current channeling occurring on the surface of shallow bodies from those of 2D induction.

The galvanic distortion is treated as an anomalous electric field, which deviates the magnetotelluric tensor from its regional value ($\underline{M}_R(\omega)$) due to local variations. The observed tensor ($\underline{M}_{obs}(\omega)$) is related to the regional one by means of the distortion tensor $\boldsymbol{C}$, which is real and frequency-independent:

$$\underline{M}_{obs}(\omega) = \boldsymbol{C} \cdot \underline{M}_R(\omega) \qquad (2.20)$$

In the general case, the reference frame of the observed tensor may not correspond to the reference frame of the regional or principal axes system. In the measurement axes system, the regional tensor ($\underline{M}_{2D}(\omega)$) is rotated through an angle θ by means of the rotation matrix R_θ:

$$\underline{M}_{obs}(\omega) = R_\theta \cdot \boldsymbol{C} \cdot \underline{M}_{2D}(\omega) \cdot R_\theta^T \qquad (2.21)$$

In a 2D problem, the measurement reference frame is rotated by θ from the regional strike direction.

The Groom and Bailey's decomposition technique factorizes the distortion tensor into four independent parameters (three tensors and a scalar):

$$\boldsymbol{C} = g\,\boldsymbol{T} \cdot \boldsymbol{S} \cdot \boldsymbol{A} \qquad (2.22)$$

where: g is the site gain, T is the twist, S is the shear and A is the anisotropy. Twist and shear refer to the orthogonality of the electric and magnetic fields, whereas anisotropy and gain are related to the static shift. However, given the ill-posedness of the problem, the Groom and Bailey's decomposition does not allow to uniquely determine the static shift. The amplitudes of the regional impedances remain undetermined even after the tensor decomposition. Since it is not possible to analytically or numerically correct the static shift by using only MT data, it is necessary to refer to external information.

The correction of the static shift represents one of the major drawbacks of the MT data analysis, since it requires to invoke either other geophysical methods less affected by distortion or geological information. Various techniques have been investigated to correct the static shift: joint analysis of MT and time domain electromagnetic (TDEM) data (Sternberg et al. 1988; Meju 1996; Meju 2005), correction by comparison with well-log data (Jones 1988), correction by using the geomagnetic transfer function (Ledo et al. 2002a) and correction by considering the static shift as an additional parameter of the inverse problem (deGroot-Hedlin 1991; Ogawa and Uchida 1996). A review of these methods can be found in Ogawa (2002) or Simpson and Bahr (2005).

In this work, we adopted the joint analysis of TDEM and MT data. TDEM data were acquired in order to assess the occurrence and, if needed, correct the static shift. The basic principles of the TDEM method are described in Section 2.5, while the correction of static shift of field data is provided in Section 3.3.2.

2.4.3 Phase tensor analysis

The analysis of the magnetotelluric phase tensor to infer the dimensionality of the regional structure was introduced by Caldwell et al. (2004) and then reviewed by Booker (2014). The phase tensor is defined as the relationship between the real and imaginary parts of the MT tensor $\underline{M}(\omega)$, that are not affected by galvanic distortion.

Given that the observed complex tensor $\underline{M}(\omega)$ can be separated into its real ($\boldsymbol{X}$) and imaginary parts ($\boldsymbol{Y}$),

$$\underline{M} = \boldsymbol{X} + i\boldsymbol{Y} \qquad (2.23)$$

equation 2.20, can be written also as:

$$\boldsymbol{X} + i\boldsymbol{Y} = \boldsymbol{C}\boldsymbol{X}_{\boldsymbol{R}} + \boldsymbol{C}i\boldsymbol{Y}_{\boldsymbol{R}} \qquad (2.24)$$

The phase of a complex number is the ratio of its real and imaginary parts. Therefore, the phase tensor is defined as:

$$\boldsymbol{\Phi} = \boldsymbol{X}^{-1}\boldsymbol{Y} = \boldsymbol{\Phi}_{\boldsymbol{R}} \qquad (2.25)$$

which is a 2x2 real-component tensor, independent from the distortion matrix $\boldsymbol{C}$ and hence from the dimensionality of the regional structure. It is worth noting that dealing with the phase tensor does not require any assumption about the geoelectrical dimensionality.

The phase tensor is characterized by one direction α and three coordinate invariants: the singular values Φ_{min} and Φ_{max} and the skew angle β. These four terms are used to write the phase tensor in the form of the Singular Value Decomposition (SVD) of a square matrix:

$$\boldsymbol{\Phi} = \boldsymbol{R}^T\,(\alpha - \beta) \cdot \begin{bmatrix} \Phi_{max} & 0 \\ 0 & \Phi_{min} \end{bmatrix} \cdot \boldsymbol{R}\,(\alpha + \beta) \qquad (2.26)$$

where: $\boldsymbol{R}(\alpha + \beta)$ represents a clockwise rotation matrix, R^T is its transpose and the angles are defined as:

$$\alpha = \frac{1}{2} tan^{-1}\left(\frac{\Phi_{12}+\Phi_{21}}{\Phi_{11}-\Phi_{22}}\right) \qquad (2.27)$$

$$\beta = \frac{1}{2} tan^{-1}\left(\frac{\Phi_{12}-\Phi_{21}}{\Phi_{11}+\Phi_{22}}\right) \qquad (2.28)$$

The direction α is related to the tensor's dependence on the coordinate system and the skew angle β measures the tensor's asymmetry.

The phase tensor assumes different values depending on the dimensionality of the regional structure. This is concisely listed in Table 2.2. In 1D, the phase tensor is diagonal, the components Φ_{min} and Φ_{max} have the same value equal to the tangent of the regional impedance phase φ (see equation 2.17) and hence the skew is null due to the tensor's symmetry. In 2D, the two components on the diagonal are not identical and corresponds to the two directions along which a linear polarization of the magnetic field leads to a linear polarization of the electric field. The principal values Φ_{min} and Φ_{max} correspond to the tangents of the impedance phases of the corresponding TM and TE polarizations. Being the tensor symmetric, the skew is null. In the general 3D case, the phase tensor is not symmetric, its components are not the same and both α and β are not null. In particular, the dimensionality is considered 3D if $|\beta| \leq 3°$. The phase tensor represents the relationship between the phases of the horizontal components of the electric and magnetic fields.

The phase tensor can be effectively represented by means of the tensor ellipse, whose major and minor axes, Φ_{max} and Φ_{min} represent the principal axes of the tensor. Figure 2.5 clearly illustrates the graphical meaning of the four SVD parameters for different dimensionality cases. In 1D, the ellipse becomes a circle of unit radius ($\Phi_{min} = \Phi_{max}$). In 2D, $\beta=0°$ is not a sufficient condition and α is null as long as the reference frame is strike-aligned, otherwise α is equal to the strike angle with respect to the observation frame of reference (x_1, x_2). The azimuth $(\alpha - \beta)$ coincides with α, which represents the strike direction or its perpendicular, depending on which mode (TE or TM) has the largest phase value. Therefore, α has a physical meaning as long as $\Phi_{min} \neq \Phi_{max}$, that is, in 2D and 3D cases. In 3D case, the asymmetry of the regional MT response is reflected by a large skew angle β. The angle $(\alpha - \beta)$ represents the direction (or azimuth) of the major axis of the ellipse and also the relationship between the tensor and the observer's reference frame (x_1, x_2).

Table 2.2 The phase tensor assumes different configurations depending on the geoelectrical dimensionality. The SVD parameters are the tensor direction α and three coordinate invariants: Φ_{min} and Φ_{max}, representing the principal axes of the tensor, and the skew angle β, representing the tensor's symmetry.

	Dimensionality		
	1D	***2D (strike-aligned)***	***3D***
Phase tensor	$\begin{bmatrix} -Y/-X & 0 \\ 0 & Y/X \end{bmatrix}$	$\begin{bmatrix} Y_{21}/X_{21} & 0 \\ 0 & Y_{12}/X_{12} \end{bmatrix}$	$\begin{bmatrix} \Phi_{11} & \Phi_{12} \\ \Phi_{21} & \Phi_{22} \end{bmatrix}$
SVD parameters	$\alpha = 0/0\ (undefined)$; $\beta = 0°$; $\Phi_{\underset{min}{max}} = \tan\varphi$	$\alpha = 0°$; $\beta = 0°$; $\Phi_{\underset{min}{max}} = \tan\varphi_{\underset{21}{12}}$	General expression (equations 2.26, 2.27, 2.28.

Caldwell et al. (2004) demonstrated that the orientation of the phase-tensor principal axes reflects the lateral variations (gradients) of the underlying regional structure. This variation can be deduced from the maps of the phase-tensor ellipses at different frequencies. If the direction of the tensor's axes is constant with period, the regional structure is 2D, whereas a rapid lateral change with period (of about 10°) is the evidence of 3D. Therefore, in 3D cases, both α and β are period-dependent.

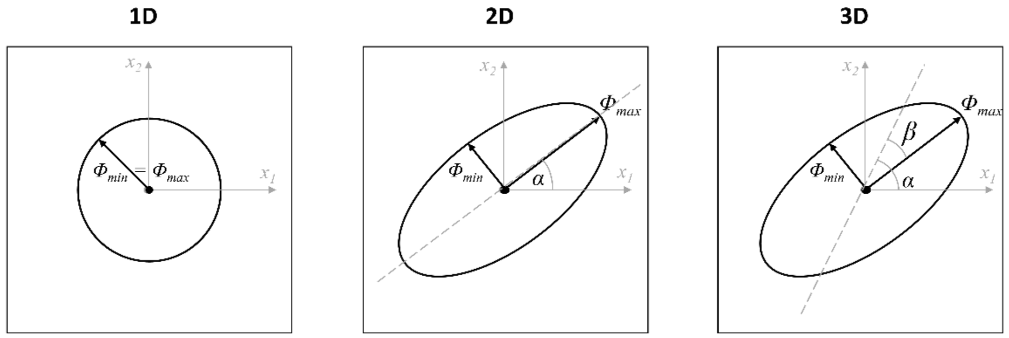

Figure 2.5 Graphical representation of the phase tensor in 1D, 2D and 3D. The lengths of the ellipse axes Φ_{min} and Φ_{max} represent the principal axes of the phase tensor. They are coincident only in 1D. The representation in 2D assumes that the coordinates coincide with the observation frame of reference. The angle β characterizes the deviation of the ellipse's major axis from the symmetry axis. β is non-zero only in 3D.

An alternative way of visualization is to depict the phase-tensor ellipse concentric with the induction arrows (namely, the real part of the vertical magnetic transfer function) (see Section 2.3.2). According to the Parkinson convention, the real part of the induction arrow points toward the region of highest conductance and is parallel to the major axis of the phase-tensor ellipse, since the direction of the major axis indicates the preferred flow direction of the induction current. However, in presence of 3D structures and at high periods, the alignment between the real induction arrow and the ellipse's major axis may not result always satisfactory due to the asymmetry of the phase tensor. Caldwell et al. (2004) provides practical examples of the simultaneous analysis of phase-tensor ellipse and induction arrows.

To sum up, the phase tensor analysis presents some advantages for a clear preview of the resistivity distribution in the subsurface because (Caldwell et al. 2004):

- it does not require any dimensionality assumption
- it is unaffected by galvanic distortion
- it reflects resistivity variations at depth with no influence from the near surface structures
- the analysis focuses on the observed tensor $\underline{M}(\omega)$ and preserves information of the regional structures
- the graphical representation of the elliptical diagrams has become an established and useful tool in MT. The maps showing the SVD parameters for each MT site at a given frequency represent a valuable indicator of the lateral variations of the regional structures. In particular, the major axis of the phase-tensor ellipse (Φ_{max}) indicates the direction of the induced current flow and it is usually parallel to the real part of the induction arrow.
- the orientation of the principal axes of the phase tensor is a generalization of the geoelectric strike to a 3D situation.

Despite the relevant advantages, the phase tensor analysis entails the ambiguity of ±90° for the determination of the strike direction. The major axes of the ellipse can be hence either parallel or perpendicular to the strike with no possibility to solve this indetermination.

Chapter 5 reports the result of the phase tensor analysis with induction arrows of the MT data set of the Travale geothermal area.

2.5. Static shift correction using TDEM

2.5.1 The TDEM method

The TDEM method, also called transient EM (TEM), is a geophysical technique based on EM induction in the Earth. TDEM soundings have been widely applied to near-surface geology, mineral prospecting, hydrogeological and environmental investigations concerning raw materials, dump sites and waste deposits (Nabighian and Macnae 1991).

The active source transmits a steady current from 1 to 20 A for some milliseconds through a loop of wire to allow a turn-on transient to be dissipated in the ground. The current has a slow rise-up to a steady value and then is interrupted by a rapid shut-off in the order of microseconds. The shut-off (or ramp-off) transient induces a secondary magnetic field, that is proportional to the decay of the electromagnetic eddy currents generated in the conductive Earth. The decay of the secondary magnetic field is measured by the receiver coil voltage and is a function of the electrical-conductivity distribution in the subsoil. The response at the receiver is usually acquired during the transmitter off-time, because the primary field signal is weak or absent. The response measured at the receiver is recorded for a number of time gates. The analysis of the transient decay of the secondary field with time allows the electrical resistivity to be estimated as a function of depth (Everett 2013; Spichak 2015).

The volume investigated by TDEM depends on the transmitted current of the source and on the length of the side of the loop, which is usually between 20 and 200 m. The transmitter and receiver can be placed on the ground according to different configurations. The “central-loop” configuration means that the transmitter and receiver loops have the same center. Alternatively, they can be located within a certain distance, according to offset geometries.

The diffusion depth represents the depth at which the local electric field (or current) reaches its maximum value and is controlled by the transient time t. The relation of the diffusion depth is (Nabighian and Macnae 1991):

$$d(t) = \sqrt{\frac{2t}{\mu_0 \sigma}} \qquad (2.29)$$

where t is the time of the response measurement after the shut-off. There is an evident similarity between the penetration depth d and the skin depth of the MT method (equation 2.14). An approximate estimation of the sounding depth is usually indicated as 3 or 4 times the side of the transmitter loop (Spichak 2015).

As evident in equation 2.29, TDEM method is extremely sensitive to conductive formations (like clay and salt water) in shallow-depth structures up to a theoretical depth of about 500 m (depending on the instrument and the sounding set up).

The basic interpretation of TDEM data is a 1D resistivity profile under the receiver position. The voltage measurement of the receiver is usually converted to apparent resistivity (ρ_a) vs time (t) according to (Spichak 2015):

$$\rho_a(t) = \left(\frac{\sqrt{\pi}}{20}\,\frac{\mu^{5/2}R^4}{t^{5/2}\,E(t)/I}\right)^{2/3} \qquad (2.30)$$

where $R = L/\sqrt{\pi}$ is the effective radius of a single-turn square loop of side L and $E(t)/I$ is the value of the normalized voltage measured at the receiver.

2.5.2 TDEM data for the correction of MT static shift

The TDEM method is commonly adopted to correct the MT static shift because it provides independent information, which is not affected by telluric distortion (Pellerin and Hohmann 1990). TDEM data have often been combined to MT data from geothermal areas even though the depth of investigation associated to TDEM data is typically much lower than that of the geothermal target (Cumming and Mackie 2010; Santilano et al. 2018).

Sternberg et al. (1988) first proposed to convert the TDEM signal to the frequency domain in order to compare the TDEM and MT apparent-resistivity curves. The TDEM curve of ρ_a vs time (see equation 2.30) provides the undistorted value of the MT ρ_a, but only at short periods because the TDEM depth of investigation is lower than that of MT soundings. However, since the distortion (or shift) is static (or period-independent), the correction provided by the TDEM ρ_a at short periods is useful for the whole MT period band. The static shift is corrected by computing joint inversion of MT and TDEM data. In this kind of inversion scheme, the static shift is accounted by including a further parameter for the vertical shift of the observed MT ρ_a.

Figure 2.6 illustrates an example of correction of the MT static shift using TDEM data (from Berdichevsky and Dmitriev 2008). The plot on the left shows the measured TDEM data (black squares from 0.001 to 0.2 s) and the observed or distorted MT data (crosses). The joint inversion of MT and TDEM data allowed the static shift to be corrected by moving the MT ρ_a curve to higher values of resistivity (ellipses) so that the two ρ_a curves perfectly matched in the period range 0.01-0.1 s. The plot on the right of Figure 2.6 displays the resistivity profiles and, specifically, the difference in the interpretation between MT distorted data (long-dashed line) and MT corrected data (short-dashed line). This curve is in agreement with the well-log profile (solid line) and with the TDEM inversion result (dotted line).

The MT data analyzed in this thesis were corrected for static shift using the method suggested in Santilano et al. (2018). Details of the optimization method are described in Section 3.3.2. The new TDEM survey and the static shift correction of the investigated MT data set are described in Section 5.5 and Appendix C, respectively.

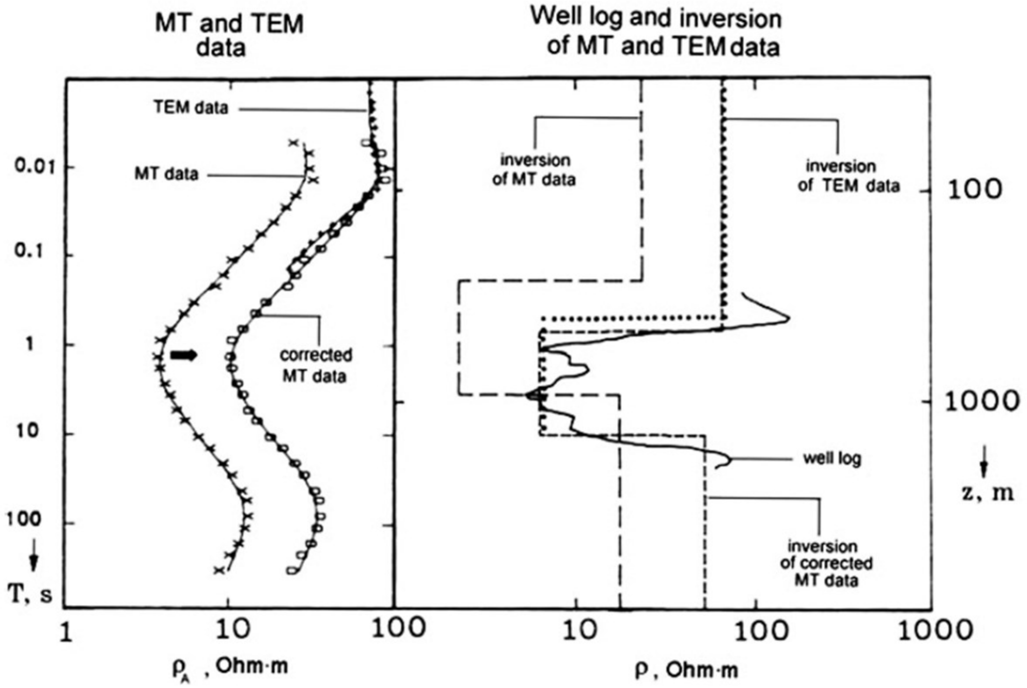

Figure 2.6 Static-shift correction of MT data using TDEM data as reference. On the left, the distorted MT data (crosses) are shifted to higher ρ_a values (ellipses) using TDEM data (black squares) at periods below 0.1 s. On the right, the resistivity profile derived from well-log data (continuous line), inversion of MT distorted data (long-dashed line), of TDEM data (dotted line) and of MT corrected data (short-dashed line) (modified from Berdichevsky and Dmitriev 2008).

2.6. MT modeling and inversion

The MT field survey is usually organized following these steps:

1. Data acquisition: the time-varying electric and magnetic fields are recorded for a long time (between a day and some months) depending on the objective of the project. The longer the acquisition time the longer the period range and the skin depth.
2. Data processing: the EM fields are converted into the frequency domain by means of the Fourier transform. The transfer functions are calculated.
3. Data analysis: dimensionality analysis, distortion evaluation and phase tensor analysis.
4. Data interpretation: forward modeling or inversion.

The link between the MT data and the Earth's resistivity distribution is provided by the modeling process, that is, forward and inverse modeling. The forward modeling elaborates the MT transfer functions starting from a given resistivity model. Usually, the forward modeling calculates the apparent resistivity and phase of the impedance tensor as model responses (see equations 2.16 and 2.17). The MT inversion is the fundamental step to obtain the resistivity distribution of the subsurface (i.e., the resistivity model) given the observed impedances. The unknowns of the inverse problem are the resistivity values of the 1D, 2D or 3D model domain. During the inversion, the resistivity model is iteratively updated in order to ensure the matching between the observed data and the model responses calculated by the forward modeling. The goal is to minimize an objective function that improves the correspondence between the observed and calculated responses. A reliable and stable forward-modeling routine is then the hearth of the MT inversion.

The MT modeling consists in numerically solving the Maxwell's equations (equations 2.8 - 2.11) following one of these three approaches: finite difference, finite elements and integral equations. While numerical simulations using finite difference are fast in convergence, finite-elements simulations can easily include topography and bathymetry in the grid. The integral equation approach has been sufficiently investigated but it is still hardly implemented due to its high computational cost (Wannamaker 1991; Avdeev et al. 2002; Kruglyakov and Bloshanskaya 2017).

From a mathematical point of view, the MT inverse problem is ill-posed in nature with nonlinear and extremely sensitive solutions. This means that there are many models that can equally fit the data within a given tolerance threshold. Therefore, dealing with the MT inverse problem means solving a nonlinear, multi-parametric and ill-posed problem affected by the equivalence of solutions. Fundamental books on the inverse theory are Tarantola (2005) and, more detailed for MT, Berdichevsky and Dmitriev (2002).

2.6.1 Derivative-based MT inversion

Various inversion algorithms have been proposed in the literature to solve the MT inverse problem for any dimensionality cases. The main inversion schemes are the standard Occam's inversion (Constable et al. 1987), the data space Occam's inversion (Siripunvaraporn and Egbert 2000), the Gauss–Newton method (Sasaki 2001), the Gauss–Newton with the conjugate gradient method (Siripunvaraporn and Egbert 2007), the non-linear conjugate gradient (NLCG) method (Rodi and Mackie 2001; Newman and Alumbaugh 2000; Kelbert et al. 2008; Commer and Newman 2009) and the quasi-Newton method (Avdeev and Avdeeva 2009). A complete mathematical review of the main inversion techniques can be found in Siripunvaraporn (2012).

The main 2D inversion codes are OCCAM2D (Degroot-Hedlin and Constable 1990), MARE2DEM (Key 2016) and MT2DInvMatlab (Lee et al. 2009). The last two decades have witnessed a tremendous progress in the development of 3D inversion and forward modeling methods (Avdeev 2005; Siripunvaraporn 2012). The most established 3D inversion codes are ModEM based on NLCG (Kelbert et al. 2014), WSINV3DMT based on data-space Occam (Siripunvaraporn et al. 2009) and AP3DMT based on NLCG (Singh et al. 2017).

All the above-mentioned methods are derivative-based inversion algorithms or local search algorithms. In fact, the standard approach in geophysics is the iterated and linearized inversion. It means that the forward function, that entails the numerical solution of the Maxwell's equations and calculates the model responses, is approximated with its first-order Taylor expansion (the first-order derivative Jacobian matrix) about some reference model. Then, a model solution is computed and regarded as a new reference model. The generation of the Jacobian and the linear inversion are repeated up until the objective function is minimized. Since the nonlinear and ill-posed problem is based on the local search of the model domain, a general weakness is that the inversion can find local rather than global solutions. Moreover, a central issue of derivative-based inversion algorithms is that the reference model used to initialize the inversion can strongly bias the result and hence the interpretation (Dong and Jones 2018). Consequently, the final solution depends on the initial assumption of the starting model. If a homogeneous half-space is adopted as a starting model, some trials have to be done to define the most appropriate value of the electrical resistivity to start with, depending on the data set and inversion code (Miensopust et al. 2013). Otherwise, the inversion can be initially constrained by an a priori model derived by external information from well-log data (Yan et al. 2017a), seismic data (Yan et al. 2017b), MT data (Santilano 2017) or other geophysical methods.

2.6.2 The global search methods

To solve the inverse problem, it is also possible to perform a global optimization instead of a linearized inversion. The global search approach, also called probabilistic or stochastic inverse modeling, is represented by methods like Monte-Carlo or metaheuristics (Sen and Stoffa 2013). Global search methods have become of major interest in geophysics because they are theoretically able to find the global minimum of a function as the final solution without being trapped in one of several local minima. The main reason is that the model space is sampled either randomly or according to a specific strategy (e.g. adaptive behavior). The consequence is that global search algorithms are time-consuming, while derivative-based algorithms come to convergence in few iterations. The essential advantage of global search algorithms is that the final solution is independent from the initial guess of the starting model. Unfortunately, for a number of years the application of global search algorithms to the geophysical inversion has been hindered by their high computational load. However, the striking improvements in computer efficiency of the present days have been essential in the decrease of the CPU-time required to run these algorithms.

The family of global search algorithms is divided into two main groups. The first one is represented by Monte Carlo and is based on the random sampling of the search space of the solutions (Sambridge and Mosegaard 2002). Much research in recent years has focused on the 1D MT inverse problem by adopting the Markov-Chain-Monte-Carlo (MCMC) method (Grandis et al. 1999; Xiang et al. 2018; Conway et al. 2018; Mandolesi et al. 2018). The second group encompasses the metaheuristic methods, such as nature-inspired evolutionary algorithms. The most important metaheuristics applied to the geophysical inversion are simulated annealing (SA), genetic algorithm (GA) (Sen and Stoffa 2013), the ant colony algorithm (ACO) (Yuan et al. 2009), grey wolf optimizer (Agarwal et al. 2018) and particle swarm optimization (PSO) (Shaw and Srivastava 2007). The 1D MT inverse problem has been addressed using SA (Dosso and Oldenburg 1991) and PSO (Shaw and Srivastava 2007; Godio and Santilano 2018; Santilano et al. 2018). To date, only a limited number of works have applied metaheuristic methods to the 2D MT problem. For GA, there are the works of Everett and Schultz (1993) and Pérez-Flores and Schultz (2002), while the first study using PSO can be found in Pace et al. (2019). The application of the global search approach to the MT inverse problem is extensively explained in the following Chapters 3 and 4.

Chapter 3

Population-based metaheuristics: the particle swarm optimization algorithm

“Every aspect of learning or any other feature of intelligence can in principle be so precisely described that a machine can be made to simulate it”

Dartmouth Summer Research Project on Artificial Intelligence, 1955

This chapter introduces the adoption of global search methods for the geophysical inverse modeling. After, a brief overview of metaheuristic methods, the chapter focuses on population-based metaheuristics and, particularly, on the particle swarm optimization algorithm. This is then applied to the magnetotelluric method, whose fundamentals have been introduced in the previous chapter. Finally, a novel method is presented: the joint optimization of multiple geophysical data sets by means of multi-objective global search methods.

3.1. Computational swarm intelligence

The past fifty years have seen increasingly rapid advances in the field of Computer Science. A dramatic improvement in the machines’ performance has allowed more complex problems to be progressively solved. Artificial intelligence (AI) has been attracting a lot of interest since its first definition as “thinking machines” by Alan Turing (Computing machinery and intelligence, 1950). Nowadays, AI is essential for a wide range of technologies in the fields of autonomous cars, healthcare (identifying skin cancers, robotic surgery) and communications (understanding human speech, interpreting images).

A sub-branch of AI is Computational Intelligence (CI). It encompasses five paradigms which are all based on biological systems: a) artificial neural networks (ANN) models biological neural systems; b) evolutionary computation (EC) models genetic and behavioral evolution; c) swarm intelligence (SI) models the social behavior of organisms living in groups; d) artificial immune systems (AIS) models the human immune system; e) fuzzy systems (FS) models the interactions between the organisms and their environment.

Among these nature-inspired metaheuristic methods, EC and SI are referred to as population-based algorithms since they are based on the behavior of groups of individuals (Engelbrecht 2007). The EC tenet is that the individuals with the best chromosomes survive (and the weakest individual have to die), so that only the selected chromosomes are inherited by new generations. The most important example of EC algorithm is the genetic algorithm (GA). SI is the problem-solving behavior emerging from the interactions of agents in a group. SI mimics the naturally-based social dynamics that provide individuals with more information than that gathered by their own senses. The algorithmic models of SI are referred to as *computational swarm intelligence* (CSI), whose main paradigms are *particle swarm optimization* (PSO) and *ant colony optimization* (ACO).

During the past two decades, EC and CSI have been widely applied to solve optimization problems. The solution of the optimization problem is found after that the objective function, that is, the quantity to be optimized, is minimized (or maximized, depending on the problem) depending or not upon some constraints. Fundamentals of optimization theory can be found in Engelbrecht (2007). The typical properties of the most common (and challenging) optimization problems are

a) Multivariate: there is more than one unknown
b) Nonlinear: the objective function is non linear
c) Constrained: the search space of the candidate solutions is restricted to specific regions according to equality or inequality constraints
d) Multimodal or multi-solution: there is not only one clear solution, but a set of feasible candidate solutions referred to as local or global optima (whose mathematical definition is here omitted).

When the optimization-minimization problem presents the a)-d) properties, the candidate solutions can be graphically represented as in Figure 3.1. The graph represents the objective function (*f(x)*) in the constrained search space of solutions (*x*). In this example, the local minima belong to the feasible region, while the global minimum is not a feasible solution due to the constraint. Therefore, the problem solution is the minimum point on the constraint.

Another distinction of optimization problems is between single-objective or multi-objective problems, meaning that there is only one or more than one objective functions to be simultaneously optimized. In geophysics, an example of multi-objective optimization problem is the joint inversion of multiple geophysical data sets. This is discussed in Section 3.4.

Global search algorithms such as GA, PSO and ACO are theoretically able to find the global minimum of the objective function as final solution without being trapped in one of the several local minima. This point is of pivotal importance in CSI application to geophysics because the geophysical inverse problem is nonlinear, multi-solution and ill-posed.

This chapter focuses on the PSO algorithm and its application to the geophysical inverse problem. In particular, Sections 3.3 and 3.4 describe PSO application to 1D optimization of magnetotelluric (MT), time-domain electromagnetic (TDEM) and vertical electrical sounding (VES) data. Chapter 4 presents the PSO application to the 2D MT inverse problem.

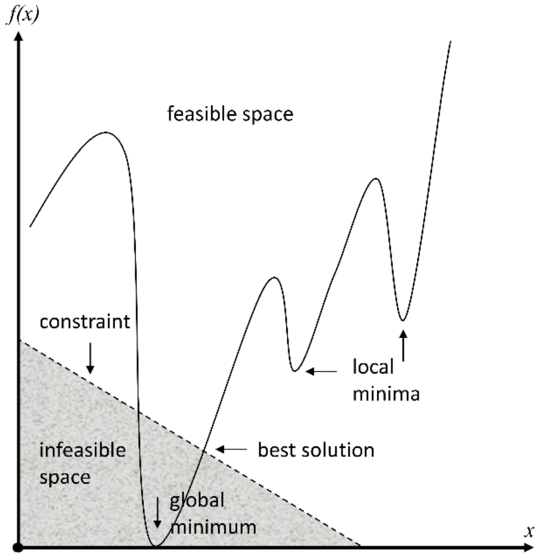

Figure 3.1 Global minimum and local minima in the search space of an optimization (minimization) constrained problem (modified from Engelbrecht 2007).

The original idea of the PSO algorithm was born from the observation of the choreography of bird flocks and schools of fish (Kennedy and Eberhart 1995). The way they share knowledge to search for food or find the best reciprocal distance in motion fascinated Kennedy and Eberhart (1995) so strongly that they proposed applying this evolutionary approach to the optimization of nonlinear problems. Pivotal references for computational swarm intelligence are Kennedy et al. (2001) and Engelbrecht (2007). It writes: "*PSO is a population-based search procedure where the individuals, referred to as particles, are grouped into a swarm. Each particle in the swarm represents a candidate solution to the optimization problem. In a PSO system, each particle is "flown" through the multidimensional search space, adjusting its position in search space according to its own experience and that of neighboring particles. A particle therefore makes use of the best position encountered by itself and the best position of its neighbors to position itself toward an optimum solution.*". Simple interactions between individuals yield a complex collective behavior, meaning that each individual is able to adapt and derive new and coherent behaviors in case of changes in the external environment. The most striking feature of this method is that every particle has a memory component that rules its behavior. This is influenced by both the cognitive knowledge of the particle and the experience of its neighbors, whose leadership can be emulated. *"The effect is that particles "fly" toward an optimum, while still searching a wide area around the current best solution. The performance of each particle (i.e. the "closeness" of a particle to the global minimum) is measured according to a predefined fitness function which is related to the problem being solved".* The fitness function is the objective function.

Many emerging real-world applications of EC and CSI are telecommunications networks, training neural networks, game learning, clustering, design, bioinformatics and data mining (Engelbrecht 2007).

As mentioned in Section 2.6, global search algorithms have been widely applied to geophysics (Sen and Stoffa 2013). Geophysical applications of GA have covered: 1D seismic waveform inversion (Stoffa and Sen 1992), resistivity sounding data (Sen et al. 1993), MT data (Everett and Schultz 1993) and permeability distribution in reservoir modeling (Sen et al. 1992). PSO applications to the geophysical inverse problem include the interpretation of: vertical electrical sounding (Fernández Martínez et al. 2010a; Pace et al. 2019b), gravity data (Darisma et al. 2017), multi-transient electromagnetic data (Olalekan and Di 2017), MT data (Shaw and Srivastava 2007; Godio and Santilano 2018; Santilano et al. 2018; Pace et al. 2019a) and Rayleigh wave dispersion curve (Song et al. 2012).

Some studies have demonstrated that PSO outperforms GA for higher accuracy and convergence in several geophysical applications (Yuan et al. 2009; Fernández Martínez et al. 2010a; Song et al. 2012). Moreover, a further reason for novel investigations on the geophysical applications of PSO is the encouraging results of PSO applied to 1D MT inverse problem (Shaw and Srivastava 2007; Godio and Santilano 2018; Santilano et al. 2018),

3.2. Particle swarm optimization (PSO)

A swarm is usually thought as a disorganized cluster of elements (insects, birds, fish, spiders, ants, bacteria) apparently moving chaotically and following random directions. They are actually sharing their knowledge to pursue the goal of escaping from predators or keeping the best reciprocal distance in motion or searching for food. Social behavior allows particles to reach a specific objective and adapt to the environment. Therefore, the elements of the swarm can be regarded as massless and volumeless mathematical abstractions aiming at optimizing the objective function. Assuming a nonlinear optimization problem affected by the non-uniqueness of its solution, the set of its possible solutions can be imagined as a set of particles grouping in a swarm. The particles populate the search space of the problem solutions and change their position to fulfill the common objective. At the beginning of the optimization, the particles are initialized being given uniformly-distributed random position and null velocity. Then, the iterative swarming behavior begins. Each iteration, each particle is stochastically accelerated, on the one hand, toward its previous best position (i.e., where it minimized/maximized the objective function) and, on the other hand, toward the neighborhood best position (i.e., where any other particle minimized/maximized the objective function). These two basic approaches are referred to as, respectively, exploration and exploitation. They compete in searching for the global best. While the exploration is associated to cognitive behavior, that is, the memory component of the particle, the exploitation is related to the social behavior, that is, the convergence toward the leader.

The ruling equations of the standard PSO are

$$\boldsymbol{v}_i^{k+1} = \omega^k \boldsymbol{v}_i^k + \alpha_1 \gamma_{1,i}\left(\boldsymbol{P}_i - \boldsymbol{x}_i^k\right) + \alpha_2 \gamma_{2,i}\left(\boldsymbol{G} - \boldsymbol{x}_i^k\right) \tag{3.1}$$

$$\boldsymbol{x}_i^{k+1} = \boldsymbol{x}_i^k + \boldsymbol{v}_i^{k+1} \tag{3.2}$$

where: $\boldsymbol{x}$ is the vector of the particle's position composed of as many components as the problem unknowns, $\boldsymbol{v}$ is the velocity vector, $i = [1, \ldots, \mathrm{N}]$, N is the number of particles forming the swarm, k is the current iteration number, $\boldsymbol{x}_i^k$ and $\boldsymbol{v}_i^k$ are the current vectors of position and velocity of the i^{th} particle, respectively, ω^k is the inertia weight that linearly decreases from 0.9 (first iteration) to 0.4 (last iteration) in order to balance the momentum remembered from the previous iteration (Shi and Eberhart 1998), α_1 is the cognitive acceleration towards the best particle position $\boldsymbol{P}$, also called "local best", α_2 is the social acceleration towards the best global position $\boldsymbol{G}$ (or "global best") found by the group leader and γ_1 and $\gamma_2 \in [0,1]$ are uniformly distributed random values which provide stochastic perturbation.

Figure 3.2 clearly represents the graphical meaning of equations 3.1 and 3.2. The *i-th* particle moves from the position at iteration k ($\boldsymbol{x}_i^k$) to the following position ($\boldsymbol{x}_i^{k+1}$) (purple arrow) as the resulting contribution of the three terms of equation 3.1: inertia ω^k (red arrow), cognitive attraction α_1 (green arrow) and social attraction α_2 (yellow arrow).

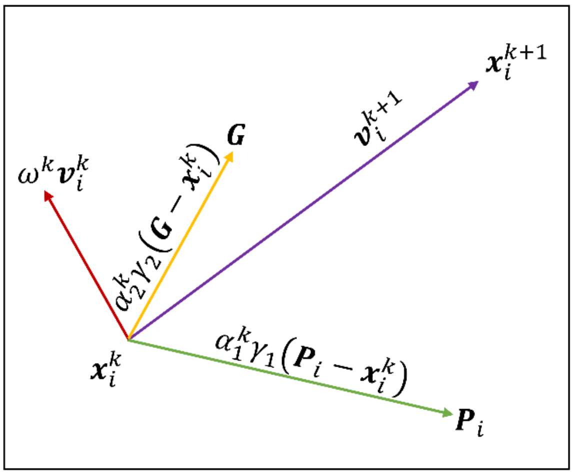

Figure 3.2 Graphical representation of the ruling equations of the PSO algorithm (adapted from Ebbesen et al. 2012).

The PSO algorithm complies with the following three steps:

1. To evaluate the objective function for each particle
2. To update the individual and global best positions (**P** and **G**)
3. To update the velocity and position of each particle.

The previous steps are repeated as long as a valid ending condition is satisfied. The most common stopping criterion is to fix a maximum number of iterations. However, since the number of iterations is problem-dependent, there are some other stopping criteria to ensure an effective optimization of the objective function: an acceptable solution found, no improvements over a number of iterations, a normalized swarm radius tending towards zero or the objective-function slope tending towards zero (Engelbrecht 2007).

The values of the accelerations (α_1 and α_2) influence the way the particles explore the model space and change their trajectory with respect to the local and global bests. The accelerations values must obey the stability solution conditions (Perez and Behdinan 2007):

$$\alpha_1 + \alpha_2 < 4 \tag{3.3}$$

$$\frac{\alpha_1+\alpha_2}{2} - 1 < \omega < 1 \tag{3.4}$$

For standard PSO, the accelerations are constant through the iterations, i.e., they are not k-dependent (Fernández Martínez et al., 2010a; Godio and Santilano, 2018; Santilano et al., 2018). However, a significant improvement in PSO efficiency has been observed by setting varying accelerations (Ratnaweera et al. 2004). A thorough sensitivity analysis on both the accelerations can be found in Ratnaweera et al. (2004), Fernández Martínez al. (2010a; 2010b) and Pace et al. (2019a).

A broad number of different PSO variants has been developed since the first algorithm of Kennedy and Eberhart (1995) appeared. The early improvements of the code concentrated on the inertia weight (Shi and Eberhart 1998) and the acceleration coefficients (Perez and Behdinan 2007). Further developments of the standard PSO proposed some sophisticated adjustments. The most important PSO developments are: the fuzzy-adaptive PSO with fuzzy system tuning the inertia weight (Shi and Eberhart 2001), the self-organizing hierarchical PSO with time-varying acceleration coefficients (Ratnaweera et al. 2004), the hybrid quadratic PSO (Ying et al. 2006), the adaptive PSO (Zhan et al. 2009) and the individual-difference evolution PSO (Gou et al. 2017).

PSO has been successfully utilized in many real-world applications, such as artificial neural networks, biomedical engineering (modeling of the spread of antibiotic resistance), hydrogeology (Fernández Martínez et al. 2012), electronics, electromagnetics, power systems, robotics (robot path planning), and signal processing (Poli 2008; Adhan and Bansal 2017 and references therein).

3.3. PSO applied to Magnetotellurics

The interpretation of the observed MT data is accomplished by solving the inverse problem, which results in a model of the resistivity distribution in the Earth's subsurface (Section 2.6). The inversion consists in finding the model parameters $\boldsymbol{m}$, considering the observed data $\boldsymbol{d_{obs}}$, and applying the functional F, which entails the physics of electromagnetic induction in the Earth.

$$F(\boldsymbol{m}) = \boldsymbol{d}_{obs} \tag{3.5}$$

In MT, the model solution $\boldsymbol{m}$ is the electrical resistivity distribution along a single vertical direction (1D), a cross-section below the profile of MT sites (2D) or a volume (3D). The observed data $\boldsymbol{d_{obs}}$ are the apparent resistivity ($\boldsymbol{\rho_{a,o}}$) and phase ($\boldsymbol{\varphi_o}$) derived from the impedance tensor $\underline{Z}$ (equations 2.16 and 2.17).

Differently from traditional inversion techniques, solving the MT inverse problem by means of global search methods like PSO means that the forward functional F calculates the predicted responses $\boldsymbol{\rho_{a,p}}$ and $\boldsymbol{\varphi_p}$ for each assumed model $\boldsymbol{m}$. The basic tenet of PSO applied to MT is that each particle of the swarm represents a possible solution of the inverse problem. The calculated responses $\boldsymbol{\rho_{a,p}}$ and $\boldsymbol{\varphi_p}$ are compared to the observed $\boldsymbol{\rho_{a,o}}$ and $\boldsymbol{\varphi_o}$ for each particle. Since the solution of the problem is affected by non-uniqueness, the search space of solutions needs to be fully explored in order to find the best model which fits the observed data. This need is fulfilled by the adaptive and swarming behavior of the particles. During the optimization process, iteration after iteration, the particles "fly" within the search space, bounded between a minimum and a maximum resistivity value. The final goal is the minimization of the objective function. The particle with the lowest fitness value is awarded with the global best position $\boldsymbol{G}$ and is going to attract neighbors depending on the social acceleration α_2 (equation 3.1). At the end of the swarming, the optimized solution is expected to be identified.

The objective function to be optimized, i.e., minimized in MT, is a misfit function that characterizes the differences between observed data and predicted responses calculated by the forward modelling from an assumed Earth model $\boldsymbol{m}$. The objective function can also include a further term that manages the model roughness according to the concept of Occam's inversion (Constable et al. 1987). It is known that in derivative-based inversion techniques, the closest fitting between observed and predicted data brings to the maximum roughness, or spurious structures. A smooth model avoids the over-interpretation of the data beyond their resolving capability. The concept of "Occam-like regularization" can be also applied to global search algorithms such as GA and PSO (Godio and Santilano 2018; Santilano et al. 2018; Pace et al. 2019a; Pace et al. 2019b). The reason is to set the optimization that minimizes not only the data deviations but also the model roughness of the electrical-resistivity vector $\boldsymbol{m}$.

3.3.1 1D MT optimization

In 1D, the Occam-like objective function has been defined as follows (Santilano et al. 2018):

$$F(\boldsymbol{m}) = \left(a\left\|\boldsymbol{\rho}_{a,o} - \boldsymbol{\rho}_{a,p}\right\|_2 + b\left\|\boldsymbol{\varphi}_o - \boldsymbol{\varphi}_p\right\|_2\right) + \lambda^2 \, \|\partial \boldsymbol{m}\|_2 \qquad (3.6)$$

where: a and b are weighting coefficients between apparent resistivity and phase, respectively; $\boldsymbol{\rho_{a,o}}$ and $\boldsymbol{\varphi_o}$ are observed apparent resistivity and phase, respectively; $\boldsymbol{\rho_{a,p}}$ and $\boldsymbol{\varphi_p}$ are predicted apparent resistivity and phase, respectively; λ is the Lagrange multiplier that regulates the model roughness; $\| \cdot \|_2$ refers to the Euclidean norm. The first term in the right side of equation 3.6 addresses the data misfit, while the second term controls the model roughness by means the Lagrange multiplier λ, which acts on $\partial \boldsymbol{m}$, the differencing operator on $\boldsymbol{m}$. The Lagrange multiplier λ acts as a smoothing factor and is chosen according to the L-curve criterion (Farquharson and Oldenburg 2004). This criterion consists in finding the optimal λ as trade-off between the misfit of the data and the roughness of the final model (i.e., the model norm). The optimal value of λ is specific for each case study. In this way, the minimization of the objective function looks for the smoothest model that fits the data, thus ensuring a balance between the data fitting and the roughness of the model.

In 1D, $\boldsymbol{m}$ is a vector composed of as many elements as the layers of the Earth model. The Occam-like optimization is an over-parametrized problem, which considers a model of many layers whose thickness is a priori fixed. It means that the layers' thicknesses are not included in the problem unknowns but are set taking into account the loss of resolving power according to the skin depth concept.

The link between equations 3.6 and 3.1 is here clarified. At each iteration of PSO, the particle that best minimizes the objective function is assumed as the global best solution (***G***), whereas the other particles can be either attracted or driven away looking for other solutions in the search space. At the end of the optimization, the particle with the minimum $F(\boldsymbol{m})$ is selected as the final solution and most of the other particles converge to it (swarming behavior).

One of the first applications of PSO to long-period MT data from a real-field data set is the work of Godio and Santilano (2018). A case study from that paper is here reported to explain a simple example before the novel 2D MT PSO, which is presented in the next chapter.

The COPROD dataset (Scotland) is publicly available for the scientific community to test 1D MT inversion routines (Jones and Hutton 1979). The Occam-like 1D PSO has been applied to a single MT site of the data set. The resistivity model was discretized into 19 layers whose thickness increased logarithmically with depth from 200 m to 350 km. The PSO ran for 200 iterations and each run was repeated 25 times (or trials) in order to check the solution variability with different randomly-distributed starting models. The swarm was composed of 300 particles and the lower and upper boundaries of the search space were 1 and 5000 Ωm, respectively. The inertia ω^k was k-dependent, while the acceleration values α_1 and α_2 were constant for the whole iterations and equal to 0.5 and 1.5, respectively. The coefficients of the objective function were: $a = 0.6$, $b = 0.4$, $\lambda = 10^{-4}$.

Figure 3.3 shows the outcome of 1D optimization of COPROD data. Figure 3.3a plots, on the left, the comparison between observed data (the red crosses) and predicted responses calculated from both the model with the minimum root-means-square error (the blue dots) and the model resulting from the median of the resistivity values at each layer for the 25 different models (the green dots). Figure 3.3*a* plots, on the right, the resistivity distribution with depth for the 25 models resulting from the PSO trials (the red lines) and for the model resulting from their median (the green line). The observed data and the predicted responses are largely comparable for both apparent resistivity and phase. Figure 3.3b reveals the validity of the PSO solution (the green line), which is largely comparable with the models published in literature and regarded as benchmark. The inversion results of Jones and Hutton (1979) and Constable et al. (1987) are plotted in black and blue, respectively. The probability density distribution of the resistivity value at each layer among the 25 trials was used as a-posteriori analysis for the validity of the 1D model. The a-posteriori analysis demonstrated unimodal distribution for the majority of the layers, thus proving the robustness of the PSO method (Godio and Santilano 2018).

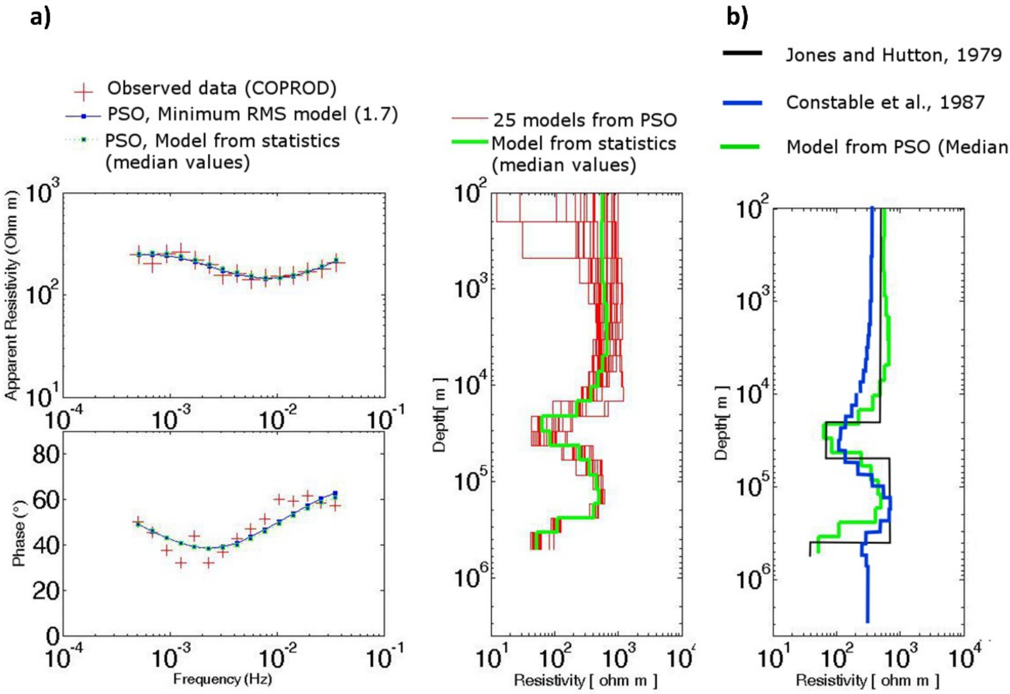

Figure 3.3 a) on the right, observed data from COPROD data set (red crosses) and predicted responses from 1D PSO (blue and green dots) for apparent resistivity and phase; on the left, the resistivity distribution with depth. The red lines represent the models resulting from the 25 PSO trials. The green line is the model calculated from the median resistivity at each layer of the 25 models**. b)** the PSO median model (green line) is compared with the benchmark solutions of Jones and Hutton (1979) and Constable et al (1987) plotted in black and blue line, respectively (modified from Godio and Santilano (2018)).

The main finding emerging from this 1D example is the independence of the final solution from the starting model, which is traditionally recognized as strong bias in conventional MT inversion techniques. The work of Godio and Santilano (2018) outlined that the implementation of PSO to the 2D MT inverse problem would have been of huge interest in order to extend the stochastic approach to the interpretation of MT profiles instead of single MT sites. At the same time, they pointed out that the increase in the complexity of the forward modeling would have represented a significant challenge in terms of computation time.

3.3.2 Static-shift correction by means of PSO

Field MT data are usually affected by telluric distortion or static shift (Section 2.4.2). The theoretical background of static shift correction by using the TDEM method was explained in Section 2.5.2. An effective method to correct the static shift by means of PSO has been proposed in Santilano et al. (2018). Their approach consists in a simultaneous optimization of MT and TDEM data measured at the same site. The objective function to be minimized is partially similar to equation 3.6 with the difference that the scalar value representing the shift of the MT apparent resistivity curve is considered as an additional problem unknown. In fact, the algorithm optimizes both the model parameters and an additional parameter accounting for the static shift. In the objective function, the observed data are composed of both the MT ρ_{app} and phase and the TDEM ρ_{app}, but the observed MT ρ_{app} is iteratively optimized to match, at low periods, the reference curve of the TDEM ρ_{app}. This method has been tested on both synthetic and field data (Santilano et al. 2018).

The MT data set investigated in this thesis comes from the geothermal area of Travale (Italy). For 2D or 3D interpretation, the different *xy* and *yx* apparent-resistivity curves were optimized separately because the two polarizations may present different levels of distortion. As an example, a typical outcome of the static shift correction using PSO is plotted in Figure 3.4 for the xy-polarization of site a1 (the complete data set is presented in Chapter 5). Figure 3.4a-b shows a remarkable overlap between the MT and TDEM data (red dots) and the calculated responses of ρ_{app} and phase (blue crosses). The occurrence and correction of the static shift is apparent in Figure 3.4a, where the MT ρ_{app} (the red dots in the range $3 \cdot 10^{-3}$ - 1000 s) are shifted upward to match the TDEM ρ_{app} between 10^{-5} and 10^{-3} s. The PSO ended after 600 iterations, when the root-mean-square-error (RMSE) was 1. The 1D resistivity model resulting from the optimization is shown in Figure 3.4c. However, its interpretation can be neglected due to the high dimensionality associated to the investigated structure. Further details on the outcomes of static shift correction of the other sites of our data set are given in Section 5.4.

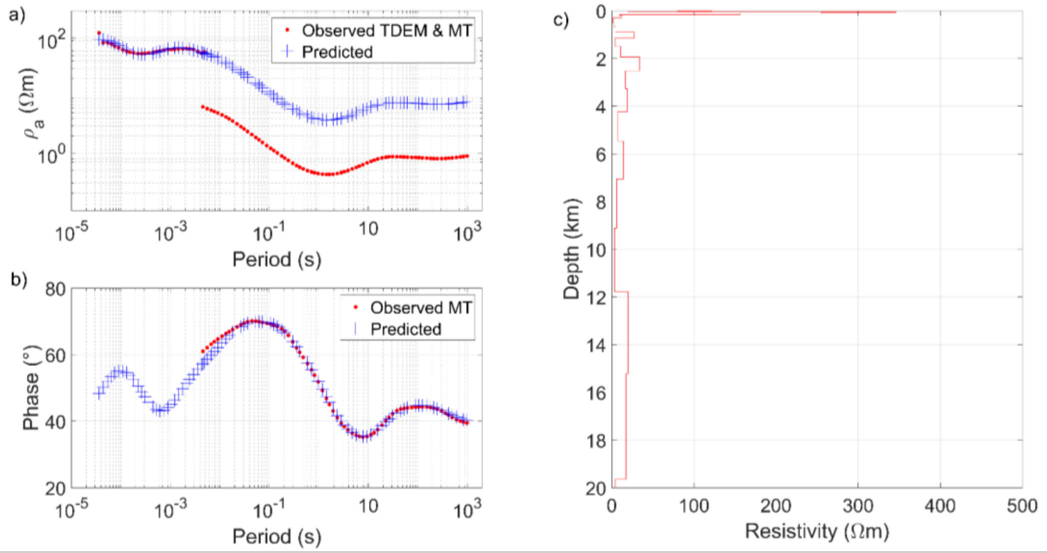

Figure 3.4 Static shift correction for site a1 (xy-mode) using PSO; **a)** The red dots are the observed apparent resistivity (ρ_{app}) of TDEM at low periods (up to 0.005 s) and of MT from 0.003 s upward. The blue crosses indicate the predicted MT ρ_{app} that correct the static shift according to TDEM information; **b)** Observed (red dots) and predicted (blue crosses) MT phase; **c)** The 1-D resistivity model.

3.4. Multi-Objective PSO

This section is conceived as a synopsis of the paper Pace et al. (2019b) dealing with the multi-objective optimization of multiple geophysical data sets (TDEM and VES) by means of global search methods.

An example of multi-objective optimization problem, whose definition is in Section 3.1, is the geophysical joint inversion. The joint inversion of multiple data sets can significantly improve their modeling by overcoming the intrinsic limitations of each geophysical method. The advantages in combining different geophysical measurements using a unique inversion scheme have been clear since the first introduction of joint inversion methods (Vozoff and Jupp 1975; Yang and Tong 1988). Joint inversion has been extensively applied to electrical and electromagnetic data to interpret one physical property, that of electrical conductivity. However, as with single inversion, joint inversion is still affected by non-uniqueness, nonlinearity and ill-posedness (Tarantola 2005).

In the last decade, many derivative-based methods have been proposed for the joint inversion of different data sets. These methods have proved to successfully image the properties of the layered subsurface, thus outperforming the separate inversions and the correspondent ambiguities (Hering et al. 1995; Musil et al. 2003; Gallardo and Meju 2003; Moorkamp et al. 2011). A main issue with joint inversion is data compatibility, since real-world data are acquired using different methods and usually present different resolutions, sensitivities, depth of investigations and/or error levels. Data incompatibility can hence lead to either a variety of final results or conflicting models. These are commonly avoided using a weighting factor between the objective functions that rule the inversion (Commer and Newman 2009; Meqbel and Ritter 2015). However, even when using appropriate weighting factors, the choice of the proper one is still critical and may not resolve the conflict (Akca et al. 2014). Moreover, the search for a single best solution for a joint-inversion problem can still produce biased results. Therefore, the main drawbacks of the derivative-based joint inversion are: 1) the simplification of a multi-objective problem (joint inversion) into a succession of single-objective optimization problems with weighted objective functions; 2) the strong influence of the starting model on the final result, which is typical of the derivative-based inversion techniques.

Multi-objective evolutionary algorithms (MOEAs) have recently been proposed for the joint inversion of multiple data sets because they deploy a multi-objective optimizer (MOO) to solve the problem, without transforming it into a series of single-objective optimizations. This approach avoids the adoption of user-dependent weighting factors. MOEAs rate the solution quality by using the concept of Pareto optimality, first introduced by Edgeworth (1881) and Pareto (1896). A solution is considered *Pareto-optimal* if there is not another feasible solution that improves one objective without deteriorating the other objective. The whole set of solutions that fulfill this criterion is called the *Pareto-optimal set*. MOEAs are attracting widespread interest since the objective function is a unique vector of as many components as the different data sets to be optimized, without any need to rank them. The most widely-used EAs are GA and PSO algorithms (Engelbrecht, 2007; Kennedy and Eberhart, 2001). Due to the positive outcomes of PSO applied to single-objective problems, it has been proposed to tackle multi-objective problems. Coello Coello et al. (2004) showed highly competitive results of multi-objective PSO (MOPSO) applied to benchmark test functions. Unfortunately, few studies have so far dealt with MOPSO applied to geophysics. One of the first works that adopted PSO for the joint inversion of synthetic data (GPR and P-wave seismic traveltimes) was given by Tronicke et al. (2011), but it actually simplified the problem into a single-objective one. Similarly, Paasche and Tronicke (2014) developed a hybrid approach on radar and P-wave traveltimes. Cheng et al. (2015) applied PSO to a whole forward process synchronized between transient electromagnetic method (TEM) and DC methods. There is hence little evidence of the potentiality of MOPSO on the geophysical joint inversion. The multi-objective version of GA has instead been more explored. Examples include the inversion of: Raleigh-wave dispersion curves and reflection travel times (Dal Moro and Pipan 2007), surface wave dispersion and horizontal-to-vertical spectral ratio (Dal Moro 2010), AMT and broad-band MT data (Schnaidt et al. 2018), magnetic resonance and Vertical Electric Sounding (VES) data (Akca et al. 2014), seismic and well-log data for reservoir modeling (Emami Niri and Lumley 2015), and receiver functions, surface wave dispersion and MT data (Moorkamp et al. 2011). Although these works have adopted the Nondominated Sorting GA called NSGA-II (Deb et al. 2002), little attention has been paid to the most recent NSGA-III (Deb and Jain 2014).

The next sub-sections present the 1D joint inversion of different geophysical data sets using MOPSO as the multi-objective solver. Each data set was composed of integrated TDEM and VES soundings, so we dealt with a bi-objective problem that avoids both simplification into a single-objective problem and the use of the weighting factor. A preliminary introduction on the method can be found in Pace et al. (2018). The performance of MOPSO was directly compared with that of a NSGA-III, which is stable and widely adopted in geophysics. The economic concept of Pareto optimality was used to identify the final set of results among the feasible solutions.

The method was first tested on synthetic data and then applied to two real data sets from two different surveys for groundwater prospecting in north-west Italy (Piedmont region). For the sake of brevity, this section reports only one field case study (Section 3.4.3). The other applications and the comparison with the single-objective PSO are described in Appendix A.

3.4.1 The method: objective-function and the Pareto optimality

Our application of MOEAs to the geophysical joint optimization focuses on two geophysical methods, TDEM and VES, which deal with the same physical parameter, i.e., the electrical resistivity. The problem unknown is the p-dimensional vector $\boldsymbol{m} = [m_1, \ldots, m_p]$ of electrical resistivity, being p the number of layers whose thickness was defined before the optimization. The 1D-profile $\boldsymbol{m}$ is a feasible solution found after the minimization of the objective function

$$\boldsymbol{f}(\boldsymbol{m}) = [f_1(\boldsymbol{m}), f_2(\boldsymbol{m})] \tag{3.7}$$

where the two components of the vector refer to TDEM and VES, respectively. These components were simultaneously minimized in the multi-dimensional space of the objective function.

Since a variety of solutions are identified at the end of the MO optimization, the choice of the best solution is a critical point. MOEAs select the best set of tradeoff solutions using the optimality notion originally proposed by Edgeworth (1881), then generalized by Vilfredo Pareto and today well-known as the *Pareto optimality* (Pareto 1896). This principle identifies a range of compromises as feasible solutions, thus avoiding the results being biased by the user-driven weighting approach. This is the mathematical definition of *Pareto dominance*: given two possible solutions $\boldsymbol{m}_a$ and $\boldsymbol{m}_b$, the vector $\boldsymbol{f}(\boldsymbol{m}_a)$ is said to dominate $\boldsymbol{f}(\boldsymbol{m}_b)$ (denoted by $\boldsymbol{f}(\boldsymbol{m}_a) \preccurlyeq \boldsymbol{f}(\boldsymbol{m}_b)$) if and only if $\forall j \in \{1, 2\}, f_j(\boldsymbol{m}_a) \leq f_j(\boldsymbol{m}_b) \wedge \exists j \in \{1, 2\}: f_j(\boldsymbol{m}_a) < f_j(\boldsymbol{m}_b)$. For us, $j=1$ refers to the TDEM component and $j=2$ to the VES component. All the non-dominated solutions form the Pareto-optimal set (P^*) or non-dominated set. The corresponding objective functions of the non-dominated solutions form the Pareto Front (*PF*) in the objective space:

$$PF = \{\boldsymbol{f}(\boldsymbol{m}) = (\boldsymbol{f}_1(\boldsymbol{m}), \boldsymbol{f}_2(\boldsymbol{m})) \,|\, \boldsymbol{m} \in P^*\} \tag{3.8}$$

That is, when P^* is projected onto a surface, it is referred to as the *PF*. In our two-dimensional objective space, the *PF* is graphically depicted as a tradeoff surface showing which component of $\boldsymbol{f(m)}$ is mostly minimized. Besides, the *PF* can be analyzed to infer the compatibility between the different data sets (Schnaidt et al. 2018; Dal Moro and Pipan 2007).

Each j^{th} component of the objective function to be minimized was defined as the Euclidean norm of the misfit between observed data and calculated response plus an additional term to regulate the model smoothness:

$$f_j(\boldsymbol{m}) = \left\| \frac{\phi_o - \phi_c}{\sigma_\phi} \right\|_2 + \lambda_j \parallel log_{10}(\partial \boldsymbol{m}) \parallel_2 \qquad (3.9)$$

where: ϕ_o is the observed TDEM signal if $j=1$ or the observed apparent resistivity if $j=2$; ϕ_c is the calculated response for TDEM signal if $j=1$ or the calculated apparent resistivity if $j=2$; the difference in $\|\cdot\|_2$ is normalized by the corresponding errors (σ_ϕ) on the observed data; λ_j is called the Lagrange-multiplier, or smoothing parameter. The right-hand side of equation 3 is composed of two terms: the first one assesses the distance of the observed data from the response calculated by the forward modeling; the second term addresses the minimization of the roughness of the model, by using the smoothing parameter λ_j on the first derivative of the model $\boldsymbol{m}$. λ_j has the subscript in order to address the different level of smoothing required by the specific geophysical method. Even though the Occam's inversion was first introduced for deterministic methods (Constable et al. 1987), the "Occam-like optimization" has been effectively proposed for PSO in Pace et al. (2019a), Godio and Santilano (2018) and Santilano et al. (2018). As explained in Section 3.3.1, we here applied the "Occam-like optimization" in order to search for the smoothest model that fitted the data, that is, a tradeoff between the minimum misfit achievable and unnecessary structure (or roughness) of the model. The proper value of λ_j was chosen following the L-curve criterion, which identified the optimal tradeoff between the misfit of the data and the roughness of the final model (i.e., the model norm) (Farquharson and Oldenburg 2004). It is obvious from equation 3.9 that a high value of λ_j results in a smooth model penalizing the misfit, while, on the contrary, a low λ_j yields a minimum data misfit and high resistivity contrasts (roughness) between the layers of the model. The forward modelling used to handle TDEM data was derived from the *CR1Dmod* algorithm (Ingeman-Nielsen and Baumgartner 2006). The VES forward modelling was adapted from the code *VES1dmod* in Ekinci and Demirci (2008).

The MO optimization of TDEM and VES data was defined as a problem without equality and inequality constraints. The problem had boundary conditions: the search space of the solutions was bounded between a minimum and maximum value of electrical resistivity. This interval was set as large to enable the exploration of all the feasible solutions.

3.4.2 The MO algorithms: MOPSO and NSGA-III

The basic principles of MOPSO applied to the geophysical inversion are the same described in Sections 3.2 and 3.3 for single-objective PSO. The ruling equation of MOPSO was slightly different from equation 3.1, which is adjusted as follows:

$$\boldsymbol{v}_i^{k+1} = \omega^k \boldsymbol{v}_i^k + \alpha_1^k \gamma_1 (\boldsymbol{P}_i - \boldsymbol{x}_i^k) + \alpha_2^k \gamma_2 (\boldsymbol{G^k} - \boldsymbol{x}_i^k) \tag{3.10}$$

The main difference with respect to equation 3.1 is that **G**, α_1 and α_2 are k-dependent. While in single-objective PSO the leader ***G*** is the unique best-particle of the swarm, in multi-objective PSO the set of non-dominated solutions worked as swarm leader. The non-dominated solutions were stored in an archive called *repository*. It was updated at each k iteration with the advantage that a high number of iterations did not directly imply a high number of non-dominated solutions since a new non-dominated solution could dominate (and hence replace) a non-dominated solution of the previous iteration (Coello Coello et al. 2004). $\boldsymbol{G}^k$ was hence selected from the repository at each iteration according to a quasi-random criterion based on the most crowded regions of the objective space. Equation 3.10 establishes that the particle's velocity resulted from the balance among three terms: the inertia ω^k, accounting for the past experiencet, the cognitive knowledge α_1^k and the social attraction α_2^k towards the leader. At the first iteration ($k=0$), the particles were initialized with null velocity ($\boldsymbol{v}_i^0 = 0$) and random positions uniformly distributed in the search space.

Since the first appearance in 2000, several MOPSO variants have been proposed (for a review see Reyes-Sierra and Coello Coello 2006). We implemented the time-variant (or TV-) MOPSO to take advantage of the k-dependent coefficients ω^k, α_1^k and α_2^k. They change at each iteration to provide global exploration of the search space at the beginning of the optimization and local exploitation at the end. In detail, the TV inertia weight was proposed by Shi and Eberhart (1999), while the TV acceleration coefficients by Ratnaweera et al. (2004) and Tripathi et al. (2007). These works clearly demonstrate that a high α_1^k improves the solution diversity, while a high α_2^k fosters the convergence toward the global best. Therefore, we set α_1^k larger than α_2^k at the initial iterations. Then, during the optimization, α_1^k linearly decreased and α_2^k linearly increased, so that at the end they were reversed. In detail:

$$\alpha_1^k = \alpha_1^{max} - (\alpha_1^{max} - \alpha_1^{min}) \left(\frac{k-1}{max(k)-1}\right) \tag{3.11}$$

$$\alpha_2^k = \alpha_2^{min} + (\alpha_2^{max} - \alpha_2^{min}) \left(\frac{k-1}{max(k)-1}\right) \tag{3.12}$$

where: α^k is the acceleration value at iteration k; α_1^{max} and α_2^{max} are the maximum values for the cognitive and social accelerations, respectively; α_1^{min} and α_2^{min} are the minimum values for the cognitive and social accelerations, respectively; and *max(k)* is the maximum number of iterations set for the optimization (Engelbrecht 2007 and references therein). Therefore, at the first iteration ($k=1$), $\alpha_1^{k=1} = \alpha_1^{\max}$ and $\alpha_2^{k=1} = \alpha_2^{min}$, while, at the last iteration ($k = max(k)$), $\alpha_1^{k=\max(k)} = \alpha_1^{\min}$ and $\alpha_2^{k=\max(k)} = \alpha_2^{max}$. Following the stability criteria in Perez and Behdinan (2007) and the sensitivity analysis in Pace et al. (2019a), we set $\alpha_1^{max} = \alpha_2^{max} = 2$ and $\alpha_1^{min} = \alpha_2^{min} = 0.5$.

Our TV-MOPSO algorithm included the mutation operator, that is typical of GA and scarcely effective in single-objective PSO. However, many theoretical studies have proposed the introduction of the mutation operator in multi-objective PSO, in order to boost the exploration of the remote regions of the search space and prevent premature convergence to the local *PF* (Coello Coello et al. 2004; Tripathi et al. 2007). We adopted the mutation operator equal to 0.5, in line with that works. It operated on a wide percentage of particles at the early iterations and then exponentially decreased its influence towards the end. The main advantage of the mutation operator is that it compensates for the loss of diversity throughout the optimization process.

The algorithm ran until a specific number of iterations was achieved, that is, up to 1000 iterations. However, the total number of iterations is problem-dependent and its initial and arbitrary choice has proven to be inadequate as the single stopping criterion (Engelbrecht 2007). Few iterations can lead to premature ending before the solution convergence and, on the other hand, too much iterations can result in unnecessary computation. Therefore, we set another stopping criterion: if the objective function did not minimize for 300 consecutive iterations, the run was terminated.

Another fundamental setting of the MOPSO was the number of particles forming the swarm, i.e., the population size. This setting is dependent on the number of unknowns of the problem, namely, the number of layers the 1D profile was discretized into. The rule of thumb prescribes the number of particles proportional to about 8-12 times the unknowns (Engelbrecht 2007; Fernández Martínez et al. 2010a; Pace et al. 2019a). We discretized the model into 19 layers and set the swarm size equal to about 9 times the unknowns, that is, 170 particles.

Our algorithm was developed in the Matlab programming environment using the Parallel Computing Toolbox. The general code of TV-MOPSO was adapted from Coello Coello et al. (2004) for the geophysical problem. The simulations ran on a 12-core node of the High Performance Computing (HPC) cluster for academic research at Politecnico di Torino. The CPU model of the single node is 2x Intel Xeon E5-2680 v3 2.50 GHz 12 cores. When the computations were executed, in October 2018, the sustained performance of the cluster was globally 20.13 TFLOPS.

This paragraph describes the NSGA-III in a concise way, being our study focused on swarm intelligence. NSGA-III was essentially chosen as basis of comparison for MOPSO, since GAs are the most common global optimizers in geophysics. The NSGA-III is a bio-inspired metaheuristic that mimics the inheritance of the highest qualities from parents to children, the natural selection and the biodiversity. The population members represented the possible solutions of joint inversion and were sorted according to the Pareto-dominance *ranking* method. The selection of the non-dominated solutions was performed using the non-domination rank and the so-called *crowding distance*, that measured the neighbors surrounding each individual. The diversity was preserved according to the tenet of *fitness sharing*, that promoted the solutions in the least populated regions of the search space (Coello Coello et al. 2007). These criteria of ranking and selection allowed the Pareto-optimal set to be identified.

Some input arguments of NSGA-III were similar to those of MOPSO and hence were set following the previously explained criteria. These inputs were the population size, the number of iterations, the boundary conditions and the stopping criteria. The main difference between NSGA-III and MOPSO are the genetic operators known as crossover and mutation, the number of reference points and the absence of the external archive called repository. The crossover percentage was 0.5, meaning that, given any two random parents, half of the population of the new generation, namely the offspring, was subjected to the genetic crossover. The mutation percentage was 0.5, so that half of the population was subjected to mutation. In detail, the mutation rate was 0.02, meaning that the 2% of the model represented by each selected individual was forced to mutate. A major novelty of NSGA-III compared to NSGA-II is the adoption of the reference points in order to enhance the diversity among the solutions found. In a two-objective problem, the reference points are placed in the line that, in the 2D-objective space, intercept the axes in 1. The population members associated to the reference points are emphasized, that is, allowed to evolve in the next generation (elitist selection). It has been proven that the most adequate number of reference points is equal to the population size, so we set it accordingly. This and further details are given in Deb and Jain (2014), which also reports the other differences and advantages with respect to the well-known NSGA-II.

3.4.3 Calibration on real data

The MOPSO was validated on synthetic TDEM and VES data to evaluate the performance of the algorithm (see Appendix A). Then, it was applied to a field data set composed of TDEM and VES soundings over a known stratigraphic setting in Piedmont, north-west Italy. The test site is located in the Stupinigi area (about 10 km south-west of Torino).

Details on the TDEM method are explained in Section 2.5. The VES is an electric method that deploys two potential electrodes that measure the electric field induced by two current electrodes. The depth of investigation depends on the configuration of the electrodes and the spacing between the current electrodes. The measurements are typically displayed as apparent resistivity as a function of the current-electrode half-spacing. Despite VES is one of the oldest geophysical methods, it is still worthy considered due to the efficiency of the setup and the sensitivity to high-resistivity contrasts. Moreover, new joint interpretations of vintage data could provide a more complete characterization if combined with new acquisitions.

The site of Stupinigi is characterized by a well-known lithological and stratigraphic sequence and a flat morphology. From a geological perspective, the site lies on an alluvial plain, characterized by sand and gravel deposits. The uppermost formation is composed of recent coarse gravel deposits and is followed by an alternation of gravel and sand (well-consolidated and cemented) up to hundreds of meters of depth. These two formations constitute two different aquifers separated by embedded clayey layers.

The TDEM data have been acquired using a coincident-loop configuration with a 50-m-long loop for both the transmitter and receiver. The injected current was equal to 3A, the turnoff time was 4 μs and a total of 27 samples were acquired in the range between 10^{-5} s and 10^{-3} s. The VES have been collected according to a Schlumberger array and deploying a 100-m maximum half-spacing of the current electrodes. The observed ρ_{app} and the corresponding error bars for TDEM and VES are plotted with red dots in Figure 3.5a-b, respectively. The TDEM measurements had the correspondent uncertainties associated to the data, while the errors of VES data were not available and hence assumed by adding 10% of Gaussian noise.

A preliminary analysis of the data was performed to assess the compatibility between the electrical and electromagnetic sounding curves. It is known that VES curves may be affected by electrical static shift, or galvanic distortion, that must be identified and removed before the joint inversion. We adopted the scaling relationship of Meju (2005) to compare, on the one hand, the VES apparent resistivity curve as a function of the equivalent TDEM delay time and, on the other hand, the TDEM apparent resistivity curve transformed from the signal as a function of the delay time. The presence of a vertical displacement between the VES and TDEM curves is generally regarded as the proof of static-shift occurrence. Conversely, a good parallelism means that the data are compatible and suitable for 1D joint inversion (Meju 2005). This preliminary analysis (not shown here) proved that there was no vertical displacement of the curves and hence the 1D joint optimization could be carried out.

The maximum depth of investigation granted by the half-spacing of VES electrodes was about 60 m. Keeping this value for the validity of the interpretation, we extended the maximum depth of the model up to 110 m to graphically represent the half-space. The model was discretized into 19 layers, whose thickness increased logarithmically with depth. Once the L-curve criterion was applied, the optimal Lagrange multiplier was set equal to 0.1 for both TDEM and VES components of the objective function. The boundary conditions of the solution search space were the minimum and maximum resistivity values of 1 Ωm and 500 Ωm, respectively. The MOPSO algorithm ran for 1000 iterations, giving in the end the family of the resistivity models, or Pareto-optimal solutions, plotted in Figure 3.5c. The solutions drawn from the *PF* are depicted in green, while the blue line corresponds to the solution with the minimum value for both the components of the objective function. As visible from Figure 3.5a-b, the fitting between the observed ρ_{app} (red dots) and calculated response (blue line) is remarkable for both TDEM and VES, respectively. The model displayed in Figure 3.5c reveals a resistive layer of about 200 Ωm in the shallow subsurface, till 10 m of depth. A conductive region of less than 50 Ωm appears from a depth of about 20 m to 40 m, while, at higher depths, the resistivity increases to 77 Ωm.

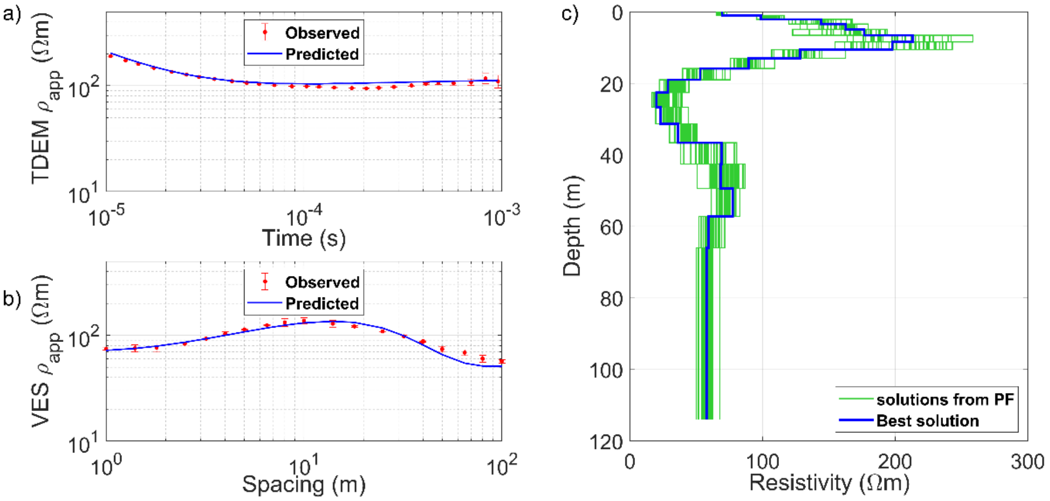

Figure 3.5 The result of TV-MOPSO applied to the Stupinigi data set: observed data (red dots with error bars) and predicted apparent resistivity (blue-line-ρ_{app}) for TDEM **(a)** and VES **(b)** data; **c)** the final resistivity models derived from the *PF* (green lines) and the best solution highlighted in blue.

Figure 3.6a-b shows on separate plots the contextual minimization of the two components of the objective function (TDEM and VES, respectively) from the first to the last iteration. The red stars correspond to the particles with the minimum $f_j(\boldsymbol{m})$, while the black circles to the mean $f_j(\boldsymbol{m})$ among the remaining particles, i.e., solutions found. Figure 3.6c displays the two-dimensional space of the objective function at the final iteration. The black circles represent the $f_j(\boldsymbol{m})$ of the particles forming the swarm, while the red stars highlight the *PF*, that is, the $f_j(\boldsymbol{m})$ of the non-dominated solutions stored in the repository. The *PF* was assayed using three metrics whose equations are provided in Appendix A. The repository index (*RI*) measured the ratio of the non-dominated solutions with respect the population size and was 21.5%. The spacing (*SP*) measured the solution distribution throughout the *PF* and was 0.0041. The deviation angle α between the ideal line and the Theil-Sen-regression line over the non-dominated solutions was 78.9°, as listed in Table 3.1. Figure 3.6d zooms in the *PF*, that gave the deviation angle between the grey-dashed ideal line and the Theil-Sen-regression blue line. As fully explained in Appendix A, $\alpha > 45°$ proved data incompatibility (Schnaidt et al. 2018) and a slight conflict between TDEM and VES was inferred from the asymmetric shape of PF (Dal Moro and Pipan 2007).

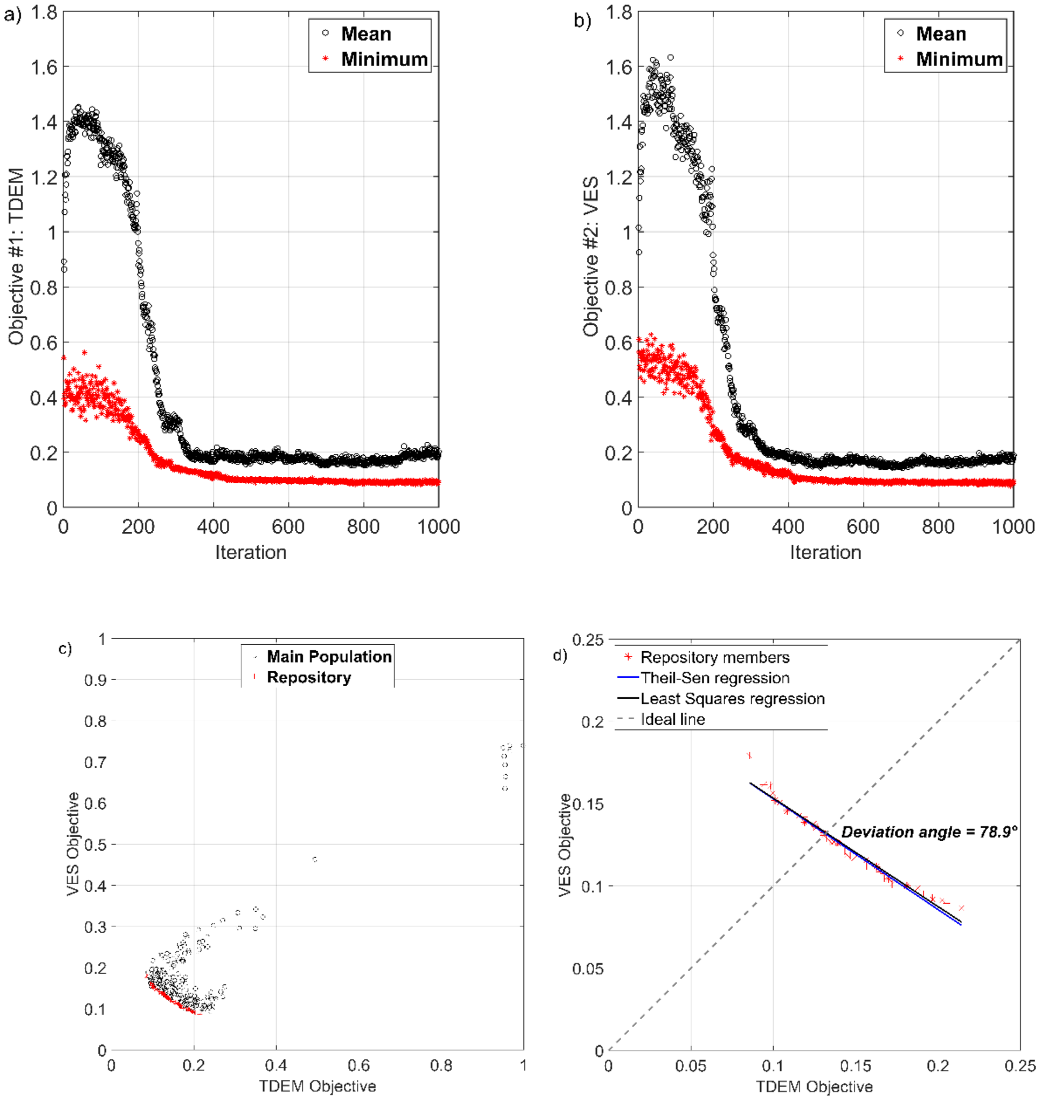

Figure 3.6 TV-MOPSO applied to the Stupinigi data set: the evolution of the TDEM **(a)** and VES **(b)** components of the objective function from the first to the last iteration for the best particle (red stars) and the remaining ones (black circles); **c)** the 2D space of the objective function (TDEM and VES components) at the last iteration: the red symbols identify the *PF* and the black circles the objective-function values assumed by the other solutions; **d)** the intersection between the ideal line (grey dashed) and the Theil-Sen regression line (blue) or the least-square regression line (black) identifies the deviation angle α.

The resistivity model obtained using NSGA-III is shown in Figure 3.7c, together with the satisfactory match between TDEM and VES observed data and computed response of Figure 3.7 a-b, respectively. The model appears considerably similar to that of Figure 3.5c. The most apparent correspondences are the resistive layer of about 200 Ωm in the shallow subsurface and the conductive region (with the minimum of 20 Ωm) from 20 m to 40 m of depth. The main difference from Figure 3.5c is the evident similarity among the non-dominated solutions (green lines of Figure 3.7c), which will be discussed later.

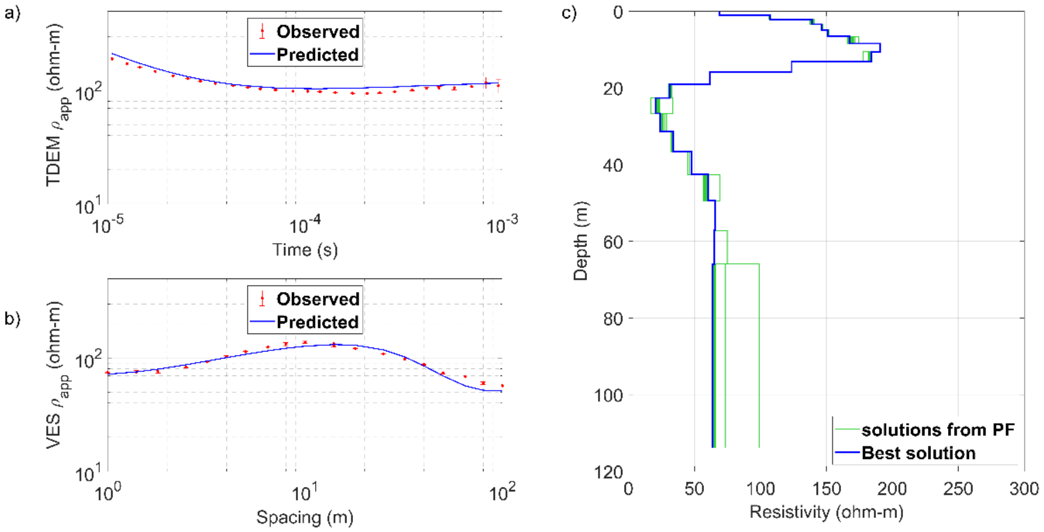

Figure 3.7 The result of NSGA-III applied to the Stupinigi data set: observed data (red dots with error bars) and predicted apparent resistivity (ρ_{app}) for TDEM (**a**) and VES (**b**) data; **c)** the final resistivity models derived from the *PF* (green lines) and the best solution highlighted in blue.

The performance of the NSGA-III algorithm can be analyzed from Figure 3.8. Figure 3.8a-b shows how, at the end of the optimization, both the TDEM and VES components converged toward the minimum value of the objective function, which is found by the best individuals of the population (red stars). Like Figure 3.6a-b, the objective decreased of more than 80% after about 400 iterations, but the effective minimization was reached in 1000 iterations. At the end, the objective space hosted the *PF*, which is plotted in Figure 3.8c with red stars that are coincident to the black circles because all the population corresponded to non-dominated solutions, thus giving *RI*=100%. The Theil-Sen regression line identified a deviation angle of 79.2° with the ideal line (Figure 3.8d), in line with that of MOPSO (see Table 3.1). The root mean square error normalized with respect to the mean value of data (NRMSE) was calculated for the results of MOPSO and NSGA-III, as listed in Table 3.1.

Table 3.1 Analysis of the performance of MOPSO and NSGA-III on the data set from Stupinigi. The rows report: the number of iterations run, repository index (*RI*), spacing (*SP*), deviation angle (α) between the ideal and Theil-Sen regression line, total runtime in hours, normalized root-mean square error (NRMSE) for TDEM and VES.

Stupinigi data set		
	MOPSO	***NSGA-III***
Iterations	1000	1000
RI (%)	21.5	100
SP	0.0041	0.0023
α (°)	78.9	79.2
Runtime (h)	8.9	8.3
NRMSE TDEM	0.1611	0.2728
NRMSE VES	0.0681	0.0645

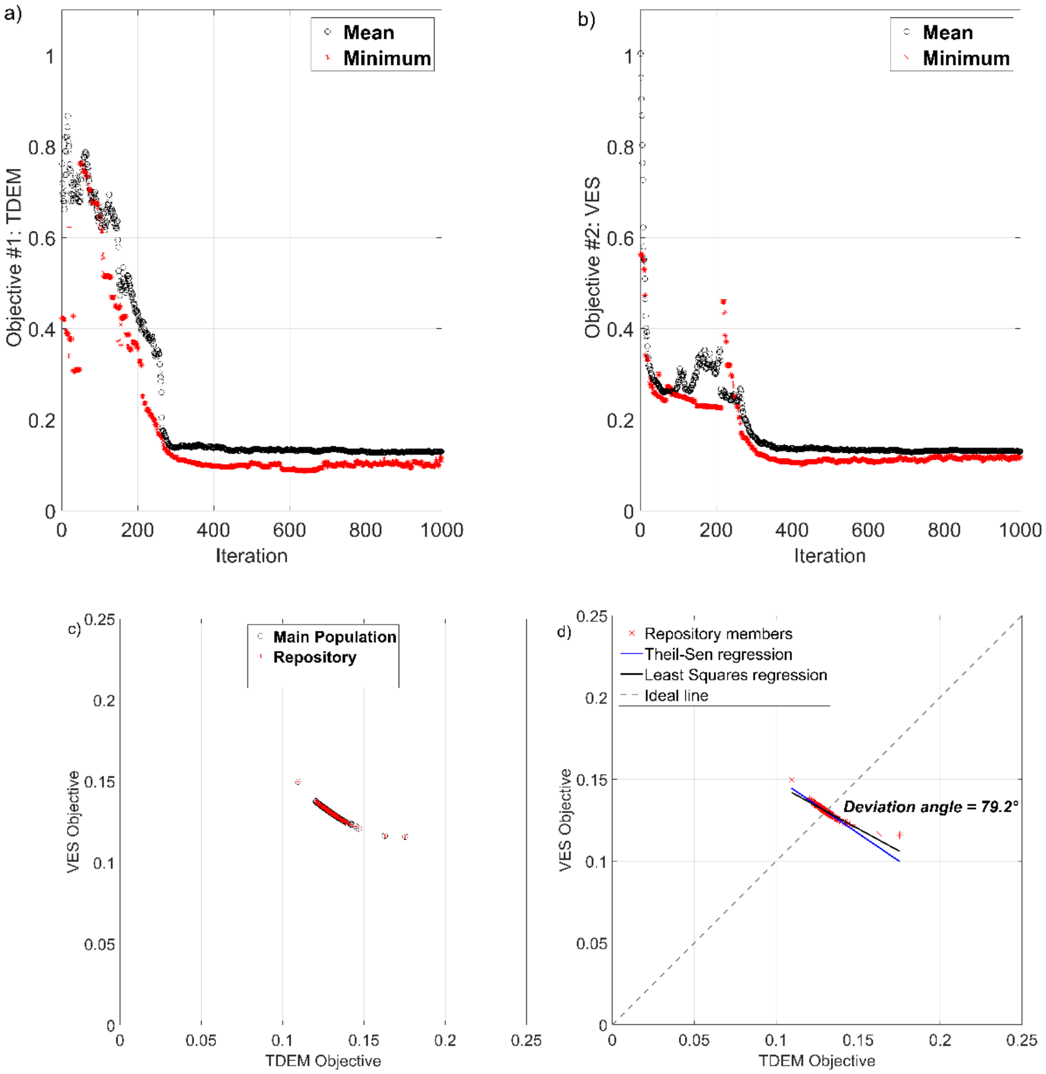

Figure 3.8 NSGA-III applied to the Stupinigi data set: the evolution of the TDEM **(a)** and VES **(b)** components of the objective function from the first to the last iteration for the best individuals (red stars) and the remaining ones (black circles); **c)** the 2D space of the objective function (TDEM and VES components) at the last iteration: the red symbols identify the *PF*, while the black circles the objective-function values assumed by the other solutions; **d)** the intersection between the ideal line (grey dashed) and the Theil-Sen regression line (blue) or the least-square regression line (black) identifies the deviation angle α.

3.4.4 Discussion

The general overview of the results coming from the MOPSO and NSGA-III algorithms suggests some preliminary comments. The objective-function components were iteratively minimized according to a sharp slope at the early stages and, later, a flat trend (see a-b of Figure 3.6 and Figure 3.8). This happened because of the initial heterogeneity of solutions and the significant changes from one iteration to another given by the *k-dependent* coefficients of MOPSO and mutation and crossover of NSGA-III. After that, the largest part of the minimization was overtaken, the models became more homogeneous even though a slight diversity was ensured in MOPSO by the accelerations.

As regards the MOPSO algorithm applied to the Stupinigi data set, the shape of the *PF* and the high deviation angle in Figure 3.6d suggested data incompatibility. It was actually expected, since it is known that a perfect compatibility can be found only for synthetic data (Schnaidt et al. 2018) and real-world problems commonly have conflicting objectives (for example, completing a task in the shortest time and in the cheapest way can be a multi-objective problem with conflicting objectives!). The incompatibility may be attributed to the different depths of investigation: that associated to the VES half-spacing was lower than that of TDEM. This difference resulted because TDEM explores subsurface volumes enlarging with depth according to the principle of the diffusion depth, while VES covers laterally extended volumes. Despite the incompatibility, we may conclude that the data were complementary, as evident from the separate optimizations supplied in Appendix A (Figure A.8 and Figure A.10). TDEM is more sensitive to the conductive region and VES to the superficial resistive layers. Our results can be directly compared to those obtained from separate Monte Carlo inversions in Piatti et al. (2010). This work was a benchmark for our models despite some differences between the two methods. TV-MOPSO deployed a random initialization and then the adaptive behavior, while the importance sampling method of Piatti et al. (2010) exploited the scale property of the apparent resistivity curves to integrate sampling and optimization. Figure 3.9 shows the solutions of our joint optimizations with MOPSO (dashed line) and NSGA-III (solid line) and the Monte Carlo inversion of TDEM (dotted line) from Piatti et al. (2010). This comparison made evidence of the clear advantages of MOPSO: the final model was achieved using a single optimizer for both the data sets instead of separate inversions. The dotted line in Figure 3.9 reveals the limit of the single inversion. Given the same forward-modelling code, Piatti et al. (2010) performed $2 \cdot 10^5$ simulations with a three-layer parametrization while MOPSO ran for 1000 iterations with a 19-layer parametrization. The samplings and the runtime were less than in Piatti et al. (2010). Our results are also supported by the geological information derived from a borehole located very close to the investigated site. The stratigraphy is depicted in the right of Figure 3.9 and is in good agreement with the inversion results. The correspondence between the gravel structure and high-resistivity layers in the shallow subsurface is remarkable. Our outcomes outperform the result of Piatti et al. (2010), which underestimated the superficial resistive structure and overestimated the thickness of the clay layer.

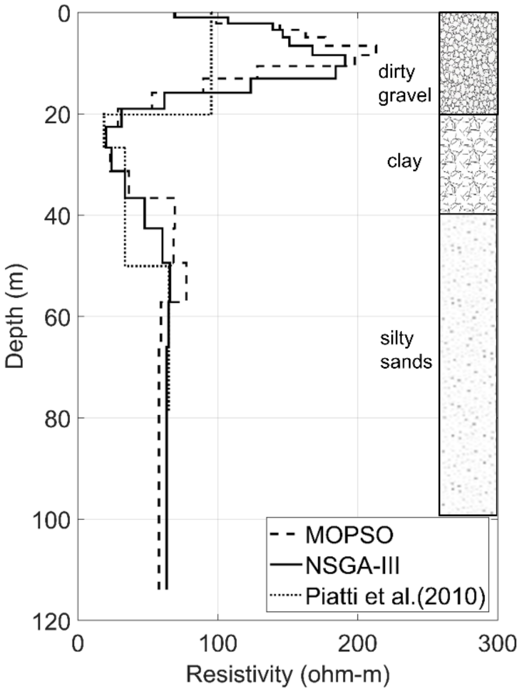

Figure 3.9 Comparison of the different interpretations of the Stupinigi data set using MOPSO (dashed line), NSGA-III (solid line) and Monte Carlo (dotted line) from Piatti et al. (2010). On the right, the stratigraphy from a borehole located very close to the sounding.

3.5. Final remarks

This chapter described the application of CSI to the geophysical inverse problem. Starting from the theoretical background of the PSO algorithm, two recent applications of PSO to magnetotellurics were reviewed. In particular, the recent implementations of PSO for the 1D MT inverse problem and for the static shift correction (Godio and Santilano 2018; Santilano et al. 2018). These contributions represented the scientific background of this work thesis in order to extend CSI to the 2D MT inverse problem, as will be presented in the next chapter.

In the context of metaheuristic methods for 1D geophysical optimization, a new method was developed during the doctorate project: the joint optimization of multiple geophysical data sets by means of a pure multi-objective optimizer, the multi-objective PSO. The MOPSO algorithm revealed a number of attractive features: a single tool to tackle multiple data sets, a set of final models without multiple conflicting solutions because of the Pareto optimality and an effective insight in the trade-off meaning of the final solutions. In fact, the best trade-off solutions and their range were identified as final solutions because of the Pareto dominance. The shape of the *PF* provided insights into the compatibility between different geophysical data sets. The comparison of the joint-optimization result with stratigraphic information coming from boreholes corroborated our findings.

Although the long computation time could be seen as a minor drawback, it must be borne in mind that the stochastic nature of the algorithm requires many forward-modelling calculations, which result in a significant computational load. We managed the computationally demanding nature of MOPSO and NSGA-III using the HPC cluster of Politecnico di Torino. However, we are aware that there is room for improvement and, given the current striking progress in computational efficiency, we are confident this issue will be addressed in future investigations.

The most important finding to emerge from the analysis was that the resistivity models obtained from MOPSO were fully comparable to the ones from NSGA-III, thus supporting the validity of the new proposed method. It can be concluded that MOPSO outperformed the NSGA-III given the more selective filling of the repository and wider variability of the non-dominated solutions (due to an effective exploration of the search space).

Chapter 4

Particle swarm optimization of 2D MT data

This chapter presents the first application of CSI to the 2D MT inverse problem. The PSO algorithm has been accurately described in the previous chapter and is here specifically implemented to properly address the complexity of the 2D inverse problem. Particular attention is paid to the selection of the PSO variant that enhances the stability and convergence of the solution, that are also ensured thanks to a detailed sensitivity analysis on the PSO input arguments. The PSO method is firstly validated on two synthetic examples of 2D MT data of different complexity. Then the method is extended to real-world data, the COPROD2 data set, that is the benchmark to test new 2D MT inversion routines. Finally, the chapter deals with the computational aspects of PSO.

The method and results of this chapter are based on Pace et al. (2019a).

4.1. Introduction

The interpretation of MT data requires the solution of the inverse problem, which is nonlinear and ill posed (Section 2.6). During the past three decades, global search algorithms as inversion methods have become of growing interest because the probabilistic approach can be adopted to find the optimum solution, which is affected by non-uniqueness. The most important global search algorithms generally used for the inversion of geophysical data are simulated annealing (SA), the genetic algorithm (GA) (Sen and Stoffa 2013), the ant colony algorithm (ACO) (Yuan et al. 2009) and PSO (Shaw and Srivastava 2007).

The inversion of MT data is usually based on algorithms such as Occam, nonlinear conjugate gradient (NLCG), and Gauss-Newton (GN), which are now widely recognized as milestones among 2D and 3D MT inversion codes (Siripunvaraporn 2012). Even if they ensure convergence in few iterations, they are all based on the local search principle. Consequently, the final solution depends on the initial assumption of the starting model. If a homogeneous half-space is adopted as a starting model, some trials have to be done to define the most appropriate value of the electrical resistivity to start with, depending on the data set and inversion code (Miensopust et al. 2013). Otherwise, the inversion should be initially constrained by an a priori model that can resolve the non-uniqueness of the solution by using information from well-log data (Yan et al. 2017a), seismic data (Yan et al. 2017b), MT data (Santilano 2017) or other geophysical methods. However, if the a priori knowledge is unreliable or unavailable, the initial guess can create a bias in the final result and interpretation (Dong and Jones 2018). Global search methods have recently become of pivotal importance in MT, with the essential advantage that the inversion is independent from the starting model. The advantage of metaheuristic methods, such as GA, SA and PSO, is that they are theoretically able to find the global minimum of a function as the final solution without being trapped in one of several local minima (Section 3.1). An essential literature review regarding global search applications to MT has been described in Section 2.6.2.

PSO applications to MT have been studied by Shaw and Srivastava (2007), Godio and Santilano (2018) and Santilano et al. (2018), even though they investigated the 1D MT inverse problem. The ensuing sections present a novel implementation of the PSO algorithm for the 2D MT inverse problem (Pace et al. 2019a). A preliminary application of this method to MT and audio-MT synthetic data has been presented in Pace et al. (2017).

The novelty of this study concerns the validation of the PSO method on two MT synthetic models of different complexity and, for the first time to our knowledge, the application to real-field data, the COPROD2 data set (Jones 1993a). This data set was made available to the electromagnetic induction scientific community with the aim of comparing different techniques for 2D MT inversion (Jones 1993b). Since several inversion solutions have been made available so far, COPROD2 represents an interesting (and challenging) field data set for the application of our method. The PSO source code has been derived from Ebbesen et al. (2012), but then modified for the specific MT application. The efficiency of the PSO algorithm was improved by applying a recent PSO variant: the hierarchical PSO with time-varying acceleration coefficients (HPSO-TVAC) (Ratnaweera et al. 2004). Previous works on PSO applied to the geophysical inverse problem have always considered constant values for the social and cognitive accelerations of equation 3.1 (Shaw and Srivastava 2007; Godio and Santilano 2018; Santilano et al. 2018). However, this assumption is not adequate for the 2D inverse problem due to its high dimensionality and complex searching behavior. A detailed sensitivity analysis was carried out to find the most appropriate values of the time-varying accelerations. Their iterative variation improved the convergence speed of the algorithm and prevented the solution from being trapped in some local minima. The tuning of the social and cognitive accelerations of the particles was hence crucial to finally achieve the convergence of the solution. In addition, a new parallelized version of the code was developed to be run on a HPC cluster with the aim of overcoming the time-consuming nature of PSO, which is computationally demanding, like the other global search algorithms.

4.2. PSO application to 2D MT inverse problem

4.2.1 The choice of the variant of the PSO algorithm

As previously explained in Section 3.3, the basic concept of PSO application to geophysics is that each particle of the swarm represents a possible solution of the MT inverse problem, that is, an electrical-resistivity model. Since the solution of the problem is affected by non-uniqueness, the search space of solutions needs to be fully explored to find the best model, which fits the observed data. This need is fulfilled by the adaptive and swarming behavior of the particles. At the end of the swarming, the optimized solution is identified.

Since the implementation of the PSO algorithm for the 2D MT problem required a high number of particles forming the swarm and numerous iterations to achieve convergence, the standard release of the code for MATLAB appeared to need some modifications. Several variations of the PSO algorithm have been proposed to accelerate convergence and avoid a solution trapped in local minima (Zhan et al. 2009). The PSO variant that showed improved outcomes, with respect to the standard PSO, was the HPSO-TVAC (Ratnaweera et al. 2004). This method takes the social and cognitive behavior of particles into account to enhance the solution convergence and stability.

In the 2D MT problem, the particle of the swarm represents a resistivity model, which is a vector whose elements are the resistivity values of the 2D mesh cells. Each particle of the swarm changes its position $\boldsymbol{x}$ within the search space by means of the velocity vector $\boldsymbol{v}$. The vectors $\boldsymbol{x}$ and $\boldsymbol{v}$ are updated iteration by iteration according to the ruling equations presented in Chapter 3. However, the ruling equations of the HPSO-TVAC are slightly different from equations 3.1 and 3.2 in that the acceleration parameters are k-dependent. For the sake of clarity, the equations ruling the PSO of 2D MT data are here reported:

$$\boldsymbol{v}_i^{k+1} = \omega^k \boldsymbol{v}_i^k + \alpha_1^k \gamma_1 (\boldsymbol{P}_i - \boldsymbol{x}_i^k) + \alpha_2^k \gamma_2 (\boldsymbol{G} - \boldsymbol{x}_i^k) \qquad (4.1)$$

$$\boldsymbol{x}_i^{k+1} = \boldsymbol{x}_i^k + \boldsymbol{v}_i^{k+1} \qquad (4.2)$$

where the equation terms have been defined in Section 3.2. Equation 4.1 is similar to equation 3.10 except for the global best $\boldsymbol{G}$, that, in single-objective optimization, is unique and not k-dependent.

At the beginning of the optimization (*k=0*), the velocity vector ($\boldsymbol{v}_i^0$) is zero and the position vector ($\boldsymbol{x}_{\mathrm{i}}^0$) is randomly initialized. Then (*k >0*), the particle velocity ($\boldsymbol{v}_i^k$) changes according to three terms: inertia component ω^k, cognitive memory $\alpha_1{}^k$ and social attraction $\alpha_2{}^k$. Finally, the particle position $\boldsymbol{x}_i^k$ is updated.

It is evident from equation 4.1 that the acceleration coefficients vary at each iteration, according to the HPSO-TVAC approach. It states that, at the beginning of the optimization, α_1 is set larger than α_2 and then they linearly reverse. In this way, at the start the diversity of the swarm ensured the search space exploration (high α_1^k), and, at the end, the exploitation of the best regions and the convergence towards the best solution were enabled (high α_2^k). The resulting adaptive behavior was hence enhanced. In more detail, the cognitive and social accelerations changed according to equations 3.11 and 3.12 and obeyed the stability equations 3.3 and 3.4.

The best range of the acceleration values ensuring the convergence and stability of the PSO algorithm has been tested and identified for several benchmark functions (Ratnaweera et al. 2004; Fernández Martínez al. 2010a, 2010b). Starting from their results, and obeying equations 3.3, 3.4, 3.11, 3.12, we performed some tests to assess the influence of several acceleration values on the solution of the 2D MT inverse problem. For the cognitive and social accelerations, we adopted three different maximum values, α_1^{max} and α_2^{max} equal to 1.5, 2, and 2.75, and three different minimum values, α_1^{min} and α_2^{min} equal to 0.25, 0.5, and 0.75. This sensitivity analysis was applied to an example of 2D MT synthetic model, and the results are presented in Section 4.3.

4.2.2 The objective function

The final goal of the optimization process is the minimization of a selected objective function. The particle with the lowest objective-function value is awarded with the global best position ***G*** and is going to attract neighbors depending on the social acceleration α_2. The objective function we adopted was the same as that of Everett and Schultz (1993) for the calculation of the data misfit, while the Occam-like regularization was added as proposed by deGroot-Hedlin and Constable (1990). Therefore, for 2D MT data, the function to be minimized was

$$F(\boldsymbol{m}) = \left(\frac{1}{M} \left\| \frac{\log(\rho_{a,o}) - \log(\rho_{a,p})}{\log(\Delta\rho_{a,o})} \right\|_2^2 + \frac{1}{M} \left\| \frac{\varphi_o - \varphi_p}{\Delta\varphi_o} \right\|_2^2 \right)^{\frac{1}{2}} + \lambda_x \, \|\partial_x \boldsymbol{m}\|_2 + \lambda_z \, \|\partial_z \boldsymbol{m}\|_2 \tag{4.3}$$

where: $\boldsymbol{\rho_{a,o}}$ and $\boldsymbol{\rho_{a,p}}$ are observed and predicted apparent resistivity, respectively; $\boldsymbol{\varphi_o}$ and $\boldsymbol{\varphi_p}$ are observed and predicted impedance phases, respectively; $\boldsymbol{\Delta\rho_{a,o}}$ and $\boldsymbol{\Delta\varphi_o}$ are the errors in observed apparent resistivity and phase, respectively; M is the number of degrees of freedom, i.e., the number of evaluated data; λ_x and λ_z are the Lagrange multipliers in the x- and z-direction, respectively, set as the tradeoff between the model and data misfit to regulate the model roughness, and $\partial_x \boldsymbol{m}$ and $\partial_z \boldsymbol{m}$ are the first derivatives of the model solution along the x- and z-directions, respectively. The solution $\boldsymbol{m}$ is the electrical-resistivity model, i.e., the vector of resistivity values of the 2D domain. This vector has as many elements as the grid cells of the 2D mesh and is represented by the particles of the swarm. At each iteration, the particle which best minimizes the objective function is assumed as the global best solution (***G***), while the other particles can be either attracted or driven away looking for other solutions in the search space. At the end of the optimization, the particle with the minimum $F(\boldsymbol{m})$ is selected as the final solution and the majority of the other particles converge to it (swarming behavior). Apparent-resistivity values were transformed to their logarithmic values since they can cover different orders of magnitude. The first part in the right-hand side of equation 4.3 addresses the minimization between observed data, apparent resistivity and impedance phase, and predicted data computed by the forward modeling. This calculation of the misfit is defined as the square root of the sum of two squared Euclidean norms, since $\boldsymbol{\rho_a}$ and $\boldsymbol{\varphi}$ can have different orders of magnitude and ranges. The forward modeling incorporates the physics of the problem and, starting from the assumed model $\boldsymbol{m}$, predicts the responses $\boldsymbol{\rho_a}$, and $\boldsymbol{\varphi}$ for each particle of the swarm. The remaining part of equation 4.3 was added in order to minimize the roughness of the model solution $\boldsymbol{m}$: in both horizontal and vertical directions, the differencing operator on $\boldsymbol{m}$ was weighted by the Lagrange multiplier λ. As explained in Section 3.3.1, this approach is the Occam-like optimization and has been adopted for 1D MT problem in Godio and Santilano (2018) and Santilano et al. (2018). The value of λ was appropriately chosen following the L-curve criterion of Farquharson and Oldenburg (2004), which finds the optimal tradeoff between the misfit of the data and the roughness of the final model (i.e., the model norm) in both horizontal and vertical directions. The synthetic and real models analyzed in this chapter had their specific optimal value of λ. In this way, the minimization of the objective function looks for the smoothest model that fits the data, thus ensuring a balance between the data fitting and the roughness of the model.

4.2.3 PSO input arguments

The main input arguments or tuning parameters of the PSO algorithm are:

a) The acceleration coefficients α_1 and α_2
b) The stopping criterion/criteria adopted to end the iterations (theory in Section 3.2)
c) The swarm size N, i.e., the number of particles forming the swarm
d) The initialization settings

The need for the sensitivity analysis on the acceleration coefficients has been explained in Section 4.2.1. The identification of the most appropriate values is presented in Section 4.3.1.

The PSO algorithm was iterated enough to guarantee as robust as possible minimization of the objective function (equation 4.3). Previous PSO applications adopted the maximum number of iterations as the unique stopping criterion (Godio and Santilano 2018; Santilano et al. 2018). However, the number of iterations is problem dependent and its arbitrary choice can lead to either an ending before the solution convergence or unnecessary computation (Engelbrecht

2007). In this study, we took into account the trend of the objective function during the minimization process. PSO ran as long as the fitness value did not minimize for 80 consecutive iterations or, if this condition was not satisfied, up to a maximum number of 6000 iterations. Another stopping criterion was the minimum root-mean-square error (RMSE) of the data equal to 1 (±10% of tolerance), to avoid the fitting of the data below their uncertainty (deGroot-Hedlin and Constable 1990).

The swarm size *N* influences the way that particles distribute over the search space to guarantee the exploration of possible solutions. The swarm size must be sufficiently high to ensure a wide initial coverage of the search space, so that the particles can efficiently explore all of the regions potentially hosting the global minimum. This behavior is missed if the swarm is too small, although giving the advantage of unburdening the computational complexity. An interesting analysis on the relation between the swarm size and the computational complexity can be found in Van den Bergh and Engelbrecht (2001). The number of particles is a problem-dependent parameter and it is usually set proportional to the number of unknowns, that is, for us, the number of resistivity cells the 2D domain was discretized into. The ratio between the problem unknowns and the number of particles was suggested to be between 8 and 12 times the unknowns by Engelbrecht (2007, p. 241) for GA and Fernández Martínez et al. (2010a) for PSO. Starting from these guidelines, we performed a sensitivity analysis to verify the influence of this ratio on the solution of the MT inverse problem. The number of particles was set at 6, 8, 9, 10 and 12 times the number of unknowns. This analysis was carried out on an example of synthetic model and the results are shown in the next section.

The initialization of the optimization is another essential feature of PSO. At the beginning, the particle distribution within the search space is, by default, completely random and bounded between a minimum and maximum value of resistivity. This range is kept constant during the optimization but might vary from each layer (or group of layers or cells) to another (Godio and Santilano 2018). The decision of the lower and upper resistivity boundaries is problem dependent and should be coherent with the desired coverage of the search space of solutions. We set the boundaries far larger than the limits of the apparent-resistivity curves. After the random initialization, the adaptive behavior controls the position updating and a stochastic perturbation is guaranteed by γ_1 and γ_2 of equation 4.1. Local search algorithms usually deploy a starting model (a homogeneous or a priori model) to initialize the geophysical inversion. The a priori information is derived from geologic (well-log) data or other geophysical methods. Although it is possible to use a priori information to partially influence the swarm behavior, the key factor of global search algorithms such as PSO is that they do not require a starting model. To demonstrate this, synthetic data were optimized starting with and without aprioristic information, which was given to the particles in the form of starting positions in the search space. This a priori information was given only to a small amount of particles, 5% of the total, so that the initial position of the rest of the swarm was randomly selected and the swarming nature of PSO was obeyed. The a priori information were derived from the solution PSO gave for the 1D MT inverse problem.

The PSO flow chart is shown in Figure 4.1. This procedure was repeated three times (or “trials”) for each study case, due to the variability on the solution given by the random initialization. In fact, the final solutions coming from different initial random distributions are quite similar but not identical, as shown in Santilano et al. (2018) for 1D MT. The solution with the lowest fitness value was then selected as the final optimized model.

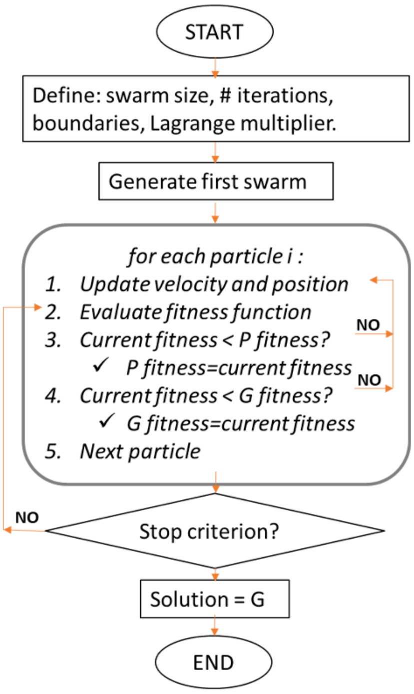

Figure 4.1 The PSO algorithm flowchart. ***P*** is the local best solution and ***G*** is the global best solution.

4.3. 2D optimization of MT synthetic data

The theoretical MT data sets were computed from two synthetic models depicted in Figure 4.2 and Figure 4.3. They covered a 2D domain 350 km long and 250 km deep, in order to take proper boundary conditions into account for the MT forward modeling (Simpson and Bahr 2005). Fifteen MT stations were centrally placed in the mesh and reciprocally spaced 1.3 km. The mesh discretization used for the generation of the synthetic data was different from that used for the optimization. Specifically, the latter was slightly coarser than the former due to the computational load given by the thousands of forward-modeling calculations within the PSO algorithm. The mesh size along the horizontal direction has been kept constant between the stations and doubled from the outer stations towards the boundaries. Along the vertical direction, the layer size increased logarithmically with depth. In the case of a priori given, the optimization ran on a subdomain of about 400 cells, because the a priori information regarded only 15 stations. In the case of random initialization, the domain extended far away from the stations due to boundary conditions and the number of cells increased up to about 900 for synthetic model 1 and about 750 for synthetic model 2.

Both synthetic models simulated the presence of one or more electrically conductive features embedded in a resistive body beneath the station sites. The first synthetic model is shown in Figure 4.2. Figure 4.2a shows the entire 2D mesh, discretized into 33 layers for a total of 957 grid cells. The synthetic model 1 is quite simple and composed of a host medium of 100 Ωm including a conductive body of 10 Ωm from 3 to 5 km depth. Figure 4.2b shows synthetic model 1 as a zoom in the center of the whole mesh.

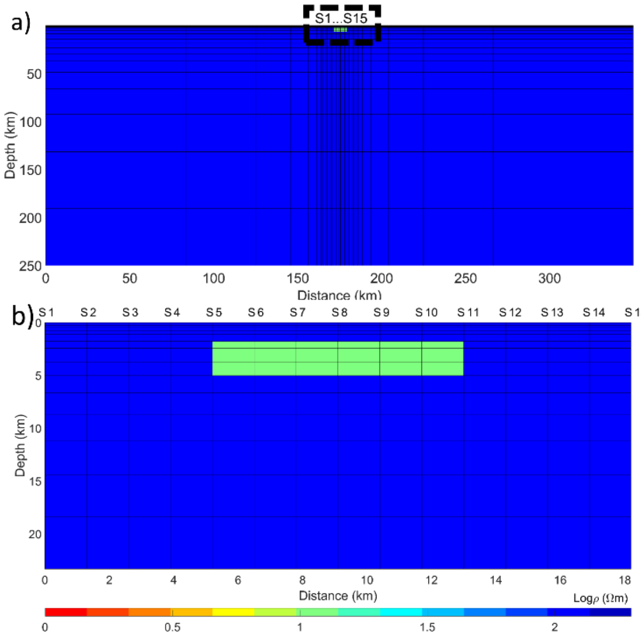

Figure 4.2 Synthetic model 1: **a)** the 2D mesh is discretized into 33 layers and a total of 957 grid cells. The labels S1, …, S15 indicate the location of the 15 MT stations. The dashed area is shown in **b)** a 10 Ωm conductive body is hosted in a 100 Ωm medium.

Figure 4.3 illustrates synthetic model 2 as a subsection of the true mesh. The mesh is discretized into 754 grid cells and, even so, the model space is not under-sampled. The 100 Ωm resistive medium hosts, from the bottom up, a 10 Ωm body 4-to-9 km deep on the left side of the mesh, a 10 Ωm body 1-to-2.5 km deep on the right side of the mesh, and a 50 Ωm body 0-to-500 m deep under stations S2-S5.

The forward modeling which created the synthetic data considered 26 frequency values between 10^{-2} and 10^{3} Hz. Synthetic data were corrupted with uncorrelated Gaussian noise of 10%. This noise corresponded to $\boldsymbol{\Delta\rho_{a,o}}$ and $\boldsymbol{\Delta\varphi_a}$ matrices in equation 4.3, which are the normalization terms of the data misfit. At each k^{th} iteration, the noise influenced the forward calculated response of the corresponding k^{th} model $\boldsymbol{m}$. The optimization process was constrained by upper and lower resistivity boundaries equal to 200 Ωm and 1 Ωm, respectively.

This section is divided into two parts. In the first sub-section (4.3.1), the Lagrange multiplier of synthetic model 1 is identified and, then, the synthetic model 1 is adopted as study case to calibrate two input arguments of PSO, the accelerations and the population size. In the second sub-section (4.3.2), the final resistivity models are presented for both synthetic model 1 and 2.

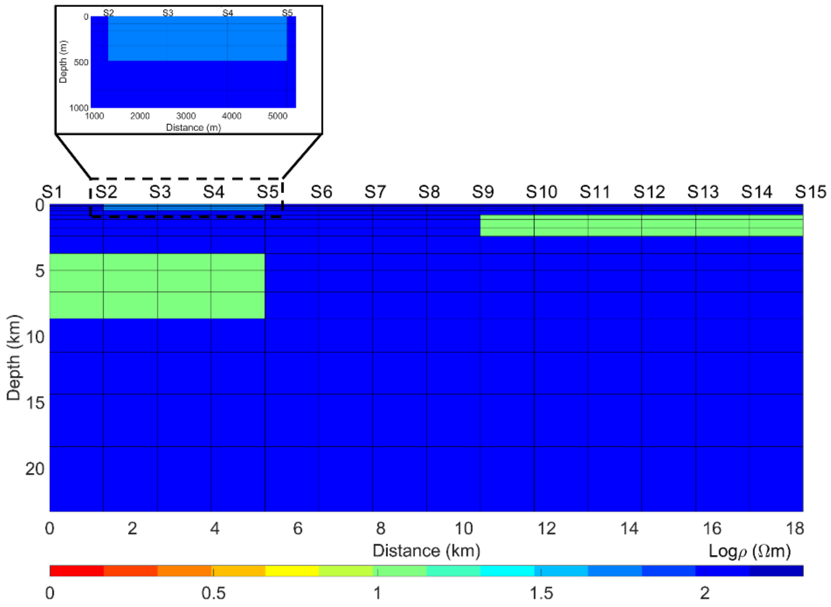

Figure 4.3 Synthetic model 2: two 10 Ωm deep anomalies and one superficial 50 Ωm body are embedded in a 100 Ωm host medium. The labels S1, S2, …, S15 indicate the 15 MT stations. The zoomed-in box on the top shows the 50- Ωm body below S2-S5.

4.3.1 Calibration of the PSO input arguments

The sensitivity analysis on the Lagrange multiplier was carried out on synthetic model 1 using benchmark values for the accelerations and the population size. These values were chosen as benchmarks for the best convergence of the solution after Ratnaweera et al. (2004). The calibration of the accelerations and population size is presented in the next paragraph because it has significance if the most appropriate Lagrange multiplier is adopted. As a benchmark, the cognitive acceleration α_1 linearly decreased from $\alpha_1^{max} = 2$ to $\alpha_1^{min} = 0.5$ and the social acceleration α_2 linearly increased from $\alpha_2^{min} = 0.5$ to $\alpha_2^{max} = 2$. The benchmark population size was about 9 times the number of unknowns, that is, given 957 cells, 8600 particles. In order to retrieve the optimal value of the Lagrange multiplier λ, we performed a sensitivity analysis on five different values in the range between 0.001 and 10. λ_x and λ_z were contextually analyzed with the same value and the optimal value was chosen as the point of maximum curvature in the plot of data misfit versus model norm. Figure 4.4 shows the data misfit of synthetic model 1 with respect to the model roughness along the horizontal (black diamonds) and vertical (red circles) directions. The best tradeoff value was equal to 0.1 for both λ_x and λ_z.

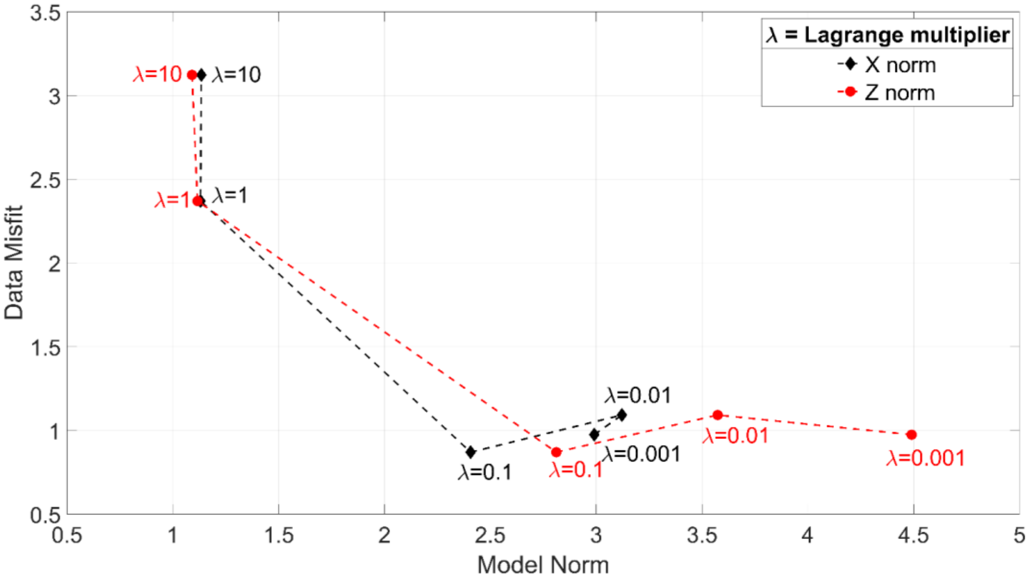

Figure 4.4 L-curve response for synthetic model 1 along the horizontal (black diamonds) and vertical (red circles) directions. The tradeoff between data misfit and model norm indicates the best Lagrange multiplier λ equal to 0.1.

The sensitivity analysis on the cognitive and social accelerations was carried on for synthetic model 1 once its optimal value of the Lagrange multiplier was identified. For this calibration, the population size was fixed to the aforementioned benchmark value of 8600 particles and its sensitivity analysis is shown in the next paragraph. The three chosen values for the maximum cognitive acceleration were $\alpha_1^{max} = 2.75, 2, 1.5$ and for the social acceleration $\alpha_2^{min} = 0.25, 0.5, 0.75$. These values were selected on the basis of the existing literature and equations 3.3 and 3.4. The solution reliability was evaluated via some parameters of the optimization process, such as the first stopping criterion achieved, the solution clustering, and the trend of the objective function at each iteration. The simulations ran until one of the three stopping criteria explained in Section 4.2.3 was first fulfilled, that is, when the objective function did not significantly decrease and (almost) all the particles converged to a unique position in the search space or solutions. Table 4.1 lists the RMSEs and the objective-function values ($F(\mathbf{m})$) at the end of the optimization of each test. Our results are largely consistent with the acceleration values pointed out in Ratnaweera et al. (2004) for other applications. The tests using $\alpha_1^{k=1} = 2.75$ with $\alpha_2^{k=1} = 0.5$ and with $\alpha_2^{k=1} = 0.75$ ended before that the RMSE was equal to 1, because the objective function did not decrease for 80 consecutive iterations. These values prevented an effective minimization, as shown in Figure 4.5, which summarizes the optimization performance using $\alpha_1^{k=1} = 2.75$ and $\alpha_2^{k=1} = 0.5$. The four subplots show, in order: Figure 4.5a the objective-function values of the best particle (red dots) and the mean values of the rest of the swarm (black dots) from the first to the final iteration; Figure 4.5b the objective-function values of the whole swarm as a function of the particle positions in two representative dimensions of the search space, i.e., the first two cells of the 2D grid, at the first (grey dots) and final (blue dots) iterations; Figure 4.5c the positions, i.e., the resistivity values, of the particles in the first two cells of the 2D grid at the first and final iterations (grey dots and blue dots, respectively); Figure 4.5d the histogram containing the distribution of the objective-function values at the last iteration among all the particles (8600 in this case). Figure 4.5 reveals that the optimization did not end in a convergence state because at the last iteration the minimum *F(***m***)* was not reached by the totality of the particles (Figure 4.5a and d), and the distribution of the particles in the search space was still scattered (blue dots in Figure 4.5b and c).

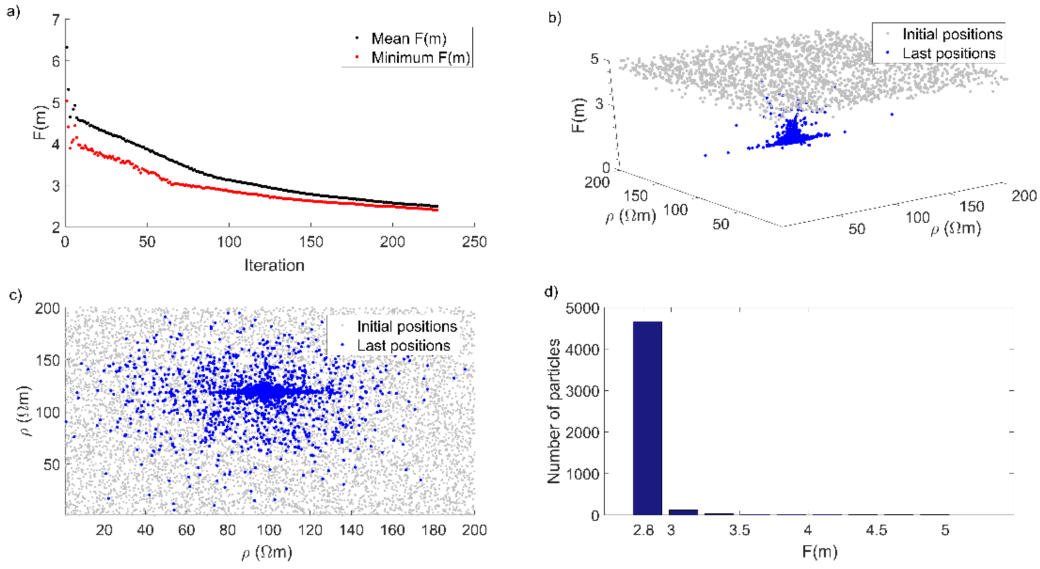

Figure 4.5 Objective function *F(m)* and particle positions at the end of the optimization: **a)** objective-function value, iteration after iteration, for the best particle (red dots) and the rest of the swarm (black dots); **b)** the objective-function value as a function of the particle positions in the resistivity (ρ) search space, at the first (grey dots) and final (blue dots) iterations; **c)** plain view of b); **d)** final distribution of the objective-function values among all the particles.

The other tests in Table 4.1 show an optimal convergence, RMSEs equal to about 1 and the minimized ***F(m)*** between 1.33 and 1.73. Figure 4.6 plots the optimization performance using $\alpha_1^{k=1} = 2$ and $\alpha_2^{k=1} = 0.5$. The minimization of the objective function was more effective than that of Figure 4.5 because all the particles converged towards a unique position (blue dots in Figure 4.6b-c) with the same objective-function value corresponding to the peak in Figure 4.6d. It is evident that, iteration by iteration, particles converged from an initial scattered distribution to a unique position following the best particle leadership. In this way, the objective-function value dropped and the histogram developed a unique peak. This sensitivity analysis outlined $\alpha_1^{\max} = 2$, $\alpha_1^{\min} = 0.5$, $\alpha_2^{min} = 0.5$, and $\alpha_2^{max} = 2$ as optimal acceleration values for a robust minimization of the objective function. These accelerations were applied to the optimization of the other MT data sets of this thesis.

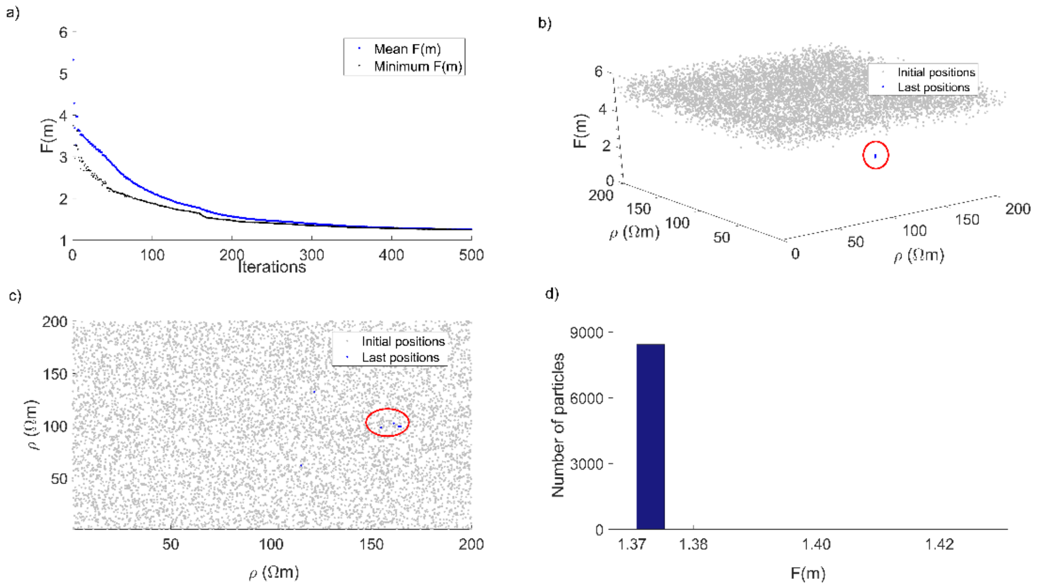

Figure 4.6 Objective function *F(m)* and particle positions at the end of the optimization: **a)** objective - function value, iteration after iteration, for the best particle (red dots) and the rest of the swarm (black dots); **b)** the objective-function value as a function of the particle positions in the resistivity (ρ) search space, at the first (grey dots) and final (blue dot) iterations; **c)** plain view of b) with all particles converged to the last position (red circled blue dot); **d)** final distribution of the objective-function values among all the particles.

The synthetic model 1 was also a study case for the sensitivity analysis on the population size (N), in order to assess the influence of the number of particles on both the solution and the runtime. The tests were performed using 5 different values, chosen as multiples of the number of unknowns (957): 5700, 7500, 8600, 9500, 11500 particles, that is, 6, 8, 9, 10, and 12 times the unknowns. The accelerations and Lagrange multiplier were set as explained before for the corresponding sensitivity analyses. The results are shown in Table 4.2. All the tests reached the minimum RMSE of about 0.9, but with different numbers of iterations and runtimes because of the different initial distributions of the particles in the search space of solutions. The test using the multiple 8 gave the worst result because the solution was found after the biggest runtime and the highest number of iterations. Differently, the multiple 9 gave the best result, with the minimum number of iterations and the second shortest runtime. The ratio of 9, i.e., 8600 particles for synthetic example 1, ensured the most effective convergence and exploration of the solution space, so that it was adopted for the other tests presented in this work.

Table 4.1 Synthetic data from example 1 were adopted to perform the calibration of the cognitive acceleration α_1 and social acceleration α_2 starting from different values at the first iteration ($k = 1$). The final values of the RMSE and objective function *F(**m**)* are listed for each test.

		$\alpha_2^{k=1} = 0.25$	$\alpha_2^{k=1} = 0.5$	$\alpha_2^{k=1} = 0.75$
$\alpha_1^{k=1} = 2.75$	*RMSE*	0.91	2.17	2.18
	F(m)	1.34	2.88	3.03
$\alpha_1^{k=1} = 2$	*RMSE*	0.88	0.86	0.91
	F(m)	1.47	1.37	1.33
$\alpha_1^{k=1} = 1.5$	*RMSE*	1.11	1.01	0.87
	F(m)	1.73	1.52	1.44

Table 4.2 Sensitivity analysis on the population size as PSO input argument. The number of particles was 6, 8, 9, 10, and 12 times the number of unknowns of the problem (957 grid cells). Results are analyzed in terms of: RMSE, total runtime in hours and the maximum number of iterations reached.

Number of particles	***Times the unknowns***	***RMSE***	***Runtime (h)***	***Iterations***
5700	6	0.88	3.47	166
7500	8	0.90	7.17	275
8600	9	0.86	4.60	154
9500	10	0.88	5.82	176
11500	12	0.87	6.52	165

4.3.2 Results from two synthetic examples

The results of PSO applied to the two synthetic examples in Figure 4.2 and Figure 4.3 are presented in this section. The optimization of MT data from the synthetic models was performed adopting the optimal values for the Lagrange multipliers, accelerations and population size reported in the previous section. The results regarding synthetic model 1 are presented in this order: the model obtained without external conditioning of the PSO initialization, the model resulting from a poorly populated swarm and finally the result after the PSO initialization with a priori information given as starting model. The resistivity model obtained without a priori information is shown in Figure 4.7. After about 150 iterations (and 4.6 hours), the RMSE stabilized around the final value of 0.86, while F(m) was 1.37. These values are listed in Table 4.3, but they can also be found in Table 4.1 for $\alpha_1^{k=1} = 2$ and $\alpha_2^{k=1} = 0.5$ and in Table 4.2 for 8600 particles. The resistivity model in Figure 4.7 was largely comparable to the true model in Figure 4.2, since the conductive anomaly was correctly detected in both size and resistivity. Figure 4.8 plots the fitting curves between synthetic and calculated data for both apparent resistivity (ρ_{app}) and phase, both TE and TM polarizations. The synthetic data are marked as dots for TE, and diamonds for TM, while the PSO-predicted data are plotted as solid lines for TE, and dashed lines for TM. Four stations were selected for their different positions in relation to the lateral discontinuities: S1, S4, S7, and S11. They show an example of poor (S4 ρ_{app}), average (S11), and good fit (S1, and S7). Considering the high number of unknowns and the wide range of variation of ρ_{app}, it could be said that these curves are clearly similar to each other as also proved by the low RMSE.

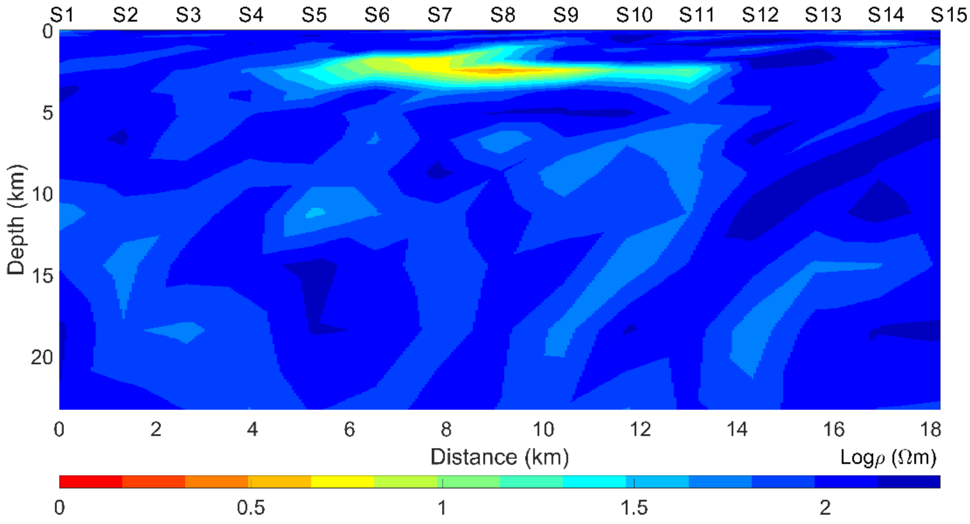

Figure 4.7 PSO solution for synthetic model 1, after about 150 iterations without a priori initialization for the 8600 particles of the swarm. Lagrange multiplier $\lambda = 0.1$.

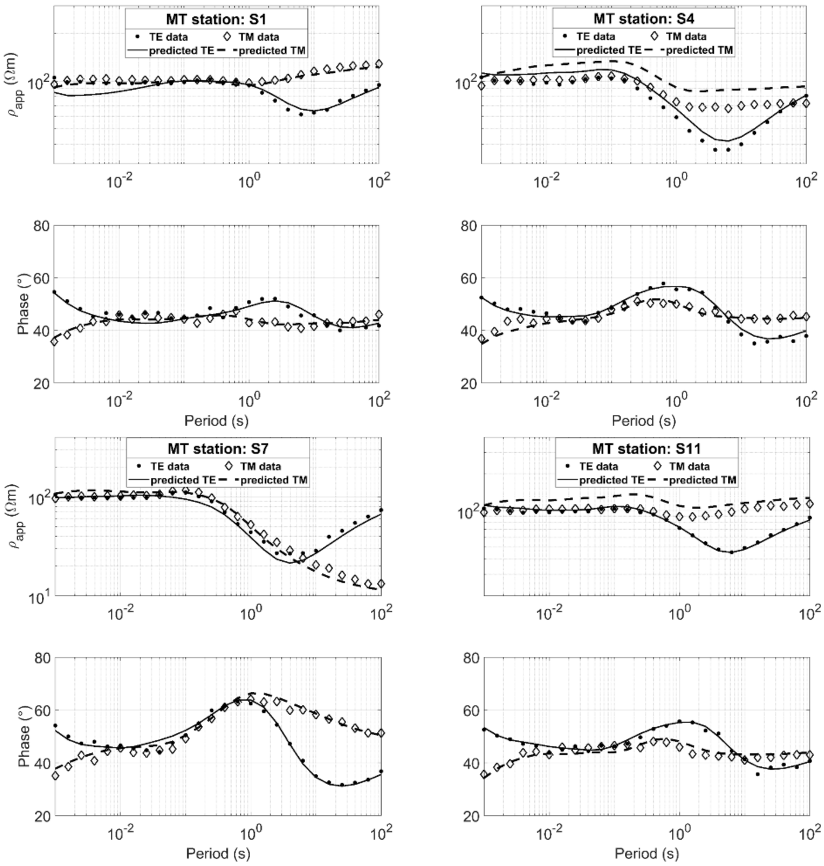

Figure 4.8 Fitting curves between data of synthetic model 1 and calculated data for apparent resistivity (ρ_{app}) and impedance phase for both TE and TM polarizations. The selected MT stations are S1, S4, S7, and S11. The synthetic data are marked as dots for TE, and diamonds for TM, while the PSO-predicted data are plotted as solid lines for TE, and dashed lines for TM. The optimization was randomly initialized.

The influence of the population size on the optimization process is presented in Table 4.2. Figure 4.9 shows the effect of a poorly populated swarm on the final resistivity model. This result followed from a population size of 5700 particles, i.e., 6 times the unknowns. The result was similar to the true model in Figure 4.2, since the conductive body was identified. However, the output was not completely appreciable due to some lateral conductive artefacts that corrupted the homogeneous 100-Ωm background. As expected, this outcome was the consequence of an ineffective initial distribution of the particles in the search space of solutions, and, possibly, of the missing of the global minimum.

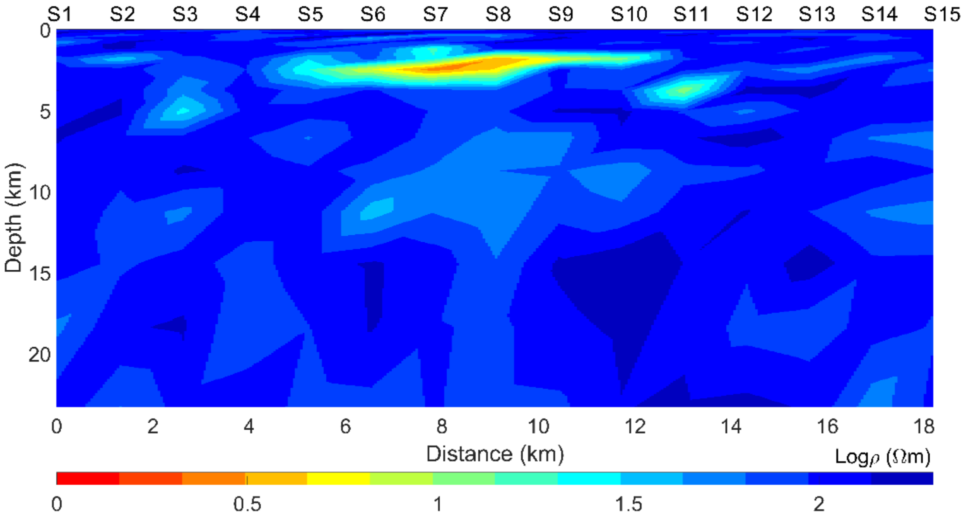

Figure 4.9 PSO solution for synthetic model 1 using a swarm size of only 5700 particles (6 times the unknowns), after about 160 iterations, without a priori initialization, and Lagrange multiplier $\lambda = 0.1$.

The a priori information used to initialize the optimization came from the PSO solutions of the 1D inverse problem for the 15 stations of synthetic model 1. Only 5% of the particles were initially influenced with this solution. After 250 iterations, the RMSE reached the minimum threshold, with a corresponding objective-function value of 1.4. The final resistivity model is shown in Figure 4.10 and is comparable with the true model (Figure 4.2), since the conductive anomaly was adequately identified. Figure 4.11 plots the fitting curves of the selected stations. The PSO-predicted responses were distinctly consistent with the synthetic data and the difference with the curves of Figure 4.8 was negligible, except for the slight improvement for ρ_{app} of S4 and S11. Table 4.3 lists the details regarding the RMSE, the runtime (in hours) and the total number of iterations.

The optimization of synthetic data from synthetic model 2 (true model in Figure 4.3) was performed after the calibration of the input arguments, the accelerations, and population size. The identification of the optimal Lagrange multiplier λ for synthetic model 2 was inferred from the L-curve response presented in Figure 4.12. It refers to the data-misfit trend as a function of the horizontal (black diamonds) and vertical (red circles) roughness of synthetic model 2. The best tradeoff value was 0.1 for both λ_x and λ_z.

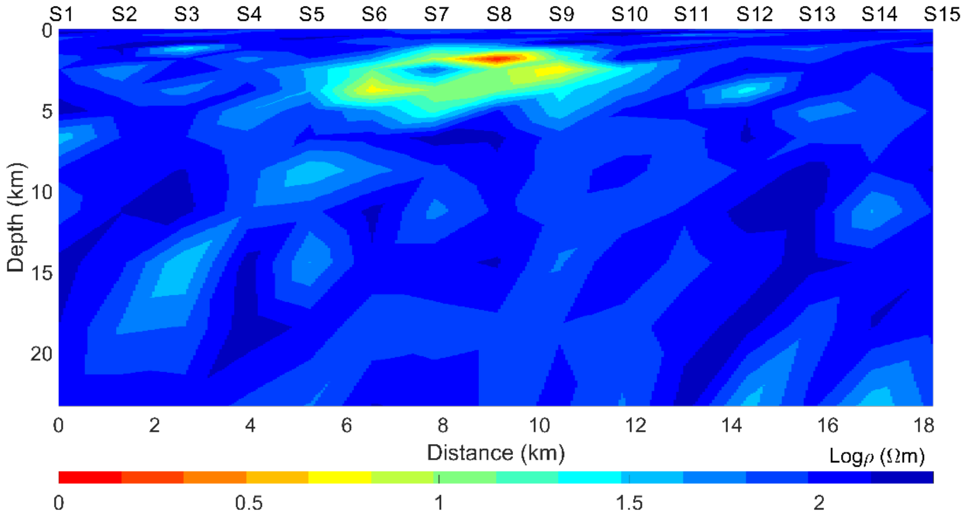

Figure 4.10 PSO solution for synthetic model 1, after about 250 iterations and with a priori information given to 5% of the particles. Lagrange multiplier $\lambda = 0.1$.

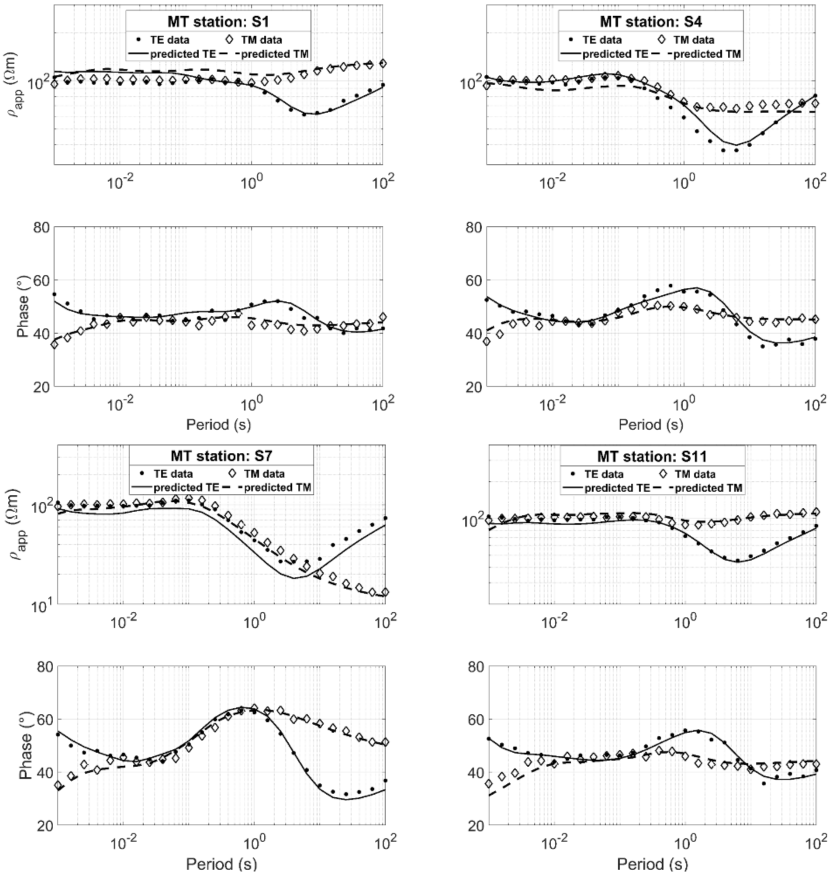

Figure 4.11 Fitting curves between data of synthetic model 1 and calculated data for apparent resistivity (ρ_{app}) and impedance phase for both TE and TM polarizations. The selected MT stations are S1, S4, S7, and S11. The synthetic data are marked as dots for TE, and diamonds for TM, while the PSO-predicted data are plotted as solid lines for TE, and dashed lines for TM. The optimization was initialized with a priori information.

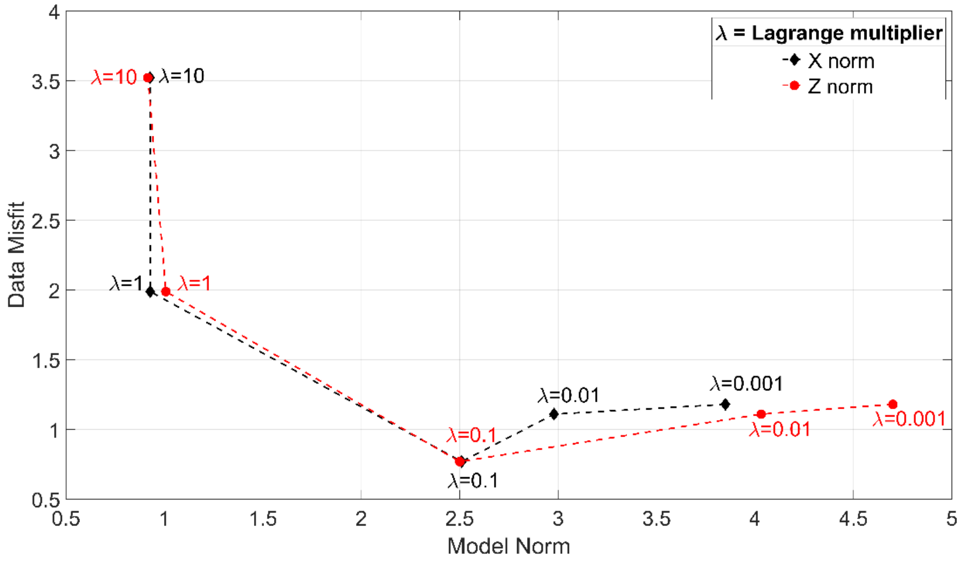

Figure 4.12 L-curve response for synthetic model 2 along horizontal (black diamonds) and vertical (red circles) directions. The tradeoff between data misfit and model norm indicates the best Lagrange multiplier λ equal to 0.1.

The best solution for synthetic model 2 without a priori initialization is illustrated in Figure 4.13. All the three low-resistivity bodies were accurately positioned as can be seen from the zoom-in panel. After 1674 iterations, the minimum objective function value was 1.3 and the RMSE was 0.9. Figure 4.14 plots the comparison between synthetic and calculated data for both apparent resistivity (ρ_{app}) and phase (TE and TM). Stations S1, S5, S9, and S12 were selected as representative for their poor (S1), average (S5 and S9), and good fit (S12). Taking the complexity of this synthetic example into proper account, the curves are in good agreement. The runtime is listed in Table 4.3.

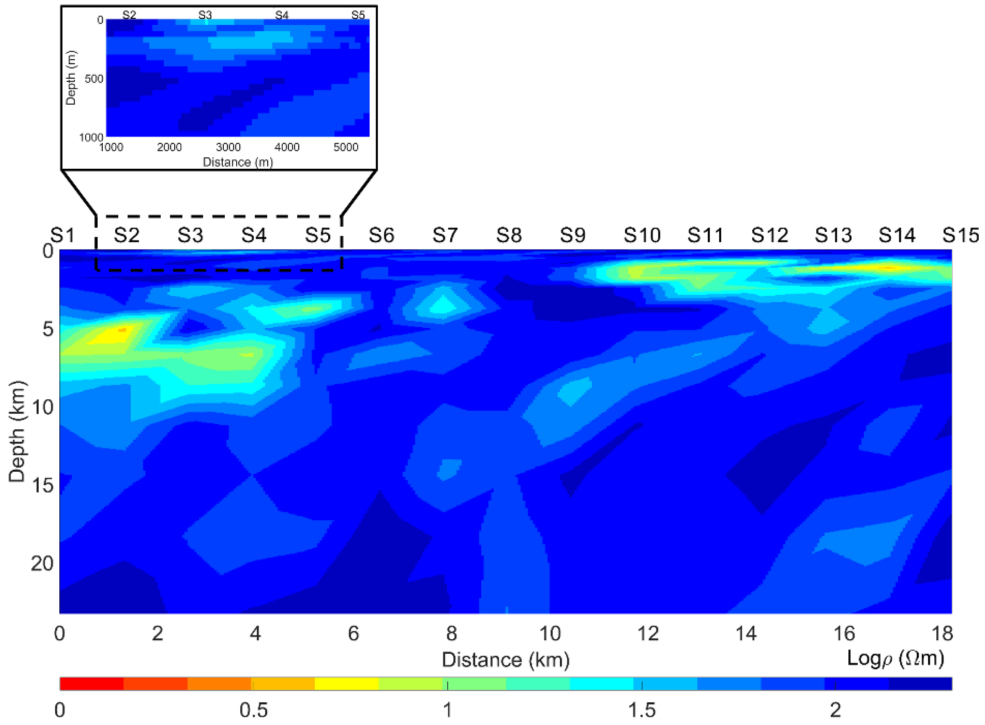

Figure 4.13 PSO solution for synthetic model 2, after 1674 iterations and without a priori initialization. Lagrange multiplier λ = 0.1.

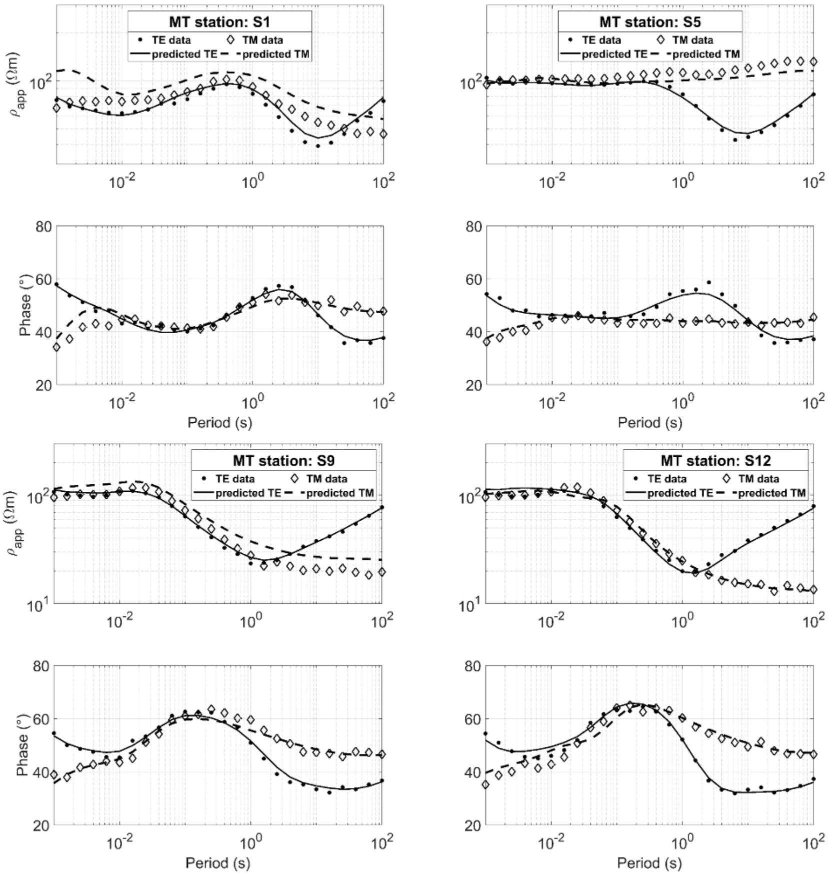

Figure 4.14 Fitting curves between data of synthetic model 2 and calculated data for apparent resistivity (ρ_{app}) and impedance phase for both TE and TM polarizations. The selected MT stations are S1, S5, S9, and S12. The synthetic data are marked as dots for TE, and diamonds for TM, while the PSO-predicted data are plotted as solid lines for TE, and dashed lines for TM. The optimization was randomly initialized.

The a priori information was set as previously explained. Once 5% of the particles were initially influenced, convergence was reached only after 53 iterations with a minimum objective-function value of 1.5. Figure 4.15 displays the final output. The 10-Ωm lateral bodies were correctly imaged, while the superficial 50-Ωm body was scarcely identified. A distinct difference between the models with and without a priori is indeed the superficial body, as can be seen in the zoom-in panels of Figure 4.13 and Figure 4.15. Figure 4.16 graphically demonstrates the low RMSE of 0.99 (Table 4.3). The fitting curves of Figure 4.16 show a good agreement between synthetic and predicted data and no significant improvements compared with Figure 4.14.

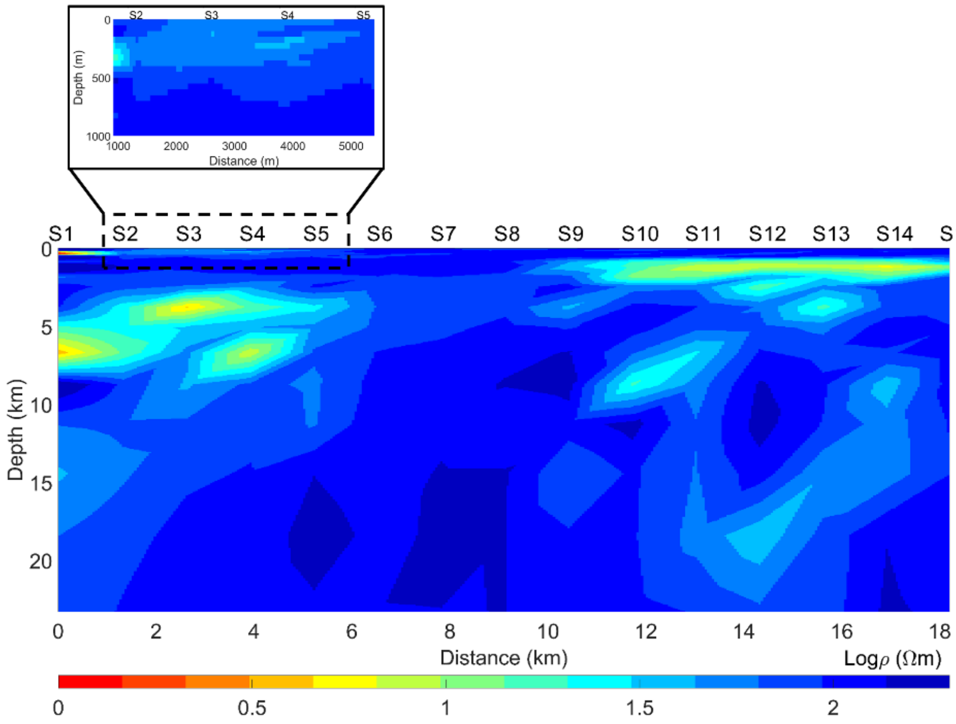

Figure 4.15 PSO solution for synthetic model 2, after 53 iterations and with a priori information given to 5% of the particles. Lagrange multiplier $\lambda = 0.1$.

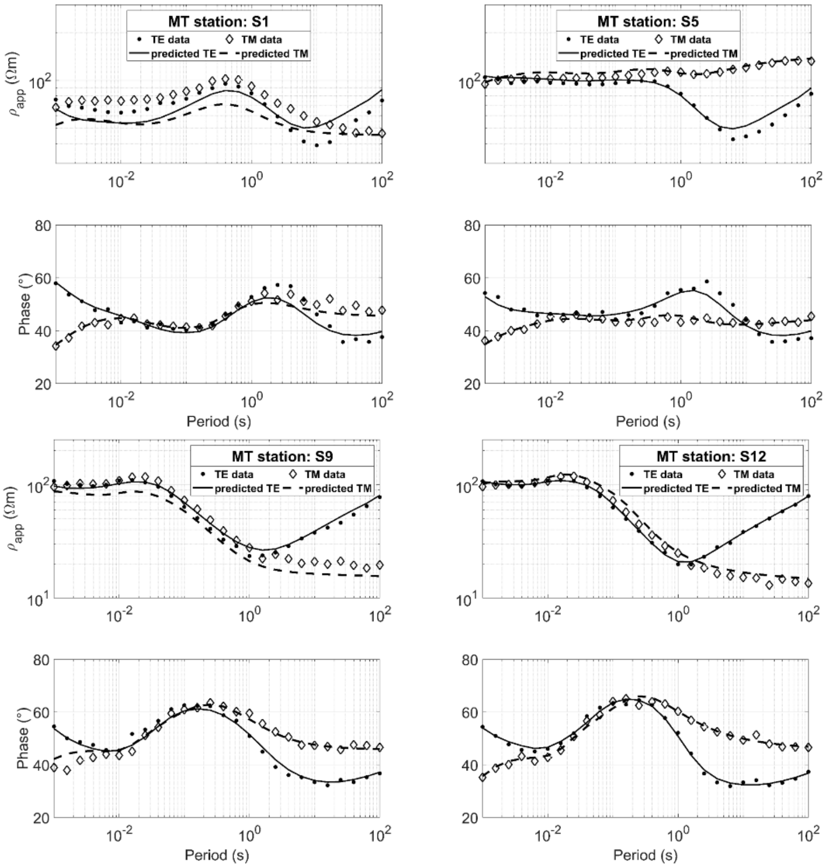

Figure 4.16 Fitting curves between data of synthetic model 2 and calculated data for apparent resistivity (ρ_{app}) and impedance phase for both TE and TM polarizations. The selected MT stations are S1, S5, S9, and S12. The synthetic data are marked as dots for TE, and diamonds for TM, while the PSO-predicted data are

plotted as solid lines for TE, and dashed lines for TM. The optimization was initialized with a priori information.

Table 4.3 Results of PSO applied to the two synthetic models (with and without a priori initialization) and to the COPROD2 data set (without a priori initialization). Results are presented in terms of: RMSE, runtime, and number of iterations performed before the optimization stop. The runtime is in hours and refers approximately to one single trial.

Data set	*Initialization*	*RMSE*	*Runtime (h)*	*Iterations*
Synthetic model 1	*No a priori*	0.86	4.6	154
	A priori	0.91	3.17	250
Synthetic model 2	*No a priori*	0.9	28.8	1674
	A priori	0.99	0.55	53
COPROD2	*No a priori*	2.42	8	6000

4.4. 2D optimization of MT field data

4.4.1 The COPROD2 data set

The COPROD2 data set collects long-period MT measurements along a profile of 35 sites crossing a 2D geoelectrical structure in Saskatchewan and Manitoba, Canada (Jones and Savage 1986). The name stands for “Comparison of One-dimensional PROfiles from MT Data”, while the “2” refers to the two-dimensionality, differently from the one-dimensional data set called “COPROD”. The most appreciable advantages of this data set are the following: a wide period bandwidth (from $2.6 \cdot 10^{-3}$ s to $1.8 \cdot 10^{3}$ s), low impedance errors (< 2%), static shift corrected, and the possibility of comparing different models from well-established inversion algorithms (Jones 1993b). Our aim is to apply the PSO algorithm to detect deep electromagnetic anomalies, while any geological interpretation is beyond the scope of this work.

Since responses at low periods (below 10 s) have been widely recognized as one-dimensional, original data were selected from 10.67 s to 910.2 s (deGroot-Hedlin and Constable 1993; Martì et al. 2009). As proposed in the aforementioned studies, a subset of 20 MT stations, from the 8th to the 27th of the original line, was chosen to focus only on the center of the 400 km east-west profile. This selection was adopted also because these 20 sites have the same number of acquisition frequencies (14) within the considered interval. The errors on the data were kept as original for both TE and TM apparent resistivity and phase. Figure 4.17 plots MT observations and error bars for stations 12, 13, and 14, chosen as representative of the subset. The maximum observed error is 1.2 for TE apparent resistivity (on logarithmic scale) and 6.92° for TM phase.

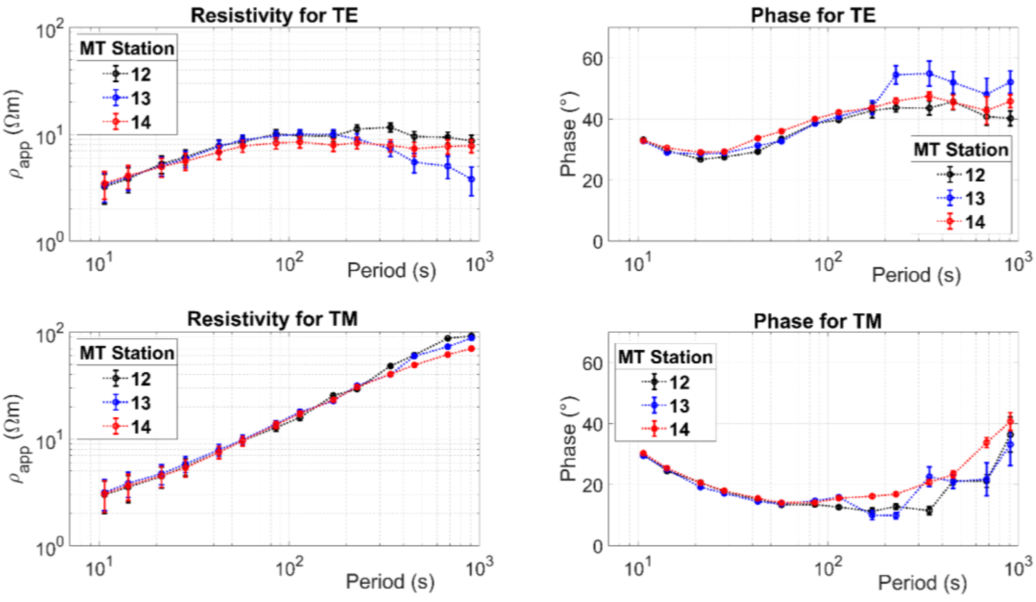

Figure 4.17 MT responses and error bars for TE and TM modes of three representative stations (12, 13, and 14) of the COPROD2 data set. They show the high quality of the data. The ρ_{app} stands for the apparent resistivity.

The 2D model was divided into 10 layers, from 1.8 km to 60.5 km of depth, and the thickness of each layer increased logarithmically with depth. Along the horizontal direction, the mesh was about 200 km long and subdivided into 34 bricks, one for each station plus others as boundary conditions. The total number of cells was 340. Since some structures of the region are known to be highly conductive, the lower boundary of the problem was set equal to 0.1 Ωm. Literature references also state that superficial sediments are far more conductive than the resistive basement. For this reason, the upper boundary of resistivity was chosen to be different between the upper and underlying layers. We observed that a search space too large for the upper layers would have driven the solution toward no convergence and erroneous local minima. In detail, the first two superficial layers, namely up to 5 km deep, had 10 Ωm as upper boundary, while, the layers below, 1000 Ωm. The population size was equal to 2500 particles, proportional to the number of cells. The Lagrange multiplier λ was chosen after a sensitivity analysis on five different values in the range between 0.001 and 10. The value that coincides with the point of maximum curvature in the plot of data misfit versus model norm is 0.1, as shown in Figure 4.18. A priori information was not given: the optimization started with a completely random initialization.

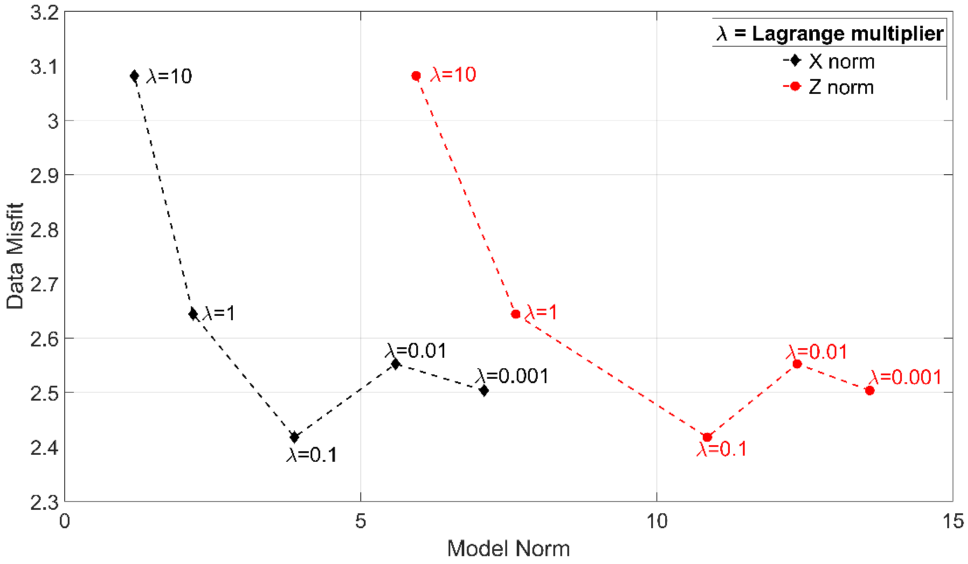

Figure 4.18 L-curve response for COPROD2 data along the horizontal (black diamonds) and vertical (red circles) directions. The tradeoff between data misfit and model norm indicates the best Lagrange multiplier λ equal to 0.1.

4.4.2 Results and discussion

The final model from COPROD2 data was computed after 6000 iterations and is depicted in Figure 4.19. The shallow conductive structure was extensively identified, while, at depth from 5 km to the bottom, the background resistivity was predominantly 1000 Ωm. The most significant feature of this model was represented by the low-resistivity anomalies below the station E3-E4 and 12-11 at around 20 to 35 km of depth. Our output is well comparable with the ones represented in Figure 4.20 and reported by Jones (1993b). For ease of comparison, both the color scale and the name of the stations of Figure 4.19 were plotted as the original ones in Figure 4.20. There was good agreement between our model and those called “degroot-2” (deGroot-Hedlin and Constable 1993), “rasmussen” (Rasmussen 1993), “wu” (Wu et al. 1993), and “uchida” (Uchida 1993): low-resistivity anomalies were identified in the same regions. The similarity can be explained by the same approach adopted in the Occam’s inversion using the smoothing parameter, excepted for “wu”, which used a different approach. In detail, the most evident similarity was the conductive region in the first 5-7 km of depth. Another similarity regarded the 30-km-deep conductor below the stations from E2 to 14 and its extension at greater depths. A further correspondence was the interruption of the 1000 Ωm structure below the stations from 13 to 11 at about 20 km of depth. Apart from the “wu” model, all the analyzed results presented a low-resistivity region (about 100 Ωm) in the westernmost part of the model at a depth greater than 30 km.

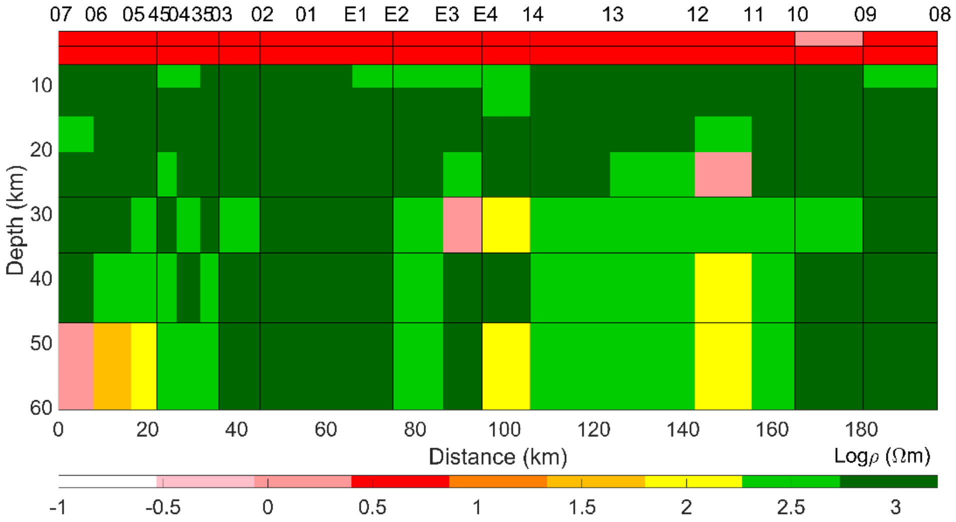

Figure 4.19 Resistivity model of COPROD2 data from PSO computation, after 6000 iterations. Lagrange multiplier $\lambda = 0.1$.

Figure 4.21 plots the apparent resistivity (ρ_{app}) and phase at selected periods for the 20 stations in the horizontal axis. The observed data are marked with dots for TE and diamonds for TM, and predicted responses are plotted with a solid line for TE and a dashed line for TM. The RMSE was 2.42, as listed in Table 4.3. The final objective-function value was 26.6.

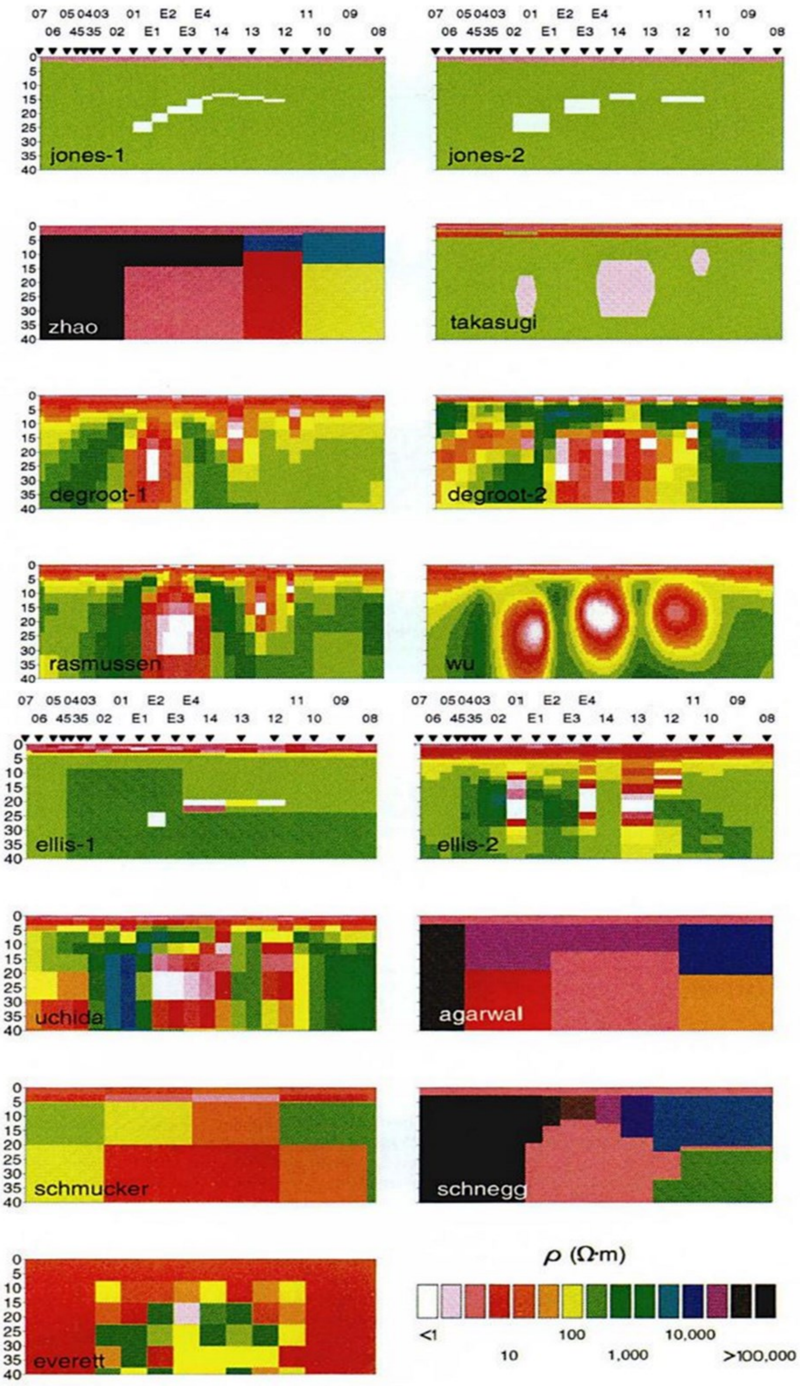

Figure 4.20 Reference models of COPROD2 data from Jones (1993b). The 20 stations are sorted and named as in Figure 4.19. The color scale for the resistivity (ρ) is consistent with Figure 4.19: white ($\rho < 1$ Ωm), pink ($\rho = 1$ Ωm), red ($\rho = 10$ Ωm), yellow ($\rho = 100$ Ωm) and green ($\rho = 1000$ Ωm)

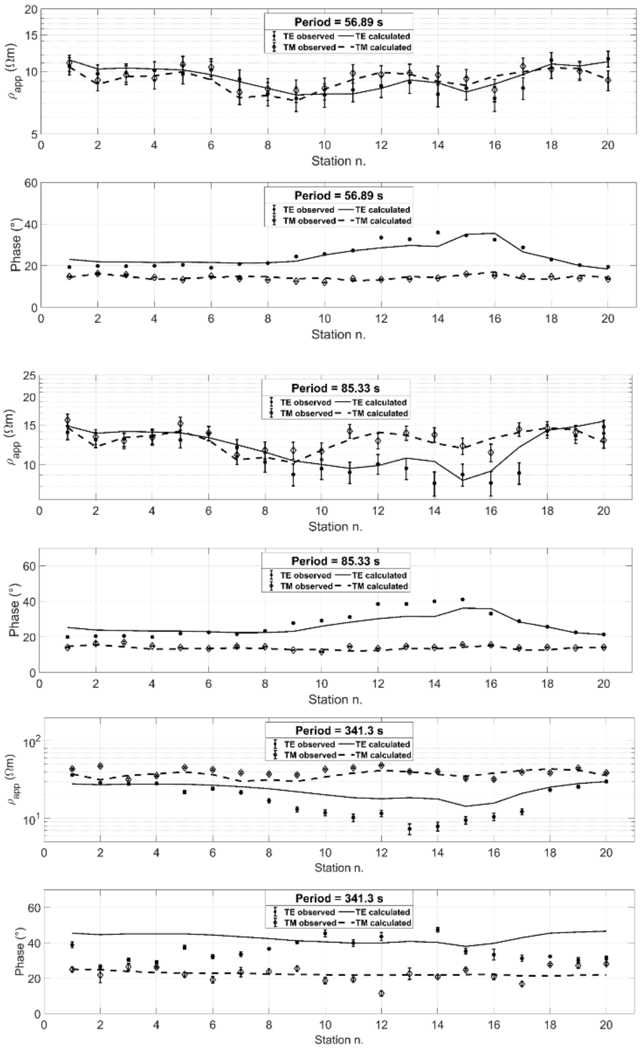

Figure 4.21 Fitting curves between observed apparent resistivity (ρ_{app}) and phase, and predicted responses at selected periods: 56.9 s, 85.3 s, 341.3 s. Observed data include error bars and are marked with dots for TE and diamonds for TM. Calculated responses are plotted with solid line for TE and dashed line for TM. The optimization was randomly initialized.

4.5. Computational aspects

Since the optimization process implied the computation of several model responses, the reliability of the solution was also related to the accuracy of the forward modeling. We adopted the 2D MT forward modeling described in Candansayar (2008) and references therein. It is based on the finite-difference technique, which solves the complex system of magnetotelluric equations for TE and TM polarizations. Firstly, the electric and magnetic fields are derived for each mesh node and, finally, the apparent resistivity and impedance phase are calculated. We adopted this forward-modelling code since it is stable, published, and written in MATLAB.

Addressing the 2D problem made the overall computation time-consuming due to several factors. The runtime was affected not only by the number of iterations, but also by the population size and the number of unknowns. The number of iterations depends on the complexity of the problem. The population size was related to the number of unknowns, i.e., to the desired resolution of the 2D model. Obviously, a mesh grid unnecessarily dense would have made the computation excessively long. All these issues are responsible for a heavy computation effort. In order to speed up the computation, we developed and applied the parallel computing option for the PSO algorithm. Firstly, we enabled the option “UseParallel”, that was potentially provided but not implemented in the standard code. Then, the most overloaded “for” loops were set to run as parallel for loops, such as, for example, the loop that evaluates the objective function for each particle. Finally, the PSO algorithm was enabled to run in parallel on the academic cluster by activating the Parallel Computing Toolbox of MATLAB. All the simulations were executed on a 24-core node of an HPC cluster for academic research. The CPU model of the single node was an Intel Xeon E5-2680 v3 2.50 GHz (turbo 3.3 GHz) with 128 GB of RAM. When the runs were computed, the sustained performance of the cluster was 9.7 TFLOPS.

The tests on the HPC cluster proved that, when 24 cores were adopted, the runtime saving was more than 80% with respect to the use of 4 cores (see Figure 4.22). A test using the non-parallelized release of the code (one single worker) would have been unfeasible in terms of machine working load. Figure 4.22 shows the dramatic speedup of PSO computation for a reference simulation of 150 iterations and 10000 particles. The black lines indicate the running duration in hours, while the blue lines the total speedup in percentage. The parallel environment “shared” (dotted lines) exploited workers of the same node, while “orte” (dashed lines) referred to workers from different machines of the cluster. It could be seen that “shared” was a bit faster than “orte”, especially at high numbers of cores.

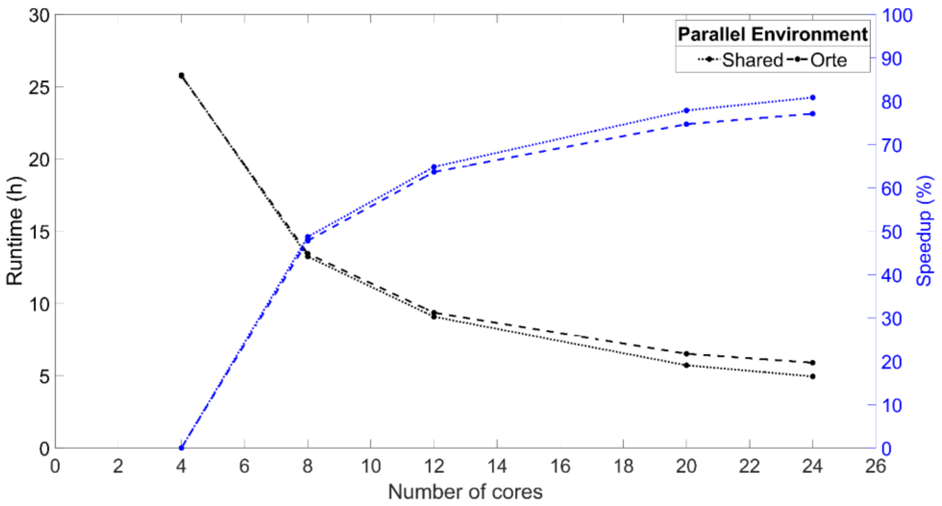

Figure 4.22 Black curves show computation time in hours (left ordinate axis) as a function of the number of cores exploited for a reference PSO simulation of 150 iterations with a 10000-particle swarm. The right ordinate axis and blue curves refer to the total runtime speedup with exploited cores increasing. Dotted lines refers to “shared” parallel environment (workers of a single node), dashed lines to “orte” (workers of different nodes).

The total runtime of PSO computations is provided in Table 4.3 for each study case. These values refer to one single trial, while a total of three trials were performed. Runtimes are not directly comparable to each other because the stopping criterion was met after different numbers of iterations, that is, less than 1600 iterations for the synthetic models and 6000 for the real data set. The optimization of synthetic examples stopped because the minimum RMSE was achieved, while the optimization of the real data stopped because the objective function did not minimize for 80 consecutive iterations. The synthetic examples were optimized in fewer iterations than those of the real data set, but the runtime was longer than that of COPROD2 data set due to the higher number of layers and particles. In fact, the big difference between the computation times is explained by the low number of layers of the COPROD2 model was discretized (about one-third of that of the synthetic models). The optimization of synthetic data without a priori differed in the number of iterations needed, but the runtimes are quite similar, if the proportion between the iterations is taken into account. The optimization of synthetic data had shorter runtimes when a priori initialization was given.

4.6. Discussion

Our tests on synthetic data demonstrate the reliability of PSO in solving the 2D inverse problem for MT data sets.

The choice of the most appropriate values of accelerations and population size was crucial for obtaining valid models. The initial sensitivity analysis on the PSO input arguments was essential to identify the most appropriate tuning coefficients which effectively minimized the objective function and enhanced the solution convergence. The calibration of the social and cognitive accelerations led to the optimal values of $\alpha_1^{\max} = 2$, $\alpha_1^{\min} = 0.5$, $\alpha_2^{min} = 0.5$, and $\alpha_2^{max} = 2$. Our findings are hence in agreement with Ratnaweera et al. (2004). We demonstrated that the population size was directly proportional to the total runtime, but, at the same time, a poorly populated swarm negatively influenced the model (Figure 4.9). The reason for this was that the search space was ineffectively covered by the initial random distribution of the particles. We showed that the best ratio between the number of unknowns and the number of particles was 9. This outcome is significant for our high-dimensional problem because, so far, the literature has suggested increasing the number of particles up to 12 times the number of unknowns. The conclusion of our analysis slightly modifies this ratio, with the advantage of avoiding extra computational load.

We showed that the application of PSO did not require an initial assumption about the solution (i.e., a priori information). At the same time, we introduced a novel and valid tool to potentially communicate external or additional information to the swarm, in terms of the initial position of particles within the search space. Our findings showed that, if the geological or geophysical information is reliable (e.g., from wells, seismic reflectors and so on), it influences the behavior of particles at the beginning of the optimization. This kind of initialization resulted in shorter runtimes (see Table 4.3) because the swarm did not waste time searching for local minima, which were already given from the beginning. On the other hand, using default random initialization, the results of synthetic models proved that there was no requirement for a priori initialization, since the final resistivity model was perfectly comparable with the original synthetic model. Moreover, there was high solution quality, despite two factors: Gaussian noise disturbing the data and the presence of equivalent solutions in the MT inverse problem. In fact, the conductive anomalies embedded in the resistive host medium were accurately identified in terms of size and resistivity values. RMSEs were around 1 and, interestingly quite similar with and without a priori initialization. Another element confirming the PSO independence from the starting model is the comparison of the fitting curves in Figure 4.8 and Figure 4.11 for synthetic model 1, and Figure 4.14 and Figure 4.16 for synthetic model 2. These plots proved that there were not substantial differences between calculated responses with and without a priori, even considering the stations above the lateral discontinuities (S4 and S11 for synthetic model 1 and S5 and S9 for synthetic model 2).

A significant result arose from the application of PSO to real 2D data, the COPROD2 data set. As regards the problem settings, the uppermost layers of the 2D mesh had different boundary conditions with respect to the underlying layers, due to the complexity of the investigated area. Many applications of global search algorithms to geophysics have considered different resistivity boundaries between one layer (or group of layers) and another, so that each unknown of the problem can independently be bounded within its search space (Godio and Santilano 2018). The setting of the boundary conditions is not a trivial step for the deterministic inversion either, because it implies full comprehension of the problem and some insight into the possible solution. For the optimization of the COPROD2 data set, preliminary information from the geology of the area facilitated the definition of a wide interval of resistivity values within which the solution could be searched. We applied this approach in order to enhance the convergence of the solution. This option distinguished the solution space of upper layers from that of deep layers. The final model had a mean resistivity of 6 Ωm in the two upper layers, thus confirming the presence of superficial sediments. At a depth of about 25 km, a conductive region breaks the 1000 Ωm background, with a minimum value of 1.2 Ωm. The final RMSE was slightly bigger than that of the synthetic examples and negatively affected by the mismatch of data at long periods (Figure 4.21). This was unexpected, given the satisfactory behavior of the fitting curves of the synthetic examples in Figure 4.8 and Figure 4.14. It would have been interesting to quantitatively compare our result with the model obtained by Everett and Schultz (1993) using GA, which is a global search algorithm too. Unfortunately, their RMS Misfit of 1.48 is not directly comparable with our value of 2.42 because there were substantial differences in the method, such as: period range, number of stations, mesh discretization, stopping criteria for iterations. Interestingly, the adoption of Occam-like optimization may provide a more effective solution of the resistivity distribution with respect to the GA. It has also been proved in literature that PSO ensures a higher convergence with respect to the other global search algorithms (Yuan et al. 2009; Fernández Martínez et al. 2010a). The application to field data represents a new encouraging approach for their optimization by means of computational swarm intelligence.

As regards the optimizations run without a priori initialization, the runtimes of the different data sets were not straightforwardly comparable due to the different number of iterations required to achieve convergence. The COPROD2 optimization needed 6000 iterations to stop at RMSE = 2.42, while the synthetic examples reached RMSE=1 in fewer iterations but taking a runtime proportionally longer than that for the real-data optimization. This is mainly explained by the high level of mesh discretization for the synthetic models, about 800 cells, compared to about 340 cells for the domain chosen for real-data interpretation. The more the unknowns, the greater the swarm size and hence the computation time.

The computationally demanding nature of the PSO algorithm was actually expected due to the high number of iterations, population size and cells assembling the mesh. The standard release of the code was not effective in addressing the 2D inverse problem, therefore we applied some modifications to develop a parallelized version of PSO. The tests performed on a HPC cluster pointed out the capability of our version of PSO to speed up the computation by more than 4 times with respect to running it on a simple machine of 4 cores. The decrease of the runtime allowed us to efficiently perform several trials of the optimization process, starting from different random distributions of the swarm. The final objective-function value of the synthetic examples was lower than that of the real data due to the peculiarity of the data sets.

The choice of the optimal Lagrangian multiplier may be seen as a computational cost, because the sensitivity analysis of different values of λ was performed. This analysis could represent a slight limitation of the presented method, since PSO ran for each investigated value of λ. However, once the balance was found, we were able to deploy the model with the adequate level of smoothing.

Although we reduced the computation time, it remained not comparable with that of deterministic algorithms. PSO applied to the 2D inverse problem is relatively time-consuming if clusters cannot be exploited and densely discretized meshes are adopted. However, the parallelization of the code has the potential of making the PSO computation reasonable. Moreover, high computing capacity has become largely available and global search algorithms, despite the skeptical view of the past, can now be considered worthy of attention. We do not see the long runtime as a scientific barrier for the application of PSO to high-dimensional geophysical problems. The computational load was balanced by the advantages of this metaheuristic method, namely, the independence from the choice of the starting model and the solution driven by the evolutionary approach.

4.7. Final remarks

The PSO algorithm has proven to be a valid method to solve the 2D inverse problem for MT data, for both synthetic and field (COPROD2) data sets. This work extended the application of PSO to MT inversion from the one-dimensional problem, already visited in the literature, to the 2D problem. The stochastic nature of PSO and the combination of exploration and exploitation behaviors played a key role in finding the optimized solution within the search space, which was composed of all the possible solutions of resistivity models.

The standard release of the code was easily implemented for our specific application. We observed striking improvements moving from standard PSO to hierarchical PSO with time-varying acceleration coefficients (HPSO-TVAC). This issue has not been addressed in previous research on PSO applied to geophysics, but was crucial in the optimization of 2D MT data. In fact, thanks to time-varying acceleration coefficients, the optimization ended with true convergence and stability. We carried out a detailed sensitivity analysis on some input parameters of the PSO algorithm due to their direct influence on the stability and convergence of the solution. The social and cognitive accelerations and the population size were investigated to retrieve their optimal values and analyze their effect on both the final resistivity models and total runtime.

The complexity of the 2D problem had a direct influence on the computation time, which we reduced with the parallelization of the code. Running PSO on a High Performance Computing (HPC) cluster resulted in runtime savings of about 80%.

We first applied PSO to 2D MT synthetic data, in order to validate the method. The initialization of the optimization was purely random by default, but we also tried to influence it with a starting model derived from PSO solutions of the 1D problem. In this case, the optimization was externally but not totally influenced, because only a small portion of the swarm was influenced. We proved that a priori information as the starting model can be avoided. The resistivity models which did not receive the a priori initialization were in line with the true synthetic models. Then, PSO was applied to the field data set COPROD2, using a random initialization. The optimization of COPROD2 data produced a valid resistivity model, largely comparable with results from existing research.

The most important conclusions of this work are that PSO can be successfully applied to the 2D MT inverse problem and the a priori starting model is not required for the achievement of valid models. Our results are encouraging enough to extend the application of evolutionary algorithms to other geophysical inverse problems, bearing in mind that the high dimensionality of the problem implies runtimes longer than those of local search methods.

The next chapters present the 2D PSO of MT data from the geothermal area of Travale (Italy), where the independence of the inversion method from the starting model could be crucial due to the geological complexity of the area and the uncertainty of external information, useful to potentially constraint the inversion.

Chapter 5

The MT data set of the Travale geothermal field (Italy)

This chapter deals with the description of the Larderello-Travale geothermal area, located in southern Tuscany, Italy. After an updated review on the geothermal prominence of the whole area, a detailed geological and geophysical framework is depicted regarding only the Travale geothermal system. Then, the MT field data set is accurately presented and analyzed in terms of geoelectrical dimensionality, phase tensor and strike direction. Finally, the static shift occurring for some MT apparent-resistivity curves is corrected by means of TDEM data, which were acquired during a recent field survey. The research questions emerging from this chapter are going to be clarified thanks to new MT inversion results presented in Chapters 6 and 7 as 2D and 3D models, respectively.

5.1. Introduction

5.1.1 General overview of the study area

The Larderello-Travale geothermal area is located in southern Tuscany (central Italy) and represents the world-renowned place where the geothermal exploitation is said to be born. The geothermal fields of Larderello and Travale cover an area of 400 km^2, as shown in Figure 5.1.

In this area, the natural geothermal manifestations have been documented since the time of Romans and hot springs and mineral deposits have been exploited along the centuries. The first case of deployment of geothermal energy for industrial uses happened in 1818, when the French merchant Francesco de Larderel exploited the geothermal fumaroles to extract the boric acid. During the XIX century, the town of Larderello grew thanks to the economic growth around the industrial plants for boric-acid extraction. The large occurrence of natural geothermal manifestations (fumaroles and hot springs) induced some scientists and innovators of the time to experiment pioneering utilization of this energy. In 1904, prince Ginori Conti succeeded in the famous five-lamps experiment, that consisted in steam-energy conversion into electrical power using the thermal energy of the hydrothermal fluids from a well drilled in Larderello (Figure 5.2 left). In 1913, the first geothermal power plant started operating under the name of "Larderello 1" (Figure 5.2 right). From then on, geothermal power production spread all over the world.

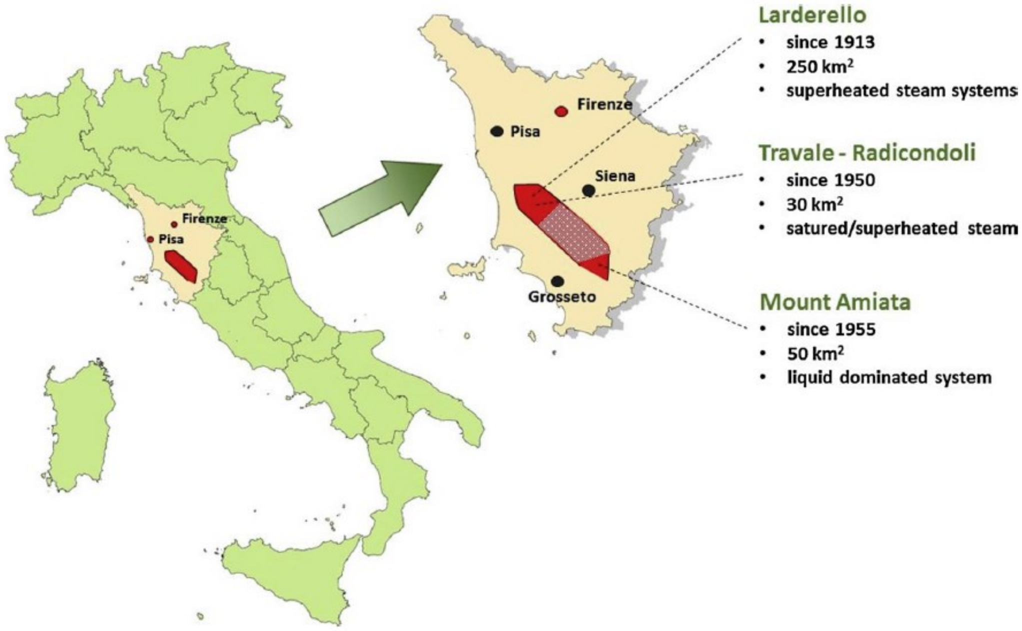

Figure 5.1 The geothermal area of Larderello-Travale is located in southern Tuscany, Italy (source: Manzella et al. 2018)

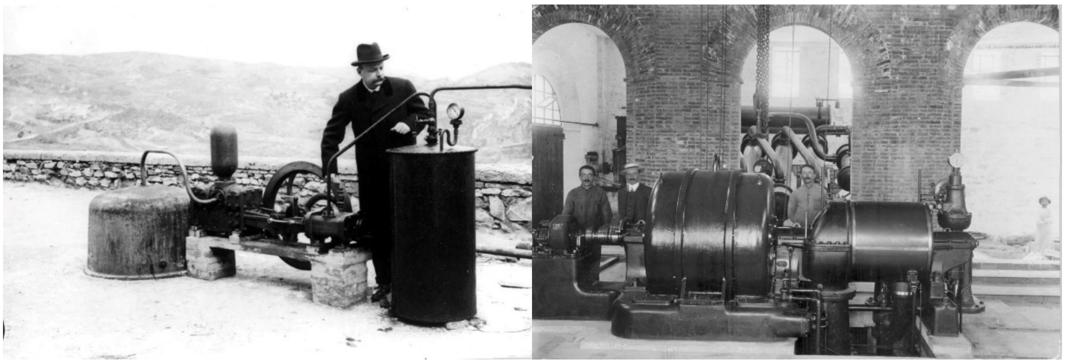

Figure 5.2 left) the experiment of Prince Ginori Conti in 1913: the geothermal energy was converted to switch on five bulb lamps (source https://www.unionegeotermica.it/esperimento_ginori_conti.asp); **right)** the first electric power plant "Larderello 1" started operating in 1913 (courtesy of Alessandro Lenzi. Presented during the GEO200 conference in Pisa, May 2018)

Nowadays, the Larderello-Travale geothermal field is one of the most productive geothermal system in the world with an installed geothermal electric capacity of 916 MWe and a yearly geothermal electricity generation of 6064 GWh (Manzella et al. 2019). According the last World Geothermal Congress in 2015, Italy is the sixth in the world and second in Europe for installed capacity (EGEC

Geothermal Market Report 2018). In the Larderello-Travale geothermal field there are today 29 geothermal plants (Enel Green Power annual report 2018), providing 2.0% of the Italian electric power need and 30% of the electric need in Tuscany (TERNA 2016; Manzella et al. 2019). Enel Green Power is the only company producing geo-electricity in Italy (Figure 5.3). To date, about 230 production wells extract hot steam within a temperature range of 150-270°C and a pressure range of 0.2-2 MPa (Conti et al. 2016).

Figure 5.3 Pictures of the Larderello-Travale geothermal area taken during the 2019 TDEM geophysical survey.

The Larderello-Travale geothermal area represents a milestone for the exploitation of geothermal resources for electric power production. More in general, it embodies a virtuous example of renewable energy in the contest of recent environment-related issues aiming at fulfilling the Sustainable Development Goals (SDGs) listed by the United Nation General Assembly in 2015. In fact, the geothermal resources are entailed in SDG 7 that prescribes to "ensure access to affordable, reliable, sustainable and modern energy for all". The mitigation of climate change, limitation of the world-temperature growth and de-carbonization were signed in 2015 as urgent actions in the famous global agreement after the Conference of the Parties 21 of Paris.

5.1.2 Geothermal background of the Larderello-Travale geothermal system

Geothermal resources provide the thermal energy generated and stored in the Earth's interior. This energy can arise in spectacular forms like volcanoes, geysers and fumaroles or can be stored in the ground and aquifers. The geothermal fluid is extracted from the underground to the surface for direct or indirect utilization. Depending on the fluid temperature and extraction depth, geothermal resources are divided into:

- High temperature fluids (more than 150 °C), which are accessible only by means of wells drilled up to 4 km of depth at very specific locations, such as Larderello-Travale in Italy, the Geysers in USA and Cerro Prieto in Mexico

- Medium temperature fluids (between 90°C and 150°C), which are useful for district heating and industrial processes
- Low temperature fluids (below 90 °C), which are stored in the shallow subsurface and exploited by means of ground-source or ground-water heat pumps for aquaculture, thermal bathing, greenhouse heating or district heating (Piga, Casasso, Pace et al. 2017).

However, this classification based only on the temperature of the geothermal fluid has been regarded simplistic because every geothermal system has its peculiar geological, petrophysical and thermodynamic conditions (Santilano et al. 2015a). Following the research of Moeck et al. (2014), the geothermal systems can be classified according to the concept of "geothermal play", based on geological and geodynamical features. The Larderello-Travale geothermal system has been classified as a convective intrusive geothermal play, meaning that the heat transfer is based on convection of the hydrothermal fluid whose high temperature results from a plutonic heat source (Santilano et al. 2015a).

Another classification of the geothermal systems is between conventional and unconventional geothermal resources, depending on the possibility of exploiting them with or without consolidated technology, respectively. Conventional geothermal systems, also called hydrothermal systems, are characterized by convective heat transfer of hot fluids whose extraction is economically and technologically feasible. The conventional hydrothermal system of Larderello-Travale has been exploited since more than 100 years. The fundamental elements that characterize a hydrothermal system are depicted in Figure 5.4 and are

- the heat source, represented by an igneous intrusion or magmatic chamber
- the reservoir, a volume of hot permeable rocks that can be vapor-dominated or water-dominated
- the heat-carrier fluid, that is water in the liquid or vapor phase (depending on its temperature and pressure) containing usually chemicals and gases such as CO_2, H_2S, etc.
- the impermeable cap rock, that prevents the cooling of the system
- the recharge area, through which the meteoric water replaces the fluids naturally flowed out or extracted by boreholes.

In the Larderello-Travale geothermal system, unconventional geothermal resources are expected at 2-5 km of depth, where supercritical fluids at high temperature can exist related to igneous intrusions (IMAGE project - EU FP7; DESCRAMBLE project – EU H2020). The deep supercritical conditions are currently under exploration in the Larderello field, in the framework of the pioneering deep-drilling project DESCRAMBLE. The first evidence of supercritical conditions resulted in 2017 from the drilling test in *Venelle-2* well, where at a depth of 2.9 km 510 °C and 300 bar were measured. To preserve safety conditions, the experiment was suspended due to the very high temperature and the unexpected behavior of drilling mud. That drilling did not prove the existence of a reservoir and supercritical fluids, but introduced new open questions for future investigations (Bertani et al. 2018).

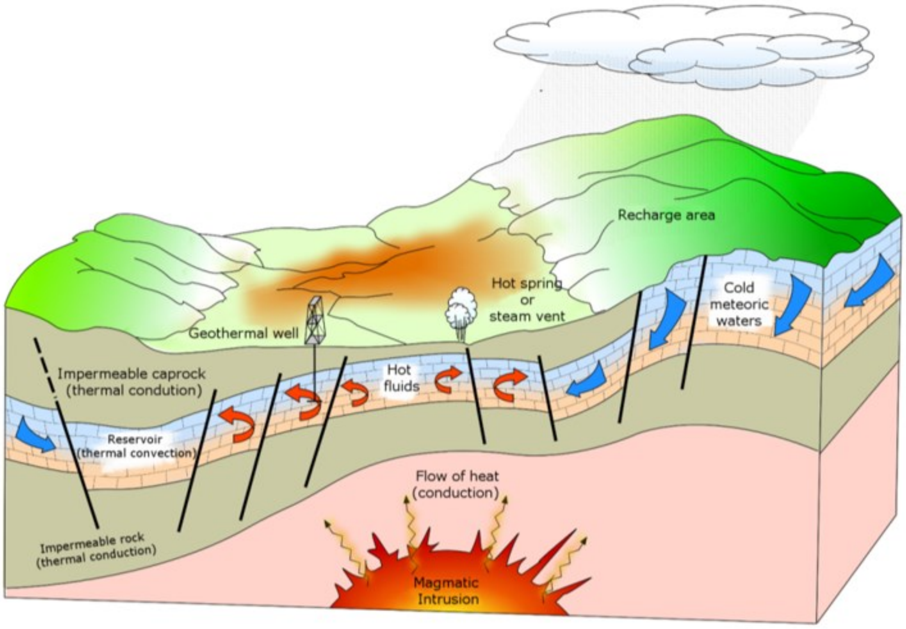

Figure 5.4 Schematic conceptual model of a typical geothermal system (Dickson and Fanelli 2004)

After the first geothermal plant settled in 1913, two different periods of industrial development can be identified in the geothermal exploitation of the Larderello-Travale field. The first phase, from the 1930s to the mid-1970s, exploited the shallow carbonate reservoir. After deep drilling projects in the ‘80s, the gross electricity generation increased thanks to a new deep target located in the crystalline reservoir.

To underline the extraordinary conditions of the Larderello-Travale system, it is worth noting the geothermal gradient and the heat flow. While the average continental geothermal gradient is 30°C/km, in the Larderello-Travale system it can reach 100 °C/km (as observed in *Venelle-2* well) and peaks of 300 °C/km (Bertani et al. 2018; Romagnoli et al. 2010). Anomalous high values of heat flow occur in southern Tuscany, with a regional background of 150-200 mW/m^2 measured at surface (Della Vedova et al. 2008). Heat flow maxima are correlated with normal faults and deep shear zones and rise by up to 1000 mW/m^2 in the Larderello area and to 500 mW/m^2 in the Travale area (Bellani et al. 2004).

Even though the Larderello-Travale geothermal area is regarded as a whole region, several differences occur between the Larderello and Travale sectors. The geothermal field has been extensively studied since more than 200 years from both the scientific community and industrial companies. Therefore, a number of works have been published and also updated with new findings. The knowledge of this geothermal field covers the scientific subjects of geology, geophysics, tectonics, geochemistry, mineralogy, geodynamics, petro-physics, hydrogeology and thermodynamics. As a consequence, it is not an easy task to grasp this dissemination of information. Moreover, despite rigorous research, the geothermal system appears so complex that some of its geological, thermodynamic, petrophysical and chemical features are still under investigation and debate (Gola et al. 2017).

5.1.3 The Travale geothermal area

The Travale-Radicondoli geothermal area (hereafter only “Travale”) is about 50 km^2 large south-east of Larderello, that is about 15 km far from the town of Travale (Figure 5.5). In 2018, 38 wells and 8 plants were in production with an installed capacity of 200 MWe (Manzella et al. 2019). The geothermal area extends over the municipalities of Montieri, Radicondoli and Chiusdino, belonging to the provinces of Grosseto and Siena (Figure 5.5).

The geothermal exploration of the last decade has pointed out two important features of the Travale system: 1) the two distinct shallow reservoirs of Larderello and Travale represent the “outcrop” of a unique deep geothermal reservoir that is 3-4 km deep and 400 km^2 large; 2) productive layers have been observed at a depth of about 4 km (Conti et al. 2016). More in detail, from 3 to 4 km of depth, the measured temperature is 300-350 °C and the pressure is 6-7 MPa (Bertani et al. 2005; Romagnoli et al. 2010; Spichak and Zakharova 2014; Manzella et al 2019). 3D numerical modeling of temperature and pressure was investigated in order to explain the nature of the heat source of the reservoir, the production mechanism of superheated steam and the field sustainability (Romagnoli et al. 2010).

The two following sections present a systematic overview of the geological framework and the geophysical knowledge of the Travale geothermal field.

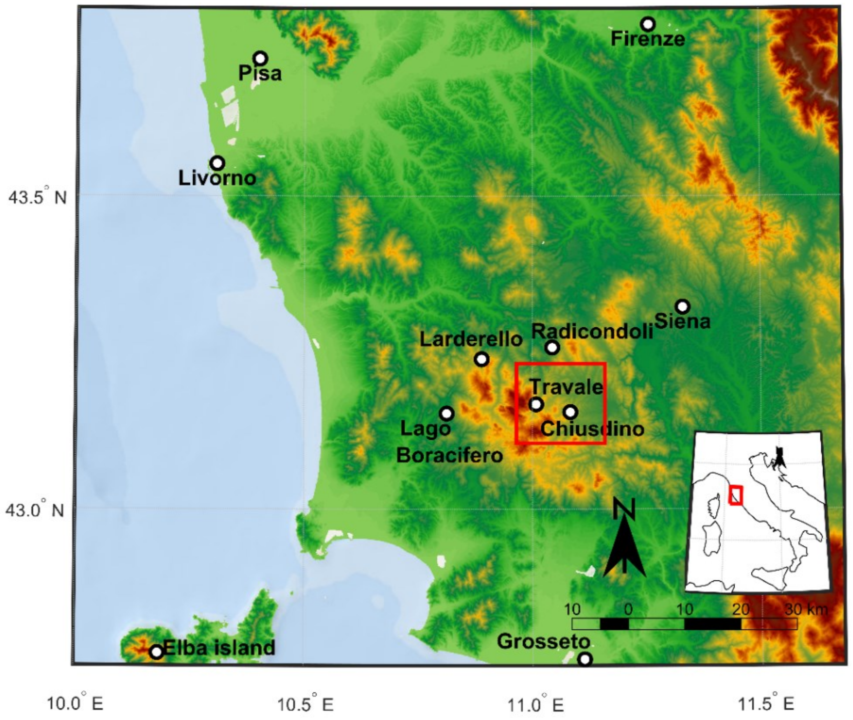

Figure 5.5 The Travale geothermal area (red box) is located in southern Tuscany, central Italy. The map in the background is a digital terrain model with cell size of 10 meters (extracted from Geoportale Geoscopio web site).

5.2. Geological framework of the Travale geothermal system

Two different reservoirs characterize the Travale geothermal field (Bertani et al. 2005; Bertini et al. 2005; Romagnoli et al. 2010). The shallow reservoir is hosted in the evaporite-carbonate units with an average temperature of around 200°C. It is characterized by an upper reservoir (called "horst") at a depth of 600-800 m exploited since the 70s and an intermediate reservoir (called "graben") at a depth of 1300-2500 m whose exploration started in the 80s. The deep reservoir is hosted in the metamorphic basement and Neogene granitoids at a depth of about 2500-4000 m.

The geological framework of the Travale area is well documented in Bellani et al. (2004), Bertini et al. (2006), Romagnoli et al. (2010) and Casini et al. (2010). Figure 5.6 reports the geology of the Travale geothermal region derived from the open-access webgis database of the Tuscan Region (Geoportale Geoscopio web site). The superficial outcrops are composed of: 1) Quaternary deposits, 2) Neoautochthonous terrigenous deposits (or Neogene sediments), 3) Ligurian and sub-ligurian flysch complex, 4a) Tuscan nappe sediments, 4b) Tuscan nappe basal evaporites. The outcropping carbonate formations represent the recharge area of the shallow reservoir, which is cooled down and hence less exploited than the deep reservoir. The thick black curves in the left side of Figure 5.6 are the main faults and normal faults, as documented in the Geoportale Geoscopio web site. The black dots are labeled with the name of the MT sites examined in this thesis, as described in more detail in Section 5.4.

The right-side of Figure 5.6 shows the geologic cross-section of the Travale area reconstructed by using data from deep wells and geophysical surveys (Bertini et al. 2006; Romagnoli et al. 2010). The structural-stratigraphic conceptual model is depicted in Figure 5.7 and outlines the following geological units: 1) Quaternary deposits, 2) Neoautochthonous terrigenous deposits (Lower Pliocene – Upper Miocene), 3) Ligurian and sub-ligurian flysch complex (Jurassic – Eocene), 4) Tuscan nappe (Triassic - Lower Miocene) including limestone, carbonate and anhydrite rocks, 5) Tectonic wedge complex (Paleozoic-Triassic), 6) phyllitic and quartzitic complex and micaschist complex, 7) gneiss complex, 8) Pliocene granite and Quaternary granite. The shallow geothermal reservoir is hosted in the carbonate units 4 and 5, while the deep metamorphic reservoir in units 6, 7 and 8. The reservoir located in the metamorphic basement is characterized by a high degree of heterogeneity and anisotropy and by the presence of superheated steam. The intrusive complex represents the heat source of the long-living geothermal system (Gola et al. 2017).

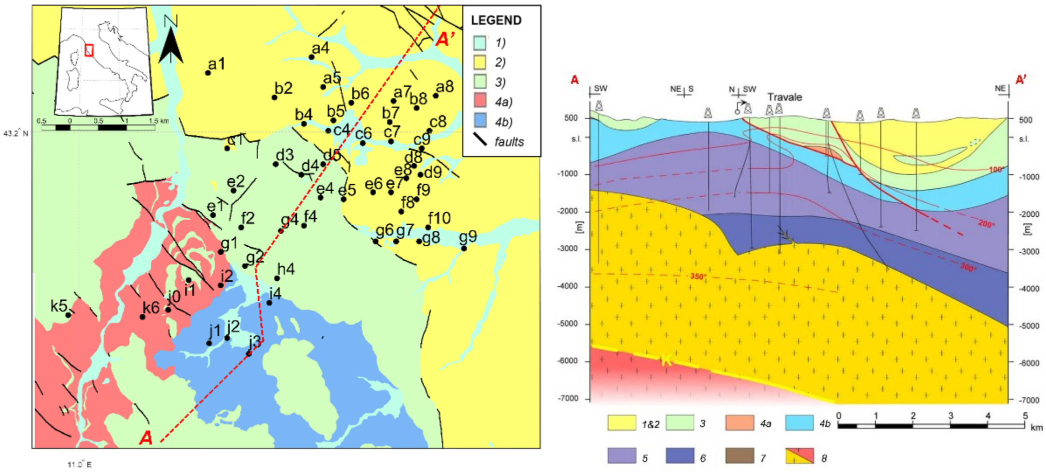

Figure 5.6 left) Geological map of the area of study: 1) Quaternary deposits, 2) Neoautochthonous terrigenous deposits, 3) Ligurian and sub-ligurian flysch complex, 4a) Tuscan nappe sediments, 4b) Tuscan nappe basal evaporites. The black dots are the 51 MT sites included in 3D inversion (Chapter 7). The thick black curves are the main faults and normal faults (source: Geoportale Geoscopio web site). The red-dashed A-A' profile tracks the geological cross-section reported in the right (modified from Romagnoli et al. 2010); **right):** 5) phyllitic and quartzitic complex, 6) micaschist complex, 7) gneiss complex, 8) Pliocene granite (yellow) and Quaternary granite (red). The red lines in the cross-section are the isotherms. The K-horizon is highlighted with the dashed-yellow line.

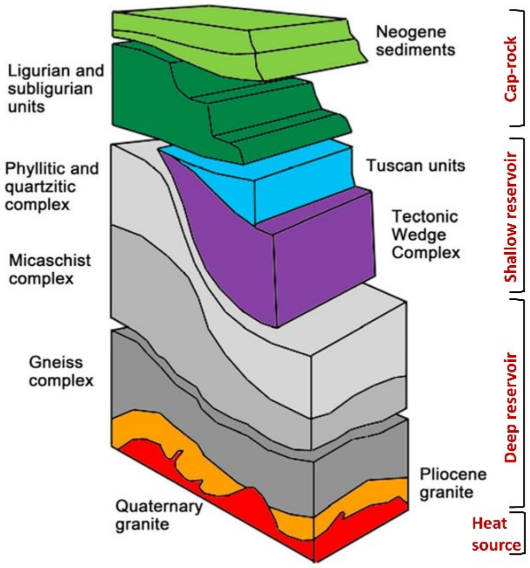

Figure 5.7 Schematic sketch of the tectono-stratigraphic and hydrogeological complexes of Larderello-Travale geothermal area (modified from Gola et al. 2017)

5.3. Geophysical knowledge of the Travale geothermal system

5.3.1 Previous MT studies

Magnetotellurics is one of the most effective geophysical techniques for the investigation of deep geothermal systems because it can image the electrical-resistivity distribution up to the depth corresponding to that of the geothermal targets (Pellerin et al. 1996; Spichak and Manzella 2009; Muñoz 2014).

The MT study of the Travale area started in the 80s, when a high conductive and fractured basement was recognized (Duprat and Gole, 1985; Hutton, 1985; Schwarz et al., 1985). From 1990 to 2009 a number of MT surveys have been carried out in the Travale geothermal field with the aim of industrial exploration or scientific research (Fiordelisi et al. 1998; Manzella 2004; Manzella et al. 2006; Santilano 2017; Santilano et al. 2018). Travale was also investigated as part of the European projects INTAS and I-GET (Cei et al. 2009; Manzella et al. 2010; Spichak and Zakharova 2014).

The collection of the "vintage" MT data is composed of three data sets, as shown in Figure 5.8. The survey acquired in 1992 is depicted with black-labeled squares and covers both the Larderello and Travale areas. The profile composed of 13 sites from *LS3* to *LS16* is investigated in Chapter 6 with more detail. The surveys acquired in 2004 and 2006-07 are depicted in blue-labeled circles (55 sites) and red-labeled triangles (19 sites), respectively. The MT data acquired in Travale have been interpreted using both 1D optimization and 2D inversion (Manzella et al. 2006; Santilano 2017). Therefore, both 2D MT optimization presented in Chapter 4 and the most recent methods for 3D MT inversion remain unexplored so far.

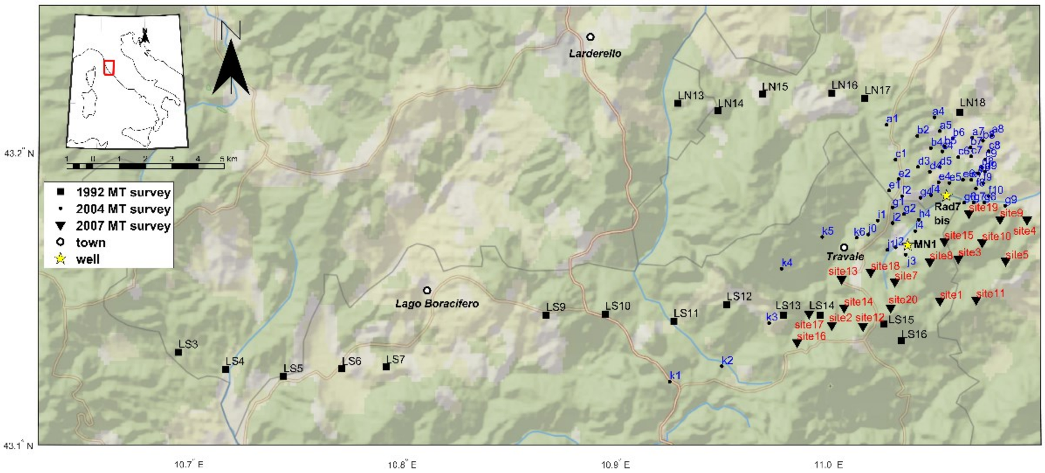

Figure 5.8 The collection of MT data sets in the Larderello-Travale area. The data set acquired in 1992 (LN13, …, LN18; LS3, …, LS16) is marked with black-labeled squares. The data set acquired in 2004 (55 sites) is marked with blue-labeled circles. The data set acquired in 2006-07 (19 sites) is marked with red-labeled triangles. The main towns of Larderello, Lago Boracifero and Travale are marked with white circles. The geothermal wells "MN1" and "Radicondoli7bis" are marked with yellow stars. This map was created by reading a georeferenced image within Matlab Mapping Toolbox by Mathworks.

A previous MT study of the Travale geothermal system converged in the 2D resistivity model of Figure 5.9 (Manzella et al. 2006; Manzella et al. 2010). The MT profile had an orientation SW-NE crossing sites k1, k2, k3, k4, k5, j0, g2, f4, e4, c7 and a8 (see Figure 5.8 for their location). 2D inversion has been performed following the algorithm of Rodi and Mackie (2001) and has adopted as starting model the a priori geological section of the profile. The 2D model in Figure 5.9

reveals a strong heterogeneity of resistivity distribution. The inversion result presents a highly conductive shallow subsurface and a large resistive body (around 800 Ωm) from 3 to 6 km of depth. This deep resistive body overlies the K-horizon, a seismic reflector whose importance is specified in the following section. The resistivity anomaly above the deep resistivity body is geometrically complex and is in contrast with the presence of super-heated steam and with the lithology registered from well-logs (Manzella et al. 2006, 2010). This reduction in resistivity was partly explained by the phyllosilicate abundances, after analyzing the average mineral content of the samples belonging to the same lithological unit (Manzella et al. 2010). Another possible interpretation was the occurrence of adsorbed or interstitial water in the reservoir. The low resistive response below 6 km of depth was related to the possible occurrence of partial melt intrusions (Manzella et al. 2010).

The main issues emerging from this investigation are 1) the possible causes of the resistivity anomaly in the steam-dominated Travale reservoir hosted in crystalline rocks and 2) the correlation between the deep conductive region (below 7 km) and the heat source of the system interpreted as igneous and melted intrusions.

Unfortunately, the works of Manzella et al. (2006; 2010) did not present any chance to appreciate the data fitting resulting from the resistivity models. Only the RMSE corresponding to the profile in Figure 5.9 was given. The interpretation in Manzella et al. (2010) led to a resistivity model (not reported here) with an RMSE of 6, an error floor of 2% for apparent resistivity and of 1% for phase. For this reason, and in the light of the most recent inversion techniques, this profile needs to be re-examined. The 2D stochastic modelling is presented in Chapter 6 and 3D inversion in Chapter 7.

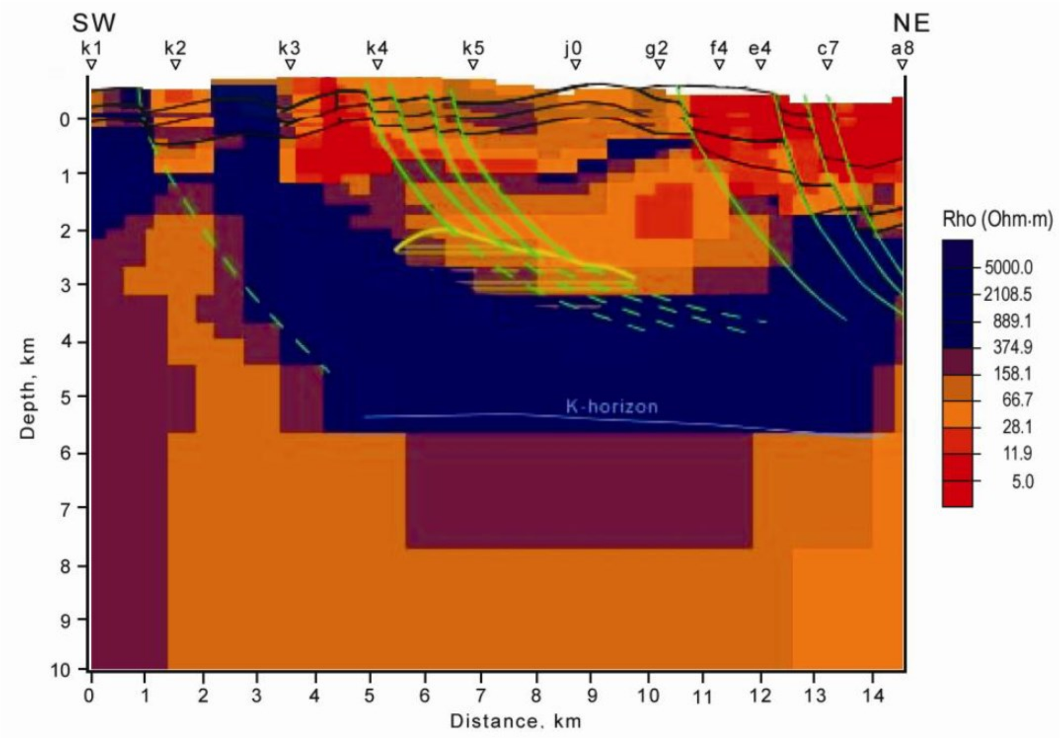

Figure 5.9 The 2D resistivity model of Travale after 2D NLCG inversion of the profile acquired in 2004 (from Manzella et al. 2006)

5.3.2 Seismic methods

A schematic conceptual model of the Travale geothermal system is shown in Figure 5.10 (from Bertini et al. 2005).

From seismic reflection data, two seismic reflectors have been detected in the deep structure of the Travale field (Bertini et al. 2006; Casini et al. 2010; De Franco et al. 2019). The shallow marker is referred to as "H-horizon" and is a discontinuous high-amplitude reflector. It is located in the metamorphic reservoir at a depth of 2.5-4 km, above the Pliocene granitoids. In Travale, this reflector represents the actual mining target and in fact all the drilled wells encountering the H-horizon are productive (Casini et al. 2010). The H-horizon could be interpreted as the metamorphic contact aureole of the old (2-3 My) granitic intrusion (Bertani et al. 2005). The deep marker "K-horizon" is a high-amplitude discontinuous reflector showing local bright spot features at a range of depths between 3 km (in Larderello) and 8 km (in Travale). This horizon occurs at the top of the Quaternary granite intrusions and could be interpreted as a metamorphic contact aureole of the Quaternary granitic intrusion (Bertini et al. 2006; Bertani et al. 2018). The K-horizon has been often associated to the 400-450 °C isotherm and to the occurrence of supercritical fluids, but a recent deep-drilling revealed dry condition and about 510 °C in proximity of the Larderello area (Bertani et al. 2018). Its origin and nature are still under debate (Vanorio et al. 2004; De Matteis et al. 2008; Sani et al 2016; Gola et al. 2017; De Franco et al. 2019).

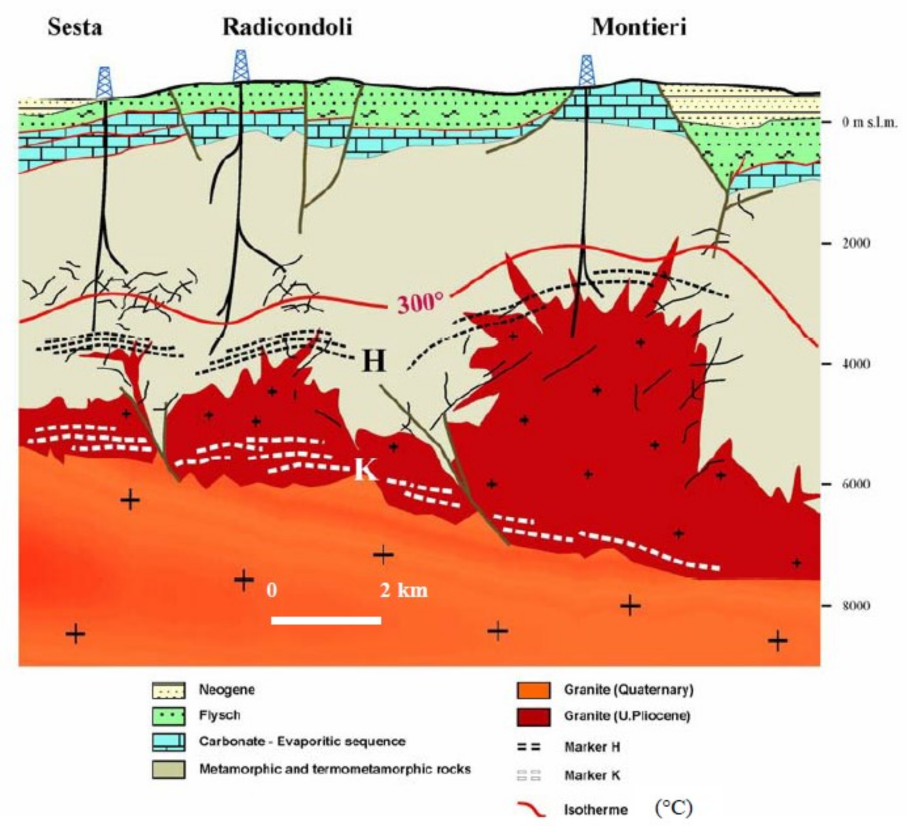

Figure 5.10 Schematic structural model of the Travale geothermal field (from Bertini et al. 2005). This section is directed NW-SE.

An interesting correlation has been pointed out between the H-horizon inferred from 2D seismic modeling and the productive levels of the drilled wells (Bertani et al. 2005; Casini et al. 2010). Figure 5.11 illustrates the seismic signal of two lines crossing the wells *Radicondoli7bis* and *MN1*. These wells are located in the same area of the MT sites, as marked in Figure 5.8 with yellow stars. Figure 5.11a shows a NW-SE section from a seismic line crossing the well *Radicondoli7bis*, whose productive levels (yellow ellipses) matches the reflections of the H-horizon. Figure 5.11b reveals that the productive areas of the well *MN1* corresponds to the fractured zone of the H-horizon at a depth of 1.7-2.2 km b.g.l., corresponding to the metamorphic basement above the top of the granite intrusion.

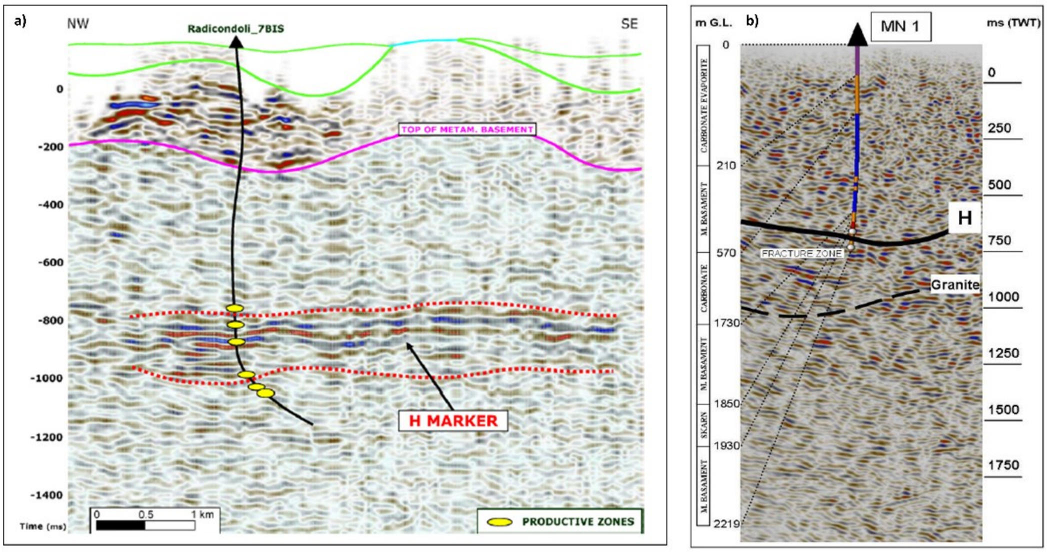

Figure 5.11 Seismic sections of two drilled wells from seismic reflection lines in the Travale area. The location of these wells is depicted in Figure 5.8. **a)** the productive zones of the well *Radicondoli7bis* (yellow ellipses) are included between the reflections of the H-horizon (from Casini et al. 2010); **b)** the well *MN1* reaches the fractured zone of the H-horizon below 1730 m of depth b.g.l. (from Bertani et al. 2005).

The most recent seismic study in the Travale area is the local-earthquake tomography derived by travel-time inversion (Bagagli et al. 2020). The 3D model of P-wave velocity (v_p) of the upper crust highlighted a deep-rooted low-velocity body ($v_p = 5.7$ km/s) from 3 to 7.5 km b.s.l. below the Travale area, between the H- and K- horizons. Figure 5.12 shows the low-velocity body as appears from two cross-sections. The eastern side of the W-E section (Figure 5.12a) is very close to the town of Travale and well *MN1* and shows an abrupt transition from a dome-shape high-velocity body to the deep-rooted low-velocity body. Another view of the same low-velocity body is given in Figure 5.12c. The CC' section is the same SW-NE section of the geological profile in Figure 5.6right (Bertini et al. 2006; Romagnoli et al. 2010). The velocity anomaly in Figure 5.12c has been attributed to the NW-SE striking and N-dipping normal faults of the area which "might have caused a thickened uppermost crustal layer of lower velocities at the eastern margin of our profile" (Bagagli et al. 2020). Considering the tectonic features of this area and, above all, the presence of a major sub-vertical transcurrent fault, this low-velocity region has been assumed as a "preferential pathway" for fluids coming from the K-horizon to the surface. From travel-time inversion emerged that the K-horizon marks a transition towards a high-velocity substratum, thus confirming the previous interpretation (of Bertini et al. 2005, 2006) for a metamorphic contact aureole at the top of the Quaternary granitic intrusions.

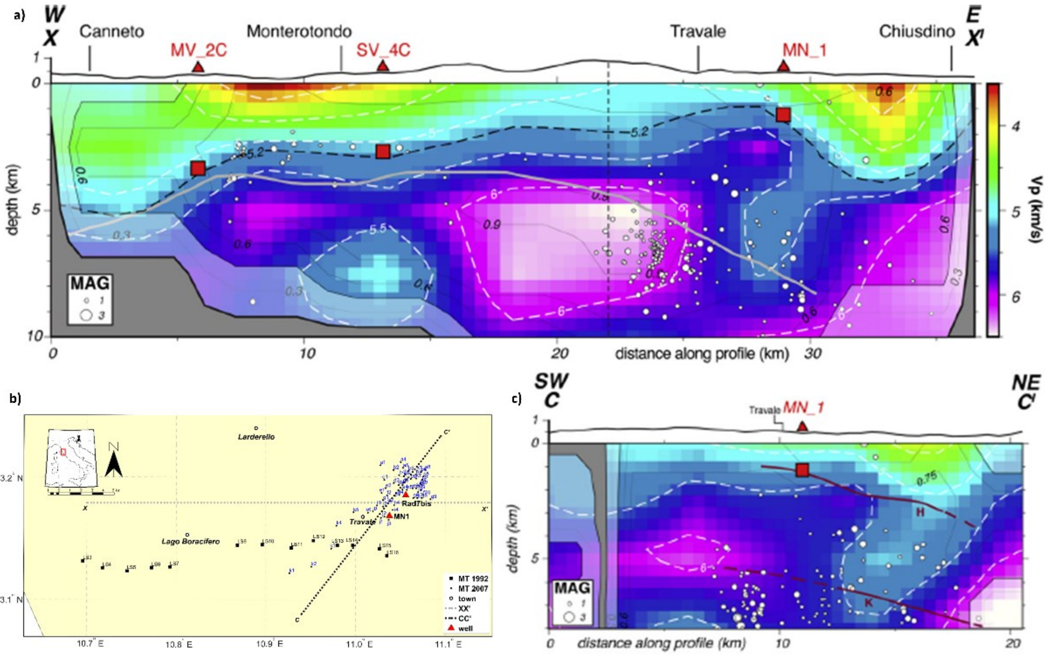

Figure 5.12 Tomographic cross-sections modified from the 3D P-wave velocity model of Bagagli et al. (2020). The red squares below the wells correspond to the encountered H-horizon. The K-horizon is plotted as grey line. The white circles are the hypocenters of local earthquakes; **a)** the W-E section (XX' profile) crosses the Travale area in the eastern sector where a velocity anomaly below well *MN1* is surrounded by the 5.7 km/s white-dashed isoline (from Bagagli et al. 2020); **b)** map of the XX' profile (grey-dotted line), CC' profile (black-dotted line), the main towns (white circles), MT sites (black dots and squares), geothermal wells (red triangles); **c)** the SW-NE section (CC' profile) shows a low-velocity body (v_p around 5 km/s) bounded between the H- and K-horizons (from Bagagli et al. 2020).

5.3.3 Other studies

The Travale geothermal area is characterized by a low gravity anomaly of about 10-20 mGal (Orlando 2005). This anomaly occurs in coincidence with the highest heat flow of about 200 mW/m^2 measured at surface.

The resistivity well-log of the well *Radicondoli7bis* (location in Figure 5.8 and productive levels in Figure 5.11a) is available from literature (Giolito et al. 2009; Manzella et al. 2010). The left side of Figure 5.13 plots the true resistivity log (grey line) and the averaged resistivity for each lithological unit (black-dotted line). Within the phyllitic quartzitic complex, the phyllite member (green blocks) has an average resistivity of around 100 Ωm, while the carbonate-anhydritic member (orange blocks) has an average resistivity of around 1000 Ωm. At higher depth corresponding to micaschists and granite, the resistivity rises by up to 1000 Ωm. The right side of Figure 5.13 shows the relative x-ray diffraction (XRD) intensity, which has been correlated with the presence of chlorite and muscovite in the framework of mineralogical studies (Giolito et al. 2009).

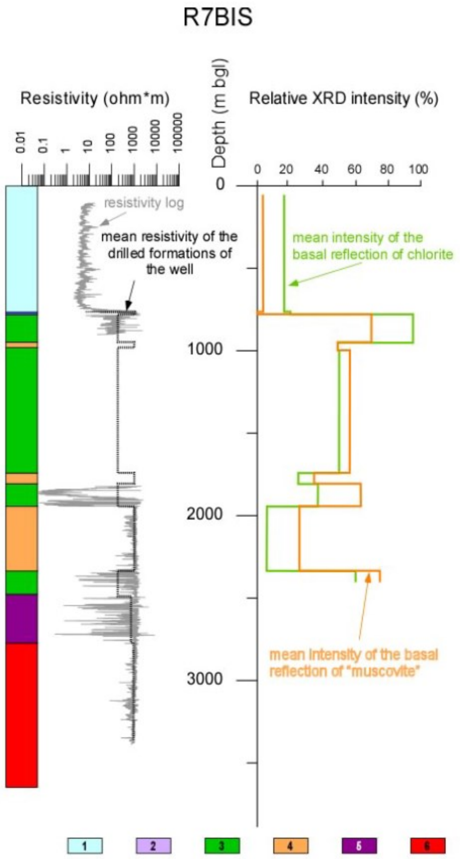

Figure 5.13 left) Resistivity-log of the well Radicondoli7bis. Litho-stratigraphic units: 1) Ligurian units, 2) anhydrites of the Tuscan complex, 3) Phyllite member of the phyllitic quartzitic complex, 4) Carbonate-anhydritic member of the phyllitic quartzitic complex, 5) Micaschists and contact-metamorphic rocks, 6) granite. The depth is in m b.g.l.; **right)** relative x-ray diffraction (XRD) intensity (from Giolito et al. 2009).

5.4. Analysis of the MT data set

Following the geological and geophysical framework outlined so far, some research questions/gaps can be outlined for the Travale geothermal system:

1. There is not direct information regarding the supercritical reservoir and the K-horizon because no well to date has been drilled below 2500 m of depth b.g.l. By contrast, for the Larderello system there was the experiment of *Venelle-2* (Section 5.1.2).

2. The deep structures of the system are not completely understood.

3. A 3D MT characterization and interpretation of the vintage data set has not yet been investigated.

5.4.1 The MT data set

The Travale geothermal field was involved in three MT campaigns conducted in 1992, 2004 and 2006-07 (Manzella et al. 2006; Santilano et al. 2017). The sites are depicted in Figure 5.8 with different symbols according to the year of acquisition. For details on the data set see Appendix B.

The acquisition settings of each of the three data sets were slightly different. The 1992 data set is composed of two long E-W profiles and was acquired as part of an exploration project using Phoenix V-5 system (Fiordelisi et al. 1998; Manzella 2004). A remote reference processing technique was applied using the remote site located in the Island of Capraia (Tuscan Archipelago).

The sites acquired in 2004 cover an area of 48 km^2 and the average distance from the coast line is 60 km. The minimum and the maximum elevations are 314 m (site c9) and 652 m (site k5) a.s.l., respectively. Figure 5.14 shows in detail the MT data set acquired in 2004 and highlights, with red dots, the sites where the vertical transfer function (or Tipper) has been acquired. A subset of 26 out of 55 sites includes the Tipper.

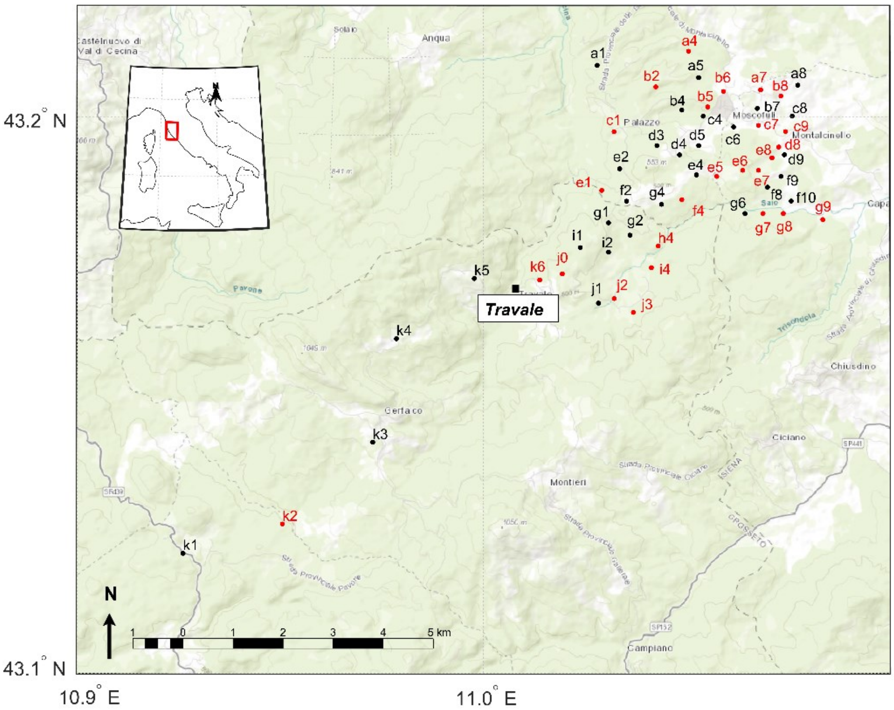

Figure 5.14 The MT data set examined in this work is composed of 55 sites. The 26 sites marked in red include the vertical transfer function (Tipper), while the remaining sites (black dots) include only the four components of the MT tensor. The town of Travale is located between sites k5 and k6. This map was created by reading a georeferenced image (coming from "openstreetmap") within Matlab Mapping Toolbox (by Mathworks).

As regards the 2004 data set, four components data (and five components for some sites) were collected using the Phoenix MTU system within the INTAS (EU) Project. At each site, the MT signal was recorded overnight for (at least) 12 hours in the range 0.003 – 993 s. Quality controls were carried out on time series, spectra and transfer functions and a strong signature of noise was observed for some sites (Manzella et al. 2006). The source of noise for short-period MT data was related to the local power plants and geothermal exploiting activities. To solve this, the remote-reference processing technique acquired synchronized data simultaneously measured at the local sites. Long-period MT data were contaminated by noise arising from the electrified railways. To solve this, a remote site was placed in Sardinia, around 500 km south-west of Travale. The whole data set was processed using Phoenix Geophysics software based on the remote reference robust processing method (Jones et al. 1989). In order to remove the industrial noise, a further manual editing and smoothing of transfer functions was carried out.

The 2006-07 dataset was acquired in the frame of the I-GET (EU) Project. Long-period MT data (period range: 0.2 - 1000 s) were measured using the MT systems "NIMS" or "LEMI", while audio-MT data (period range: 0.001 - 10 s) using the Stratagem system (Manzella et al. 2010).

In this study, the data set acquired in 2004 was selected for 2D stochastic modeling and 3D inversion (blue-labeled dots in Figure 5.8). The main reasons of this choice were low level of noise, coherence of the frequency band and regular spatial distribution of the site locations. It should be clarified that for the dimensionality and directionality analyses we included the whole data set of the Travale area (86 sites listed in Appendix B), while for 3D inversion modeling we selected the subset of 51 MT soundings acquired in 2004.

5.4.2 Dimensionality analysis

The dimensionality analysis was carried out for the whole MT data set depicted in Figure 5.8 in order to provide a general overview of the region. The geoelectrical dimensionality was determined by using the WALDIM software described in Section 2.4.1 (Martì et al. 2009). This dimensionality analysis gives a first indication of the spatial distribution (1D, 2D or 3D) of the electrical resistivity at depth by analyzing the "WAL" invariants derived by the MT tensor (Weaver et al. 2000). To perform the dimensionality analysis on the WALDIM software, an error level of 5% was considered for the four impedance components. The threshold value for the WAL invariants was 0.15. The results were grouped in seven decades of period bands, covering the period range 10^{-3} – 10^{4} s (only the data set of 2006-07 was acquired with periods higher than 10^{3} s).

Figure 5.15a-g illustrates the response of the dimensionality analysis. The responses were predominantly 3D for all the periods, as shown also in the bar graphs. At periods lower than 1 s (Figure 5.15a-c), a discrete number of 1D and 2D structures were identified north-east of the area. At longer periods (Figure 5.15d-g), a 3D behavior, with or without regional 2D structures, characterized the totality of sites. Only 17% of sites, that is, the data set acquired in 2007, had periods above 1000 s. Considering the whole period range, a negligible number of sites, less than 8%, had undetermined dimensionality due to errors overlapping the used threshold (the stars in Figure 5.15a-g). The dimensionality analysis clearly outlined the 3D nature of the subsurface electrical structures at periods higher than 10 s.

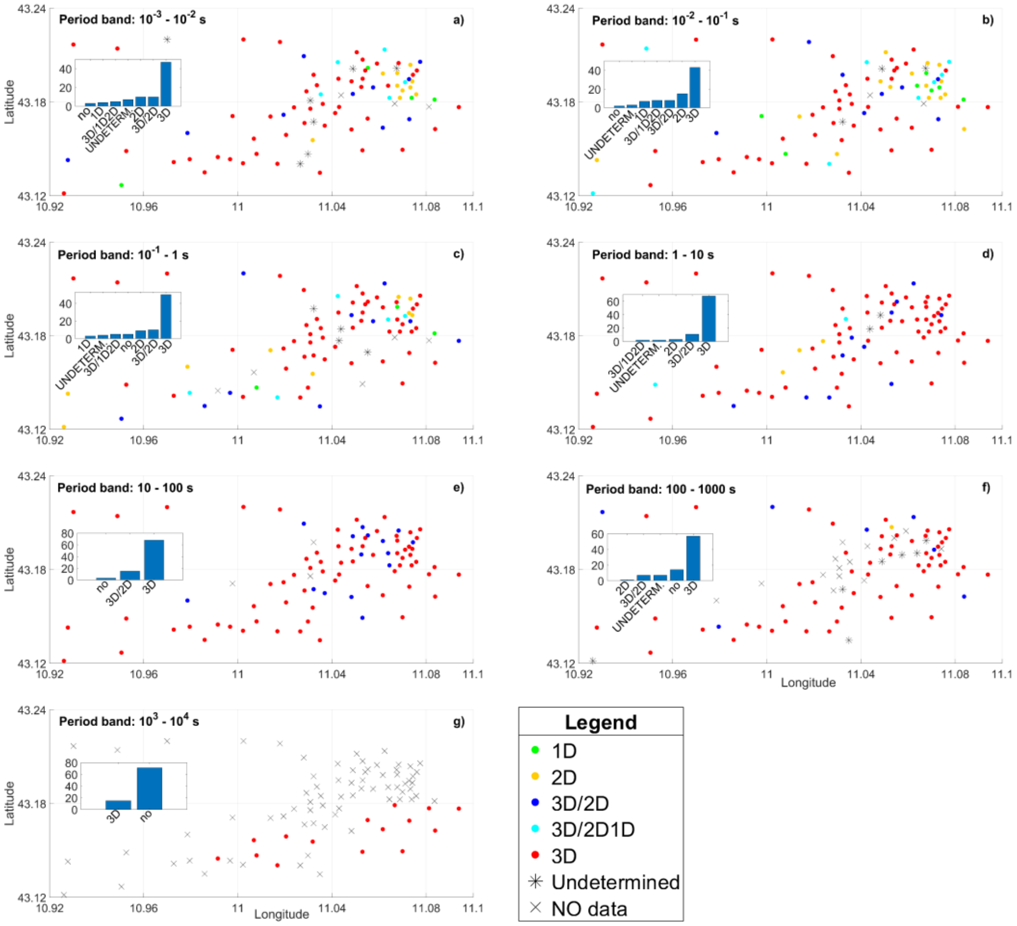

Figure 5.15 Dimensionality analysis results of the MT data from the Travale geothermal area from WALDIM software (Martì et al. 2009). The output was classified in seven decades of periods: **a)**10^{-3}-10^{-2} s, …, **g)** 10^{3}-10^{4} s according to one of the following dimensionality: 1D, 2D, 3D/2D (regional 2D structure affected by galvanic distortion), 3D/2D1D (galvanic distortion over a 1D or 2D structure), 3D, undetermined (errors higher than the threshold), no data acquired in that period.

5.4.3 Phase tensor analysis

Further insight into the data came from the phase tensor analysis, based on the observed impedance tensor (Caldwell et al. 2004). The phase tensor ($\boldsymbol{\Phi}$) is not affected by the galvanic distortion and does not require any assumption of dimensionality (Section 2.4.3). Therefore, the analysis of Φ could provide further insight into the interpretation of the underlying conductivity distribution. The direction of the tensor and the three coordinate invariants (Φ_{min}, Φ_{max}, β) are graphically represented by means of the tensor ellipse, which may disclose the orientation as well as the lateral variations of the underlying electrical structures. We adopted the open-source python toolbox *MTpy* for the phase tensor analysis (Krieger and Peacock 2014; Kirkby et al. 2019). Figure 5.16a-f shows the tensor ellipses of the MT sites at six selected periods. The color scale considers the skew angle β of the phase tensor, which measures the asymmetry of the tensor. Some considerations can be outlined:

a) The circular shape of some ellipses at periods lower than 0.1 s revealed local 1D resistivity distributions in the shallow subsurface, in line with the dimensionality analysis of Figure 5.16a-b.

b) Low values of the skew angle, i.e. $\beta \sim 0$, were infrequent, meaning scarce 1D or 2D distribution (for 2D, $\beta = 0$ is a necessary but not sufficient condition).

c) Non-zero values of β imply the non-symmetry of the phase tensor. If $-3 < \beta < 3$ and if there is a significant difference between major and minor axes of the ellipse, the distribution is 3D. This occurred for the majority of the sites and periods, thus stating a mostly 3-D resistivity distribution and confirming the previous interpretation of dimensionality.

d) The orientation of the ellipses is related to the strike direction (with 90° of ambiguity). The ellipses in Figure 5.16a-f had an N130°E orientation (see also Figure 5.18), representing also the strike of the main tectonic structures parallel to the Apennine chain. Few sites presented an ellipse orientation of about N40-50°E. This can be related either to tectonic structures with NE-SW trend, whose occurrence has already been pointed out in southern Tuscany, or to the intrinsic ambiguity of 90°. Given the orientation of the majority of the ellipses at periods above 1 s, a low resistivity region can be expected with a NW-SE trend.

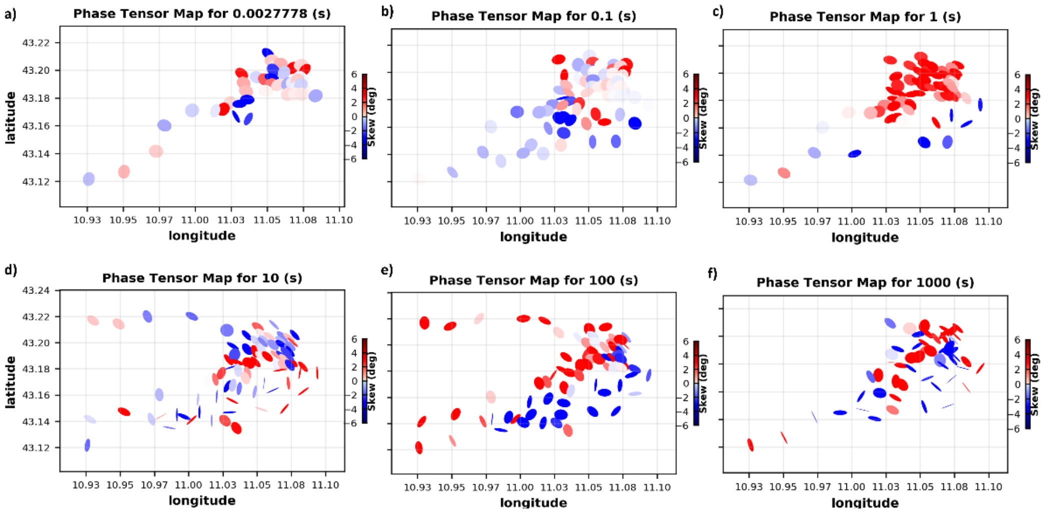

Figure 5.16 Phase tensor ellipses at selected periods from 10^{-3} s **(a)** to 10^{3} s **(f)**. The phase tensor skew angle β (°) is null (white) in case of 1D distribution and increases in magnitude (red or blue colors) in case of 3D distribution. The elongated ellipses indicate a 3D distribution and point toward a conductive region.

The geomagnetic transfer function, also known as Tipper, represents the ratio between the vertical and horizontal components of the magnetic field. The real part of the Tipper vector is usually represented by means of induction arrows pointing toward the region of highest conductance according to the Parkinson criterion (Parkinson 1959). Figure 5.17a-f shows the phase-tensor ellipses overlapped by the Tipper vectors of the subset of 26 sites whose vertical transfer function has been measured. At periods of 1 s and 10 s (Figure 5.17c-d), the vectors were mainly orientated orthogonally to the strike direction and, similarly to the ellipses in Figure 5.16, their direction suggested a possible NW-SE-oriented conductive region. The color scale of the ellipses in Figure 5.17 ranges from 0° to 90° and refers to the phase-tensor determinant. It deviates from an angle of 45° if there is not 1D regional distribution in the subsurface.

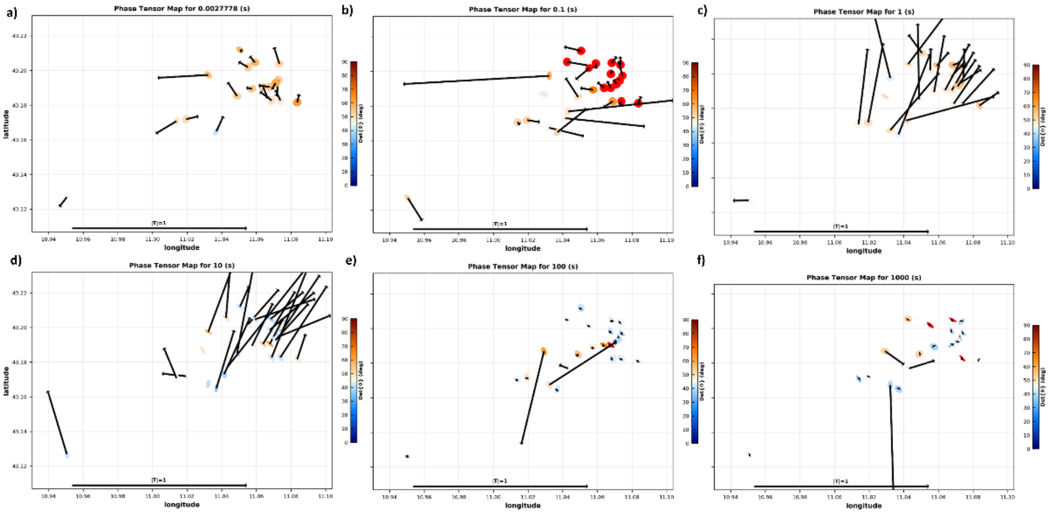

Figure 5.17 Tipper arrows at selected periods from 10^{-3} s **(a)** to 10^{3} s **(f)** for the 26 sites with measured geomagnetic transfer function. Most of the vectors point toward a predictable North-Eastern conductive region (Parkinson criterion) and are fairly orthogonal to the strike direction shown in Figure 5.18. The horizontal arrow on the bottom of the graph shows the Tipper vector length in case of magnitude 1. The color scale of the phase-tensor ellipses refers to its determinant.

5.4.4 Strike analysis

The tensor ellipses gave an approximate idea of the strike direction, which was definitely confirmed by the strike analysis. We deployed the strike-analysis tool of the *MTpy* package (Krieger and Peacock 2014; Kirkby et al. 2019). The strike direction was estimated from the impedance invariants (Weaver et al. 2000), the phase tensor azimuth (Caldwell et al. 2004) and the induction arrows. Figure 5.18 reports the rose diagram of the strike direction calculated from the impedance tensor $\underline{Z}$ (Figure 5.18a), the phase-tensor azimuth (Figure 5.18b) and the Tipper matrix (Figure 5.18c). These three outcomes were in agreement with each other and defined the direction of N130°E for the geoelectrical strike. This value represents the strike direction averaged on the frequency full range. A detailed analysis of the strike direction estimated at each period decade is shown in Figure 5.19. In the range 0.1-100 s, there was a clear and unambiguous strike direction because all the histogram bins aligned toward a unique value of 130°. At higher periods, there was a leading direction of around N150°E, but a small number of histogram bins were oriented around N45°E.

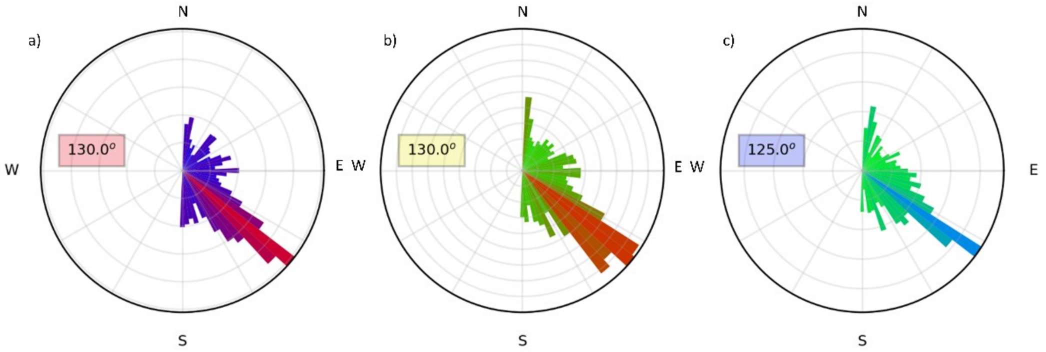

Figure 5.18 Rose diagrams of the strike direction calculated over the whole period range from **a)** the impedance tensor <u>Z</u>, **b)** the phase tensor azimuth and **c)** the Tipper matrix.

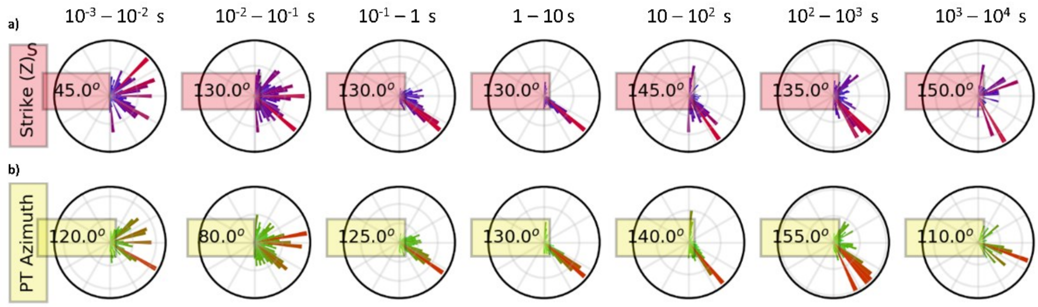

Figure 5.19 Rose diagrams of the strike direction calculated at each period decade from **a)** the impedance tensor <u>Z</u> and **b)** the phase tensor azimuth.

Finally, there is a good agreement in the orthogonality between the strike direction and the orientation of the induction arrows (Figure 5.19 and Figure 5.17, respectively). Moreover, there is a substantial parallelism between the strike direction and the NNW-SSE orientation of the main faults shown in Figure 5.6left for the Radicondoli-Volterra basin (Sani et al. 2016). This pointed out the role of the NNW-SSE-oriented Radicondoli sedimentary basin, which is located North-East of the study area (sensu Brogi et al. 2003 or Sani et al. 2016). The direction of the normal faults and strike are also reflected in the surface fracture patterns detected by satellite images, which have displayed a N110°E – N150°E trend (Bertini et al. 2005).

5.5. The new TDEM soundings for static shift correction

TDEM data have often been combined to MT data from geothermal areas even though their depth of investigation is usually much lower than that of the geothermal target (Section 2.5). We carried out a TDEM survey in the Travale area to manage the static shift that could affect one or both the polarizations of the MT apparent-resistivity curves.

In February 2019, we acquired 8 TDEM soundings in order to constrain the MT soundings placed in different geological settings and to ensure a wide spatial coverage. The sites were a1, b2, b6, e1, g1, k1, k4 and k5 (see Figure 5.14 for locations). Unfortunately, it was not possible to acquire more soundings due to logistic issues.

TDEM data were acquired using the *TEM-FAST 48* instrument by AEMR company. The acquisition configuration was a coincident loop of 100 x 100 m or 75 x 75 m, depending on the accessibility of the site. The injected current was 3 A, the turn-off time was 7-8 μs and a total of 32-40 samples were acquired in the range 4 - 4000 μs.

Figure 5.20 Some pictures of the TDEM survey carried out around Travale in February 2019 **left)** the instrument used for TDEM acquisition was a TEMFAST48; **right)** the most accessible sites allowed a loop-size of 100 m to be set up.

At first, the TDEM data were adopted to directly correct the static shift of the correspondent MT site and then to verify and, if needed, correct the static shift of the closest MT site belonging to the same geological unit. The correction was carried out using the PSO approach previously explained in Section 3.3.2. The optimization was performed for each MT polarization. The algorithm optimizes both the model parameters, i.e. the resistivity model, and an additional parameter accounting for the static shift. Input data were both the MT ρ_{app} and phase and the TDEM ρ_{app}, but the observed MT ρ_{app} was iteratively optimized to match the reference curve of the TDEM ρ_{app}.

An example of static shift correction using PSO was presented in Chapter 3 for site *a1* (Figure 3.4). As another example, site *b6* is shown in Figure 5.21 and Figure 5.22 for the xy- and yx- modes, respectively. The raw apparent resistivity showing the level of distortion of the data can be appreciated from the red dots in Figure 5.21a and Figure 5.22a. Figure 5.21a shows that at short periods (below $6 \cdot 10^{-3}$ s) the TDEM curve of ρ_{app} (red dots) provides the undistorted value of the MT ρ_{app} (blue crosses). The multiplicative factor calculated for static-shift correction was around 2. Since the distortion (or shift) is static (or period-independent), the correction provided by TDEM ρ_{app} at short periods is useful for the whole MT period band (blue crosses at periods above $3 \cdot 10^{-3}$ s). The 1D model in Figure 5.21c is negligible for our interpretation. The optimization terminated when the RMSE was 1. Figure 5.22a shows that the yx-mode of site *b6* was barely affected by static shift, being the corrective factor equal to 1.

The static shift correction of the other MT sites is supplied in Appendix C. As regards the other sites affected by static shift, the majority of the observed ρ_{app} curves which, at the lowest periods, lay either above 100 Ωm or below 10 Ωm were shifted in the range 10 - 100 Ωm. In particular, the sites on the quaternary deposits (such as *a1* and *b2*) had a corrected ρ_{app} starting from around 100 Ωm, while the sites on the Ligurian unit (such as *e1* and *d3*) had a corrected ρ_{app} starting from around 20-30 Ωm. In general, the static-shift factor was between 0.5 and 10.

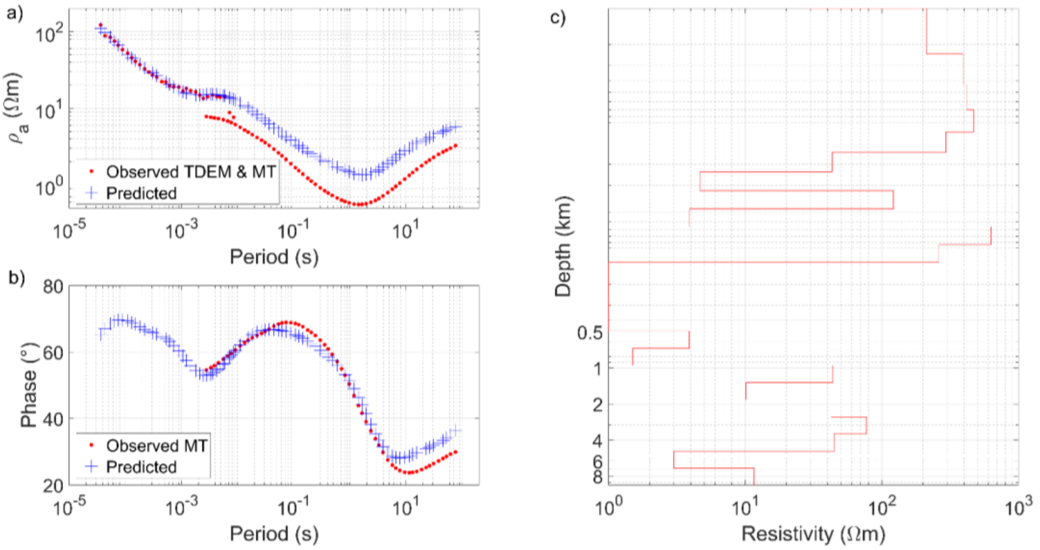

Figure 5.21 Static shift correction for site b6 (xy-mode) using PSO. **a)** The red dots are the observed apparent resistivity (ρ_{app}) of TDEM at low periods (up to 0.005 s) and of MT from 0.003 s upward. The blue crosses indicate the predicted MT ρ_{app} that correct the static shift according to TDEM information; **b)** Observed (red dots) and predicted (blue crosses) MT phase; **c)** The 1D resistivity model (not interpreted here).

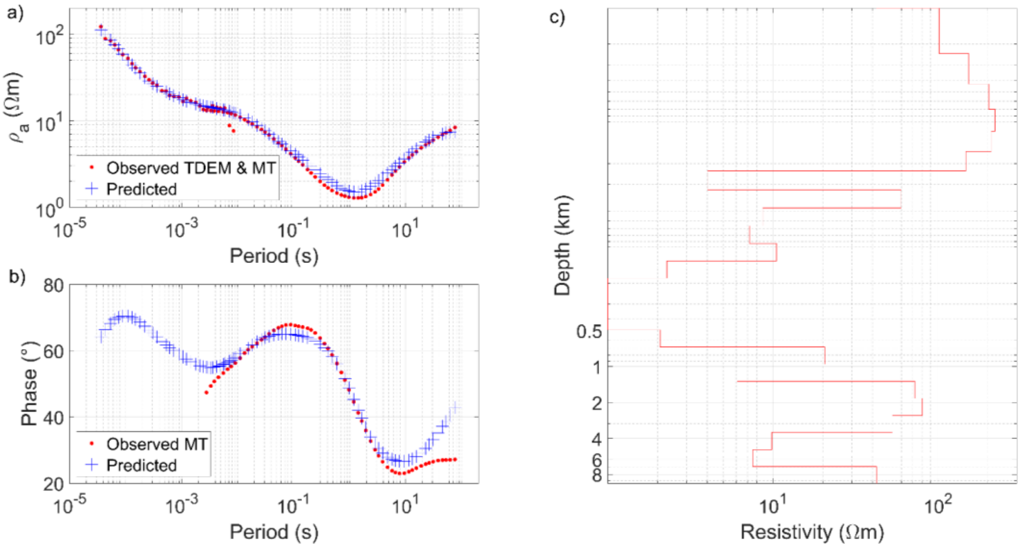

Figure 5.22 Static shift correction for site b6 (yx-mode) using PSO. **a)** The red dots are the observed apparent resistivity (ρ_{app}) of TDEM at low periods (up to 0.005 s) and of MT from 0.003 s upward. The blue crosses indicate the predicted MT ρ_{app} that correct the static shift according to TDEM information; **b)** Observed (red dots) and predicted (blue crosses) MT phase; **c)** The 1D resistivity model (not interpreted here).

5.6. Final considerations

This chapter set out the framework of the geothermal area of Travale from the geothermal, geologic and geophysical point of view. The state of the art of the MT characterization of the area pointed out a scientific gap. The vintage MT data set acquired over the last few decades was recovered and thoroughly studied following the latest tools of MT data analysis. The detailed analysis carried out in this section proved that, although a 2D strike direction around N130°E could be considered as a "first approach", the most appropriated interpretation of our data needs for 3D MT inversion. Therefore, further knowledge may arise from the interpretation of the data set presented in this chapter by using two new methodical approaches:

a) The novel 2D particle swarm optimization of MT data. It was applied to two MT profiles and is presented in Chapter 6
b) The 3D inversion, that is the recent hot topic in the MT community. A 3D resistivity model of the geothermal system is revealed in Chapter 7.

Chapter 6

Stochastic inverse modeling of MT data from the Larderello-Travale geothermal area

This chapter is concerned with the 2D stochastic inverse modeling of two MT profiles located in the Larderello and Travale geothermal areas. The method adopted for this purpose was the novel PSO specifically implemented for 2D MT data, as accurately described in Chapter 4. The MT data set was presented and analyzed in Chapter 5 (further details in Appendix B). The results of this chapter highlight the importance of the stochastic approach to interpret MT data from geothermal areas, where the geological complexity and the difficulty in retrieving reliable external constraints (e.g., from well-log or other geophysical methods) can negatively affect the solution of the inverse problem.

Even though the dimensionality analysis depicted in Chapter 5 may suggest 3D interpretation as the most appropriate for this data set, there are some conditions for the validity of 2D interpretation: inadequate spatial coverage (isolated MT profile), a clear strike direction (as suggested in Section 5.4.4, Figure 5.18 and Figure 5.19) and the extremely computational and numerical complexity of 3D modeling (Ledo 2005).

The 2D optimization of the MT profile located close to Lago Boracifero (hereafter "LS" profile) was presented as a talk during the 1st Conference on Geophysics for Geothermal and Renewable Energy Storage (European Association of Geosicentists and Engineers (EAGE), The Hague, Netherlands, September 08 - 12, 2019). The conference proceeding is Pace et al. (2019c). The 2D optimization of the MT profile close to Travale (hereafter "Travale" profile) was presented as a talk during the 38° Convegno Nazionale Gruppo Nazionale di Geofisica della Terra Solida (Rome, Italy, November 12 - 14, 2019). The abstract is Pace et al. (2019d).

6.1. The MT profiles

6.1.1 The “LS” profile

The “LS” profile is located south of Larderello and south-west of Travale and belongs to the data set acquired in 1992 as described in Section 5.4.1 (Figure 5.8). As shown more in detail in Figure 6.1, it is composed of 13 MT sites because three of the original sites were discarded due to the poor quality of measured data.

This profile has been investigated in the past by means of the 2D inversion scheme based on non-linear conjugate gradient (Santilano et al. 2015b; Santilano 2017; Rodi and Mackie 2001).

Figure 6.2 plots the phase-tensor ellipses in a pseudo-section format for the “LS” profile (Caldwell et al. 2004). At each period, the ellipses are depicted according to the value of the skew angle (β) and are overlapped by the arrow representing the real value of the Tipper vector. The considerations arising from this phase-tensor pseudo-section are similar to those written in Section 5.4.3. Some ellipses have a circular shape at low periods, e.g., *ls04* and *ls15* at 0.1 s or *ls09* and *ls13* at around 1 s. Low values of the skew angle, i.e., $\beta \sim 0$, appears only at periods lower than 1 s, meaning 1D or 2D dimensionality only in the shallow subsurface (see the color scale in Figure 6.2). At higher periods, the non-symmetry of the phase tensor and hence 3D dimensionality are proved by $-3 < \beta < 3$ and a significant difference between the major and minor axes of the ellipses. For this reason, the period range selected for 2D optimization was from 10^{-3} s to 23 s.

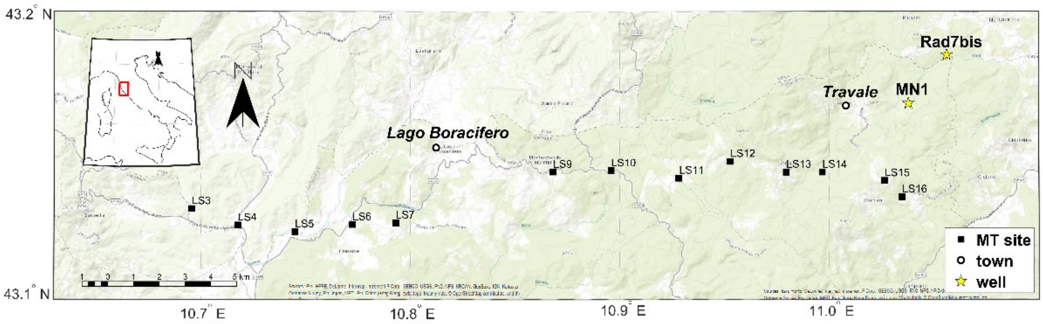

Figure 6.1 The “LS” profile is composed of 13 MT sites (LS3, .., LS16) and is located south of Lago Boracifero and south-west of Travale. This map was created by reading a georeferenced image (extracted from “Open Street Map”) within Matlab Mapping Toolbox (by Mathworks).

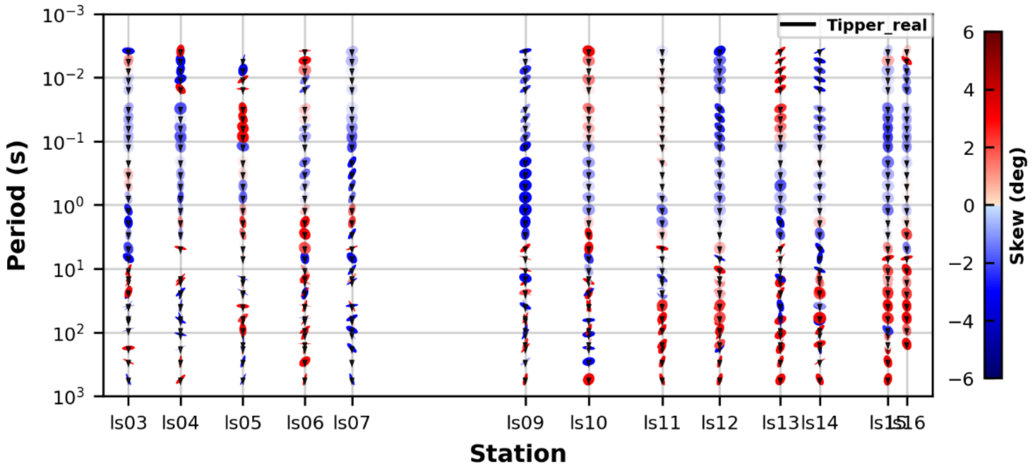

Figure 6.2 Phase-tensor map in a pseudo-section format for profile "LS". The color scale refers to the skew angle *β* and the arrows to the real part of the Tipper vector.

6.1.2 The "Travale" profile

The "Travale" profile is depicted in Figure 6.3. It is composed of 11 sites acquired in 2004 (Manzella et al. 2006). The strike analysis reported in Section 5.4.4 outlined a strike direction of N130°E (Figure 5.18 and Figure 5.19). As can be seen from Figure 6.3, the investigated profile is orthogonal to this direction. Figure 6.4 presents the phase-tensor map as a function of the period for the 11 sites of the "Travale" profile (Caldwell et al. 2004). The circular shape of the phase-tensor ellipses and the low value of the skew angle ($|\beta| < 3$) are evident at periods lower than 1 s. As demonstrated in the previous chapter, we obtained evidence of three-dimensionality at periods above 10 s.

Some MT sites were affected by static shift due to local shallow heterogeneities that may provoke the telluric distortion of the impedance tensor. We corrected the static shift by performing the joint optimization (PSO) of TDEM and MT data of the same site (Section 3.3.2). We selected 8 MT sites, with static shift effects, for TDEM data acquisition. The TDEM survey was carried out in February 2019 using a TEM-FAST48 instrument (Section 5.5 and Appendix C).

In addition to what stated in the introduction, a further reason of our 2D approach is to enrich the investigation of this area with the contribution of stochastic inverse modeling. Manzella et al. (2006) inverted this profile using 2D NLCG inversion (Rodi and Mackie 2001) and adopting an external geological model as starting model. Our contribution is to overcome the external bias on the solution by taking advantage of random initialization and adaptive global search.

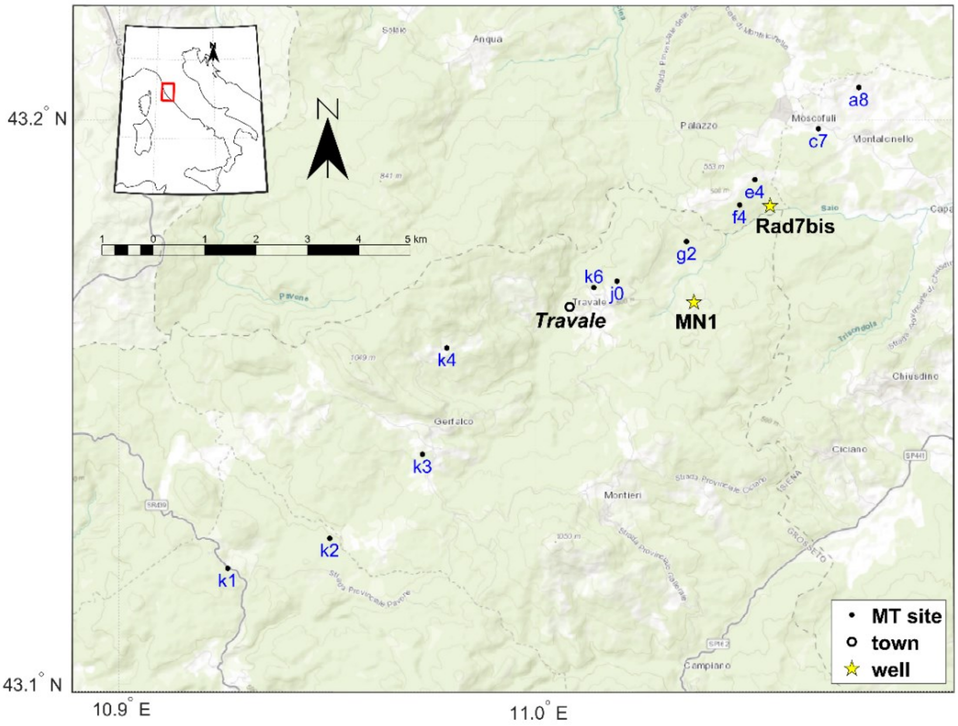

Figure 6.3 The “Travale” profile is directed SW-NE and is composed of 11 MT sites (*k1, .., a8*) crossing the town of Travale. This map was created by reading a georeferenced image (extracted from “Open Street Map”) within Matlab Mapping Toolbox (by Mathworks).

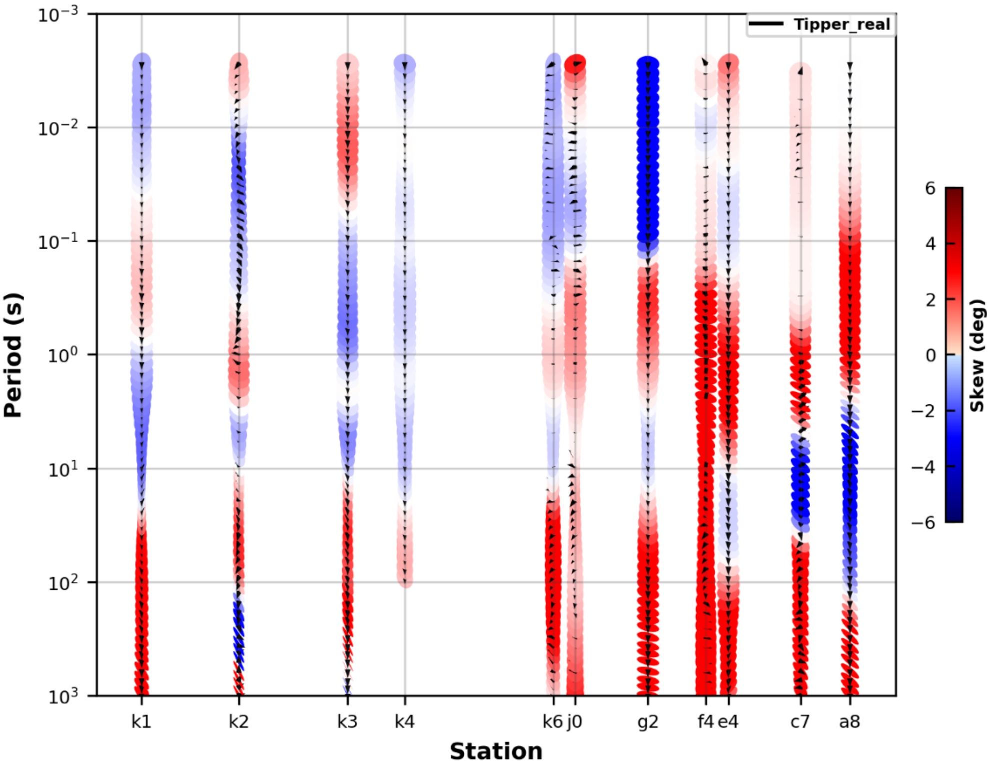

Figure 6.4 Phase-tensor map in a pseudo-section format for profile "Travale". The color scale refers to the skew angle β and the arrows to the real part of the Tipper vector.

6.2. Result from 2D PSO

The objective function to be minimized to find the 2D electrical-resistivity model was provided in equation 4.3. This objective function was defined to minimize the data misfit (between the observed data and calculated response) and the model roughness. We adopted the optimization with the Occam’s razor principle, that minimizes the effect of spurious features derived by the closest fitting between observed data and calculated response. The high computational cost (in the order of hours) was due to the thousands of MT forward calculations to be performed and was managed by using 24 cores from the HPC cluster at Politecnico di Torino.

The PSO input arguments, namely, the accelerations coefficients and the swarm size, were selected according to the sensitive analysis reported in Section 4.3.1 in order to ensure the solution stability, the convergence speed and an effective minimization of the objective function.

6.2.1 The model from the “LS” profile

The application of the PSO algorithm to the “LS” profile represents the first case study of 2D stochastic inverse modeling of MT data coming from the Larderello-Travale geothermal area.

To perform the optimization, the errors associated to the data were kept as original, despite they were higher than 20% at high periods. The mesh of the 2D model was discretized into 10 layers and a total of 270 cells. The number of particles (i.e., the solutions explored) was 2430 because, following our previous sensitivity analysis, it should be 9 times the number of unknowns (i.e., the model cells). After applying the L-curve criterion to calibrate the level of smoothing of the model, the optimal Lagrange multiplier was 0.01 for both the horizontal and vertical directions. The minimum and maximum boundaries of the search space of solutions were 1 Ωm and 1000 Ωm, respectively. As for the field data set COPROD2 (Section 4.4), each PSO run was repeated three times (or “trials”) in order to assess the final solutions coming from different initial random distributions, which are quite similar, but not identical. Among the three trials, the one that gave the solution with the lowest RMSE was selected as the final model. The total number of iterations was 1626 and obeyed the stopping criteria established in Section 4.2.3. No external information was used to initialize the PSO. The starting model was hence created by a random initialization. This was a novelty with respect to the previous results published in literature, that used homogeneous and geological starting models (Santilano et al. 2015b; Santilano 2017).

The runtime of a single trials was 3.8 hours, the final RMSE was 3.55 and the objective-function value at the last iteration was 3.65. The resistivity model following from PSO is depicted in Figure 6.2. In the shallow subsurface, the local resistivity anomalies (<30 Ωm) correspond to the Neoautochthonous and Ligurian

Complexes. A moderately resistive region (average 100 Ωm) up to a depth of 2.5 km is associated with the Tuscan unit, Tectonic Wedge Complex and Phyllitic complex. This low resistivity value in this region of metamorphic rocks has been justified by the presence of high resistive layers alternated to very conductive layers (possibly due to graphite, Santilano 2017) and confirmed by surface-hole ERT (Capozzoli et al. 2016). The main deep structures are the high-resistivity bodies of about 1000 Ωm below sites from *LS3* to *LS5* and from *LS10* to *LS14* at a depth from 4 to 8 km. They could be associated to the Pliocene granite and the gneiss unit (Romagnoli et al. 2010). At about the same depth, the large conductive region below sites from *LS5* to *LS10* is associated with the deep geothermal reservoir, that in the Lago Boracifero area lies below the K-horizon. This anomaly has been interpreted as belonging to a deep 3D conductive structure elongated N30E (Santilano 2017).

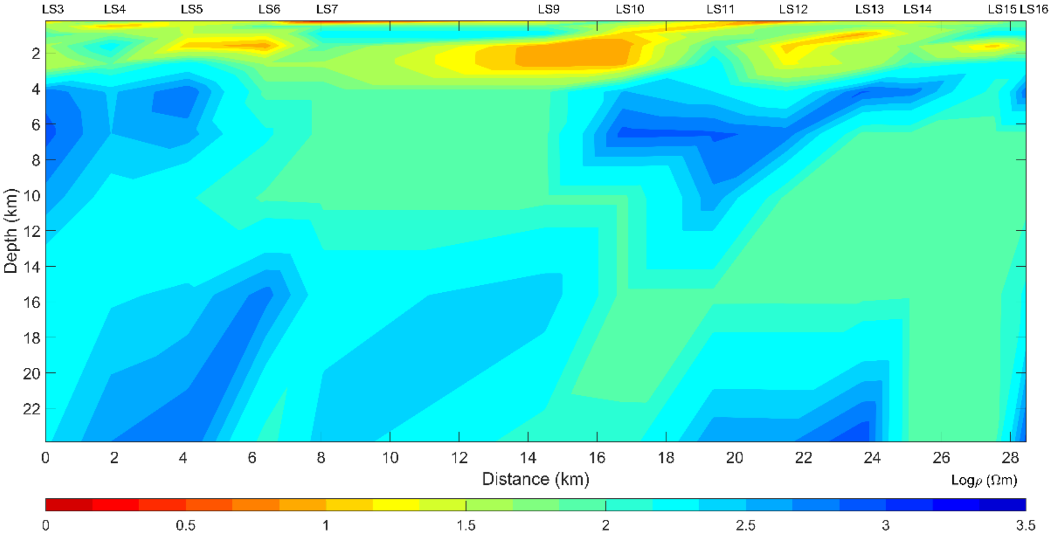

Figure 6.5 The 2D resistivity model of "LS" profile from PSO computation, after 1626 iterations and random initialization of the model.

Figure 6.6 and Figure 6.7 show the fitting curves between observed data and calculated response for apparent resistivity (ρ_{app}) and impedance phase for transverse-electric (TE) and transverse-magnetic (TM) polarizations. Two periods were selected according to their satisfactory matching: 0.02 s and 0.2 s.

Generally speaking, our result is consistent with the 2D resistivity models of previous interpretations (Santilano 2017; Santilano et al. 2015b; Fiordelisi et al. 1998). The advantage of our method was that the modelling was not initially constrained by an external starting model. The relevant improvement was that the final RMSE was lower than those of the previous models. In fact, in Santilano (2017), the inversion was constrained by an initial geological model and the final RMSE was 6.69 (5% error floor for apparent resistivity and phase). In Santilano et al. (2015b), the inversion started from a homogeneous starting model and ended with an RMSE of 4.68 (5% error floor for apparent resistivity and 2% for phase).

Our result can be compared with the geophysical interpretation of seismic tomography by De Matteis et al. (2008). In that work, they presented the cross-section of the ratio between P- and S-wave velocities (v_p / v_s) for a seismic profile whose orientation and extension were similar to our "LS" profile. The ratio v_p / v_s assumed a maximum value around 2 in an 8-km-large region at a depth between 3 and 7 km, fairly corresponding to the conductive anomaly below sites *LS5-LS10* in Figure 6.5. The lateral high-resistivity structures at the same depth compare well with the regions characterized by a v_p / v_s anomaly (≈ 1.3-1.5) and associated to the presence of steam-bearing formations or steam saturation.

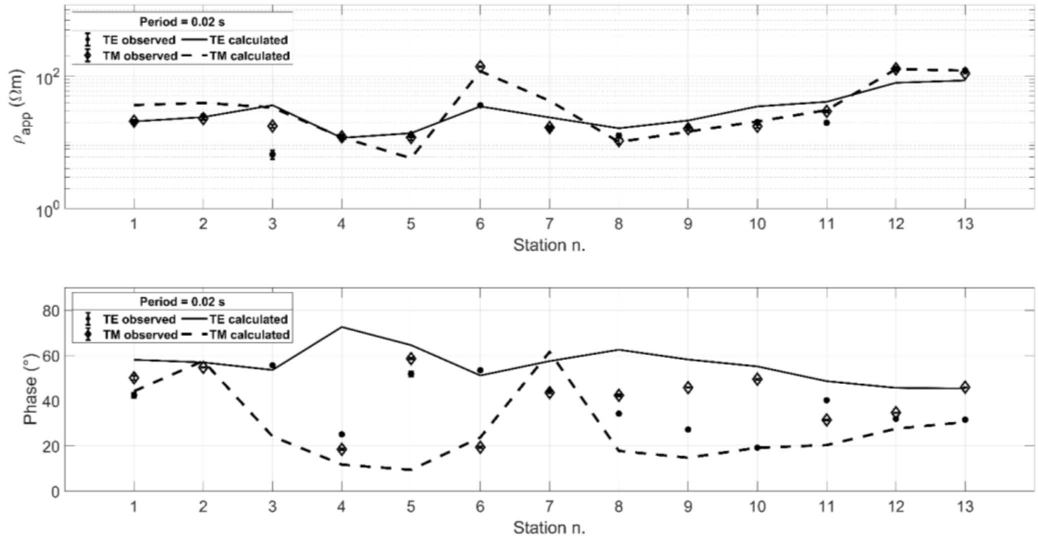

Figure 6.6 Data fitting for TE and TM apparent resistivity (ρ_{app}) and phase at selected period 0.02 s for the 13 MT sites of "LS" profile.

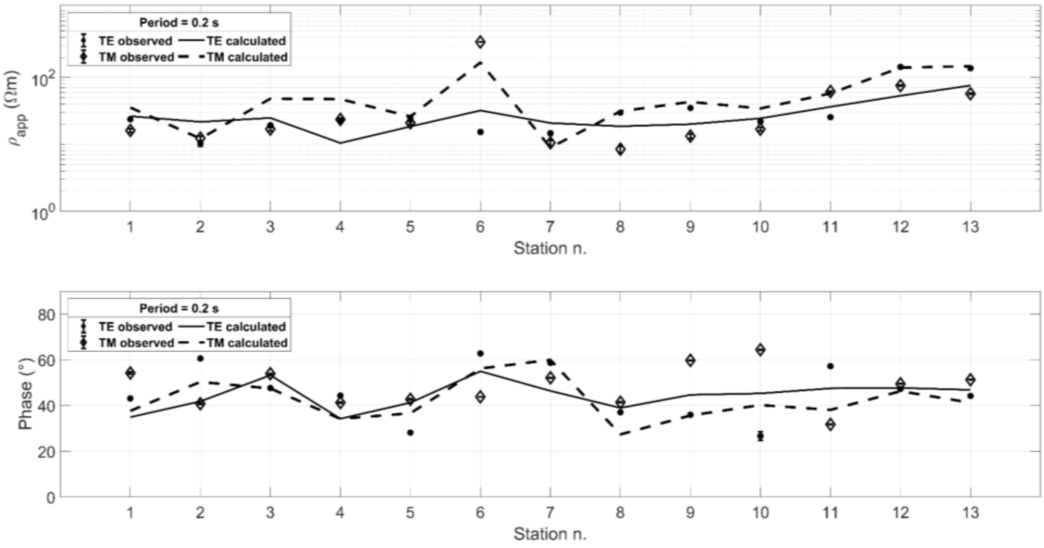

Figure 6.7 Data fitting for TE and TM apparent resistivity (ρ_{app}) and phase at selected period 0.2 s for the 13 MT sites of "LS" profile.

6.2.2 The model from the "Travale" profile

The period range of the data was between 0.003 s and 993 s. The data were perturbed with random error up to 10%. The 2D mesh of the model was discretized to logarithmically increase towards the boundaries, with a total of 375 cells. The PSO input arguments were set as follows: the number of particles (i.e., the solutions explored) was 3400; the optimal Lagrange multiplier λ was 0.01 for both the horizontal and vertical directions; the boundaries of the search space of solutions were 0.1 Ωm and 10000 Ωm.

The resistivity model resulting from PSO after about 4000 iterations is shown in Figure 6.8. The resistivity distribution of the subsurface presents a shallow conductive area below sites *g2-a8*, in line with the geology of the area (sedimentary deposits according to Romagnoli et al. 2010). In the first kilometer of depth below sites *k4-j0*, a high-resistivity region is imaged and justified by the formations of the Tuscan Nappe. From 2 to 5 km of depth in the central part of the 2D model a large body of about 1000 Ωm was identified. This body is coherent with the geological information because of the presence of granite (see Figure 5.6) and supports the model of Manzella et al. (2006) in Figure 5.9. The only evident difference is that in the PSO model the deep resistive body does not result laterally continuous. A possible reason may be the presence of trans-current faults conveying the geothermal fluid. In fact, the geological information overlapping the model of Figure 5.9 reveals the presence of faults between sites *k3* and *k4* and between *e4* and *c7*. (These faults can be also appreciated from Figure 2 in Manzella et al. (2006) and from Figure 9 in Sani et al. (2016)). Another possible reason for the lateral discontinuity of the deep resistive body in the PSO model can be the random initialization of the stochastic inverse modeling, because the horizontally-layered geological model given as a priori in the inversion of Manzella et al. (2006) definitely affected (and probably biased) the final inversion model. Further comments on this result will be reported in the next chapter, together with the findings from the 3D MT inversion of the Travale data set.

The final PSO model in Figure 6.8 is associated to an RMSE of 4.18. Details of the fitting between observed and calculated data are plotted in Figure 6.9 and Figure 6.10 for apparent resistivity (ρ_{app}) and phase of transverse-electric (TE) and transverse-magnetic (TM) polarizations. The data fitting was not ideal for apparent resistivity of stations 8-11 (i.e., sites *f4*, *e4*, *c7*, *a8*), but the matching was satisfactory for the other sites at both low (Figure 6.9) and high periods (Figure 6.10).

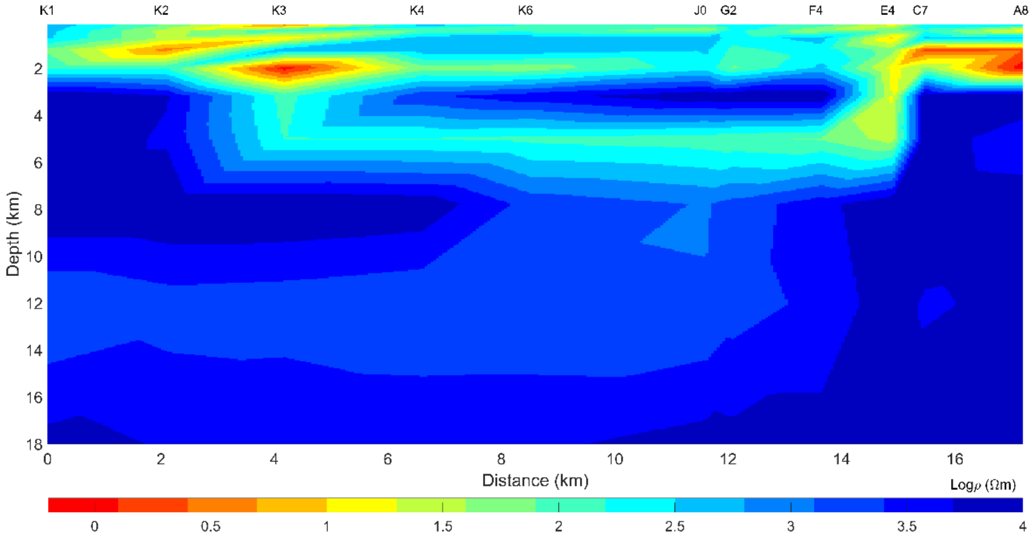

Figure 6.8 The 2D resistivity model of "Travale" profile from PSO computation, after 4000 iterations and random initialization of the model.

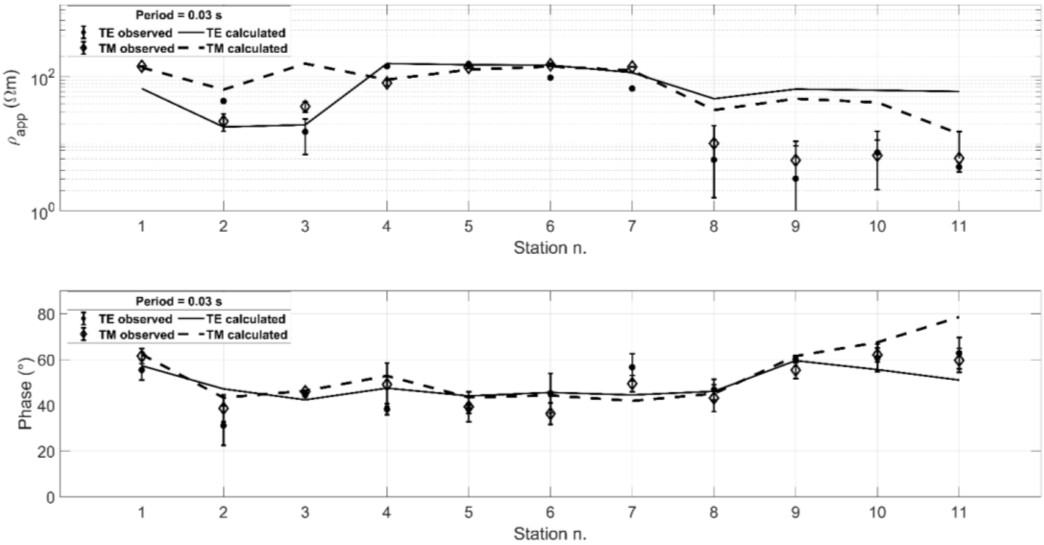

Figure 6.9 Data fitting for TE and TM apparent resistivity (ρ_{app}) and phase at selected period 0.03 s for the 11 MT sites of "Travale" profile.

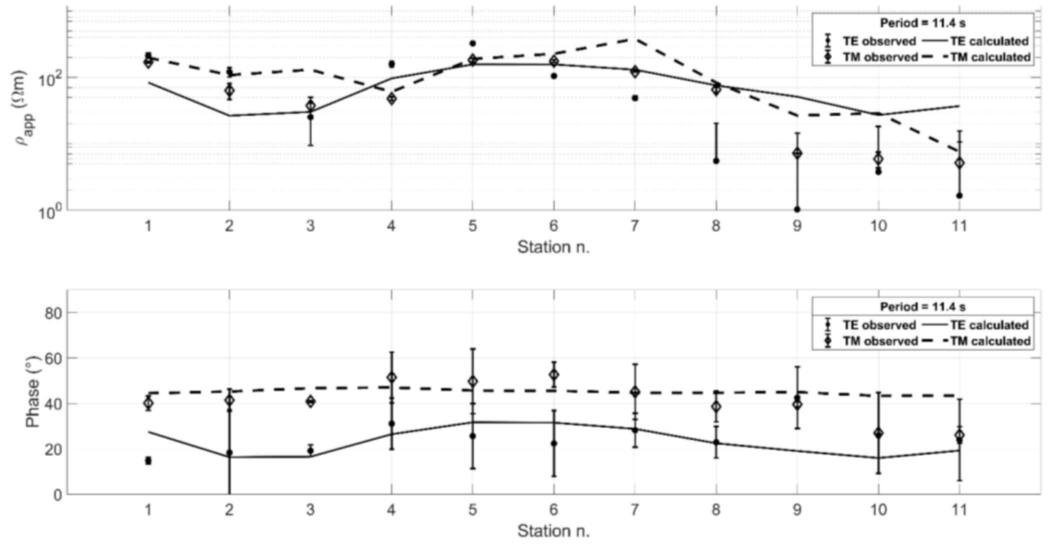

Figure 6.10 Data fitting for TE and TM apparent resistivity (ρ_{app}) and phase at selected period 11.4 s for the 11 MT sites of "Travale" profile.

6.3. Final considerations

The PSO algorithm was adopted for the 2D stochastic inverse modelling of two MT profiles located in the Larderello-Travale geothermal area. This kind of field data set was 2D interpreted for the first time using a metaheuristic method. The final models imaged resistivity structures similar to those presented in previous research, but some advantages emerge from the application of PSO:

1. Differently from previous interpretations, the modelling was not initially biased by an external starting model derived from geology (see Santilano (2015b, 2017) for the "LS" profile and Manzella et al. (2006) for the "Travale" profile)
2. The stochastic approach was beneficial to improve the data fitting. For both the case studies, the final RMSE associated to the final PSO model was lower than those associated to the models obtained in the past using derivative-based inversion techniques (Santilano et al. 2015b; Santilano 2017; Manzella et al. 2006; Manzella et al. 2010)
3. Although sometimes the data fitting was not ideal, our outcome can be appreciated in detail thanks to the graphs showing the fitting between observed data and calculated response (Figure 6.6, Figure 6.7, Figure 6.9 and Figure 6.10). This level of insight was not available for the previously cited works reporting the 2D inverted models.

The application of PSO to solve the 2D MT inverse problem has proven to be a valid tool for the investigation of very complex electrical structures. A novel and broad characterization of the Travale geothermal system will emerge from the 3D MT inversion presented in the next chapter.

Chapter 7

3D MT inversion of the Travale data set

The 3D resistivity model is derived from pure 3D MT inversion and provides new insight into the geoelectrical structures of the Travale geothermal field. No work to date has focused on the 3D MT characterization of the Travale geothermal system. The main objective is to enlighten some debated issues by taking advantage of the information obtained from the full MT impedance tensor and the vertical magnetic transfer function (i.e. Tipper).

This chapter is based on the manuscript recently submitted to the journal *Surveys in geophysics* with the title: “Three-dimensional magnetotelluric characterization of the Travale geothermal field (Italy)” (Pace et al. submitted).

7.1. Preliminary considerations

The geoelectrical dimensionality and strike direction of the MT data set was discussed in Chapter 5, where phase tensor analysis was performed to ensure a complete understanding of the data. Static shift was corrected through new TDEM measurements (Appendix C, Figure 5.21 and Figure 5.22). So far, the MT data from the Travale geothermal area have been 2D interpreted by means of NLCG inversion (Manzella et al. 2006) and stochastic inverse modeling (Chapter 6; Pace et al. 2019c and 2019d). However, the detailed analysis carried out in Chapter 5 proved that, although a 2D strike direction around N130°E could be considered as a “first approach”, the most appropriated interpretation of our data needs for 3D MT inversion.

The MT data set acquired in 2004 was selected for 3D inversion because of low level of noise, coherence of the frequency band and regular spatial distribution of the site locations (see Appendix B and Figure 5.14). Sites *k1*, *k2*, *k3* and *k4* were not included in the 3D inversion because they strictly belong to the

2D profile and would have corrupted the 3D modeling and meshing. Therefore, the final data set addressed to the inversion was composed of 51 sites, which are depicted in Figure 7.1 on the geological map. The data acquisition included a period range between 0.003 and 993 s, originally discretized into 75 values, then resampled in 20 values to unburden the time-consuming 3D computation.

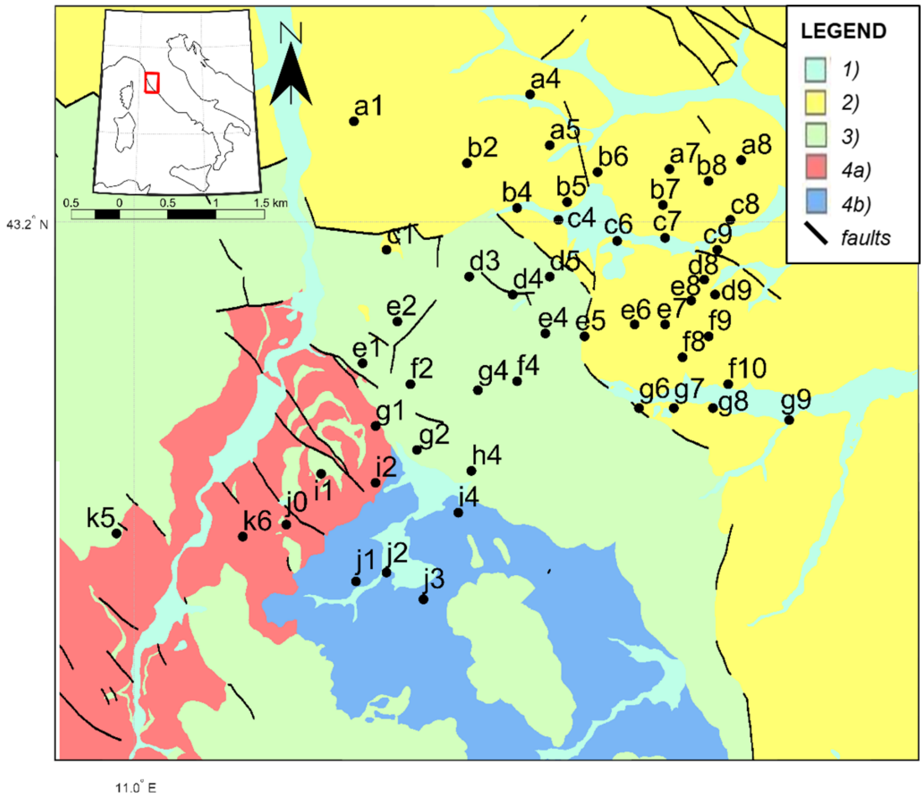

Figure 7.1 Geological map of the area of study: 1) Quaternary deposits, 2) Neoautochthonous terrigenous deposits, 3) Ligurian and sub-ligurian flysch complex, 4a) Tuscan nappe sediments, 4b) Tuscan nappe carbonates. The black dots are the 51 MT sites included in 3D inversion. The thick black curves are the main faults and normal faults (source: Geoportale Geoscopio web site).

The 3D inversion was computed using the ModEM software, which is available for the EM research community (Egbert and Kelbert 2012; Kelbert et al. 2014). Both the inversion settings and the result analysis were arranged in 3D-GRID Academic, a supporting tool kindly provided by prof. N. Meqbel for research purposes. The inversion scheme of ModEM is based on NLCG and the objective function minimizes both the data misfit and model roughness penalizing the deviations from the starting model. Being the inverse problem over-parametrized, the choice of the smoothing factor as well as of the starting model is crucial to obtain a valid outcome (Tietze and Ritter 2013).

Finding a proper numerical solution of the 3D MT inverse problem is not an easy task for several reasons: the inverse problem is ill-posed with nonlinear and extremely sensitive solutions, the choice of the stabilizing functional is critical for the obtained solution (since it accounts for smoothness and/or a priori information), the 3D forward routine must be fast and accurate, the intensive computational load (thousands of data to be inverted and tens of thousands of model parameters) makes necessary to run the computation on HPC clusters (Avdeev 2005; Siripunvaraporn 2012).

The preliminary inversion tests of this work were executed on the 32-core workstation in the Department of Geodynamics and Geophysics of the University of Barcelona, during the research period spent there in spring 2019. The last simulations were executed using 72 cores (3 nodes) of the HPC cluster of Politecnico di Torino. The CPU model of the single node was an Intel Xeon E5-2680 v3 2.50 GHz (turbo 3.3 GHz) with 3.6 TB (DDR4) of RAM. When the runs were computed, the sustained performance of the HPC cluster was 20.13 TFLOPS.

7.2. 3D MT modeling and inversion

The 3D mesh was prepared in the software package 3D-GRID (kindly provided by prof. N. Meqbel). The domain is depicted in Figure 7.2. It was 200 km large and around 350 km deep, consistently with the boundary conditions and the electromagnetic skin depth. The mesh included the topography and bathymetry and the resistivity of the sea was fixed to 0.3 Ωm. Along the horizontal directions, the model mesh was discretized into 100 x 100 cells, whose size was constant (191 m) for the central 58 x 58 cells and linearly increasing by a factor of 1.25 for the external cells (21 planes for each lateral side towards the boundary of the domain). The vertical direction was discretized into 75 layers, whose thickness was 100 m from the air layers up to 3000 m of depth, then increasing by a factor of 1.15.

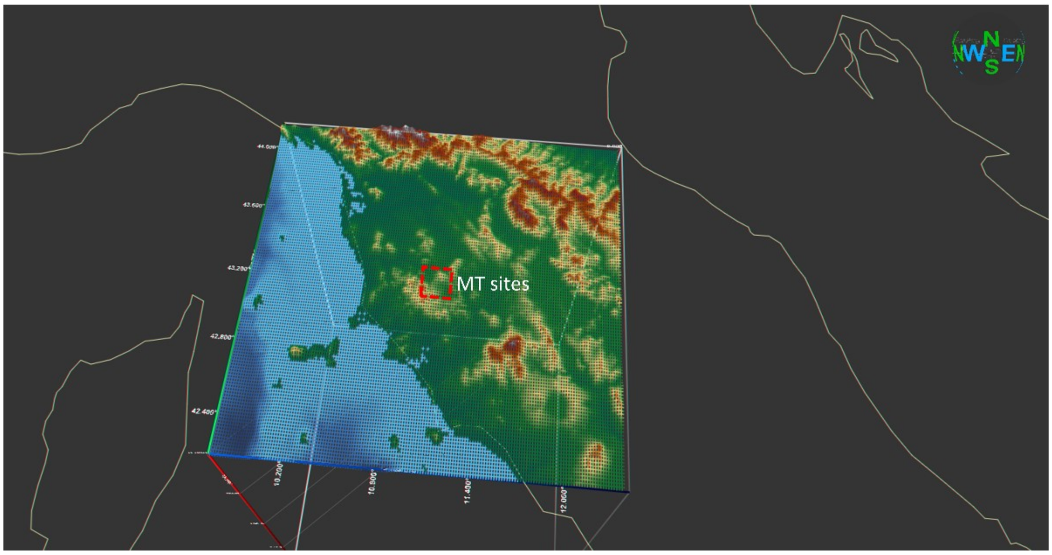

Figure 7.2 The 3D model is 200 x 200 km large and 350 km deep. The mesh included the topography and bathymetry. The figure was created in 3D-GRID Academic.

The starting model that initialized the inversion was a homogeneous body of 100 Ωm, because it gave the minimum initial RMSE compared to other resistivity values. We also performed a further inversion test with an a priori starting model derived from the 2D inversion result of Manzella et al. (2006). That SW-NE profile was orthogonal to the Radicondoli Basin and to the strike direction plotted in Figure 5.18. The essential feature of that 2D model was an elongated high-resistivity body (around 800 Ωm) at a depth of 3-6 km b.s.l. within the metamorphic basement. This body represented the key factor to setup our a priori model for 3D inversion. The a priori model had a 500-Ωm body buried in a 100-Ωm domain below sites from *k5* to *a8* at a depth from 3 to 7 km. The main reason of this choice came from the observation of preliminary 3D inversion tests: the final models presented many superficial structures, but the model heterogeneity disappeared with depth. Therefore, the 3D discontinuity of the a priori model was located below 3 km of depth in order to prevent the strong bias given by specific superficial features of a local solution.

The smoothing factor controls the model regularization along the three dimensions. Its choice was as critical as that of the starting model because of the over-parametrization of the inverse problem that can lead to different outcomes. After some trials, we set 0.2 as smoothing factor for the horizontal directions and 0.1 for the vertical direction, in order to emphasize the vertical contrasts among the deep structures. When the inversion was initialized by the a priori starting model, the smoothing factors were increased to 0.5 and 0.4, respectively. The main reason was evident after some tests on the regularization terms: the inversion required high smoothing factors to enable slight adjustments of the a priori-given 3D contrasts.

The inversions were performed using two different coordinate systems. The first coordinate system presented the x-axis aligned with the geographic North (N0°), as usually set for 3D modeling. The second coordinate system (N130°E) was aligned with the geoelectrical strike (i.e., x-axis parallel to the strike) in order to consider the a priori model coming from 2D interpretation. Even though the coherence between the strike direction and the rotation of the model mesh and data is fundamental in 2D modeling, it has turned out to be critical in 3D modeling as well (Tietze and Ritter 2013; Kiyan et al. 2014). Tietze and Ritter (2013) demonstrated that the 3D inversion result is not independent from the coordinate system and recommended a strike-oriented model mesh since it mostly minimizes the coupling among the four components of the impedance tensor (which, in ModEM, are handled independently). The MT tensors were rotated accordingly to the coordinate system, that is, 0° in the case of geographic coordinate system (N0°) and N50°W in the case of strike-oriented model mesh (N130°E).

We inverted all the components of the impedance tensor ($\underline{Z}$) because, in a 3D environment, the information about the subsurface resistivity distribution is included in all the tensor elements, which can improve the spatial resolution. In addition, the inversion of the vertical transfer function (the Tipper ***T***) was included to improve the sensitivity at depth and to seek out lateral constraints (Čuma et al. 2017). After evaluating the quality of our data for the inversion, we selected 24 out of 26 sites with Tipper. We explored both the separate inversions of $\underline{Z}$ and ***T*** and the full inversion of both $\underline{Z}$ and ***T***.

The error floor was set as portion of the absolute value of the impedance components ($|Z_{ij}|$) instead of as a portion of the mean of the off-diagonal components ($|Z_{xy} \cdot Z_{xy}|^{0.5}$), because the mean value could have underestimated one component of the tensor with respect to the other ones (Tietze and Ritter 2013). Since the original errors of the data were not negligible, we set an error floor of 10% for the off-diagonal components of $\underline{Z}$ and of 15% for the on-diagonal components $\underline{Z}$, which presented relatively high magnitude. The error floor of the Tipper components was assigned following Gabàs and Marcuello (2003), that is, equal to the error associated to the logarithm of the apparent resistivity, i.e., 10%. For the separate inversions of $\underline{Z}$ and ***T***, the error floor was decreased in order to amplify the information stored in the tensor. In fact, it is known from the literature that, if the signal-to-noise ratio increases, the inversion performance is expected to improve (Newman et al. 2008). In the separate inversions of $\underline{Z}$ and ***T***, the error floor was 5% for the off-diagonal components of $\underline{Z}$ and for ***T*** and 10% for the diagonal components of $\underline{Z}$.

A summary of the performed inversion tests is given in Table 7.1.

7.3. Inversion result

For the first time, to the authors' knowledge, this work presents a 3D inversion resistivity model of the Travale geothermal system. The 3D inversion of MT data offered new insight into the electrical resistivity distribution in the subsurface of the Travale geothermal field.

The choice of different settings to drive the inversion regarded the starting model, the smoothing factors, mesh orientation and error floors. These settings were chosen following the most recent literature findings but also adapted to our specific data set.

An overview of the settings for the performed inversion tests is listed in Table 7.1. Inversion tests A-D inverted both the full $\underline{Z}$ and ***T***, inversion E included only full $\underline{Z}$ and test F only ***T***. Excepting inversion test A, based on the geographic coordinate system, all the inversions were performed using the strike-aligned mesh (N130°E). Inversion test C was the only test adopting the a priori starting model and higher smoothing factors, whereas all the other inversions assumed a homogeneous starting model. The error floor of inversions D, E and F was 5% lower than that of inversions A, B and C.

Taken together, the final models led to good data fitting, as proved by the normalized RMSEs in Table 7.1. The inversions of full $\underline{Z}$ and ***T*** (tests A, B and C) always ended with an RMSE lower than 2. There was a slight increasing of RMSE in test B compared with test A, being the rotation of the grid the only difference for inversion. The decrease of the error floor in tests D, E and F resulted in a slight worsening of the RMSE.

The final resistivity models of the different tests were similar to each other. The following sections present the inversion result of tests A and D, as they both properly represented the geology of the area. The specific result of the other inversion tests listed in Table 7.1 is provided in Appendix E, in order to compare different grid rotations and error floors.

Table 7.1 The inversion tests performed on the MT data set of Travale. Inversion A had the coordinate system aligned with the geographic North (N0°). Inversions B-F had the strike-aligned mesh (N130°E). Inversion C was initialized with a priori starting model derived from the 2D model of Manzella et al. (2006). Inversions E and F separately inverted the impedance ($\underline{Z}$) and Tipper ($\boldsymbol{T}$) tensor, respectively.

	Inversion tests					
Settings	***A***	***B***	***C***	***D***	***E***	***F***
Grid rotation	N0°	N130°E	N130°E	N130°E	N130°E	N130°E
Tensor inverted	Z & T	Z & T	Z & T	Z & T	Z	T
Error floor Z_{xy}, Z_{yx}	10%	10%	10%	5%	5%	-
Error floor Z_{xx}, Z_{yy}	15%	15%	15%	10%	10%	-
Error floor T_{xz}, T_{yz}	10%	10%	10%	5%	-	5%
Starting model	homogeneous	homogeneous	a priori	homogeneous	homogeneous	homogeneous
Smoothing (x, y, z)	(0.2,0.2,0.1)	(0.2,0.2,0.1)	(0.5,0.5,0.4)	(0.2,0.2,0.1)	(0.2,0.2,0.1)	(0.2,0.2,0.1)
Final RMSE	1.62	1.72	1.95	2.79	3.14	2.22

7.3.1 Inversion of full Z and T with north-oriented grid (test A)

The 3D resistivity model obtained with the coordinate system aligned with the geographic North is shown in Figure 7.3, Figure 7.5 and Figure 7.6. Figure 7.3 presents the plain view of the resistivity distribution at four different depths: 78 m a.s.l., 222 m, 522 m and 4.7 km b.s.l. As expected from the induction arrow representation (Figure 5.17), the North-Eastern region is characterized by low conductivity values (< 10 Ωm), hereafter C1, and is elongated according to the strike direction. The resistivity in the southern region has a maximum of 800 Ωm and keeps a value much higher than the surroundings up to a depth of about 1.5 km b.s.l. This remarkable contrast, hereafter R1, is in line with the geological setting of the area, characterized by the carbonates of the Tuscan unit (see Figure 7.1). Figure 7.4 shows some vertical cross sections along the ZY and ZX plains (the traces of these sections are marked in the plain view of Figure 7.3b).

Figure 7.5 plots the SW-NE vertical cross-section corresponding to the MT profile investigated in Section 6.3. The most important feature required by long period data is a large 200-Ωm body, hereafter R2, imaged between 3 and 7 km of depth. This resistive body extends orthogonally to the strike direction, as emerged also from the plain view of Figure 7.3d.

The RMSE was 1.60 for $\underline{Z}$ and 1.72 for $\boldsymbol{T}$. The exact RMSE at each site normalized for the full period range is shown in Figure 7.6a-b, which plots the distribution of RMSE in the frequency–space domain for $\underline{Z}$ and $\boldsymbol{T}$, respectively. Considering only $\underline{Z}$, the majority of sites had a final RMSE lower than 2: the best data fitting resulted in site *c6* (RMSE = 1.01), while the worst one in site *g1* (RMSE = 4.94). For the data fitting of *T*, the worst RMSE was 3 for site c1, while the majority of sites resulted in an appreciable data fitting (RMSE < 2). Details of the fitting between the four-components of the observed impedance tensor and the calculated data are provided in Appendix D for all the 51 sites.

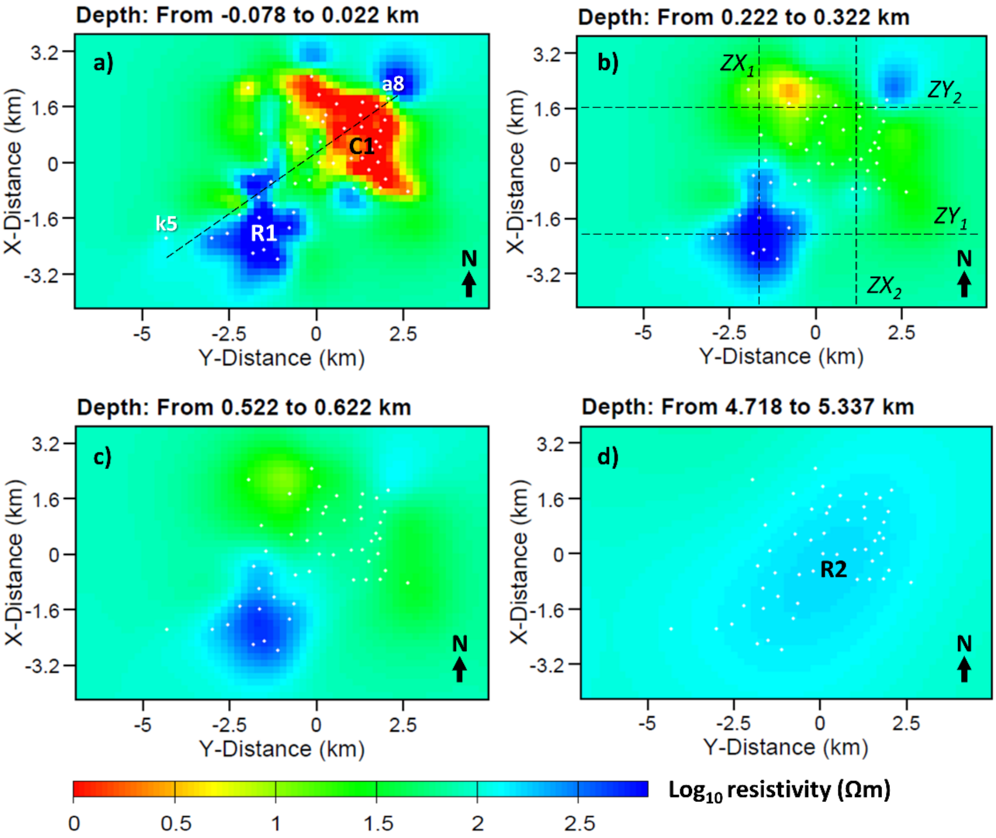

Figure 7.3 Plain view of the 3D resistivity model of test A at different depths: **a)** 78 m a.s.l., **b)** 222 m, **c)** 522 m, **d)** 4.7 km b.s.l. The x-axis of the mesh is aligned with the geographic North (N0°). The lines in **b)** are the vertical cross-sections shown in Figure 7.4. The black-dashed profile drawn in **a)** from site *k5* to *a8* is the cross-section reported in Figure 7.5.

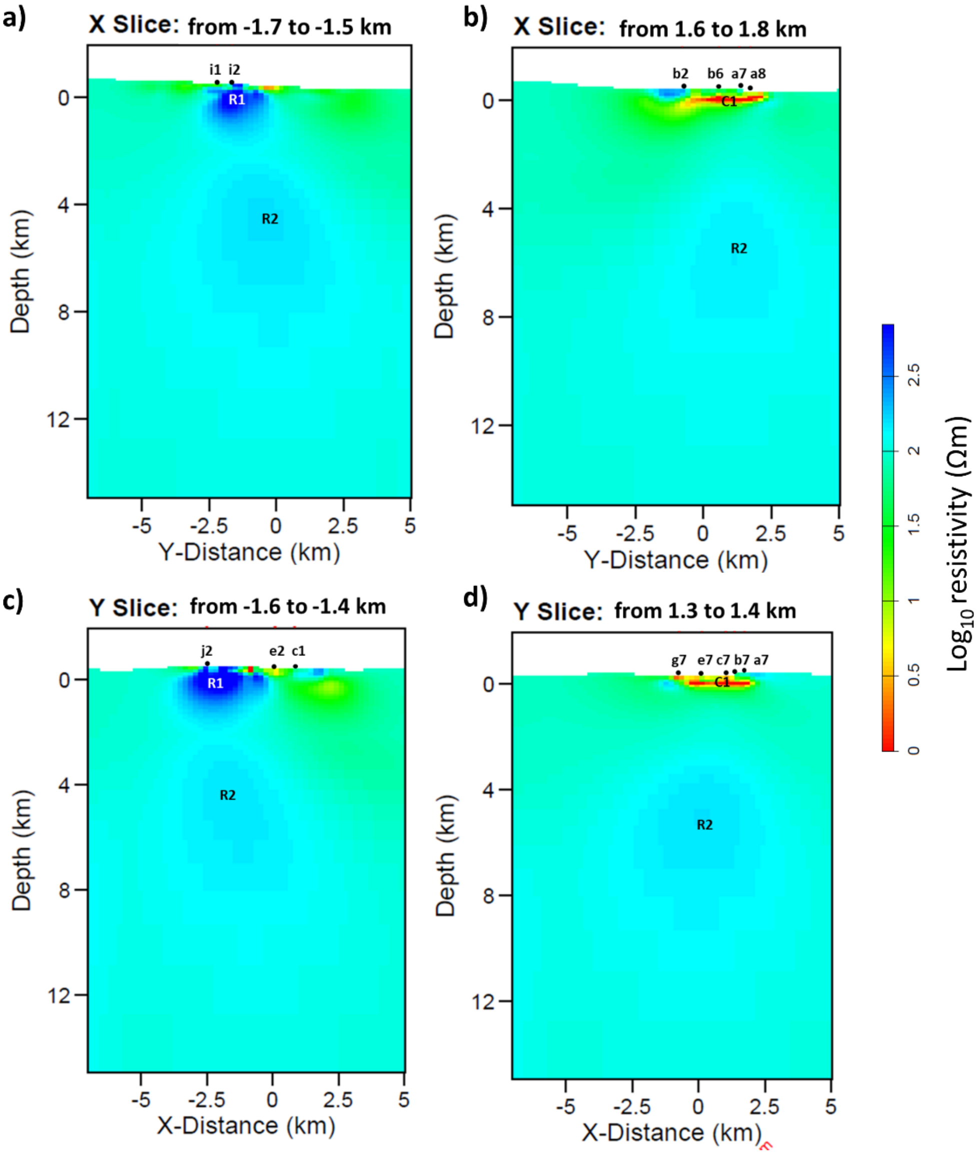

Figure 7.4 Vertical cross-sections of the model from test A: **a)** ZY_1 section at X=-1.7 km; **b)** ZY_2 section at X=1.6 km**; c)** ZX_1 section at Y=-1.6 km; **d)** ZX_2 section at Y=1.3 km.

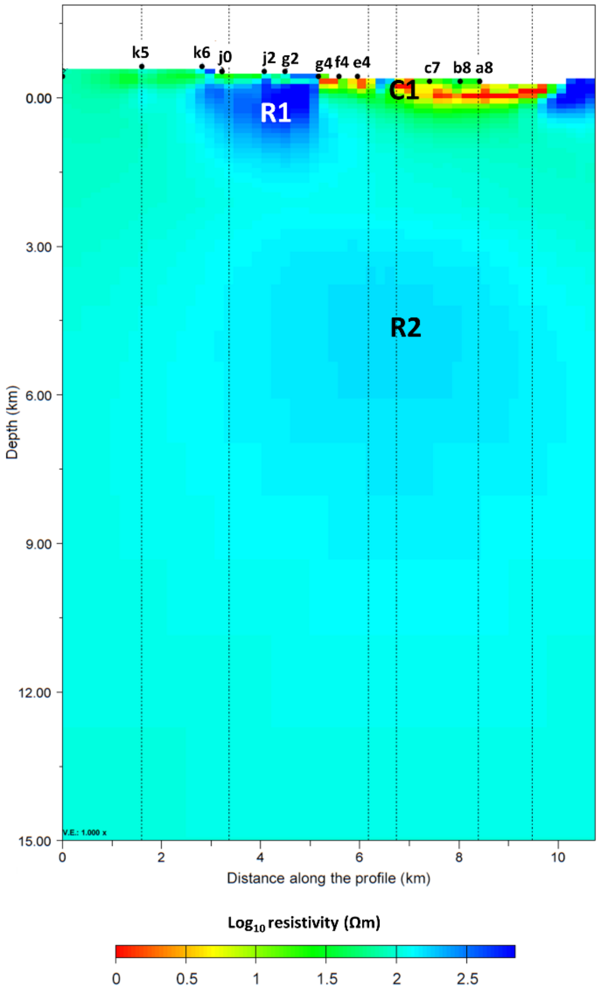

Figure 7.5 Vertical cross-section of the model from test A corresponding to the MT profile investigated in Section 6.3. The SW-NE profile is orthogonal to the strike direction and crosses sites from *k5* to *a8* (see Figure 7.3).

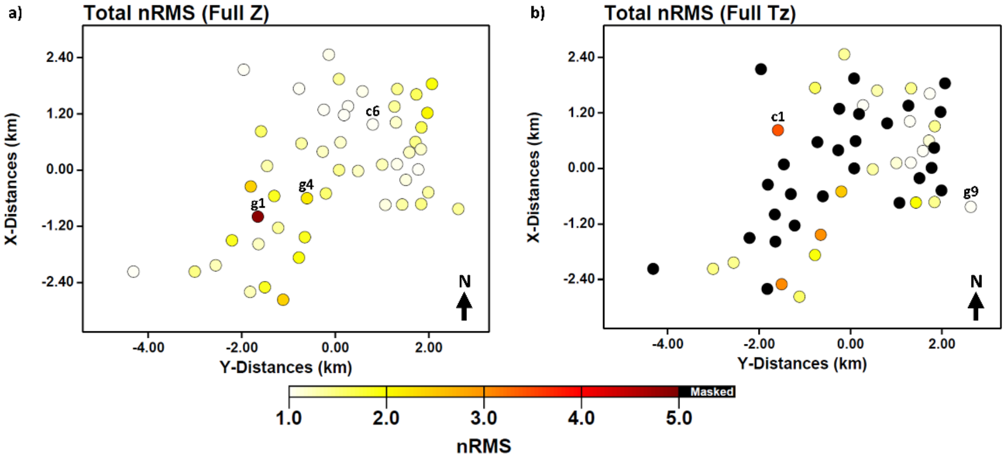

Figure 7.6 Distribution of RMSE at each site for test A **a)** Total normalized RMSE for the impedance tensor ($\underline{Z}$). **b)** Total normalized RMSE for the Tipper matrix (***T***). The black dots in **b)** mean no Tipper data. The errors are normalized for the full period range.

7.3.2 Inversion of full Z and T with strike-aligned mesh (test D)

This section reports the result of inversion test D (Table 7.1). Differently from test A, the coordinate system was aligned with the geoelectrical strike and the error floor for both $\underline{Z}$ and $\boldsymbol{T}$ was 5% lower than that of test A.

The key results are displayed as in the previous section. Figure 7.7 shows the resistivity distribution in the horizontal plain at four different depths: 78 m a.s.l., 222 m, 522 m and 4.7 km b.s.l. In the superficial structures (Figure 7.7a-b), there is a clear difference between the North-Eeastern conductive region C1 (< 10 Ωm) extending parallel to the x-axis and the south-western region where the resistivity rises by up to 1300 Ωm (R1 in left side of the subplots). At around 5 km of depth (Figure 7.7d), the resistive body R2 of around 250 Ωm elongates orthogonally to the strike (i.e., in parallel to the y-axis). Figure 7.8 shows some vertical cross sections along the ZY and ZX plains (the traces of these sections are marked in the plain view of Figure 7.7b).

The vertical cross-section depicted in Figure 7.9 is directly comparable with the 2D model in Section 6.3. It shows superficial features similar to those imaged from inversion test A (Figure 7.5). At a depth between 300 m and 1.5 km b.s.l., the area located in the central-eastern part of Figure 7.7b-c (sites *g4-a8* in Figure 7.9) imaged a mildly resistive region of about 100 Ωm. The most relevant feature at greater depth is the large resistive body R2 also visible in Figure 7.7d and Figure 7.8.

The data fitting was negatively affected by the low error-floor setting, as can be seen from Figure 7.10a-b. The final RMSE normalized for the full period bandwidth was 2.78 for $\underline{Z}$ and 2.91 for $\boldsymbol{T}$. The lowest RMSE for Z was measured in site *k5* (1.31) and for T in site *b8*. The worst RMSE resulted in site *g1* (9.2) for $\underline{Z}$ and in site *c1* for $\boldsymbol{T}$. The data fitting for all the sites is provided in Appendix D.

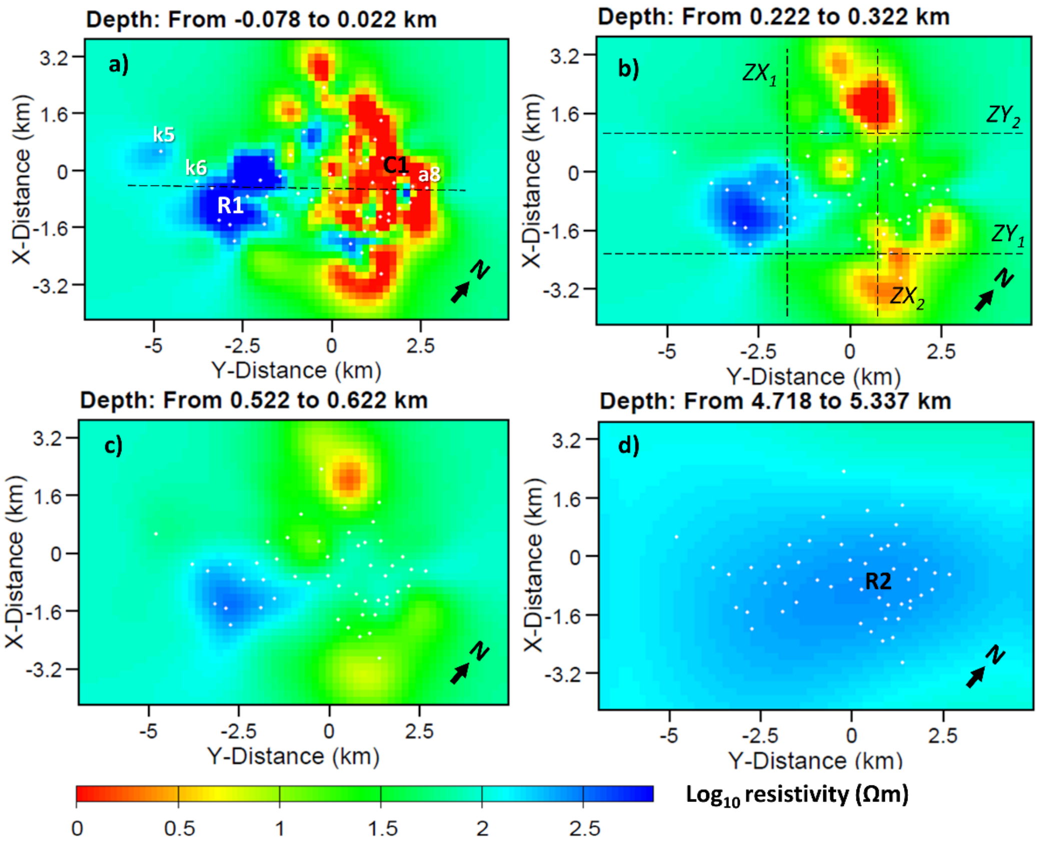

Figure 7.7 Plain view of the 3D resistivity model of test D at different depths: **a)** 78 m a.s.l., **b)** 222 m, **c)** 522 m, **d)** 4.7 km b.s.l. The mesh is aligned with the geoelectrical strike (N130°E), that is, the North is rotated 40° clockwise and the x-axis is parallel to the strike. The lines in **b)** are the vertical cross-sections shown in Figure 7.8. The black-dashed profile drawn in **a)** from site *k5* to *a8* is the cross-section reported in Figure 7.9.

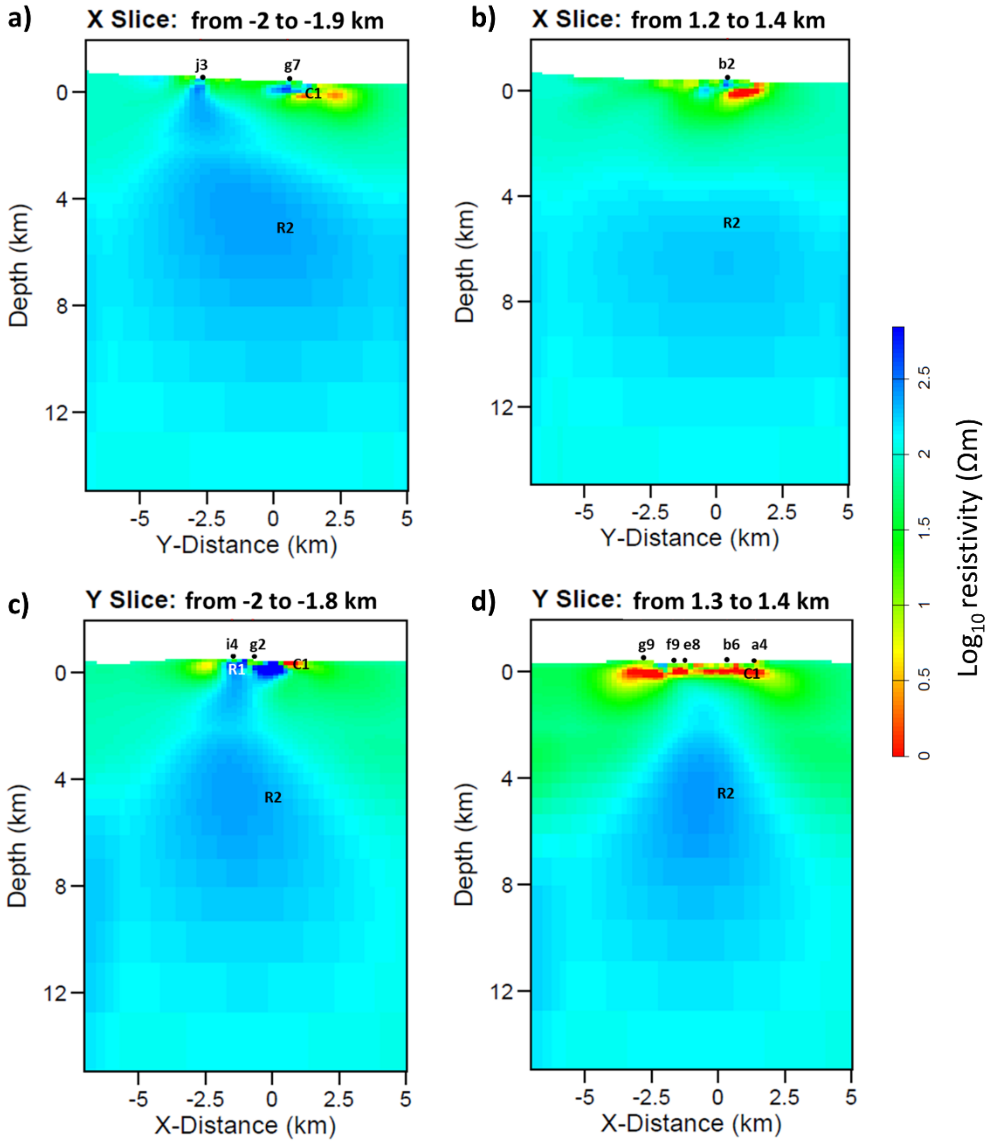

Figure 7.8 Vertical cross-sections of the model from test A: **a)** ZY_1 section at X=-2 km; **b)** ZY_2 section at X=1.2 km; **c)** ZX_1 section at Y=-2 km; **d)** ZX_2 section at Y=1.3 km.

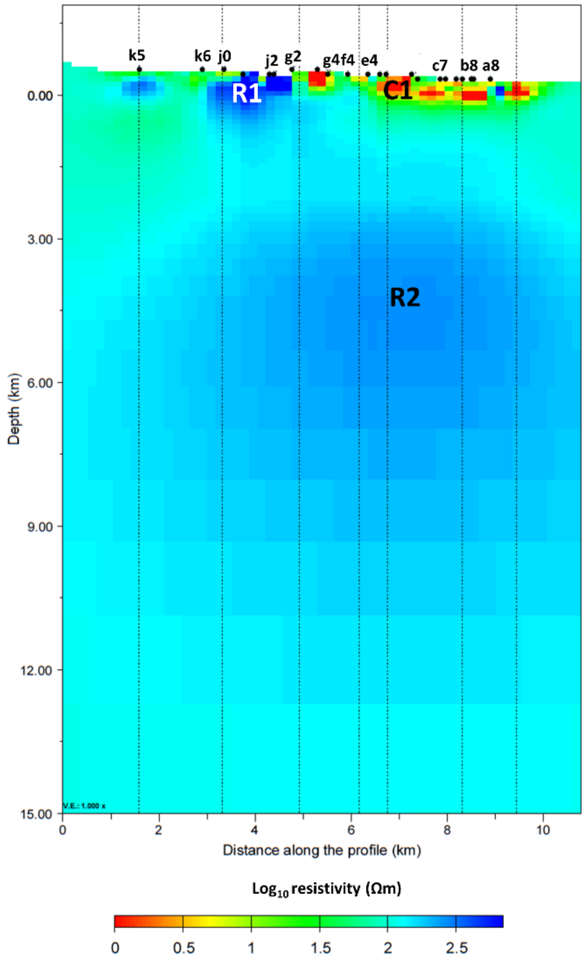

Figure 7.9 Vertical cross-section of the model from test D corresponding to the MT profile investigated in Section 6.3. The SW-NE profile is orthogonal to the strike direction and crosses sites from *k5* to *a8* (see Figure 7.6)

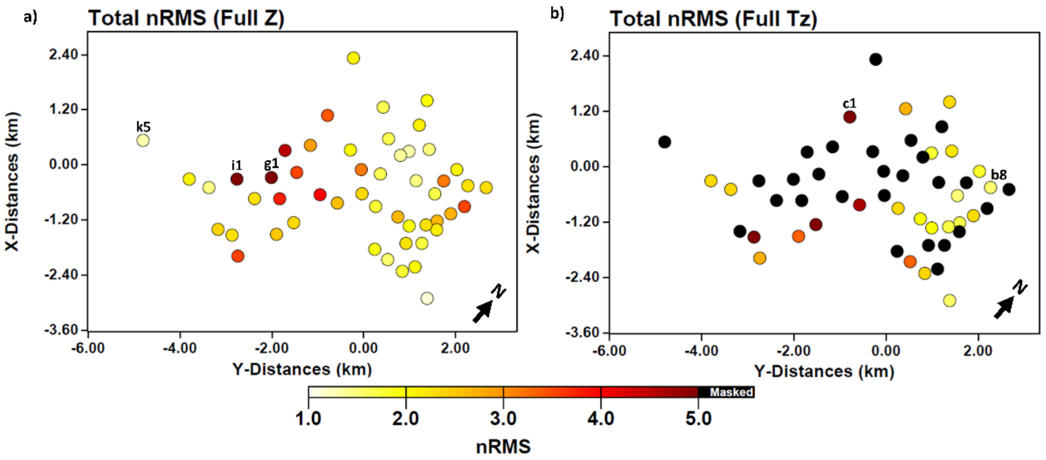

Figure 7.10 Distribution of RMSE at each site for test D resistivity model. **a)** Total normalized RMSE for the impedance tensor $\underline{Z}$ **b)** Total normalized RMSE for the Tipper matrix ($\boldsymbol{T}$). The black dots in **b)** mean no Tipper data. The errors are normalized for the full period

7.4. Discussion

The 3D resistivity model represents a fundamental contribution to the investigation of the Travale geothermal field, as previous MT studies only converged in a 2D characterization. We explored different inversion setups given that 3D inversion in geothermal areas is potentially challenging, mainly due to their complex geology. Inversion test D confirmed the main resistivity structures of test A, but the strike-aligned approach had the advantage of showing more clearly the features at high depth (compare Figure 7.3d with Figure 7.7d and Figure 7.5 with Figure 7.9).

Our result is consistent with the known geology of the Travale geothermal system. The xy-plain view of the resistivity distribution at shallow depth in Figure 7.3a and Figure 7.7a is in agreement with the expected resistivity of the outcropping rocks described in the geological map of Figure 7.1. The North-Eastern conductive area (C1) corresponds to the quaternary deposits and Neoautochthonous terrigenous deposits and was imaged up to a depth of 300 m b.s.l. The central mildly resistive area (10-50 Ωm) corresponds to the spatial coverage of the Ligurian and sub-ligurian flysch complex. Finally, the southern region R1, showing 800 Ωm in resistivity, matches the sediments and carbonates of the Tuscan Nappe. It should be noted, however, that the irregular space-covering of the sites may have influenced the shape of the imaged resistive structures, as can be seen in Figure 7.3 and Figure 7.7. Figure 7.3c-d and Figure 7.7c-d display the loss of resolution with depth, which can be explained by two main reasons. The first reason is related to the data set: around 20% of sites had no data above 10 s and the amplitudes of the on-diagonal and off-diagonal components of $\underline{Z}$ were similar at high period. The second reason regards the imaged shallow conductors (such as C1), which may have reduced the potential skin depth.

Interestingly, we found a resistivity contrast in correspondence to the bottom of the Neogene sediments of the Radicondoli basin and separating it from the underlying units piled in the chain. Figure 7.11 shows a North-South section of the model crossing sites *a4*, *b4*, *d4* and *f4*. The geological surface (in pink) was processed in Petrel environment from the findings of Casini et al. (2010) and represents the base of the Neogene sedimentary unit. To the North, below site *b4*, the basin-bottom surface descends to a depth of around 600 m b.s.l., where the resistivity jumps from 5 Ωm to 40 Ωm. This outcome represents a remarkable link between the resistivity contrast and the features of the geothermal system.

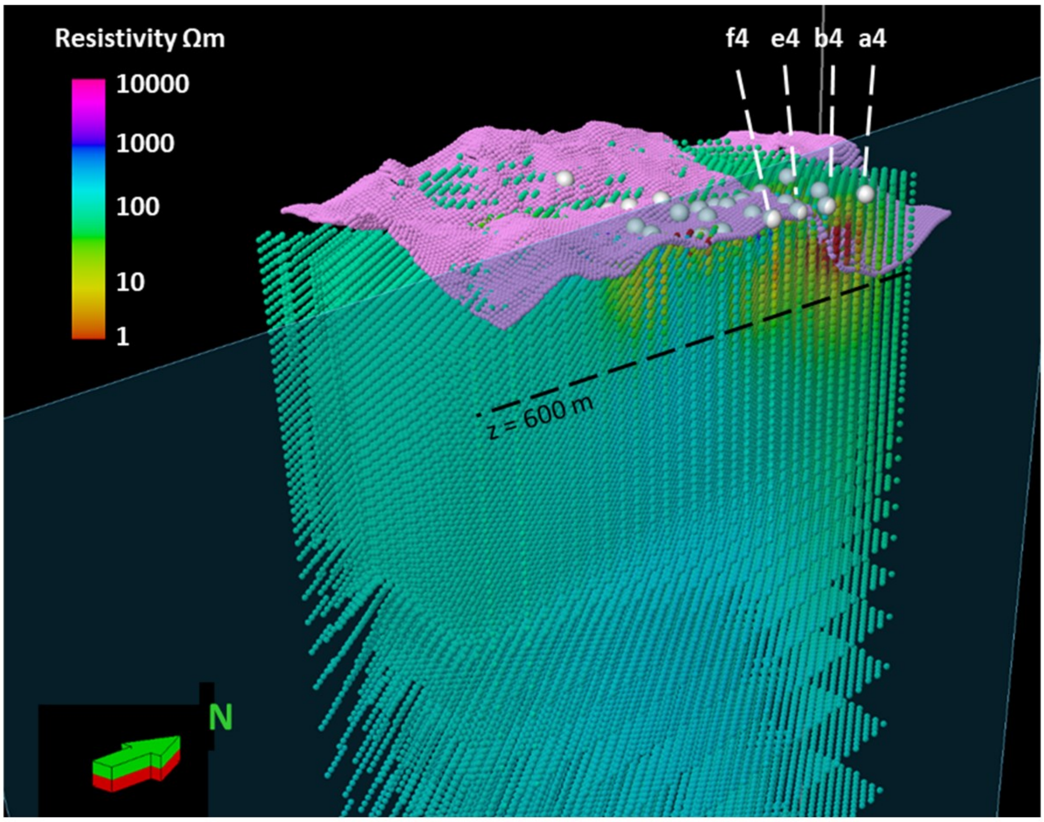

Figure 7.11 The 3D resistivity model of test D is compared with the pink surface corresponding to the base of the geological unit of Neogene (from Casini et al. 2010). The section goes North-South and crosses sites *a4, b4, e4* and *f4*.

The sections of the 3D model in Figure 7.5 and Figure 7.9 correspond to the profile investigated in Section 6.3 and in Manzella et al. (2006), except for 4 sites strictly belonging to the 2D line. The resistivity distribution of the 3D model is generally similar to that of the 2D model of Manzella et al. 2006 (Figure 5.9), but a few new features emerged from 3D inversion: the shallow structure R1 (up to 1.5 km b.s.l.) below sites *k6-g2* was far more resistive (800 Ωm); below sites *g4-a8* from 0 to around 3 km b.s.l. there was a moderately resistive region (100 Ωm) and not an anomaly; the resistive body R2 at 3-8 km b.s.l. had a different shape, boundaries and resistive value. The section from the 3D model can be also compared with the PSO result of Figure 6.8. The shallow resistive body below sites from *k6* to *g2* from 500 m to 1500 m of depth is in line with R1 in terms of resistivity value. Below sites from *e4* to *a8*, there is a highly conductive structure, but C1 is shallower than the body imaged in Figure 6.8. Finally, R2 from 3D inversion resulted deeper and larger than the deep resistive body in Figure 6.8. The 3D-inversion result overcame the main limitations of the 2D model, which might have missed some heterogeneities due to the adoption of a 2D approach for the inversion of 3D data. Moreover, the 2D model in Figure 5.9 could have been strongly biased by the a priori geological cross section used as starting model. Our results also provided the data fitting and RMS distribution, which have not been shown in previous works.

The deep resistive body (R2) of Figure 7.3d-Figure 7.5, Figure 7.7d-Figure 7.9 was imaged in all the inversion models and showed high resistivity (>200 Ωm) between 3 and 8 km of depth. Figure 7.12 displays the model of test D for selected resistivity values higher than 200 Ωm. The deep resistive body R2 is oriented orthogonally to the main strike direction. This can be justified because some of the soundings showed a strike direction of N40-50°E (Figure 5.19). Moreover, this orientation around N40°E is quite similar to that observed for the deep 3D structures imaged below the "Lago Boracifero" area in the adjacent Larderello geothermal field (Santilano 2017; Santilano et al. in preparation). The deep conductive anomaly in the Larderello field has been justified by the occurrence of mineral alteration processes and residually melted intrusions (Santilano 2017; Santilano et al. in preparation). Given the same spatial orientation, the deep structures differ in that the one in the Larderello field is low resistive (< 100 Ωm), while the one imaged in the Travale geothermal field is more resistive than the background (> 200 Ωm). The resistive nature of the deep body was actually not unexpected because it is hosted in a vapor-dominated system in correspondence to the granite units.

The orientation of R2 represents a major outcome in terms of interpretation for the knowledge improving of the Travale geothermal field. A strict relation between the strike-slip tectonics transversal to the Apennine direction and the deep magma emplacement or hydrothermal circulation was recently claimed by various studies (Acocella et al. 2006; Sani et al. 2016; Santilano et al. 2017; Santilano et al. in preparation; Liotta and Brogi 2020).

An interesting relationship can be inferred between our resistivity model and the seismic marker K-horizon. The bottom of R2 in Figure 7.12 was around 8 km deep, thus coinciding with the depth of the K-horizon, i.e., in Travale from 6 to 8 km (Romagnoli et al. 2010). This deep contrast and the seismic marker have been previously associated with a depth of around 5 km (Manzella et al. 2006), but our model highlighted a higher depth, in line with the recent updates on the K-horizon (Romagnoli et al. 2010).

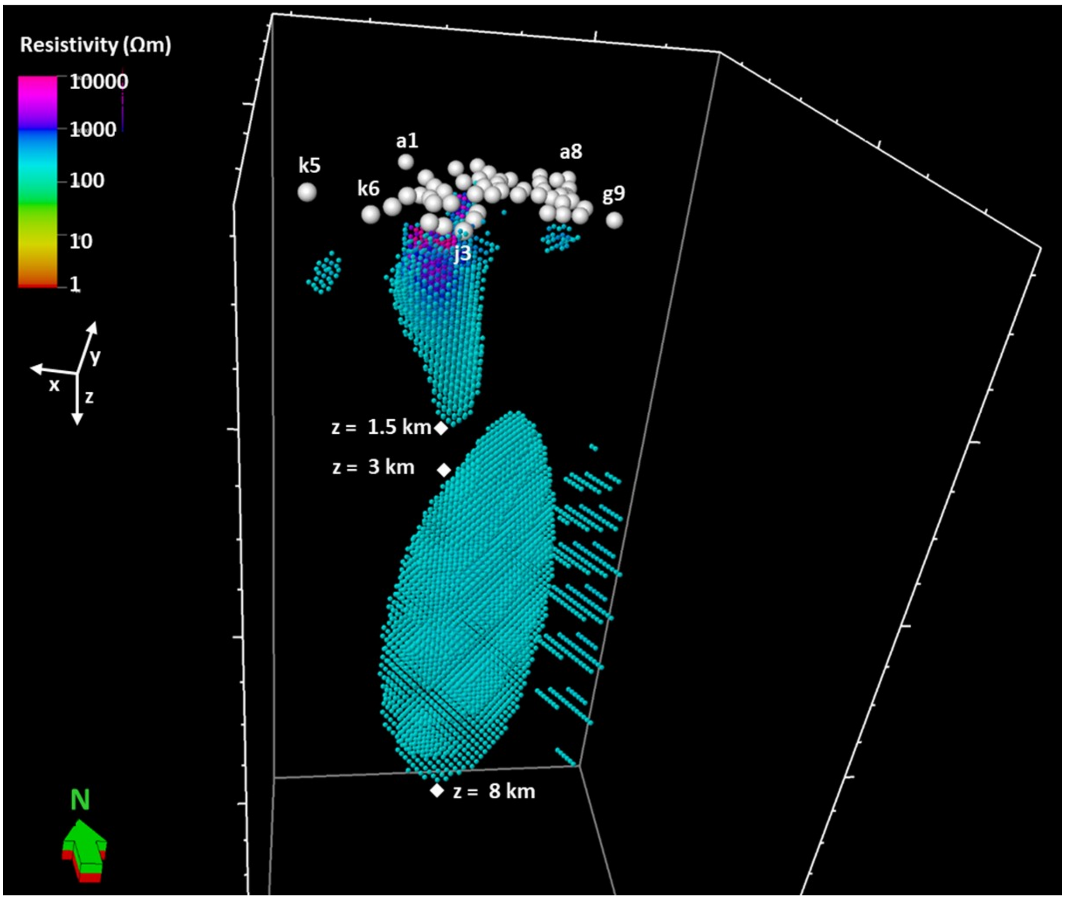

Figure 7.12 The 3D model of inversion test D displayed for selected resistivity values higher than 200 Ωm. The deep resistive body is imaged between 3 and 8 km of depth and is directed about N40°E. The white circles represent the MT sites.

In order to constrain the interpretation of the resistive body (R2) below the Travale-Radicondoli field, we compared the 3-D resistivity model with the 3-D local earthquake tomography of Bagagli et al. (2020) (see Figure 5.12). An impressive correspondence occurs between the resistive body R2 and the low-velocity body detected in the v_p images below the Travale area. The velocity model revealed a 5-km-wide low velocity body (v_p about 5 km/s) deeply rooted in the crust and bounded between the H- and K-horizons (at 3-7 km of depth). The similarity with our deep resistivity body is remarkable. Furthermore, that authors showed the occurrence of several hypocenters in correspondence of the anomalous volume. This implies the occurrence of fragile regime and rocks fracturing.

It should be noted that, in Bagagli et al. (2020), the orientation of the low velocity body seems different from that of the R2 body, even though some tests performed in Bagagli et al. (2020) showed a NE-SW trend at 7.5 km of depth (starting-model velocity of 6 km/s). The NE-SW orientation of R2 is largely supported by observing the map of the 3D v_p velocity model between 5 and 7 km of depth obtained by Vanorio et al. (2004) and De Matteis et al. (2008).

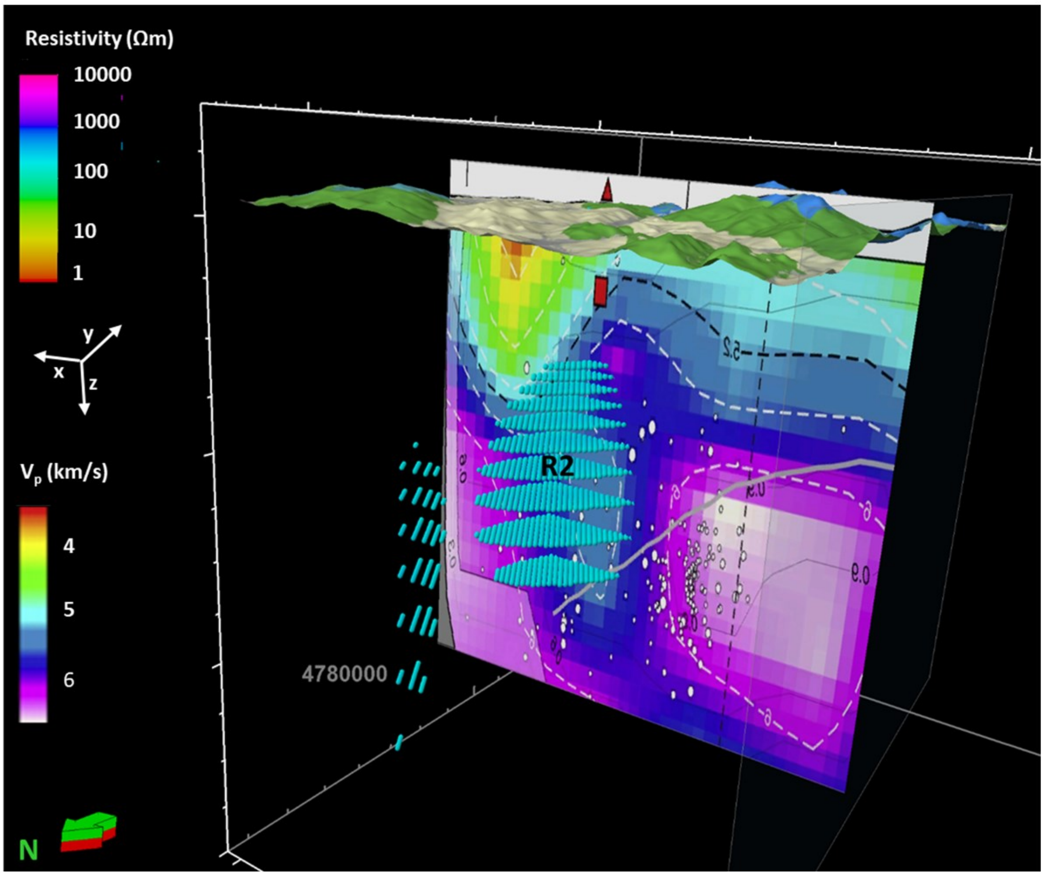

Figure 7.13 The resistive body (R2) from test-D inversion model is compared with the 3D velocity model from local earthquake tomography of Bagagli et al. (2020). The R2 body (> 200 Ωm) and the low-velocity body with v_p around 5 km/s are highly comparable and extend both between 3 and 7 km of depth.

In our opinion the R2 body can correspond to a highly fractured volume of crystalline rocks hosting a high-temperature hydrothermal circulation. The resistive nature of the deep body is explained with the vapor-dominated condition of the crystalline reservoir, i.e., highly resistive fluids circulating in highly restive rocks. Moreover, the results of the I-GET project proved the absence of pervasive alteration in the area of Travale by analyzing well cuttings and cores, which were suitable to decrease the bulk resistivity of the rocks (Giolito et al. 2009; Manzella et al. 2010). Our 3D model had scarce resolution below R2, but the general decrease in resistivity might be associated to the presence of the main heat source of the geothermal system.

The resistivity distribution of the inversion models can be correlated with the resistivity well-logs. Unfortunately, the database of the wells is not published except for the well log of *Radicondoli-7bis*, located south of sites *e4* and *e5* and shown in Figures 5.8, 5.11 and 5.13 (Giolito et al. 2009; Manzella et al. 2010; IMAGE final report). Giolito et al. (2009) reported the litho-stratigraphy, the resistivity well-log and the mean resistivity of the drilled formations of the well. The results of the IMAGE project (IMAGE D5.01; Santilano 2017; Santilano et al. in preparation) can lend support for the interpretation of the volume of rocks with about 100 Ωm at depth of about 800-2000 m embedded between the low-resistive cap-rock (C1) and the high-resistive body (R2) (see Figure 7.3c, Figure 7.5, Figure 7.7c and Figure 7.9). At this level, an extremely heterogeneous unit (Tectonic Wedge Complex) occurs with a very wide range of electrical resistivity (from 10^{-1} to 10^{4} Ωm), as measured from the geophysical well logs (such as the wells *Radicondoli 7bis* in Figure 5.13). This could have affected the measured EM signal, which provided an averaged resistivity of this geological unit (also confirmed by Surface-Hole ERT in the area of Larderello from Capozzoli et al. 2016). The reliability of this 100 Ωm volume of rocks in the 3D inversion model was confirmed by a sensitivity analysis performing forward calculation with perturbed resistivity models (example in Appendix E, Figure E.11).

Below 2300 m b.s.l., the well-log mean resistivity rises by up to around one order of magnitude in coincidence of the Phyllitic-Quartzitic Complex, micaschists and granite. This trend is largely comparable with the resistivity of R2 (Figure 7.5, Figure 7.9 and Figure 7.12). The significant variation of the acoustic impedance measured in the *Radicondoli-7bis* has been associated with a fractured zone at around 2500 m of depth b.s.l., in correspondence to the H-horizon and the productive levels of 13 geothermal wells (Casini et al. 2010).

7.5. Conclusion

We presented the first 3D resistivity model of the geothermal area of Travale (Italy) resulting from a complete 3D MT inversion. The MT data set was accurately analyzed in terms of geoelectrical dimensionality and the static shift was carefully corrected by means of recently-acquired TDEM soundings. A number of 3D inversion tests were performed by varying the grid rotation, error floor and initialization in order to assess the resistivity distribution of this complex and largely-investigated geothermal system.

The inversion model shed light on the 3D subsurface structures, thus extending previous knowledge of those structures, which so far have been interpreted only for a single MT profile. The validity of our result is supported by geological information, resistivity well-logs and seismic data. A distinct correlation emerged between the resistivity contrast at shallow depth and the geological surface of the base of the Neogene unit. At intermediate depth, about 800-2000 m b.s.l., the moderate resistivity (100 Ωm) may be interpreted as an average value of a heterogeneous geological unit composed of a wide range of lithology. The contribution of hydrothermal circulation is not recognizable at this level. A deep resistive body was imaged in agreement with the 2D model of previous literature but with new insight into its spatial extension and orientation. At a depth of 3-7 km, the resistivity was higher than 200 Ωm and the orientation N40-50°E. This high-resistive body corresponds to a low velocity body and can be interpreted as a highly-fractured volume of rocks with vapor-dominated circulation.

3D MT inversion was challenging due to the time-consuming computation which can involve 100 times more the unknowns of a 2D inversion. Furthermore, the framework of the geothermal system is still under debate. Our work offers the first 3D subsurface electrical distribution in the Travale area from a geophysical interpretation and can pave the way to further insight about the geothermal system.

Future work should broaden the MT characterization of the Travale area by means of new acquisition campaigns that would enlarge the investigated zone, ideally with a regular space-covering of the sites. The existing data set need to be enriched for all the sites with the acquisition of the geomagnetic transfer function, which is fundamental for 3D inversion. The integration of multiple geophysical data sets would also be beneficial for a comprehensive study of the geothermal system.

Chapter 8

Conclusions

This doctoral research was developed around two main cores with the MT method as common thread (Chapter 2). The first main core investigated a new method, based on computational swarm intelligence, to perform stochastic inverse modeling of both multiple geophysical data sets (Chapter 3) and 2D MT data (Chapter 4). The second core comprised the MT study of the Larderello-Travale geothermal area (Chapter 5) by means of PSO (Chapter 6) and 3D MT inversion (Chapter 7).

The initial purpose of the work was to extend the adoption of metaheuristic algorithms from 1D to 2D to solve the MT inverse problem. In fact, the state of the art of global search methods in MT is composed of a few 1D applications (Monte Carlo, PSO and GA) and a single 2D example (GA by Everett and Schulz, 1993). As well as this scientific gap in the methodology, metaheuristic methods were recognized to be effectively applied to the characterization of geothermal areas, where the geological complexity and the difficulty in retrieving reliable external constraints can negatively affect the solution of the inverse problem. A second aim of this study was to investigate the LTGA, where some geological, physical and thermo-dynamical aspects are still unclear or under debate, despite more than a century of scientific research. Furthermore, 3D MT inversion is currently an area of very intensive research and no work to date has focused on 3D inversion of MT data from the Travale geothermal area.

This thesis has proved that the PSO algorithm can be a valid method to solve the 2D inverse problem for both synthetic and field MT data sets. This work also presented a new MT characterization of the Travale geothermal system. Even though a new MT field campaign was not carried out, we recovered the MT data acquired in the geothermal area in the past to provide new interpretation in the light of new methodologies. The new MT inversion results were presented as 2D and 3D models, after stochastic inverse modeling and NLCG inversion, respectively. New TDEM data were acquired in 2019 to correct the MT static shift.

The main findings of this thesis are:

1. A new method for 2D MT *stochastic inverse modeling* has successfully been applied to synthetic and field data. Thus the application of PSO to MT inversion has been extended from the 1D problem, already visited in the literature, to the 2D problem. After validating the method on synthetic data of different complexity, it was applied to the benchmark for real-field MT data, the COPROD2 data set (Canada). The optimization of the COPROD2 data set provided a resistivity model of the Earth in line with results from previous interpretations. The stochastic nature of PSO and the combination of exploration and exploitation behaviors played a key role in finding the global minimum of the search space as final solution.
2. The standard release of the PSO code was not ideal to properly address the complexity of the 2D MT inverse problem, which entails hundreds of unknowns and thousands of forward-modeling calculations. We observed striking improvements in the shift from standard PSO to *hierarchical PSO with time-varying acceleration coefficients* (HPSO-TVAC). This issue has not been addressed in previous research on PSO applied to geophysics, but was crucial in the optimization of 2D MT data. In fact, the optimization ended with true convergence and stability because some input arguments (namely, the acceleration coefficients) were set as iteration-varying parameters and not as constants. Moreover, a detailed sensitivity analysis has been carried out on the acceleration coefficients and population size to calibrate and retrieve their optimal values and to ensure the stability and convergence of the solution. This represents an upgrade of previous PSO applications to geophysical data.
3. PSO did not require an initial assumption about the solution, i.e., *a priori information*. To prove this, PSO of synthetic data was performed both by giving a priori information at the beginning and by using a random initialization. The a priori information was given to a small portion of the swarm as initial position within the search space of solutions (i.e., proposed models), so that the swarming behavior was only slightly influenced. In this way, if the data agreed with a-priori information, the optimization was influenced by it, otherwise the optimization disregarded the information and searched for a valid solution thanks to its adaptive behavior. We have demonstrated that there is no need for a priori initialization to obtain robust 2D models, since the a-priori-initialized results were largely comparable with the randomly initialized results. In fact, when no a-priori information was set, a random initial model ensured the exploration of all the possible

solutions and then the adaptive behavior ensured the convergence towards the global minimum. An advantage of the PSO method is that it is independent of the starting model, and consequently, it does not necessarily require external information to initialize the optimization.

4. The complexity of the 2D MT inverse problem and the computationally demanding nature of PSO as a global search algorithm had a direct influence on the *computation time*, which has been reduced with the parallelization of the code. In order to speed up the computation, we developed and applied the parallel computing option for the PSO algorithm. Running PSO on a High Performance Computing (HPC) cluster resulted in runtime savings of about 80%.
5. The PSO algorithm has been applied to *two MT profiles* located in the Larderello-Travale geothermal area. For the first time, MT data from this geothermal area have been 2D interpreted using a metaheuristic method. The final models succeeded in imaging very complex resistivity structures similar to those presented in previous research, but with a number of advantages derived from the application of PSO. Firstly, the final models were not initially biased by an external starting model derived from geology. Secondly, the RMSEs associated to the final PSO models were lower than those associated to the models obtained by derivative-based inversion techniques.
6. A first *3D inversion resistivity model* of the Travale geothermal system has been obtained from NLCG 3D MT inversion. This outcome provides comprehensive insight into the complex and still-uncertain electrical resistivity distribution in the subsurface of the Travale geothermal field. The 3D resistivity model has extended our knowledge of 3D subsurface structures, in particular their spatial orientation and extension. The findings of the 3D inversion complement those of earlier studies, that have interpreted only isolated profiles. This final outcome has been successfully correlated to geological information, resistivity well-logs and seismic data. Finally, the identification of the deep resistivity contrasts has significant implications for the understanding of the vapor-dominated circulation in the deep reservoir of the geothermalfield.

PSO of 2D MT data and 3D MT inversion share a common issue: a high computational load. This represented a scientific and technological barrier up to few years ago, but today is being overcome thanks to the rapid progress of parallel and cloud computing, which have become globally available. The computational effort was managed by running the simulations on the HPC cluster of Politecnico di Torino.

One possible source of weakness of the 3D MT study of the Travale geothermal system was the inhomogeneous spatial covering of the MT sites, which may have affected the inversion result. It is also unfortunate that some MT sites have not been included in the 3D inversion due do the high level of noise.

Overall, the MT study of the Travale geothermal system provides continuity of the past European projects INTAS and I-GET and contributes to the characterization of the deep structures, in line with the recent projects IMAGE and DESCRAMBLE. The 3D inversion model presented in this thesis may have practical implications for future deep explorations of the geothermal field of Travale, as it represents the first important result that clearly depicts 3D bodies and lateral discontinuities in resistivity. Furthermore, this study strengthens the idea that vintage data can save essential information if re-evaluated in the light of new methodologies.

A natural development of this work could be to acquire new MT data covering the whole LTGA to draw a very broad resistivity model at a regional scale. A larger number of sites, ideally displaced with regular spatial covering, would be of help for a greater degree of accuracy in the 3D inversion model.

Given the encouraging results from PSO of 2D MT data, a further possible direction for future work could be the adoption of the models resulting from PSO to initially constrain the 3D MT inversion.

Finally, a fruitful area would be 3D MT stochastic inverse modeling. The main premises are that 3D MT forward-modeling routines are beginning to be released to the research community and that global search methods are starting to be positively accepted in spite of the skeptical view of the past. A greater focus on 3D stochastic inverse modeling could produce interesting findings that account more for complex geoelectrical structures. The challenge now is to manage the computational demand, but we are confident that it will be promptly overcome in the near future.

References

Acocella, V., Funiciello, R. (2006). Transverse systems along the extensional Tyrrhenian margin of central Italy and their influence on volcanism. Tectonics, 25, 1-24. doi:10.1029/2005TC001845.

Adhan, S., and Bansal, P. (2017). Applications and Variants of Particle Swarm Optimization: A Review. International Journal of Electronics, Electrical and Computational System, 6(6), 215–223.

Agarwal, A., Chandra, A., Shalivahan, S., and Singh, R. K. (2018). Grey wolf optimizer: a new strategy to invert geophysical data sets. Geophys. Prospect., 66(6), 1215-1226.

Akca, I., Günther, T., Müller-Petke, M., Başokur, A.T. and Yaramanci, U. (2014). Joint parameter estimation from magnetic resonance and vertical electric soundings using a multi-objective genetic algorithm. Geophys. Prospect., 62(2), 364–376.

Avdeev, D. B. (2005). Three-dimensional electromagnetic modelling and inversion from theory to application. Surveys in Geophysics, 26(6), 767-799.

Avdeev, D. B., Kuvshinov, A. V., Pankratov, O. V., and Newman, G. A. (2002). Three-Dimensional Induction Logging Problems. Part I. An Integral Equation Solution and Model Comparisons. Geophysics, 67, 413–426.

Avdeev D. and Avdeeva, A. (2009). 3D Magnetotelluric inversion using a limited-memory quasi-Newton optimization. Geophysics, 74, F45–F57.

Bagagli, M., Kissling, E., Piccinini, D. and Saccorotti, G. (2020). Local earthquake tomography of the Larderello-Travale geothermal field. Geothermics, 83, 101731.

Bahr, K. (1988). Interpretation of the magnetotelluric impedance tensor: regional induction and local telluric distortion. J. Geophys., 62, 119-127.

Bahr, K. (1991). Geological noise in magnetotelluric data: a classification of distortion types. Phys. Earth planet. Inter., 66, 24-38.

Bellani, S., Brogi, A., Lazzarotto, A., Liotta, D. and Ranalli, G. (2004). Heat flow, deep temperatures and extensional structures in the Larderello Geothermal Field (Italy): constraints on geothermal fluid flow. J. Volcan. Geotherm. Res., 132, 15-29.

Berdichevsky, M.N. and Dmitriev, I.V. (2002). Magnetotellurics in the context of the theory of ill-posed problems. Society of Exploration Geophysicists, USA, 214 pp.

Berdichevsky, M.N. and Dmitriev, I.V. (2008). Models and Methods of Magnetotellurics. Springer, Berlin, Heidelberg, p. 327-338.

Bertani, R., Bertini G., Cappetti, G., Fiordelisi, A. and Marocco, B.M. (2005). An update of the Larderello-Travale/Radicondoli deep geothermal system. World Geothermal Congress proceedings. Antalya, Turkey, April, 24-29, 2005, p. 24-29.

Bertani, R. (2016). Geothermal power generation in the world 2010–2014 update report. Geothermics, 60, 31–43.

Bertani, R., Büsing, H., Buske, S., Dini, A., Hjelstuen, M., Luchini, M., ... and Serniotti, L. (2018). The first results of the Descramble project. Forty-third

Workshop on Geothermal Reservoir Engineering proceedings. Stanford, California, February, 12-14, 2018, p. 1-16.

Bertini, G., Casini, M., Ciulli, B., Ciuffi, S. and Fiordelisi, A. (2005). Data revision and upgrading of the structural model of the Travale geothermal field (Italy). World Geothermal Congress proceedings. Antalya, Turkey, April, 24-29, 2005, paper 2612, p. 1-8.

Bertini, G., Casini, M., Gianelli, G. and Pandeli E. (2006). Geological structure of a long-living geothermal system, Larderello, Italy. Terra Nova, 18, 163-169.

Booker, J. R. (2014). The magnetotelluric phase tensor: a critical review. Surveys in Geophysics, 35(1), 7-40.

Brogi, A., Lazzarotto, A., Liotta, D., Ranalli, G. (2003). Extensional shear zones as imaged by reflection seismic lines: the Larderello geothermal field (Central Italy). Tectonophysics, 363,127-139.

Cagniard, L. (1953). Basic theory of the magnetotelluric method of geophysical prospecting. Geophysics, 18, 605-635.

Caldwell, T.G., Bibby, H. and Brown, C. (2004). The magnetotelluric phase tensor. Geophys. J. Int., 158. doi: 10.1111/j.1365-246X.2004.02281.x

Candansayar, M. E. (2008). Two-dimensional inversion of magnetotelluric data with consecutive use of conjugate gradient and least-squares solution with singular value decomposition algorithms. Geophys. Prospect., 56 (1), 141-157.

Cantwell, T. (1960). Detection and analysis of low-frequency magnetotelluric signals. Ph.D. Thesis, Dept. Geol. Geophys. Massachusetts Institute of Technology.

Capozzoli L, De Martino G, Giampaolo V, Godio A, Manzella A, Perciante F, Rizzo E, Santilano A (2016) Deep electrical resistivity model of the Larderello geothermal field (Italy): preliminary results of the FP7 IMAGE experiment. 35° Convegno Nazionale Gruppo Nazionale di Geofisica della Terra Solida proceedings, Lecce, Italy, November 22-24, 2016 p 1-3

Casini, M., Ciuffi, S., Fiordelisi, A., Mazzotti, A. and Stucchi, E. (2010b). Results of a 3D Seismic Survey at Travale geothermal field (Italy). Geothermics, 39, 4–12.

Chave, A.D. and Jones, A.G. (2012). The Magnetotelluric Method, Theory and Practice. Cambridge University Press. 604 pp.

Cheng, F., Li, F., Peng, S., Sun, X., Zheng, J. and Jia, Z., 2015. Joint inversion of TEM and DC in roadway advanced detection based on particle swarm optimization. J. Appl. Geophys., 123, 30–35.

Città di Asti, Ricerche Idriche, 1962. Studio Idrogeologico e prospezione elettrica nella Val maggiore e zone limitrofe.

Coello Coello, C.A., Pulido, G.T. and Lechuga, M.S. (2004). Handling multiple objectives with particle swarm optimization. IEEE Trans. Evol. Comput., 8(3), 256–279.

Coello Coello, C.A., Lamont, G.B. and Veldhuizen, D.A.V. (2007). Evolutionary Algorithms for Solving Multi-Objective Problems, Vol. 5., 2nd edn, New York, Springer, 800 pp.

Commer, M. and Newman, G.A. (2009). Three-dimensional controlled-source electromagnetic and Magnetotelluric joint inversion. Geophys. J. Int. doi:10.1111/j.1365-246X.2009.04216.x

Constable, S.C., Parker, R.l. and Constable, G.C. (1987). Occam's inversion: A practical algorithm for generating smooth models from electromagnetic sounding data. Geophysics, 52 (3), 289-300.

Conti, P., Cei, M. and Razzano, F. (2015). Geothermal energy use, country update for Italy (2010–2015). European Geothermal Congress proceedings. Strasbourg, France, September, 19-24, 2016, p. 1-17.

Conway, D., Simpson, J., Didana, Y., Rugari, J. and Heinson, G. (2018). Probabilistic magnetotelluric inversion with adaptive regularisation using the No-U-Turns sampler. Pure and Applied Geophysics, 175, 2881–2894. doi: 10.1007/s00024-018-1870-5.

Cumming, W. and Mackie, R. (2010) Resistivity imaging of geothermal resources using 1D, 2D and 3D MT inversion and TDEM static shift correction illustrated by a Glass Mountain case history. World Geothermal Congress proceedings. Bali, Indonesia, April, 25–30, 2010, p. 1–10.

Dal Moro, G. (2010). Insights on surface wave dispersion and HVSR: joint analysis via Pareto optimality. J. Appl. Geophys., 72(2), 129–140.

Dal Moro, G. and Pipan, M. (2007). Joint inversion of surface wave dispersion curves and reflection travel times via multi-objective evolutionary algorithms. J. Appl. Geophys., 61, 56–81.

Darisma, D., U. Said, and Srigutomo, W. (2017). 2D gravity inversion using particle swarm optimization method. 23rd European Meeting of Environmental and Engineering Geophysics (EAGE) proceedings, extended abstract We23P216. doi: 10.3997/2214-4609.201702117

De Franco, R., Petracchini, L., Scrocca, D. et al. (2019). Synthetic Seismic Reflection Modelling in a Supercritical Geothermal System: An Image of the K-Horizon in the Larderello Field (Italy). Geofluids, ID 8492453, 1-21. https://doi.org/10.1155/2019/8492453

De Luca, D.A., Destefanis, E., Forno, M.G., Lasagna, M. and Masciocco, L. (2014). The genesis and the hydrogeological features of the Turin Po Plain fontanili, typical lowland springs in Northern Italy. Bull. Eng. Geol. Environ., 73(2), 409–427.

De Luca, D.A., Comina, C., Lasagna, M., Destefanis, E., Masciocco, L., Godio, A. and Stocco, S. (2018). Effectiveness of geophysical surveys for water wells relocation in overexploited aquifers (the example of Maggiore and Traversola Valleys, northwestern Italy). Environ. Earth Sci., 77, 19, doi:10.1007/s12665-017-7218-0.

De Matteis, R., Vanorio, T., Zollo, A., Ciuffi, S., Fiordelisi, A. and Spinelli, E. (2008). Three-dimensional tomography and rock properties of the Larderello-Travale geothermal area, Italy. Physics of the Earth and Planetary Interiors, 168, 37-48.

Deb, K. and Jain, H. (2014). An evolutionary many-objective optimization algorithm using reference-point-based nondominated sorting approach, part I: solving problems with box constraints. IEEE Trans. Evol. Comput., 18(4), 577–601.

Deb, K., Pratap, A., Agarwal, S. and Meyarivan, T. (2002). A fast and elitist multiobjective genetic algorithm, IEEE Trans. Evol. Comput., 6, 182–197.

Degroot-Hedlin, C. (1991). Removal of static shift in two dimensions by regularized inversion. Geophysics, 56, 2102-2106.

Degroot-Hedlin, C. and Constable, S. (1990). Occam's inversion to generate smooth, two-dimensional models from magnetotelluric data. Geophysics, 55(12), 1613–1624.

Degroot-Hedlin, C. and Constable, S. (1993). Occam's inversion and the North American Central Plains electrical anomaly. J. Geomagn. Geoelectr., 45(9), 985-999.

Della Vedova, B., Vecellio, C., Bellani, S. and Tinivella, U. (2008). Thermal modelling of the Larderello geothermal field (Tuscany, Italy). Int. J. Earth Sci. (Geol Rundsch), 97, 317–332. http://dx.doi.org/10.1007/s00531-007-0249-0

DESCRAMBLE project web site: http://www.descramble-h2020.eu/

Dickson, M.H. and Fanelli, M. (2004). What is Geothermal Energy? IGA International Geothermal association website (last accessed 06/2015). http://www.geothermal-energy.org/what_is_geothermal_energy.html

Dong, H. and Jones, A.G. (2018). On the influences of random starting/prior models in three-dimensional magnetotelluric inversion. 24th Electro-Magnetic Induction Workshop proceedings, abstract 258, Helsingør, Denmark, August, 12-19, 2018.

Dosso, S. and Oldenburg, D. (1991). Magnetotelluric appraisal using simulated annealing. Geophys. J. Int., 106, 379–385. doi: 10.1111/j.1365-246X.1991.tb03899.x

Dupis, A. (1997). 1961–1994: A third of a century of magnetotellurics. The Leading Edge, 16(5), 497-502.

Duprat, A. and Cole, F. (1985). Magnetotelluric soundings in the Travale area, Tuscany. Geothermics, 14, 689–696.

Ebbesen, S., Kiwitz, P. and Guzzella, L. (2012). A generic particle swarm optimization matlab function. American Control Conference (IEEE) proceedings, 1519–1524. doi: 10.1109/ACC.2012.6314697

Edgeworth, F.Y. (1881). Mathematical Physics. London: C., Kengan Paul and Co.

EGEC, 2019. EGEC Geothermal Market Report 2018 Key findings. https://www.egec.org/media-publications/egec-geothermal-market-report-2018/

Ekinci, Y.L. and Demirci, A. (2008). A damped least-squares inversion program for the interpretation of Schlumberger sounding curves. J. Appl. Sci., 8, 4070–4078.

Emami Niri, M. and Lumley, D.E. (2015). Simultaneous optimization of multiple objective functions for reservoir modeling, Geophysics, 80(5), M53–M67.

Enel Green Power (2019). Enel Green Power annual report 2018. https://www.enel.com/content/dam/enel-com/governance_pdf/reports/annual-financial-report/2018/annual-report-2018.pdf

Engelbrecht, A. P. (2007). Computational intelligence: An introduction. John Wiley and Sons Ltd.

Evans, R.I. (2012) Earth's electromagnetic environment, Conductivity of Earth materials. In: Chave A.D., Jones A.G., The Magnetotelluric method, theory and practice. Cambridge University Press.

Everett, M. E. (2013). Near-surface applied geophysics. Cambridge University Press.

Everett, M. and Schultz, A. (1993). Two-dimensional nonlinear magnetotelluric inversion using a genetic algorithm. J. Geomagn. Geoelectr., 45, 1013–1026. doi: 10.5636/jgg.45.1013

Farquharson, C. G., and Oldenburg, D.W. (2004). A comparison of automatic techniques for estimating the regularization parameter in non-linear inverse problems. Geophys. J. Int., 156, 411–425. doi:10.1111/j.1365-246X.2004.02190.x

Fernández Martínez, J. L., García Gonzalo, E., Fernández Álvarez, .J. P., Kuzma, H. A. and Menéndez Pérez, C. O. (2010a). PSO: A powerful algorithm to solve geophysical inverse problems: Application to a 1D-DC resistivity case. J. Appl. Geophys, 71, 13–25. doi: 10.1016/j.jappgeo.2010.02.001

Fernández Martínez, J. L., García-Gonzalo, E. and Naudet, V. (2010b). Particle swarm optimization applied to solving and appraising the streaming-potential inverse problem. Geophysics, 75(4), WA3–WA15. doi: 10.1190/1.3460842.

Fernández Martínez, J. L., Mukerji, T., García Gonzalo, E. and Suman, A. (2012). Reservoir characterization and inversion uncertainty via a family of particle swarm optimizers. Geophysics, 77(1), M1-M16.

Fiordelisi, A., Mackie, R., Manzella, A. and Zaja, A. (1998). Electrical features of deep structures in Southern Tuscany (Italy). Annals of Geophysics, 41(3), 333-341.

Gallardo, L.A. and Meju, M.A. (2003). Characterization of heterogeneous near-surface materials by joint 2D inversion of dc resistivity and seismic data. Geophys. Res. Lett., 30(13), 1658, p- 1-4. doi:10.1029/2003GL017370.

Geoportale geoscopio della Regione Toscana. http://www502.regione.toscana.it/geoscopio/cartoteca.html (last accessed July 2019)

Giolito, C., Ruggieri, G. and Manzella A. (2009). The relationship between resistivity and mineralogy at Travale, Italy. Geothermal Resource Council Transaction, 33,929-934, Geothermal Resources Council Annual Meeting, Reno, Nevada, October, 4-7, 2009, p. 1-6 .

Godio, A. and Santilano, A. (2018). On the optimization of electromagnetic geophysical data: Application of the PSO algorithm. J. Appl. Geophys, 148, 163–174. doi: 10.1016/j.jappgeo.2017.11.016.

Gola, G., Bertini, G., Bonini, M., Botteghi, S., Brogi, A., De Franco, R., ... and Manzella, A. (2017). Data integration and conceptual modelling of the Larderello geothermal area, Italy. Energy Procedia, 125, 300-309.

Gou, J., Lei, Y. X., Guo, W. P., Wang, C., Cai, Y. Q. and Luo, W. (2017). A novel improved particle swarm optimization algorithm based on individual difference evolution. Applied Soft Computing, 57, 468-481.

Grandis, H., Menvielle, M. and Roussignol, M. (1999). Bayesian inversion with Markov chains—I. The magnetotelluric one-dimensional case. Geophys. J. Int., 138, 757–768.

Groom, R.W. and Bailey, R.C. (1989). Decomposition of the magnetotelluric impedance tensor in the presence of local three-dimensional galvanic distortion. J. Geophys. Res., 94, 1913-1925.

Hering, A., Misiek, R., Gyulai, A., Ormos, T., Dobroka, M. and Dresen, L. (1995). A joint inversion algorithm to process geoelectric and surface wave seismic data. Part I: basic ideas. Geophys. Prospect., 43(2), 135–156.

Hutton, V.R.S. (1985). Magnetic, telluric and magnetotelluric measurements at the Travale test site, Tuscany, Italy, 1980–1983: An overview. Geothermics, 14, 637–644.

IMAGE web site. http://www.image-fp7.fr/Pages/default.aspx

Ingeman-Nielsen, T. and Baumgartner, F. (2006). CR1Dmod: a Matlab program to model 1D complex resistivity effects in electrical and electromagnetic surveys. Comput. Geosci., 32, 1411–1419.

Jones, A.G. (1988). Static shift of magnetotelluric data and its removal in a sedimentary basin environment. Geophysics, 53 (7), 967-978.

Jones, A.G. (1992). Electrical Conductivity of the Continental Lower Crust. In *Continental Lower Crust*, edited by D.M. Fountain, R.J. Arculus and R.W. Kay. Elsevier, 81-143.

Jones, A.G. (1993a). COPROD2 Data set accessed October 2017 at http://www.complete-mt-solutions.com/mtnet/data/coprod2/coprod2.html.

Jones, A.G. (1993b). The COPROD2 dataset: Tectonic setting, recorded MT data, and comparison of models: J. Geomagn. Geoelectr., 45(9), 933-955.

Jones, A.G., Chave, A.D., Egbert, G., Auld, D. and Bahr, K. (1989). A Comparison of techniques for magnetotelluric response function estimation. J. Geophys. Res. (Solid Earth), 94(10), 14201 – 14213.

Jones, A.G. and Hutton, R. (1979). A multi-station magnetotelluric study in Southern Scotland, I. Fieldwork, data analysis and results. Geophys. J. R. Astron. Soc., 56, 329–349.

Jones, A. G. and Savage, P. J. (1986). North American Central Plains conductivity anomaly goes east. Geophys. Res. Lett., 13, 7, 685-688.

Kelbert, A., Egbert, G.D. and Schultz, A. (2008). Non-linear conjugate gradient inversion for global EM induction: resolution studies. Geophys. J. Int., 173, 365–381.

Kelbert, A., Meqbel, N., Egbert, G.D. and Tandon, K. (2014). ModEM: A modular system for inversion of electromagnetic geophysical data. Comput. Geosci. http://dx.doi.org/10.1016/j.cageo.2014.01.010

Kennedy, J. and Eberhart, R. (1995). Particle swarm optimization. International Conference on Neural Networks IV (IEEE) proceedings, extended abstracts, 1942–1948. doi: 10.1109/ICNN.1995.488968.

Kennedy, J., Eberhart, R. and Shi, Y. H. (2001). Swarm intelligence. Morgan Kaufmann Publishers.

Key, K. (2016). MARE2DEM: a 2-D inversion code for controlled-source electromagnetic and magnetotelluric data. Geophys. J. Int., 207(1), 571-588.

Kirkby, A., Zhang, F., Peacock, J., Hassan, R. and Duan, J. (2019). The MTPy software package for magnetotelluric data analysis and visualization. Journal of Open Source Software 4(37), 1358. https://doi.org/10.21105/joss.01358

Krieger, L. and Peacock, J. R. (2014). MTpy: A Python toolbox for magnetotellurics. Comput. Geosci., 72, 167-175.

Kruglyakov, M. and Bloshanskaya, L. (2017). High-performance parallel solver for integral equations of electromagnetics based on Galerkin method. Mathematical Geosciences, 49(6), 751-776.

Lasagna, M., Caviglia, C. and De Luca, D.A. (2014). Simulation modeling for groundwater safety in an overexploitation situation: the Maggiore Valley context (Piedmont, Italy). Bull. Eng. Geol. Environ., 73, 341–355.

Ledo, J., Gabàs, A. and Marcuello, A., (2002a). Static shift levelling using geomagnetic transfer functions. Earth Planets Space, 54, 493-398.

Ledo, J., Queralt, P., Martí, A. and Jones, A.G. (2002b). Two-dimensional interpretation of three-dimensional magnetotelluric data: an example of limitations and resolution. Geophys. J. Int., 150,127-139.

Ledo, J. (2005). 2-D versus 3-D Magnetotelluric data interpretation. Surveys in Geophysics, 26, 511–543.

Lee, S. K., Kim, H. J., Song, Y. and Lee, C. K. (2009). MT2DInvMatlab—A program in MATLAB and FORTRAN for two-dimensional magnetotelluric inversion. Comput. Geosci., 35(8), 1722-1734.

Lilley, F.E.M. and Weaver, J.T. (2010). Phases greater than 90° in MT data: analysis using dimensionality tools. J. Appl. Geophys., 70, 9–16.

Liotta, D., Brogi, A. (2020). Pliocene-Quaternary fault kinematics in the Larderello geothermal area (Italy): Insights for the interpretation of the present stress field. Geothermics, 83, 101714, ISSN 0375-6505. https://doi.org/10.1016/j.geothermics.2019.101714.

Mandolesi, E., Ogaya, X., Campanyà, J. and Agostinetti, N. P. (2018). A reversible-jump Markov chain Monte Carlo algorithm for 1D inversion of magnetotelluric data. Comput. Geosci., 113, 94-105.

Manzella, A. (2004). Resistivity and heterogeneity of Earth crust in an active tectonic region, Southern Tuscany (Italy). Annals of Geophysics, 47(1), 107-118.

Manzella, A., Spichak, V., Pushkarev, P., Sileva, D., Oskooi, B., Ruggieri, G. and Sizov, Y. (2006). Deep fluid circulation in the Travale geothermal area and its relation with tectonic structure investigated by a magnetotelluric survey. Thirty-First Workshop on Geothermal Reservoir Engineering proceedings, Stanford University, Stanford, California, January 30 – February 1, 2006, p. 1-6.

Manzella, A., Ungarelli C., Ruggieri G., Giolito C. and Fiordelisi A. (2010). Electrical resistivity at the Travale geothermal field (Italy). World Geothermal Congress proceedings, Bali, Indonesia, April, 25-30, 2006, p. 1-8.

Manzella, A., Bonciani, R., Allansdottir, A., Botteghi, S., Donato, A., Giamberini, S., ... and Scrocca, D. (2018). Environmental and social aspects of geothermal energy in Italy. Geothermics, 72, 232-248.

Manzella A, Serra D, Cesari G, Bargiavchi E, Cei M, Cerutti P, Conti P, Giudetti G, Lupi M, Vaccaro M (2019) Geothermal Energy Use, Country Update for Italy. European Geothermal Congress proceedings. Den Haag, The Netherlands, 11-14 June 2019, 2019 p 1-17

Marti, A., Queralt, P., Jones, A.G. and Ledo, J. (2005). Improving Bahr's invariant parameters using the WAL approach. Geophys. J. Int., 163, 38–41.

Marti, A., Queralt, P. and Ledo, J. (2009). WALDIM: A code for the dimensionality analysis of magnetotelluric data using the rotational invariants of the magnetotelluric tensor. Comput. Geosci., 35, 2295–2303.

McNeice G. and Jones, A.G. (2001) Multisite, multi frequency tensor decomposition of Magnetotelluric data.

Geophysics, 66,158–173.

Meju, M.A. (1996). Joint inversion of TEM and distorted MT soundings: Some effective practical considerations. Geophysics, 61, 56–65.

Meju, M.A. (2005). Simple relative space time scaling of electrical and electromagnetic depth sounding arrays: implications for electrical static shift removal and joint DC-TEM data inversion with the most-squares criterion. Geophys. Prospect., 53, 463-479.

Meqbel, N. and Ritter, O., (2015). Joint 3Dinversion of multiple electromagnetic datasets. Geophys. Prospect., 63, 1450–1467.

Miensopust, M. P., Queralt, P., Jones, A. G. and 3D MT modellers (2013). Magnetotelluric 3-D inversion — A review of two successful workshops on forward and inversion code testing and comparison. Geophys. J. Int., 193, 1216–1238. doi: 10.1093/gji/ggt066

Moeck, I.S. (2014). Catalog of geothermal play types based on geologic controls. Renew. Sust. Energ. Rev., 37, 867-882. doi:10.1016/j.rser.2014.05.032.

Moorkamp, M., Heincke, B., Jegen, M., Roberts, A.W. and Hobbs, R.W. (2011). A framework for 3-D joint inversion of MT, gravity and seismic refraction data. Geophys. J. Int., 184, 477–493.

Muñoz, G. (2014). Exploring for Geothermal Resources with Electromagnetic Methods. Surveys in Geophysics, 35, 101-122. Doi:10.1007/s10712-013-9236-0

Musil, M., Maurer, H.R. and Green, A.G. (2003). Discrete tomography and joint inversion for loosely connected or unconnected physical properties: application to crosshole seismic and georadar data sets. Geophys. J. Int., 153(2), 389–402.

Nabighian, M. N. and Macnae, J. C. (1991). Time domain electromagnetic prospecting methods. In *Electromagnetic Methods in Applied Geophysics*, Volume 2, ed. M. N. Nabighian. Tulsa, OK: Society of Exploration Geophysicists, p. 427–450.

Newman, G.A. and Alumbaugh, D.L. (2000). Three-dimensional magnetotelluric inversion using non-linear conjugate gradients. Geophys. J. Int., 140, 410–424.

Ogawa, Y. and Uchida, T. (1996). A two-dimensional magnetotelluric inversion assuming Gaussian static shift. Geophys. J. Internat., 126, 69–76.

Ogawa, Y. (2002). On two-dimensional modeling of magnetotelluric field data. Surveys in Geophysics, 23, 251-273.

Olalekan, F. and Di, Q. (2017). Particle swarm optimization method for 1D and 2D MTEM data inversion. 87th Annual International Meeting (SEG) expanded abstracts, 1219–1224. doi: 10.1190/segam2017-17671977.1.

Orlando, L. (2005). Interpretation of Tuscan gravity data. Bollettino Società Geologica Italiana, Volume Speciale 3, 179 – 186.

Paasche, H. and Tronicke, L. (2014). Nonlinear joint inversion of tomographic data using swarm intelligence. Geophysics, 79(4), R133–R149.

Pace, F., Santilano, A. and Godio, A. (2017). Particle Swarm Optimization of Electromagnetic Data with Parallel Computing in the 2D Case. 23rd European Meeting of Environmental and Engineering Geophysics (EAGE) proceedings, Extended Abstracts Tu23B04, Malmö, Sweden, September, 3-7, 2017, p. 1-5.

Pace, F., Santilano, A. and Godio, A. (2018). Multi-objective particle swarm optimization of vertical electrical sounding and time-domain electromagnetic data. 24th European Meeting of Environmental and Engineering Geophysics (EAGE) proceedings, Extended abstract We24A01, Porto, Portugal, September, 9-12, 2018, p. 1-5. doi:10.3997/2214-4609.201802624.

Pace, F., Santilano, A. and Godio, A. (2019a). Particle Swarm Optimization of 2D Magnetotelluric data. Geophysics, 84(3), E125-E141. https://doi.org/10.1190/geo2018-0166.1

Pace, F., Santilano, A., Godio, A. and Comina, C. (2019b). Joint optimization of geophysical data using multi-objective swarm intelligence. Geophys. J. Int., 218 (3), 1502–1521. https://doi.org/10.1093/gji/ggz243

Pace, F., Santilano, A., Godio, A. and Manzella, A. (2019c). Stochastic inverse modeling of magnetotelluric data from the Larderello-Travale geothermal area (Italy). 1st Conference on Geophysics for Geothermal and Renewable Energy Storage (EAGE) proceedings, Extended abstract We1GEOT11, The Hague, Netherlands, September, 08 - 12, 2019, p. 1-5. doi: 10.3997/2214-4609.201902507

Pace, F., Santilano, A., Godio, A. and Manzella, A. (2019d). Modeling of magnetotelluric data using computational swarm intelligence: applications to geothermal areas. 38° Convegno Nazionale Gruppo Nazionale di Geofisica della Terra Solida proceedings, Rome, Italy, November, 12-14, 2019, p. 1-4.

Palacky, G. J. (1987). Resistivity characteristics of geologic targets. In: M. N. Nabighian (ed), *Electromagnetic Methods in Applied Geophysics, volume 1 – Theory*. Society of Exploration Geophysicists.

Pareto, V. (1896). Cours d'Economie Politique, Vols. I and II, F. Rouge.

Parkinson, W. (1959). Directions of rapid geomagnetic variations. Geophys. J. R. Astr. Soc., 2, 1–14.

Pellerin, L. and Hohmann, G.W. (1990). Transient electromagnetic inversion: A remedy for magnetotelluric static shifts. Geophysics 55(9), 1242-1250.

Pellerin, L., Johnston, J. M., and Hohmann, G. W. (1996). A numerical evaluation of electromagnetic methods in geothermal exploration. Geophysics, 61(1), 121-130.

Perez, R. E. and Behdinan, K. (2007). Particle swarm approach for structural design optimization. Computers and Structures, 85, 1579–1588. doi: 10 .1016/j.compstruc.2006.10.013.

Pérez-Flores, M. A. and Schultz, A. (2002). Application of 2-D inversion with genetic algorithms to magnetotelluric data from geothermal areas. Earth, Planets and Space, 54, 607–61., doi: 10.1186/BF03353049.

Piatti, C., Boiero, D., Godio, A. and Socco, L.V. (2010). Improved Monte Carlo 1D inversion of vertical electrical sounding and time-domain electromagnetic data. Near Surf. Geophys., 8, 117–133.

Piga, B., Casasso, A., Pace, F., Godio, A. and Sethi, R. (2017). Thermal Impact Assessment of Groundwater Heat Pumps (GWHPs): Rigorous vs. Simplified Models. Energies, 10 (1385), 19 pp. doi: 10.3390/en10091385

Poli, R. (2008). Analysis of the Publications on the Applications of Particle Swarm Optimisation. Journal of Artificial Evolution and Applications, 2008, 1–10, doi: 10.1155/2008/685175.

Rasmussen, T. M. (1993). Two-dimensional Occam model of COPROD2 data-first order description of resolution and variance. J. Geomagn. Geoelectr., 45, 9, 1027-1037.

Ratnaweera, A., Halgamuge, S. K. and Watson, H. C. (2004). Self-organizing hierarchical particle swarm optimizer with time-varying acceleration coefficients. IEEE Transactions on Evolutionary Computation, 8, 240–255. doi: 10.1109/TEVC.2004.826071.

Reyes-Sierra, M. and Coello Coello, C.A. (2006). Multi-objective particle swarm optimizers: a survey of the state-of the-art. Int. J. Comput. Intell. Res., **2**(3), 287–308.

Rodi, W. and Mackie, R.L. (2001). Nonlinear conjugate gradients algorithm for 2-D magnetotelluric inversion. Geophysics, 66, 174–187.

Romagnoli, P., Arias, A., Barelli, A., Cei, M. and Casini, M. (2010). An updated numerical model of the Larderello–Travale geothermal system, Italy. Geothermics, 39, 292-313.

Sambridge, M. and Mosegaard, K. (2002). Monte Carlo methods in geophysical inverse problems. Reviews of Geophysics, 40(3), 3-1.

Sani, F., Bonini, M., Montanari, D., Moratti, G., Corti, G., and Del Ventisette, C. (2016). The structural evolution of the Radicondoli–Volterra Basin (southern Tuscany, Italy): Relationships with magmatism and geothermal implications. Geothermics, 59, Part A, 38 – 55.

Santilano, A., Manzella, A., Gianelli, G., Donato, A., Gola, G., Nardini, I., Trumpy, E. and Botteghi, S. (2015a). Convective, Intrusive Geothermal Plays: what about tectonics? Geothermal Energy Science, 3, 51-59. doi:10.5194/gtes-3-51-2015.

Santilano, A., Godio A., Manzella A., Dini I. (2015b). Electrical Resistivity Structures and their Relation to Geological Features at the Larderello Geothermal Field (Italy). Near Surface Geoscience 2015 proceedings, Extended abstract Tu21B08, Turin, Italy, September, 6-10, 2015, p. 1-5. doi: 10.3997/2214-4609.201413727.

Santilano, A. (2017). Deep geothermal exploration by means of electromagnetic methods: New insights from the Larderello geothermal field (Italy). Ph.D. Thesis, Politecnico di Torino.

Santilano, A., Godio, A. and Manzella, A. (2018). Particle swarm optimization for simultaneous analysis of magnetotelluric and time-domain electromagnetic data. Geophysics, 83(3), E151–E159. doi: 10.1190/geo2017-0261.1.

Sasaki, Y. (2001). Full 3D inversion of electromagnetic data on PC. J. Appl. Geophys., 46, 45–54.

Schnaidt, S., Conway, D., Krieger, L. and Heinson, G. (2018). Pareto-optimal multi-objective inversion of geophysical data. Pure appl. Geophys., 175(6), 2221-2236. doi:10.1007/s00024-018-1784-2.

Schwartz, G., Haak, V. and Rath, V. (1985). Electrical conductivity studies in the Travale geothermal field, Italy. Geothermics, 14, 653–662.

Sen, M. K., Duttagupta, A., Stoffa, P. L., Lake, L. and Pope, G. (1992). Stochastic reservoir modeling by simulated annealing and genetic algorithms: A comparative analysis. Sixty-Seventh Annual Technical Conference and Exhibition of the Society of Petroleum Engineers proceedings, paper no. SPE 24754, Washington, D.C., USA, p. 939–950.

Sen, M. K., Bhattacharya, B. B. and Stoffa, P. L. (1993). Nonlinear inversion of resistivity sounding data. Geophysics, 58, 496 –507.

Sen, M. K. and Stoffa, P. L. (2013). Global optimization methods in geophysical inversion. Cambridge University Press.

Shaw, R. and Srivastava, S. (2007). Particle swarm optimization: A new tool to invert geophysical data. Geophysics, 72(2), F75–F83. doi: 10.1190/1.2432481

Shi, Y. and Eberhart, R. (1998). A modified particle swarm optimizer. IEEE International Conference on Evolutionary Computation proceedings, p. 69–73. doi: 10.1109/ICEC.1998.699146.

Shi, Y. and Eberhart, R. C. (2001). Fuzzy adaptive particle swarm optimization. 2001 Congress on evolutionary computation proceedings (IEEE), Vol. 1, p. 101-106 (Cat. No. 01TH8546)

Simpson, F. and Bahr, K. (2005). Practical Magnetotellurics. Cambridge University Press.

Singh, A., Dehiya, R., Gupta, P. K., and Israil, M. (2017). A MATLAB based 3D modeling and inversion code for MT data. Comput. Geosci., 104, 1-11.

Siripunvaraporn, W. (2012). Three-dimensional magnetotelluric inversion: an introductory guide for developers and users. Surveys in geophysics, 33(1), 5-27.

Siripunvaraporn, W. and Egbert, G. (2000). An efficient data-subspace inversion method for 2D magnetotelluric data. Geophysics, 65(3), 791–803.

Siripunvaraporn, W. and Egbert, G. (2007). Data space conjugate gradient inversion for 2-D Magnetotelluric data. Geophys, J, Int., 170, 986–994.

Siripunvaraporn, W. and Egbert, G. (2009). WSINV3DMT: vertical magnetic field transfer function inversion and parallel implementation. Phys. Earth Planet. Int., 173, 317–329.

Smith, J.T. (1995). Understanding telluric distortion matrices. Geophys. J. Int., 122, 219-226.

Song, X., Tang, L., Lv, X., Fang, H. and Gu, H. (2012). Application of particle swarm optimization to interpret Rayleigh wave dispersion curves. J. Appl. Geophys., 84, 1-13.

Spichak, V. V. (2015). Electromagnetic sounding of the Earth's interior. Vol. 40, Elsevier.

Spichak, V.V. and Manzella, A. (2009). Electromagnetic sounding of geothermal zones. J. Appl. Geophys., 68, 459-478. doi:10.1016/j.jappgeo.2008.05.007.

Spichak, V.V. and Zakharova, O.K. (2014). Gaseous vs aqueous fluids: Travale (Italy) case study using EM geothermometry. 39th Workshop on Geothermal Reservoir Engineering proceedings, Stanford University, USA.

Sternberg, B.K., Washburne, J.C. and Pellerin, L. (1988). Correction for the static shift in magnetotellurics using transient electromagnetic soundings. Geophysics, 53(11), 1459-1468. doi: 10.1190/1.1442426

Stoffa, P. L. and Sen, M. K. (1992). Seismic waveform inversion using global optimization. J. Seism. Exp., 1, 9-27.

Tarantola, A. (2005). Inverse Problem Theory and Methods for Model Parameter Estimation. Society for Industrial and Applied Mathematics. Philadelphia. 342 pp.

TERNA, 2016. Electrical power production in Italy (in Italian). Open File Report http://download.terna.it/terna/0000/0964/24.PDF

Tikhonov, A.N. (1950). On determination of electric characteristics of deep layers of the earth’s crust. Dokl. Acad. Nauk SSSR, 151, 295–297.

Tripathi, P.K., Bandyopadhyay, S.and Pal, S.K. (2007). Multi-objective particle swarm optimization with time variant inertia and acceleration coefficients. Inf. Sci., 177, 5033–5049.

Tronicke, J., Paasche, H. and Böniger, U. (2011). Joint global inversion of GPR and P-wave seismic travel-times using particle swarm optimization. 6th International Workshop on Advanced Ground Penetrating Radar (IWAGPR) proceedings, Aachen, Germany, p. 1–4.

Turing, A.M. (1950). Computing Machinery and Intelligence. Mind, 59, p. 433–460.

Uchida, T. (1993). Inversion of COPROD2 magnetotelluric data by use of ABIC minimization method. J. Geomagn. Geoelectr., 45, 9, 1063-1071.

Van den Bergh, F. and Engelbrecht, A. P. (2001). Effect of swarm size on cooperative particle swarm optimizers. Genetic Evolutionary Computation Conference (GECCO-2001) proceedings, 892–899.

Vanorio, T., De Matteis, R., Zollo, A., Batini, F., Fiordelisi, A., and Ciulli, B. (2004). The deep structure of the Larderello-Travale geothermal field from 3D microearthquake traveltime tomography. Geophys. Res. Lett., 31, L07613, 1 – 4.

Vozoff, K. (1972). The magnetotelluric method in the exploration of sedimentary basins. Geophysics, 37(1), 98-141.

Vozoff, K. (1991). The magnetotelluric method. In *Electromagnetic Methods in Applied Geophysics: Volume 2, Application, Parts A and B* (p. 641-712). Society of Exploration Geophysicists.

Vozoff, K. and Jupp, D.L. (1975). Joint inversion of geophysical data. Geophys. J. R. Astr. Soc., 42, 977–991.

Wannamaker, P. E. (1991). Advances in Three-Dimensional Magnetotelluric Modeling Using Integral Equations. Geophysics, 56, 1716–1728.

Weaver, J.T., Agarwal, A.K. and Lilley, F.E.M. (2000). Characterization of the magnetotelluric tensor in terms of its invariants. Geophys. J. Int., 141, 321-336.

Wu, N., Booker, J. R. and Smith, J. T. (1993). Rapid two-dimensional inversion of COPROD2 data. J. Geomagn. Geoelectr., 45, 9, 1073-1087.

Xiang, E., Guo, R., Dosso, S. E., Liu, J., Dong, H. and Ren, Z. (2018). Efficient hierarchical trans-dimensional Bayesian inversion of magnetotelluric data. Geophys. J. Int., 213, 1751–1767. doi: 10.1093/gji/ggy071.

Yan, P., Garcia Juanatey, M. A., Kalscheuer, T., Juhlin, C., Hedin, P., Savvaidis, A., Lorenz, H. and Kück, J. (2017a). A magnetotelluric investigation of the Scandinavian Caledonides in western Jämtland, Sweden, using the COSC borehole logs as prior information. Geophys. J. Int., 208, 1465–1489. doi: 10.1093/gji/ggw457.

Yan, P., Kalscheuer, T., Hedin, P. and Garcia Juanatey, M. A. (2017b). Two-dimensional magnetotelluric inversion using reflection seismic data as constraints and application in the COSC project. Geophys. Res. Lett., 44, 3554–3563. doi: 10.1002/2017GL072953.

Yang, C.H. and Tong, L.T. (1988). Joint inversion of DC, TEM, and MT data. 58th Annual International Meeting Society of Exploration Geophysicists, SEG Technical Program Expanded Abstracts, p. 408–410.

Ying, T., Yang, Y. P. and Zeng, J. C. (2006). An enhanced hybrid quadratic particle swarm optimization. Sixth International Conference on Intelligent Systems Design and Applications proceedings (IEEE), (Vol. 2, p. 980-985).

Yuan, S., Wang, S. and Tian, N. (2009). Swarm intelligence optimization and its application in geophysical data inversion. Applied Geophysics, 6, 166–174. doi: 10.1007/s11770-009-0018-x.

Zhan, Z.-H., Zhang, J., Li, Y. and Chung, H. S.-H. (2009). Adaptive particle swarm optimization. IEEE Transactions on Systems, Man, and Cybernetics, Part B (Cybernetics), 39, 1362–1381, doi: 10.1109/TSMCB.2009.2015956.

Zhang, P., Roberts, R.G. and Pedersen, L.B. (1987). Magnetotelluric Strike Rules. Geophysics, 52, 267-278.

Zhdanov, M.S. (2009). Geophysical Electromagnetic Theory and Methods. Amsterdam, Elsevier, 848 pp.

Appendix A

Joint optimization of geophysical data using multi-objective swarm intelligence

A.1 Solution evaluation

We adopted three metrics as performance measures assessing both the number of non-dominated solutions and the *PF*.

1) The repository index (***RI***):

$$\boldsymbol{RI}\ (\%) = \frac{\boldsymbol{N_{rep}}}{\boldsymbol{N_{tot}}} \qquad (\text{A.1})$$

where: N_{rep} is the number of non-dominated solutions (or, in MOPSO, the particles stored in the repository), and N_{tot} is the total number of solutions analyzed (i.e., the population size in both MOPSO and NSGA-III). *RI* measured the level of non-dominated solutions at the last iteration.

2) The spacing (**SP**):

$$\mathbf{SP} = \sqrt{\frac{1}{N_{rep}-1}\sum_{i=1}^{N_{rep}}\left(\bar{d}-d_i\right)^2} \qquad (\text{A.2})$$

where: $d_i = min_j\left(\left|f_1^i(\boldsymbol{m}) - f_1^j(\boldsymbol{m})\right| + \left|f_2^i(\boldsymbol{m}) - f_2^j(\boldsymbol{m})\right|\right)$; $i,j = 1,\ \ldots, N_{rep}$, and $\bar{d}$ is the mean of all d_i (Coello Coello et al., 2004). This metric effectively measured the distribution of the solutions throughout the *PF* and was 0 in case of uniform distribution (i.e., equidistant spacing) between the beginning and the end of the *PF*-curve.

3) The deviation angle (α) between two lines: the bisector of the objective space (with slope 1) and the linear fit of the *PF* calculated using the Theil-Sen estimator (Theil 1950; Sen 1968). The angle α was derived from the tangent:

$$\tan\alpha = \left|\frac{\tilde{m}-1}{1+\tilde{m}}\right| \qquad (\text{A.3})$$

where $\tilde{m}$ is the median of the slopes between all the possible pairs of points of the 2D PF $\{(x_i, y_i)|i = 1, \dots, N_{rep}\}$:

$$\tilde{m} = median\{m_{i,j}|i, j = 1, \dots, N_{rep}, i \neq j, i > j\} \qquad (\text{A.4})$$

$$m_{i,j} = \frac{y_j - y_i}{x_j - x_i} \qquad (\text{A.5})$$

The deviation angle $\boldsymbol{\alpha}$ is an indicator of the data set compatibility because only if the data sets are perfectly compatible, the objective components converge to the same value and the *PF* aligns along the ideal line of slope 1 (Schnaidt et al. 2018). Otherwise, conflicting objective components lead to a marked deviation of the Theil-Sen regression line. In detail, the condition $0° < \alpha < 45°$ proves data compatibility and can be easily observed in case of synthetic data sets. If, instead, $45° < \alpha < 90°$ data incompatibility occurs, and the *PF* deviates from the ideal line. Unfortunately, field data sets are commonly affected by incompatibility or partial compatibility due to the specific differences of the geophysical methods. However, the regression line, or simply, the *PF* shape is effective in showing how much one objective-component is in contrast with the other one (Dal Moro 2010).

A.2 Validation on synthetic data

Our novel joint-optimization algorithm was first validated on a synthetic example. The true model was conceived in some ways similar to the experimental data to be tested. The synthetic model was composed of five layers of different resistivity and is shown in Figure A.1c with a red-dashed line, while the TDEM and VES curves are marked with red dots in Figure A.1a-b, respectively. These curves were computed using the forward solvers mentioned before and adopted for the optimization. The error bars refer to 10% Gaussian noise added to the data.

The model solution was discretized into 19 layers and its maximum depth was consistent with the concept of electromagnetic diffusion depth. The application of the L-curve criterion identified the optimal Lagrange multipliers equal to 0.1 for TDEM and 0.01 for VES. The boundary conditions of the search space of solutions were 1 and 500 Ωm. The TV-MOPSO stopped after 1000 iterations and the outcome is presented in Figure A.1. On the left (Figure A.1a-b), the blue lines represent the calculated responses satisfactory fitting the synthetic curves. Figure A.1c displays the final result (blue line) compared to the true model (red-dashed line) and the other optimized solutions belonging to the Pareto Front (green lines). The MOPSO outcome was largely consistent with the true synthetic model, thus demonstrating its applicability to real data. Table A.1 lists other details of the optimization, such as: the *RI* (equation A.1), the *SP* (equation A.2), the angle α (equation A.3), the total runtime (in hours), the data misfit and model misfit calculated as the root mean square error normalized by the mean value (NRMSE).

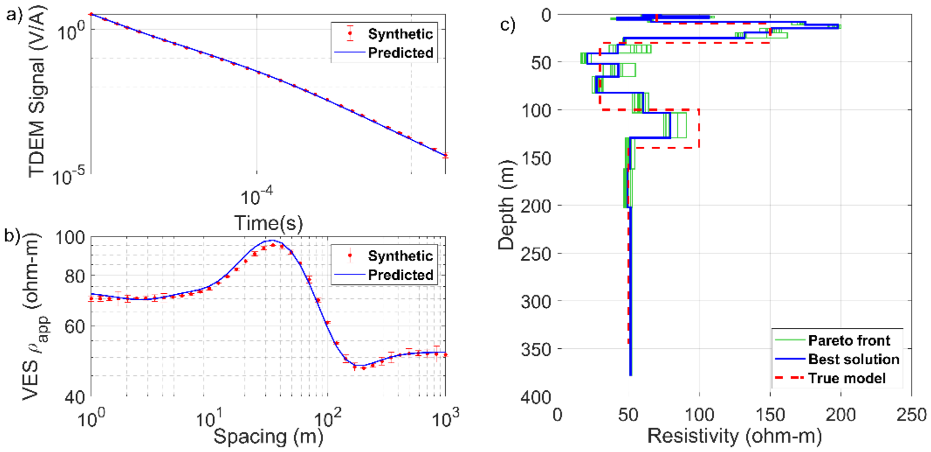

Figure A.1 The result of TV-MOPSO applied to the synthetic example; **a)** TDEM theoretical signal (red dots with error bars) and predicted response in the range $0.9 \cdot 10^{-5}$ - $2 \cdot 10^{-3}$ s; **b)** VES data cover 1 to 1000 m of half-spacing; **c)** the true model (red-dashed line), the final resistivity models derived from the *PF* (green lines) and the best solution highlighted in blue.

Table A.1 Analysis of the performance of MOPSO on the synthetic example. The rows report: the number of iterations run, repository index (*RI*), spacing (*SP*), deviation angle (α) between the ideal and Theil-Sen regression line, total runtime in hours, data misfit (NRMSE) for TDEM and VES and model misfit (NRMSE).

Synthetic data	
	MOPSO
Iterations	1000
RI (%)	7.6
SP	0.0033
α (°)	48.3
Runtime (h)	13
Data NRMSE TDEM	0.0367
Data NRMSE VES	0.0209
Model NRMSE	0.188

A.3 Test on the Villafranca data set (Italy)

The site of Villafranca d'Asti is located about 40 km south-east of Torino and represents an exploration site, where a large well-field extensively exploits a confined aquifer to supply drinking water to 43 municipalities within the Asti Province (De Luca et al. 2018). The exploited aquifer consists of Pliocene marine deposits (mainly "Asti Sands" formation) bounded at the base by a Pre-pliocene marine complex, consisting of silty-clayey sediments, and by a Lower-Middle Pliocene marine complex (represented by the Lugagnano Clay), consisting of sandy-marly clay, upward intercalated with coarser sediments (De Luca et al. 2014; Lasagna et al. 2014). Both these lower complexes have a very low or negligible permeability and represent an aquiclude, under the overlying Asti Sands. By contrast, the Asti Sands are sandy sediments, alternated with levels of fine sand, sandy-gravel, clayey sand, silty-sandy and silty-clayey levels with very low permeability. The alternation between mainly sandy sediments with a good permeability and poorly permeable levels makes this complex a multi-layered aquifer system, in which the various aquifer levels can intercommunicate through semi-permeable levels.

A geophysical survey has been carried out in the area to better understand the formation of this aquifer layer and potentially identify new positions for water wells (De Luca et al., 2018). Within the performed surveys, acquisition of TDEM data has been carried out using a coil size of 100 × 100 m for the transmitter, and both 0.6 × 0.6 m (20 turns) and 10 × 10 m (2 turns) receiver coils for the receiver, located at the center of the transmitter coil. TDEM transient curve has consisted of 40 measuring points, from 1.2×10^{-6} s to 8.8×10^{-3} s. Injected current has been around 10 A and a stacking of 2000 measurements has been performed. The acquisition has been carried out using an *ABEM WalkTEM* instrument. Several of these soundings have been performed over the area and then globally inversed with a Spatially Constrained Inversion (SCI) algorithm (De Luca et al. 2018). In our study, a single TDEM sounding was integrated with one VES sounding. The available vintage VES acquisition has been performed using the Schlumberger configuration with a maximum half-spacing of about 850 m between the current electrodes (Città di Asti 1962). As in the Stupinigi case study, the TDEM measurements had the original uncertainties associated to the data, while the errors of VES data were assumed by adding 10% of Gaussian noise. This may be regarded as the contribution of: the original experimental errors, the possible inaccuracy of the conversion from the original data to the digital form and the inaccuracy of editing and smoothing apparent-resistivity curves.

VES and TDEM curves were preliminary analyzed to infer the possible occurrence of the electrical static shift. After applying the scaling relationship of Meju (2005), we verified that the two data sets were acceptably compatible for joint inversion.

In the MOPSO algorithm, the lower and upper boundaries of the search space were fixed at 1 and 200 Ωm, respectively. The application of the L-curve criterion identified the optimal Lagrange multipliers equal to 0.1 for TDEM and 10^{-4} for VES. The results from MOPSO are presented in Figure A.2. On the left, the fitting between observed (red error bars) and calculated (blue line) data is noteworthy for both TDEM signal (Figure A.2a) and VES apparent resistivity (Figure A.2b). On the right, Figure A.2c) displays the set of Pareto-optimal solutions in green and the selected one with the minimum components of ***f(m)*** in blue. The 1D vertical profile was composed of 19 layers, up to a maximum depth of about 380 m. The family of non-dominated solutions reveals two resistive regions. The first region overcomes 100 Ωm in the shallow subsurface (about 20 m of depth). The second ranges from 100 Ωm to 200 Ωm at a depth from about 50 to 150 m. This last resistive layer may be related to the confined aquifer object of the investigation in the area, as mentioned before.

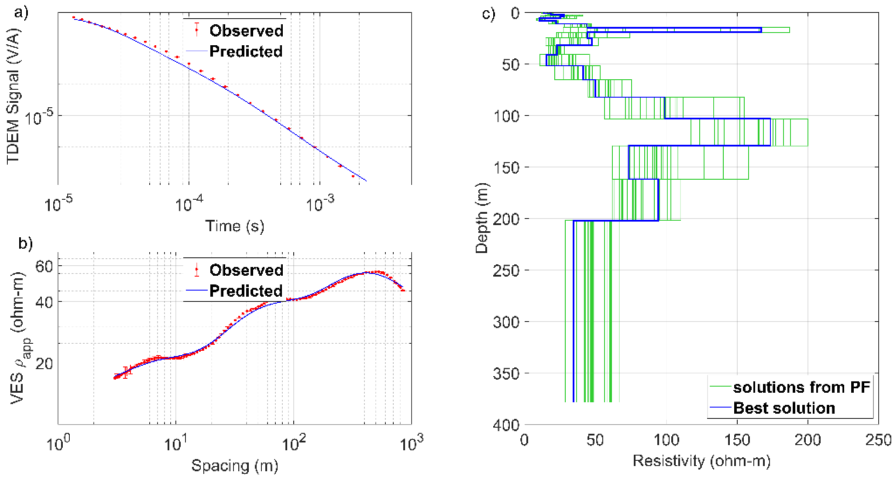

Figure A.2 The result of TV-MOPSO applied to the Villafranca data set: observed data (red dots with error bars) and predicted apparent resistivity (ρ_{app}) for TDEM **(a)** and VES **(b)** data; **c)** the final resistivity models belonging to the *PF* (green lines) and the best solution highlighted in blue.

The MOPSO ran for 600 out of 1000 iterations, since the repository was not filled for 300 consecutive iterations (second stopping criterion). Figure A.3a-b plots the trend, iteration after iteration, of the TDEM and VES components of the objective function, respectively. At the final stages of the optimization, the mean $f_j(\boldsymbol{m})$ (black circles) slightly increased, but the minimum $f_j(\boldsymbol{m})$ (red stars) showed convergence. At the last iteration, the *PF* took the shape shown in Figure A.3c) with red stars. The objective-function values of the other particles of the swarm are marked with black circles. The zoom-in box reveals a complete view of the search space and, in particular, the wide range of the VES-component values for the particles outside the repository. The metrics for the solution appraisal are listed in Table A.2: the *RI* was 12.4% and the *SP* was 0.3584. The deviation angle of 47.3° is highlighted in Figure A.3d) between the Theil-Sen-regression and ideal line, that is, the blue and grey-dashed lines, respectively. The vertical shape of the *PF* as well as the α slightly greater than 45° suggested a partial compatibility between the data sets.

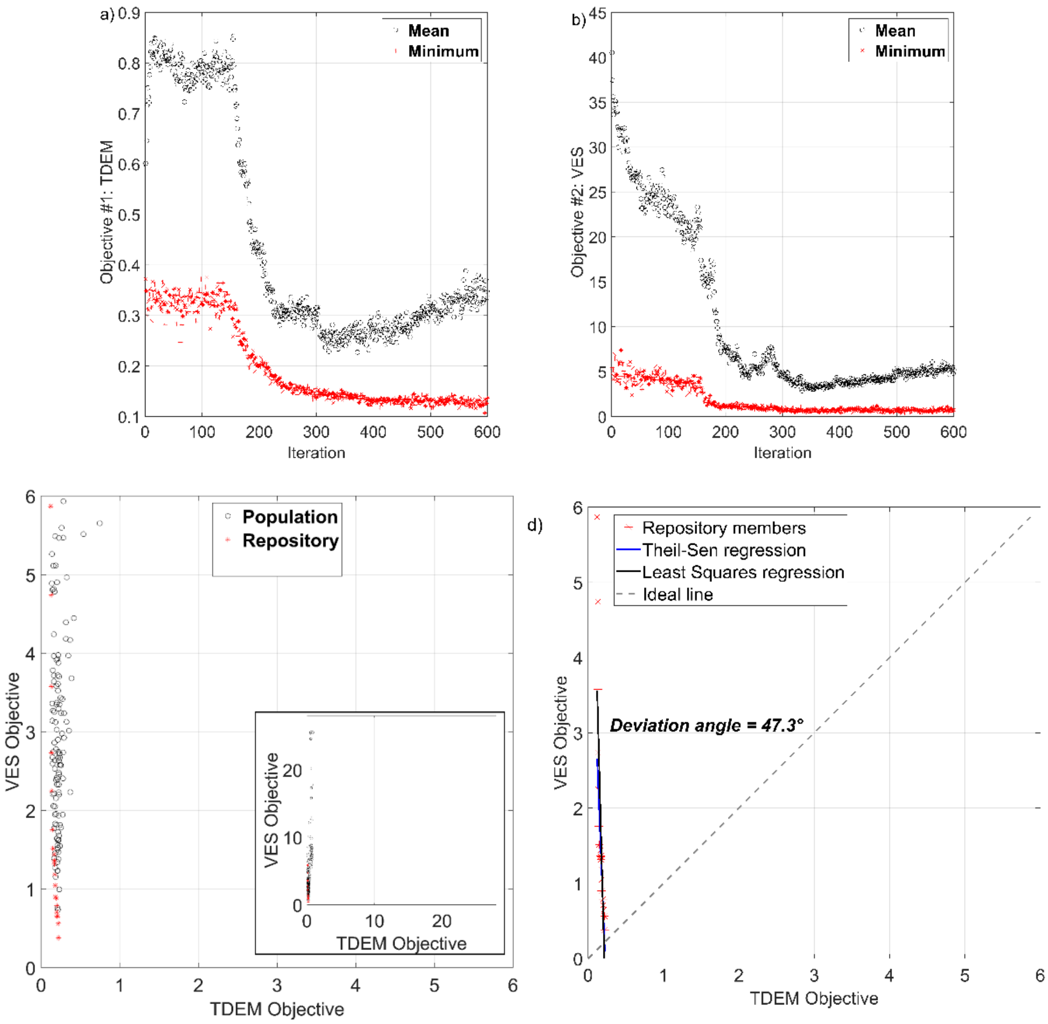

Figure A.3 TV-MOPSO applied to the Villafranca data set: the evolution of the TDEM **(a)** and VES **(b)** components of the objective function from the first to the last iteration for the best particle (red stars) and the remaining ones (black circles); **c)** the 2D space of the objective function (TDEM and VES components) at the last iteration: the red symbols identify the *PF* and the black circles the objective-function values assumed by the other solutions; **d)** the intersection between the ideal line (grey dashed) and the Theil-Sen regression line (red) or the least-square regression line (blue) identifies the deviation angle α.

The benchmark algorithm NSGA-III was applied to the Villafranca data set yielding the outcome illustrated in Figure A.4. Figure A.4a shows the appreciable match between observed TDEM signal (red dots) and calculated response (blue line), while Figure A.4b reports an acceptable fitting for the VES ρ_{app}. The non-dominated solutions drawn from the *PF* are plotted in green in Figure A.4c and the selected blue-model does not present significant differences from them. A resistive body with a peak of 130 Ωm is imaged at about 10-15 m of depth, while from 50 m to 100 m of depth the resistivity increases up to a maximum of 85 Ωm. Then it gradually decreases to 50 Ωm.

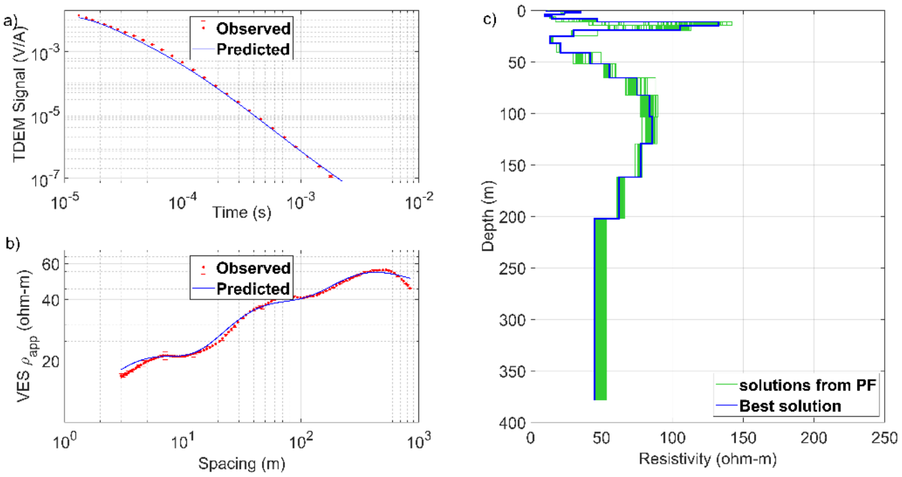

Figure A.4 The result of NSGA-III applied to the Villafranca data set: observed data (red dots with error bars) and predicted apparent resistivity (ρ_{app}) for TDEM **(a)** and VES **(b)** data; **c)** the final resistivity models belonging to the *PF* (green lines) and the best solution highlighted in blue.

The performance of NSGA-III can be read from Figure A.5 and Table A.2. 1000 iterations were requested for a robust minimization of both components of the objective function. Even though Figure A.5a-b shows a decreasing trend, the mean value of the VES component (black circles in Figure A.5b) was two orders of magnitude larger than the corresponding TDEM. However, at the end of the optimization, the minimum values of the TDEM and VES components were quite similar, as depicted in Figure A.5c. It is the snapshot of the objective space at the last iteration. All the population members were evaluated as non-dominated solutions and hence the corresponding objective-function values were marked with black circles and red symbols at the same time (*RI*=100%). The *PF* is plotted with red stars in Figure A.5d, to highlight the deviation angle α = 46.7° between the Theil-Sen-regression blue line and grey-dashed ideal line. The NRMSE is listed in Table A.2 for the results from MOPSO and NSGA-III.

Table A.2 Analysis of the performance of MOPSO and NSGA-III on the data set from Villafranca. The rows report: the number of iterations run, repository index (*RI*), spacing (*SP*), deviation angle (α) between the ideal and Theil-Sen regression line, total runtime in hours, normalized root-mean square error (NRMSE) for TDEM and VES.

Villafranca data set		
	MOPSO	***NSGA-III***
Iterations	600	1000
RI (%)	12.4	100
SP	0.3584	0.0164
α (°)	47.3	46.7
Runtime (h)	7.1	10.8
NRMSE TDEM	0.173	0.2009
NRMSE VES	0.0272	0.0384

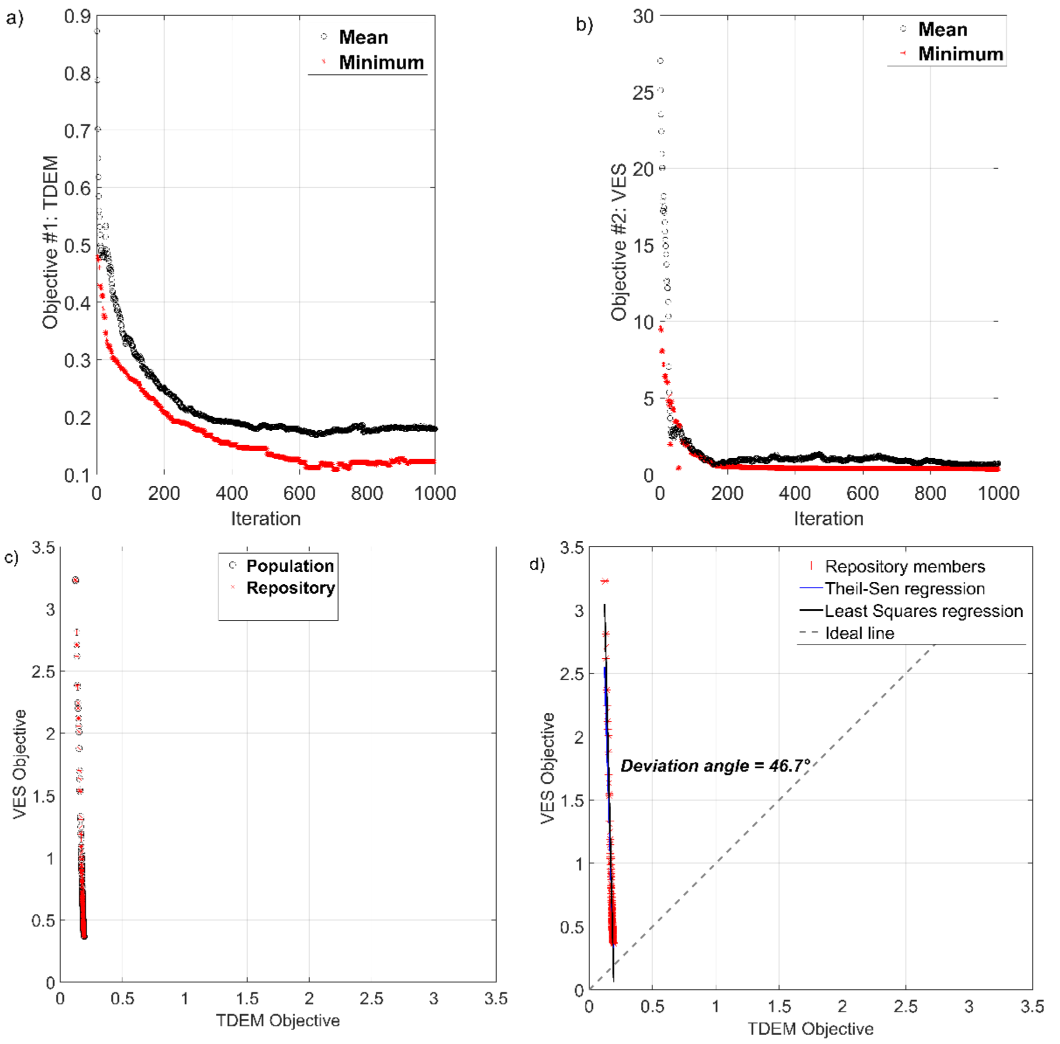

Figure A.5 NSGA-III applied to the Villafranca data set: the evolution of the TDEM **(a)** and VES **(b)** components of the objective function from the first to the last iteration for the best individuals (red stars) and the remaining ones (black circles); **c)** the 2D space of the objective function (TDEM and VES components) at the last iteration: the red symbols identify the *PF*, while the black circles the objective-function values assumed by the other solutions; **d)** the intersection between the ideal line (grey dashed) and the Theil-Sen regression line (red) or the least-square regression line (blue) identifies the deviation angle α.

The application of MOPSO to the Villafranca data set offered an insight into data compatibility. Given the maximum half-spacing of the current electrodes (844 m), the VES reached a depth of investigation higher than that of TDEM sounding, that was negatively affected by the superficial conductive region. The deviation angle of 47.3° > 45° proved the lack of data compatibility. However, a partial compatibility may be assumed because α was slightly bigger than 45° and the *PF* was almost vertical, as proved by the Theil-Sen regression line that tends to bend towards the y-axis (VES component in Figure A.3c). From 40 m of depth downwards, the TDEM data lost resolution and hence the tradeoff solutions from MOPSO mainly interpreted the information from VES. In fact, Figure A.3c showed a clear convergence of the particles on the same value for the TDEM component and, in contrast, a large distribution for the VES components. This explains the vertical shape of the *PF* and the high value of *SP*. The resistivity model obtained from the Villafranca data set using the MOPSO algorithm is in line with the results published in De Luca et al. (2018) using the same TDEM data set. Both the models are in good agreement about the top and bottom of the deep resistive layer constituting the aquifer. Moreover, the introduction of VES information in the MOPSO inversion allowed a more refined definition of the highest resistive portions of the multi-layered aquifer system. From literature, these portions are supposed to be related to the more permeable sandy layers and therefore relevant for water exploitation. Unfortunately, there is no availability of geological or geophysical information on this specific site (well logs, seismic, etc.). In fact, this was the reason for the recent geophysical investigations.

A.4 Results from the single-objective separate optimizations

This section presents the separate optimizations of the synthetic and real data sets using the single-objective PSO. The input parameters of the algorithm were kept as previously explained: the model was discretized into 19 layers, the swarm was composed of 170 particles and the L-curve criterion identified the optimal the Lagrange multiplier. Since the process of separate optimization is simpler than the multi-objective problem, few iterations were required to gain the solution convergence. The PSO algorithm ran for a maximum of 500 iterations or stopped before if the fitness functions did not minimize for 100 consecutive iterations (second stopping criterion). Each run was launched ten times (or “trials”) in order to test the solution variability coming from the initial random distributions. Santilano et al. (2018) indeed proved for 1D MT that different random initializations of the model resulted in highly comparable but not identical final solutions. The MOPSO was not launched for different trials because the dominance criterion exercised, among the possible solutions, the same selective choice performed by several trials of single-objective PSO. In MOPSO, the best-solution selection is a mathematically refined process, while in simple PSO it is based on the straightforward minimization of a single objective. The solution with the minimum NRMSE among the ten solutions was eventually selected as the best optimized model. The boundary conditions of the search space of the solutions were kept as reported in the previous paragraphs for the two data sets, respectively. The simulations have been run by adopting only two workers of the HPC cluster because unnecessary computational resources were not allowed. For this reason, the comparison between the multi-objective and single-objective optimizer could not be assessed in terms of runtime.

For the single-objective PSO of synthetic data, the Lagrange multiplier was 10^{-3}. The best trial of TDEM optimization ran for 398 iterations and the corresponding predicted response and final resistivity model are plotted in blue in Figure A.6a-b, respectively. The outcomes from the other trials are marked in green, while the true model in red. The final NRMSE of the data fitting was 0.0277 and of the model fitting was 0.4445 (Table A.3). The best result from PSO of VES synthetic data, after 419 iterations, is shown in Figure A.7 and gave a final NRMSE of 0.0065 as data misfit and of 0.27 as model misfit (Table A.3). The validity of the synthetic test was evident from the model misfit: the one of MOPSO (Table A.1) was lower than those of the single optimizations (Table A.3). By contrast, the data misfits from the single optimizations (Table A.3) were a little lower than those from MOPSO, but this was not surprising. It is reasonable to assume that the interpretation of both TDEM and VES information limited the data fitting but yielded a better definition of the final model (i.e., lower model misfit).

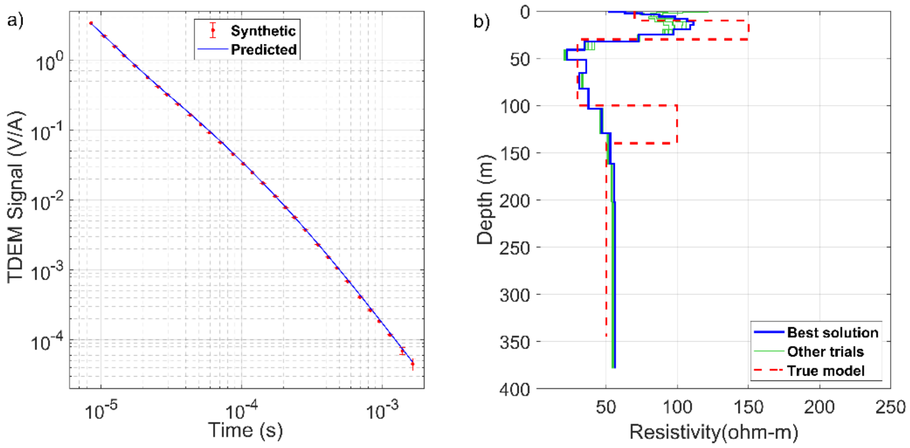

Figure A.6 Single PSO of TDEM synthetic data. **a)** fitting between observed signal (red dots and error bars) and predicted response (blue line); **b)** the red-dashed line is the true model, the green lines correspond to the resistivity models from different PSO trials while the blue line is the best solution.

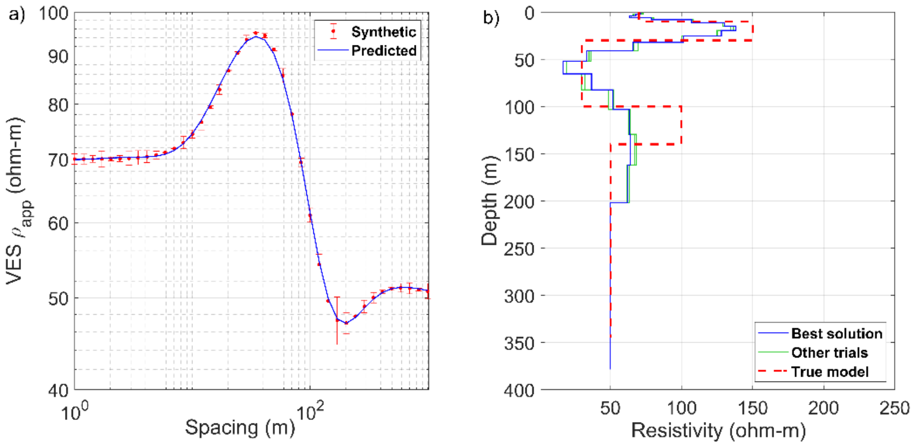

Figure A.7 Single PSO of VES synthetic data. **a)** fitting between observed apparent resistivity ρ_{app} (red dots and error bars) and predicted response (blue line); **b)** the red-dashed line is the true model, the green lines correspond to the resistivity models from different PSO trials while the blue line is the best solution.

As regard the Stupinigi site, the Lagrange multiplier was 10^{-3} and the best trial ran for 500 iterations. The response from PSO of TDEM data is shown in Figure A.8. Figure A.8a plots the significant match between the observed data (red dots and error bars) and the calculated response (blue line) from the best model. It is marked in blue in Figure A.8b and the solutions from other trials in green. All the models concur in identifying a conductive region of about 30 Ωm between 20 and 40 m of depth. Table A.3 lists the final NRMSE of 0.0791.

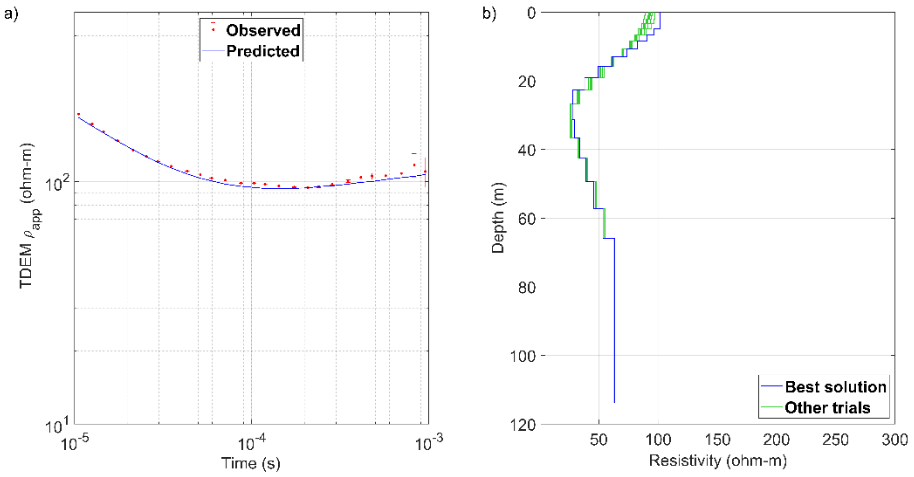

Figure A.8 Single PSO of TDEM measurements at Stupinigi site. **a)** fitting between observed apparent resistivity ρ_{app} (red dots and error bars) and predicted response (blue line); **b)** the resistivity models in green correspond to the different PSO trials while the best solution is marked in blue.

The trend of the optimization is visible in Figure A.9. Figure A.9a plots the decrease of the objective function (***f(m)***) from the first to the last iteration as assumed by the best particle (black dots) and the mean value of the remaining particles (blue dots). Figure A.9b represents the value of ***f(m)*** assumed by the particles as a function of their position in the first two layers of the model (represented by the two horizontal axes): the grey dots reveal the initial random positions of the particles, while the red-circled blue dot is the final position of the whole swarm at convergence. Figure A.9c is the plain view of Figure A.9b and highlights the random initialization of the particles (grey dots). The bar plot of Figure A.9d displays how many particles had the same ***f(m)*** at the end of PSO.

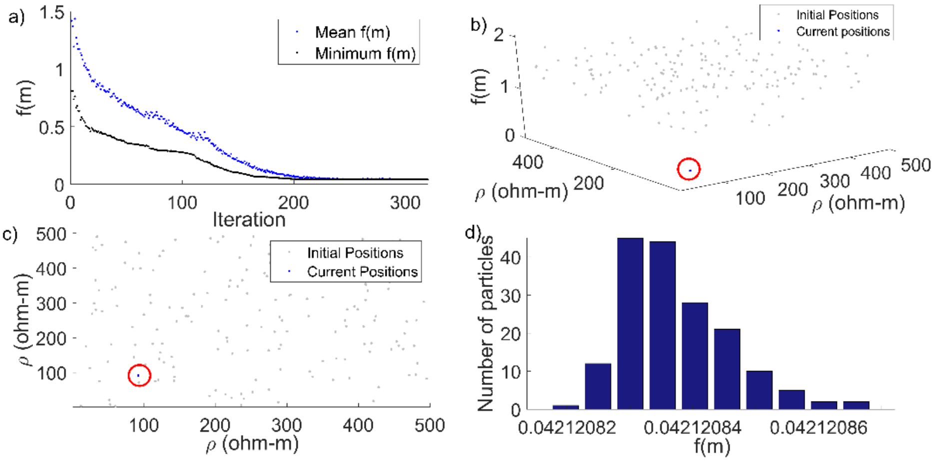

Figure A.9 PSO performance at the end of the optimization: **a)** the decrease of the fitness function, iteration after iteration, for the best particle (black dots) and the remaining swarm (blue dots); **b)** the fitness-function value as a function of the particle positions in the resistivity (ρ) search space, at the first (grey dots) and final (red-circled blue dots) iterations; **c)** plain view of b); **d)** final distribution of the fitness-function values among all the particles.

The response from PSO of VES data is shown in Figure A.10. Figure A.10a plots the significant match between the observed ρ_{app} (red dots and error bars) and the calculated response (blue line) from the best model, that is marked in blue in Figure A.10b. Excepting one trial, the remaining models (green lines), are highly comparable and image a resistive body of about 180 Ωm at about 5 m of depth. Table A.3 lists the final NRMSE of 0.0288.

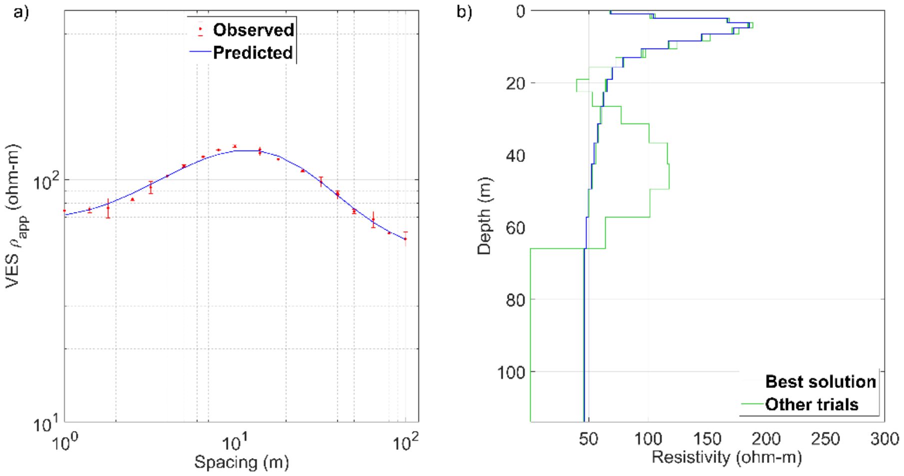

Figure A.10 Single PSO of VES data at Stupinigi site. **a)** fitting between observed apparent resistivity ρ_{app} (red dots and error bars) and predicted response (blue line); **b)** the resistivity models in green correspond to the different PSO trials while the best solution is marked in blue.

The independent optimizations of TDEM and VES from the Villafranca data set spawned the results of Figure A.11 and Figure A.12, respectively. The predicted TDEM signal of Figure A.11a is not dissimilar to the observed data marked with red dots and error bars. The resistivity models of Figure A.11b are plotted in green, while the best trial is marked in blue and was obtained after 325 iterations. The model shows a slight decrease of resistivity from 10 to 25 m of depth and then at 40 m deep an increase from 20 Ωm to 80 Ωm. The NRMSE was 0.2106, as listed in Table A.3. The VES ρ_{app} was distinctly matched after 421 iterations as shown in Figure A.12a. The observed ρ_{app} is plotted with red dots and without the error bars because the measurements were resampled on the original smoothed curve, thus making ambiguous any consideration about errors. Figure A.12b shows the solutions obtained after the ten trials: the best trial is plotted in blue and gave an NRMSE of 0.0148 (Table A.3). The best model images in top-down order: a resistive subsurface of about 90 Ωm, a conductive break with the minimum 6 Ωm at about 30 m of depth and a deep resistive region of about 100 Ωm.

Table A.3 Analysis of the performance of single-objective PSO on the synthetic, Stupinigi and Villafranca data sets. The columns report: the method, the number of iterations run, the normalized root-mean square error (NRMSE) and the runtime of a single trial (in minutes').

	Method	*Iterations*	*NRMSE*	*one-trial runtime(')*
Synthetic test	*TDEM*	302	0.0299 *(data)* 0.4276 *(model)*	122.45
	VES	465	0.0053 *(data)* 0.2621 *(model)*	2.6
Stupinigi data set	*TDEM*	500	0.0791	21.37
	VES	500	0.0288	1.48
Villafranca data set	*TDEM*	325	0.2106	84.86
	VES	421	0.0148	3.61

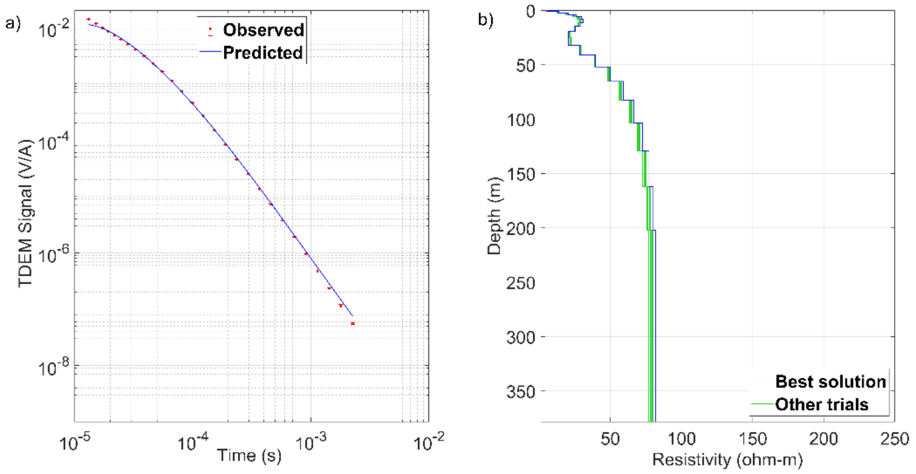

Figure A.11 Single PSO of TDEM measurements at Villafranca site. **a)** fitting between observed signal (red dots and error bars) and predicted response (blue line); **b)** the resistivity models in green correspond to the different PSO trials while the best solution is marked in blue.

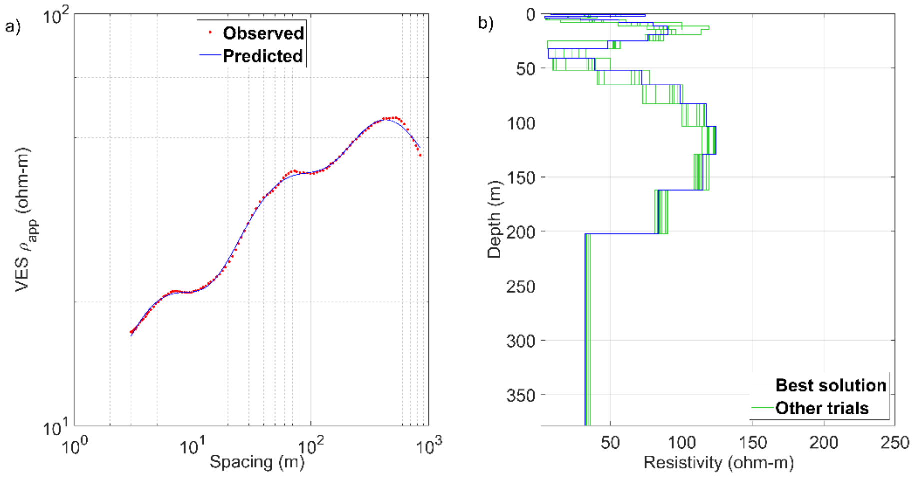

Figure A.12 Single PSO of VES data at Villafranca site. **a)** fitting between observed apparent resistivity ρ_{app} (red dots) and predicted response (blue line); **b)** the resistivity models in green correspond to the different PSO trials while the best solution is marked in blue.

Appendix B

The MT sites of the Larderello-Travale data set

The following table lists complete information on the MT site examined in this thesis. The 86 MT sites were analyzed in terms of dimensionality, strike and phase tensor analysis (Section 5.4). Eleven sites belonging to the same profile were selected for 2D optimization using PSO: *k1, k2, k3, k4, k6, j0, g2, f4, e4, c7, a8*. The 3D MT inversion was carried out on 51 sites due to the regularity of their spatial distribution and the good quality of measurements. The Tipper vector, where measured, was included in 3D inversion.

SITE NAME	LATITUDE	LONGITUDE	ALTITUDE (m.a.s.l.)	TIPPER?	# PERIODS	MIN. PERIOD	MAX. PERIOD	2D OPTIMIZATION	3D INVERSION
A1	43.209359	11.028041	426		72	0.0045	993.0487		yes
A4	43.211859	11.050540	386	yes	69	0.0028	364.0334		yes
A5	43.207137	11.053040	378		75	0.0028	993.0487		yes
A7	43.204915	11.068317	411	yes	74	0.0033	993.0487		yes
A8	43.205748	11.077483	387		75	0.0028	993.0487	yes	yes
B2	43.205471	11.042485	440	yes	74	0.0033	993.0487		yes
B4	43.201304	11.048873	391		70	0.0067	993.0487		yes
B5	43.201860	11.055262	375	yes	75	0.0028	993.0487		yes
B6	43.204637	11.059151	351	yes	60	0.0028	75.8725		yes
B7	43.201582	11.067483	378		75	0.0028	993.0487		yes
B8	43.203804	11.073317	391	yes	35	0.0028	0.9699		yes
C1	43.197415	11.032207	438	yes	48	0.0028	9.4787		yes
C4	43.200193	11.054151	364		55	0.0028	31.0270		yes
C6	43.198249	11.061650	342		75	0.0028	993.0487		yes
C7	43.198526	11.067761	341	yes	74	0.0033	993.0487	yes	yes
C8	43.200193	11.076094	350		75	0.0028	993.0487		yes
C9	43.197415	11.074428	314	yes	74	0.0033	993.0487		yes
D3	43.194915	11.042762	451		56	0.0028	37.9219		yes
D4	43.193249	11.048318	438		75	0.0028	993.0487		yes
D5	43.194915	11.053040	374		75	0.0028	993.0487		yes
D8	43.194638	11.072761	350	yes	75	0.0028	993.0487		yes
D9	43.193249	11.074150	338		61	0.0028	90.9918		yes
E1	43.186860	11.029152	407	yes	63	0.0222	993.0487		yes
E2	43.190749	11.033596	447		75	0.0028	993.0487		yes
E4	43.189638	11.052484	457		75	0.0028	993.0487	yes	yes
E5	43.189360	11.057484	425	yes	75	0.0028	993.0487		yes
E6	43.190471	11.063872	414	yes	62	0.0028	105.0310		yes

E7	43.190471	11.067761	387	yes	75	0.0028	993.0487		yes
E8	43.192693	11.071094	385	yes	75	0.0028	993.0487		yes
F2	43.184915	11.035263	489		53	0.0028	22.7531		yes
F4	43.185193	11.048873	482	yes	75	0.0028	993.0487	yes	yes
F8	43.187416	11.069983	388		75	0.0028	993.0487		yes
F9	43.189360	11.073316	384		75	0.0028	993.0487		yes
F10	43.184916	11.075816	379		60	0.0028	75.8725		yes
G1	43.181027	11.030818	475		63	0.0222	993.0487		yes
G2	43.178804	11.036096	472		75	0.0028	993.0487	yes	yes
G4	43.184360	11.043873	493		41	0.9699	993.0487		yes
G6	43.182693	11.064428	346		75	0.0028	993.0487		yes
G7	43.182693	11.068872	337	yes	69	0.0028	364.0334		yes
G8	43.182693	11.073872	333	yes	75	0.0028	993.0487		yes
G9	43.181582	11.083594	318	yes	75	0.0028	993.0487		yes
H4	43.176860	11.043040	411	yes	74	0.0033	993.0487		yes
I1	43.176582	11.023874	569		61	0.0028	90.9918		yes
I2	43.175749	11.030818	516		44	0.0028	4.7416		yes
I4	43.172971	11.041373	405	yes	56	0.0056	75.8725		yes
J0	43.171860	11.019430	527	yes	75	0.0028	993.0487	yes	yes
J1	43.166583	11.028318	472		50	0.0028	13.1285		yes
J2	43.167416	11.032207	422	yes	68	0.0091	993.0487		yes
J3	43.164916	11.036929	429	yes	75	0.0028	993.0487		yes
K1	43.121583	10.926101	595		75	0.0028	993.0487	yes	
K2	43.126861	10.950544	506	yes	68	0.0028	303.3981	yes	
K3	43.141583	10.972765	755		75	0.0028	993.0487	yes	
K4	43.160194	10.978599	763		61	0.0028	90.9918	yes	
K5	43.171027	10.997764	652		47	0.0045	7.7580		yes
K6	43.170749	11.013875	453	yes	75	0.0028	993.0487	yes	yes
LN13	43.216784	10.930136	435		31	0.0038	546.1496		
LN14	43.214216	10.948829	575		30	0.0038	287.4390		
LN15	43.219932	10.969941	390		31	0.0038	287.4390		
LN16	43.220044	11.002386	325		34	0.0038	546.1496		
LN17	43.218421	11.017907	275		32	0.0038	546.1496		
LN18	43.213575	11.062373	350		32	0.0038	546.1496		
LS11	43.142904	10.927778	460		19	0.0038	10.4221		
LS12	43.148679	10.952587	700		30	0.0038	546.1496		
LS13	43.143456	10.979546	713		20	0.0306	546.1496		
LS14	43.143455	10.996711	570		34	0.0038	546.1496		
LS15	43.140454	11.026542	630		34	0.0038	546.1496		
LS16	43.134787	11.034875	560		26	0.0038	151.6991		
SITE 1	43.149140	11.052961	600		91	0.0013	3276.540		
SITE 2	43.140856	11.002197	596		78	0.0013	3276.540		
SITE 3	43.163571	11.061612	481		78	0.0013	3276.540		
SITE 4	43.176761	11.093921	358		94	0.0010	3276.540		
SITE 5	43.162718	11.083847	380		88	0.0010	3276.540		

SITE 7	43.155640	11.031828	529		73	0.0079	3276.540		
SITE 8	43.162460	11.048290	600		63	0.0013	3276.540		
SITE 9	43.176992	11.081256	348		55	0.0126	3276.540		
SITE 10	43.169040	11.072867	458		95	0.0010	3276.540		
SITE 11	43.149473	11.069980	300		86	0.0010	3276.540		
SITE 12	43.140509	11.016818	642		81	0.0010	3276.540		
SITE 13	43.156577	11.006818	300		58	0.0025	3276.540		
SITE 14	43.146842	11.007963	520		82	0.0010	3276.540		
SITE 15	43.169450	11.055167	526		66	0.0020	1424.704		
SITE 16	43.135017	10.985900	636		72	0.0010	1170.274		
SITE 17	43.144824	10.991505	553		70	0.0010	3276.540		
SITE 18	43.158993	11.020501	509		86	0.0013	3276.540		
SITE 19	43.178967	11.066670	300		61	1.2191	3276.540		
SITE 20	43.146762	11.029812	690		89	0.0016	1424.704		

Appendix C
Static shift correction for the MT sites of the Travale data set

C.1 The new time-domain electromagnetic (TDEM) survey

During the last year of the doctorate program, a TDEM survey was carried out in the geothermal area of Travale in order to correct the static shift occurring for some MT sites. The following figure shows the location of the eight TDEM soundings, whose name was the same of the correspondent MT site.

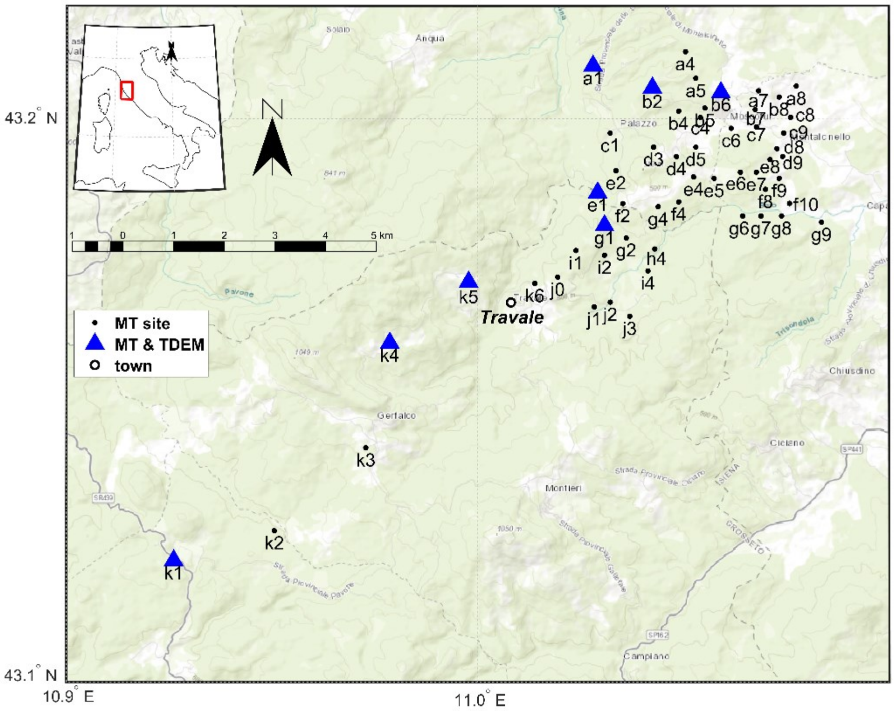

Figure C.1 The MT data set investigated for 2D PSO and 3D inversion covers the Travale geothermal area. The 8 TDEM sites are marked with blue triangles. The town of Travale is located between sites *k5* and *k6*. This map was created by reading a georeferenced image (coming from "openstreetmap") within Matlab Mapping Toolbox (by Mathworks).

C.2 The static-shift corrected curves

The MT apparent-resistivity curves were corrected for the static shift using the optimization method explained in Section 3.3.2. The result for site *b6* was presented in Section 5.5. The following figures show the corrected MT curves (both *xy* and *yx* modes) for the sites: *a1, b2, e1, g1, k1, k4* and *k5*. The raw apparent-resistivity curves (ρ_{app}) affected by distortion are marked with red dots in the box *a)* of each Figure.

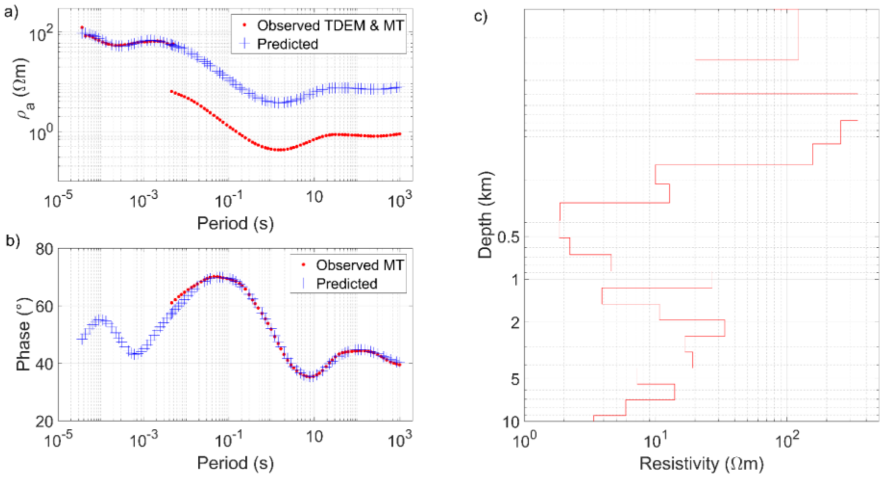

Figure C.2 Static shift correction for site *a1* (xy-mode) using PSO. **a)** The red dots are the observed apparent resistivity (ρ_{app}) of TDEM at low periods (up to 0.005 s) and of MT from 0.004 s upward. The blue crosses indicate the predicted MT ρ_{app} that correct the static shift according to TDEM information; **b)** Observed (red dots) and predicted (blue crosses) MT phase; **c)** The 1D resistivity model (not interpreted here).

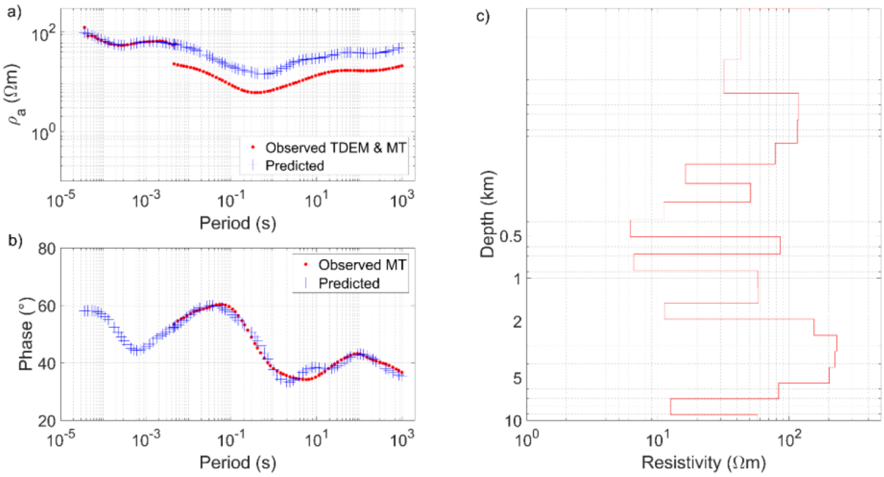

Figure C.3 Static shift correction for site *a1* (yx-mode) using PSO. **a)** The red dots are the observed apparent resistivity (ρ_{app}) of TDEM at low periods (up to 0.005 s) and of MT from 0.004 s upward. The blue crosses indicate the predicted MT ρ_{app} that correct the static shift according to TDEM information; **b)** Observed (red dots) and predicted (blue crosses) MT phase; **c)** The 1D resistivity model (not interpreted here).

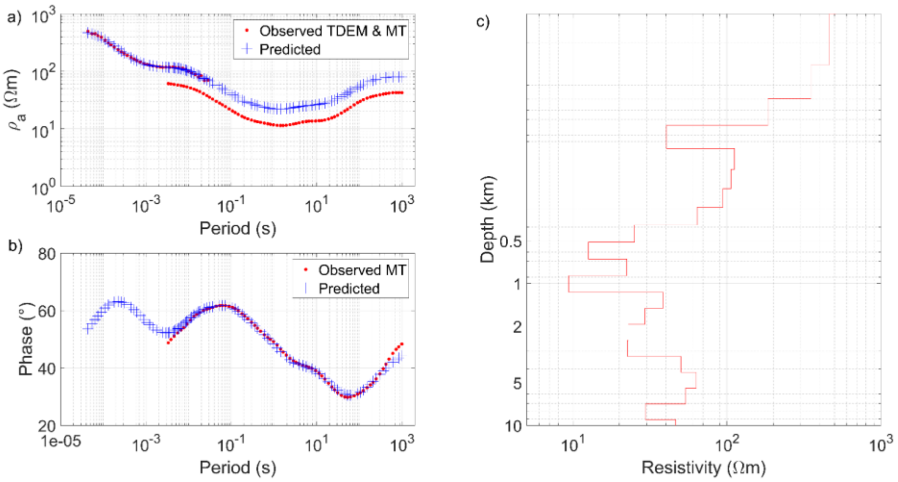

Figure C.4 Static shift correction for site *b2* (xy-mode) using PSO. **a)** The red dots are the observed apparent resistivity (ρ_{app}) of TDEM at low periods (up to 0.005 s) and of MT from 0.003 s upward. The blue crosses indicate the predicted MT ρ_{app} that correct the static shift according to TDEM information; **b)** Observed (red dots) and predicted (blue crosses) MT phase; **c)** The 1D resistivity model (not interpreted here).

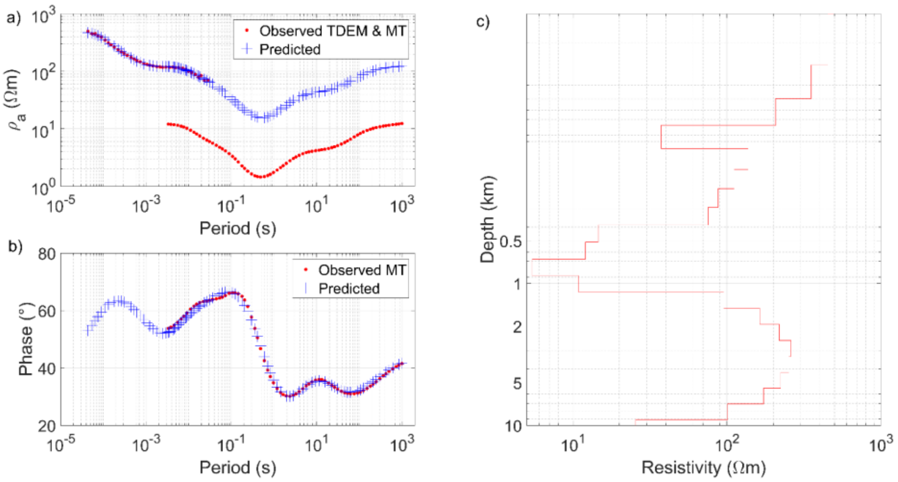

Figure C.5 Static shift correction for site *b2* (yx-mode) using PSO. **a)** The red dots are the observed apparent resistivity (ρ_{app}) of TDEM at low periods (up to 0.03 s) and of MT from 0.003 s upward. The blue crosses indicate the predicted MT ρ_{app} that correct the static shift according to TDEM information; **b)** Observed (red dots) and predicted (blue crosses) MT phase; **c)** The 1D resistivity model (not interpreted here).

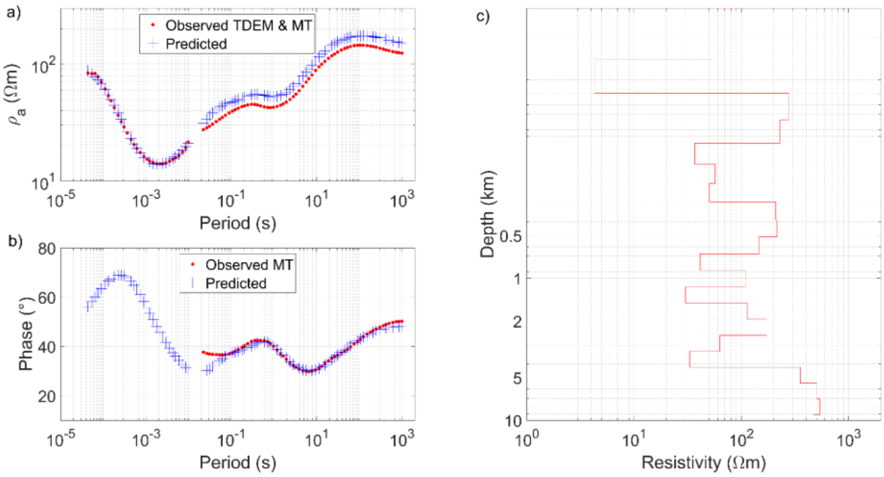

Figure C.6 Static shift correction for site *e1* (xy-mode) using PSO. **a)** The red dots are the observed apparent resistivity (ρ_{app}) of TDEM at low periods (up to 0.01 s) and of MT from 0.02 s upward. The blue crosses indicate the predicted MT ρ_{app} that correct the static shift according to TDEM information; **b)** Observed (red dots) and predicted (blue crosses) MT phase; **c)** The 1D resistivity model (not interpreted here).

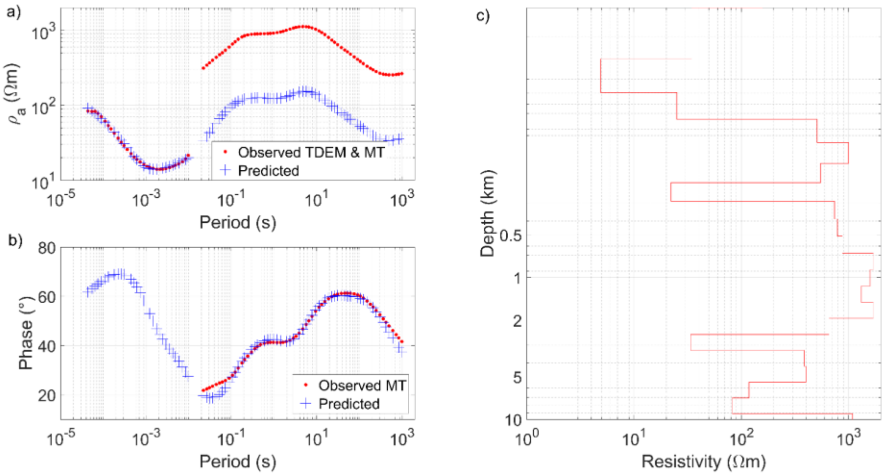

Figure C.7 Static shift correction for site *e1* (yx-mode) using PSO. **a)** The red dots are the observed apparent resistivity (ρ_{app}) of TDEM at low periods (up to 0.01 s) and of MT from 0.02 s upward. The blue crosses indicate the predicted MT ρ_{app} that correct the static shift according to TDEM information; **b)** Observed (red dots) and predicted (blue crosses) MT phase; **c)** The 1D resistivity model (not interpreted here).

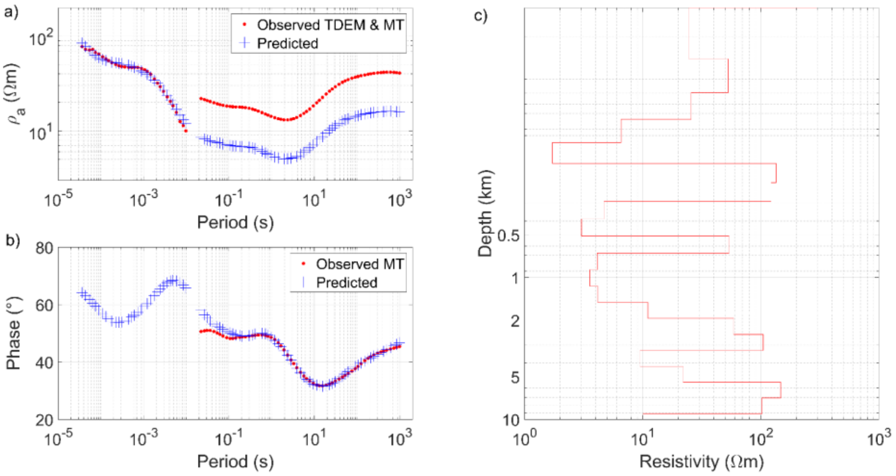

Figure C.8 Static shift correction for site *g1* (xy-mode) using PSO. **a)** The red dots are the observed apparent resistivity (ρ_{app}) of TDEM at low periods (up to 0.001 s) and of MT from 0.002 s upward. The blue crosses indicate the predicted MT ρ_{app} that correct the static shift according to TDEM information; **b)** Observed (red dots) and predicted (blue crosses) MT phase; **c)** The 1D resistivity model (not interpreted here).

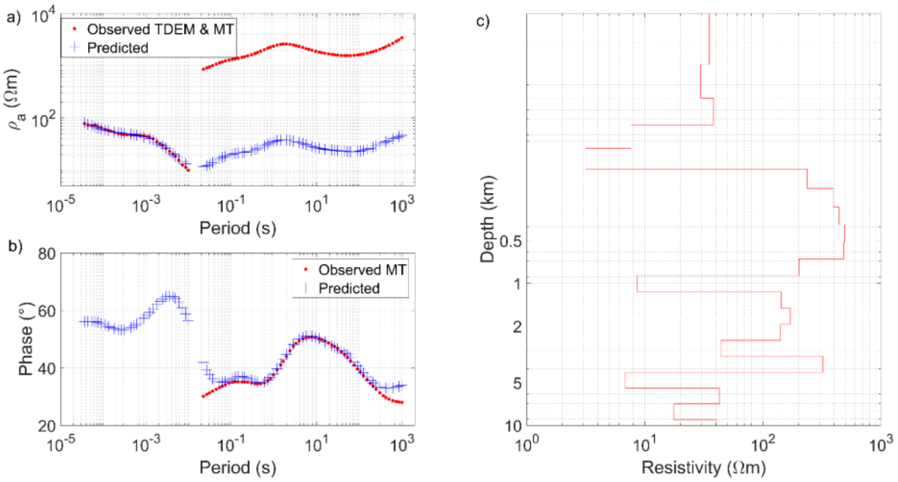

Figure C.9 Static shift correction for site *g1* (yx-mode) using PSO. **a)** The red dots are the observed apparent resistivity (ρ_{app}) of TDEM at low periods (up to 0.001 s) and of MT from 0.002 s upward. The blue crosses indicate the predicted MT ρ_{app} that correct the static shift according to TDEM information; **b)** Observed (red dots) and predicted (blue crosses) MT phase; **c)** The 1D resistivity model (not interpreted here).

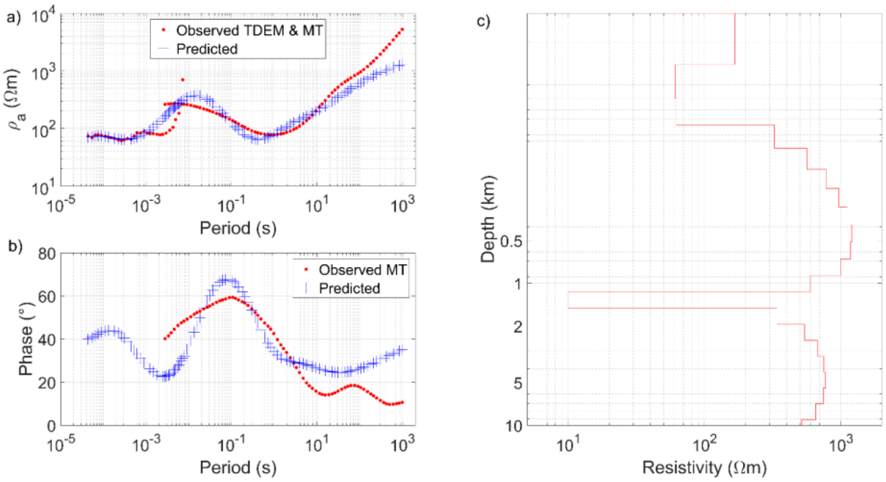

Figure C.10 Static shift correction for site *k1* (xy-mode) using PSO. **a)** The red dots are the observed apparent resistivity (ρ_{app}) of TDEM at low periods (up to 0.007 s) and of MT from 0.003 s upward. The blue crosses indicate the predicted MT ρ_{app} that correct the static shift according to TDEM information; **b)** Observed (red dots) and predicted (blue crosses) MT phase; **c)** The 1D resistivity model (not interpreted here).

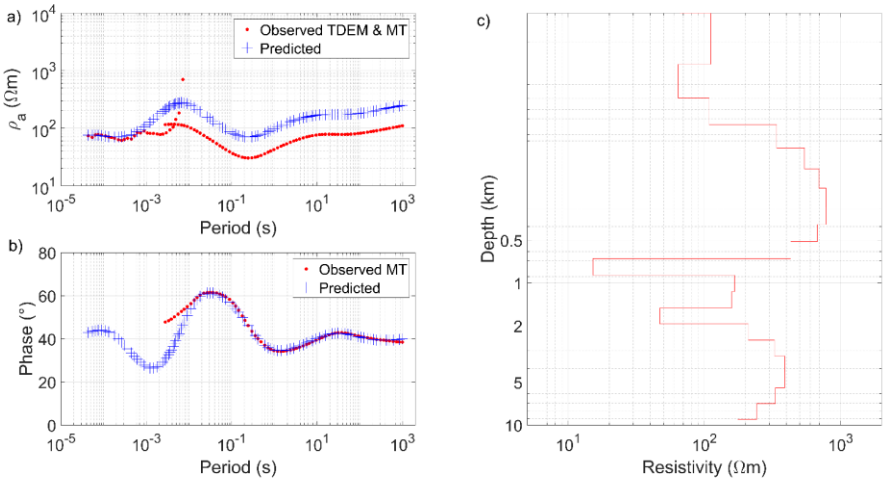

Figure C.11 Static shift correction for site *k1* (yx-mode) using PSO. **a)** The red dots are the observed apparent resistivity (ρ_{app}) of TDEM at low periods (up to 0.007 s) and of MT from 0.003 s upward. The blue crosses indicate the predicted MT ρ_{app} that correct the static shift according to TDEM information; **b)** Observed (red dots) and predicted (blue crosses) MT phase; **c)** The 1D resistivity model (not interpreted here).

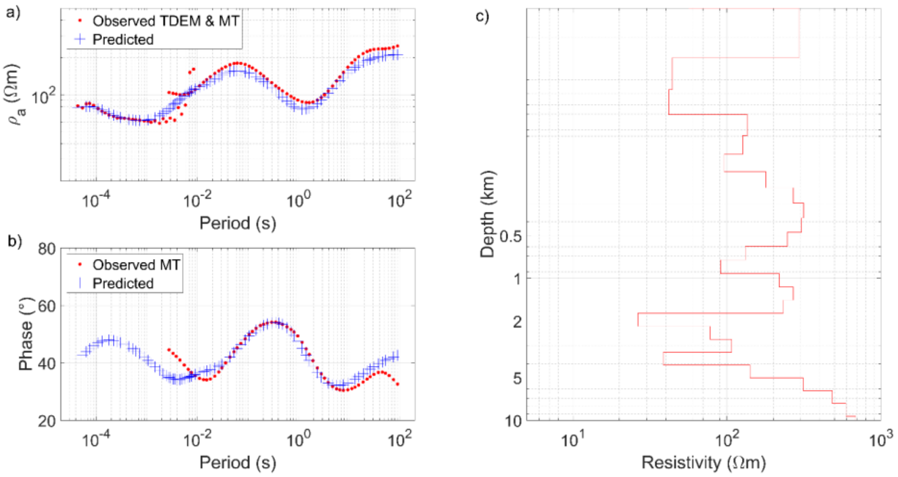

Figure C.12 Static shift correction for site *k4* (xy-mode) using PSO. **a)** The red dots are the observed apparent resistivity (ρ_{app}) of TDEM at low periods (up to 0.006 s) and of MT from 0.003 s upward. The blue crosses indicate the predicted MT ρ_{app} that correct the static shift according to TDEM information; **b)** Observed (red dots) and predicted (blue crosses) MT phase; **c)** The 1D resistivity model (not interpreted here).

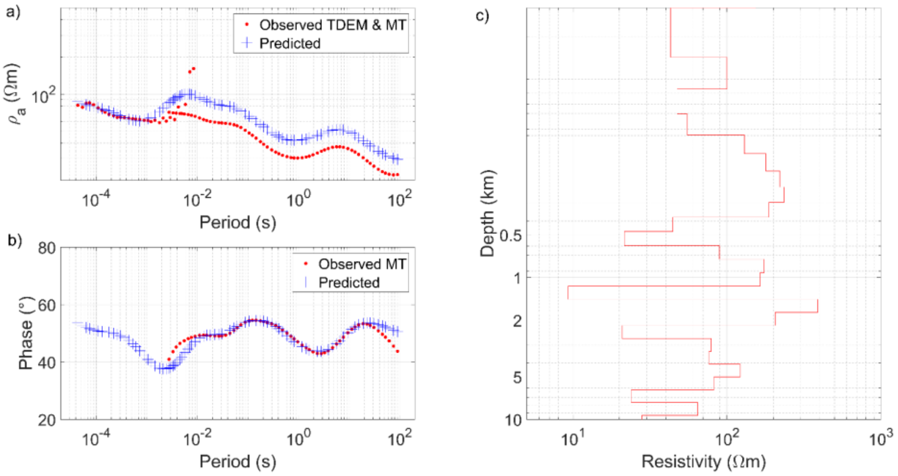

Figure C.13 Static shift correction for site *k4* (yx-mode) using PSO. **a)** The red dots are the observed apparent resistivity (ρ_{app}) of TDEM at low periods (up to 0.006 s) and of MT from 0.003 s upward. The blue crosses indicate the predicted MT ρ_{app} that correct the static shift according to TDEM information; **b)** Observed (red dots) and predicted (blue crosses) MT phase; **c)** The 1D resistivity model (not interpreted here).

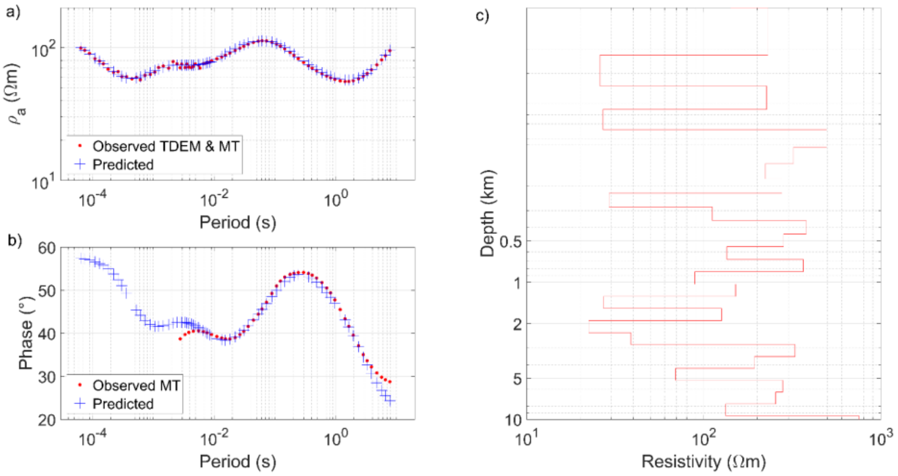

Figure C.14 Static shift correction for site *k5* (xy-mode) using PSO. **a)** The red dots are the observed apparent resistivity (ρ_{app}) of TDEM at low periods (up to 0.006 s) and of MT from 0.003 s upward. The blue crosses indicate the predicted MT ρ_{app} that correct the static shift according to TDEM information; **b)** Observed (red dots) and predicted (blue crosses) MT phase; **c)** The 1D resistivity model (not interpreted here).

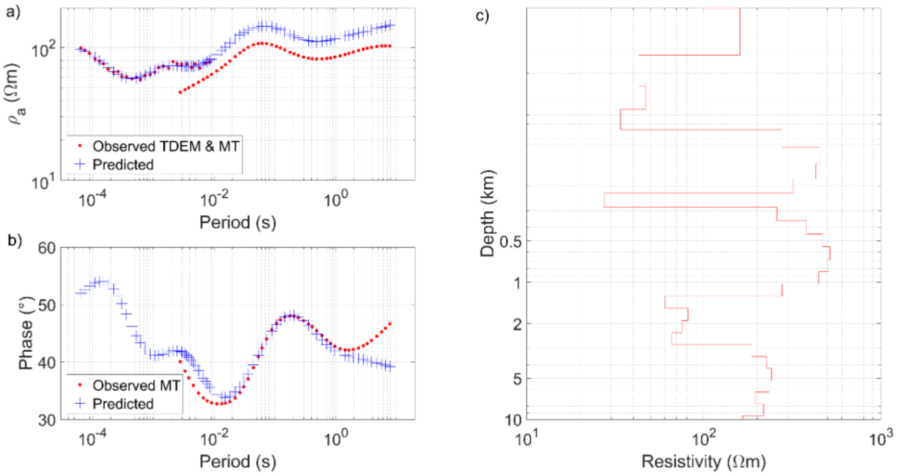

Figure C.15 Static shift correction for site *k5* (yx-mode) using PSO. **a)** The red dots are the observed apparent resistivity (ρ_{app}) of TDEM at low periods (up to 0.006 s) and of MT from 0.003 s upward. The blue crosses indicate the predicted MT ρ_{app} that correct the static shift according to TDEM information; **b)** Observed (red dots) and predicted (blue crosses) MT phase; **c)** The 1D resistivity model (not interpreted here).

Appendix D
Supplementary material of 3D MT inversion: data fitting of inversion test A

The following figures show the data fitting for the 51 MT sites after the inversion test A, whose inversion setting are north-oriented grid, full *Z* and *T* inversion, 10% error floor for Z_{xy}, Z_{yx} and *T*, 15% error floor for Z_{xx} and Z_{yy}, homogeneous starting model and smoothing factors along the horizontal and vertical directions equal to 0.2, 0.2 and 0.1, respectively (Table 7.1) The fitting between measured data (colored dots) and predicted response (colored lines) is plotted for apparent resistivity and phase of the impedance tensor components.

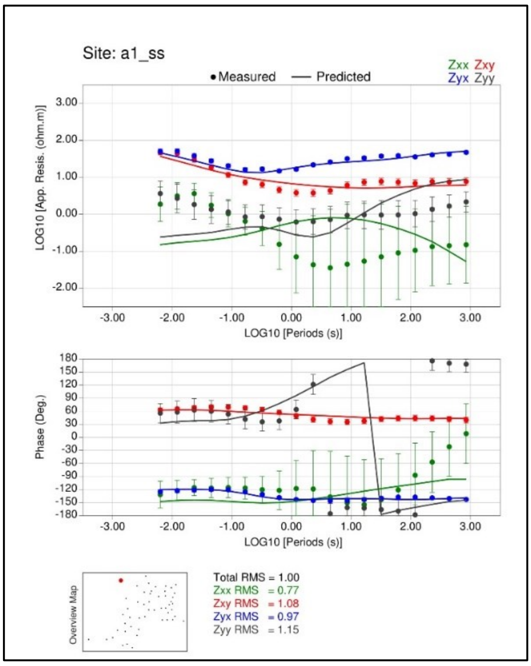

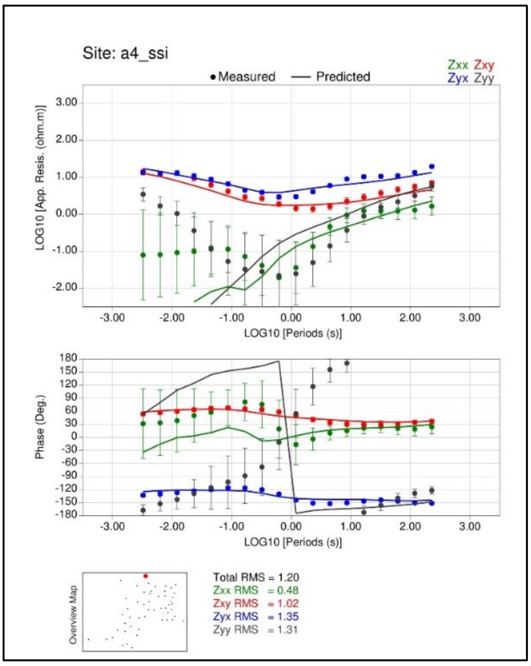

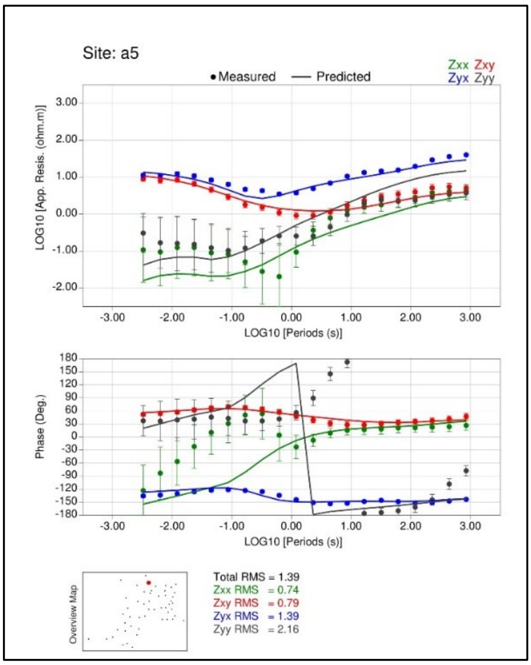
Site: a5
• Measured — Predicted
Zxx Zxy
Zyx Zyy
LOG10 [App. Resis. (ohm.m)]
LOG10 [Periods (s)]
Phase (Deg.)
LOG10 [Periods (s)]
Overview Map
Total RMS = 1.39
Zxx RMS = 0.74
Zxy RMS = 0.79
Zyx RMS = 1.39
Zyy RMS = 2.16

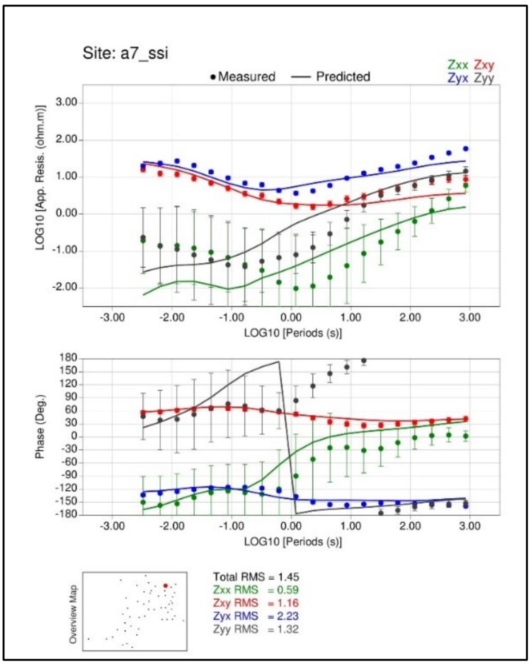
Site: a7_ssi
• Measured — Predicted
Zxx Zxy
Zyx Zyy
LOG10 [App. Resis. (ohm.m)]
LOG10 [Periods (s)]
Phase (Deg.)
LOG10 [Periods (s)]
Overview Map
Total RMS = 1.45
Zxx RMS = 0.59
Zxy RMS = 1.16
Zyx RMS = 2.23
Zyy RMS = 1.32

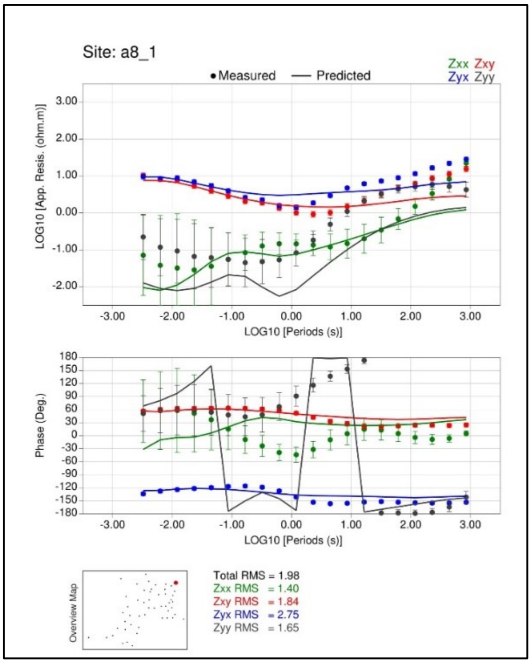
Site: a8_1
• Measured — Predicted
Zxx Zxy
Zyx Zyy
LOG10 [App. Resis. (ohm.m)]
LOG10 [Periods (s)]
Phase (Deg.)
LOG10 [Periods (s)]
Overview Map
Total RMS = 1.98
Zxx RMS = 1.40
Zxy RMS = 1.84
Zyx RMS = 2.75
Zyy RMS = 1.65

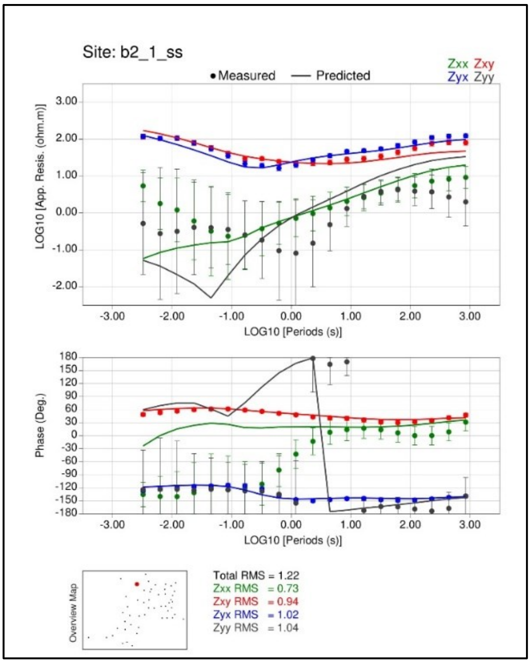
Site: b2_1_ss
• Measured — Predicted
Zxx Zxy
Zyx Zyy
LOG10 [App. Resis. (ohm.m)]
LOG10 [Periods (s)]
Phase (Deg.)
LOG10 [Periods (s)]
Overview Map
Total RMS = 1.22
Zxx RMS = 0.73
Zxy RMS = 0.94
Zyx RMS = 1.02
Zyy RMS = 1.04

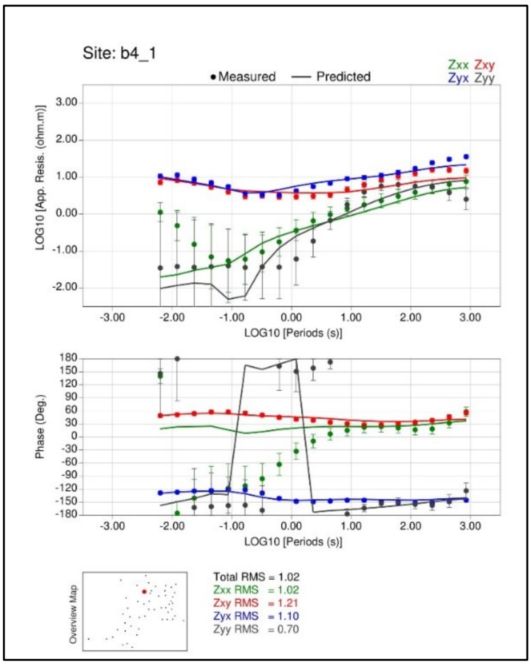
Site: b4_1
• Measured — Predicted
Zxx Zxy
Zyx Zyy
LOG10 [App. Resis. (ohm.m)]
LOG10 [Periods (s)]
Phase (Deg.)
LOG10 [Periods (s)]
Overview Map
Total RMS = 1.02
Zxx RMS = 1.02
Zxy RMS = 1.21
Zyx RMS = 1.10
Zyy RMS = 0.70

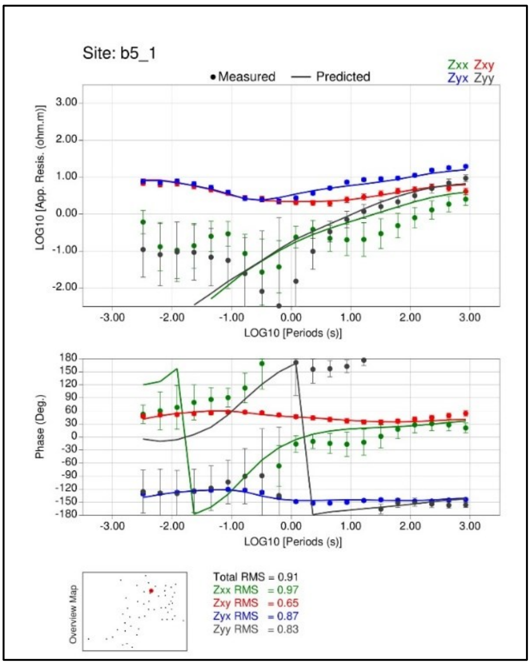
Site: b5_1
• Measured — Predicted
Zxx Zxy
Zyx Zyy
LOG10 [App. Resis. (ohm.m)]
LOG10 [Periods (s)]
Phase (Deg.)
LOG10 [Periods (s)]
Overview Map
Total RMS = 0.91
Zxx RMS = 0.97
Zxy RMS = 0.65
Zyx RMS = 0.87
Zyy RMS = 0.83

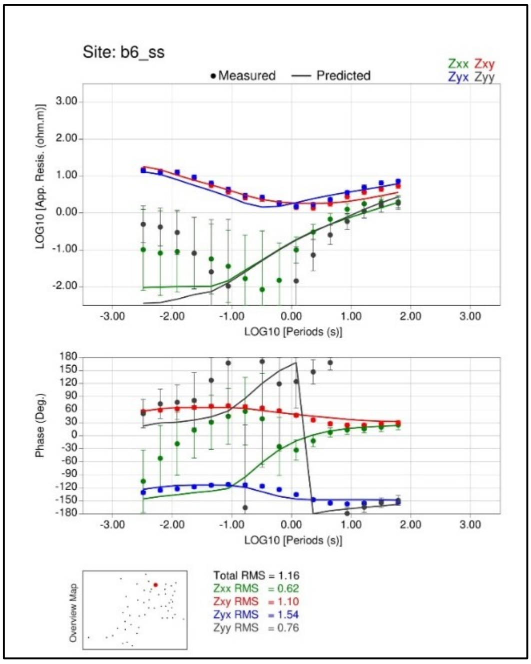
Site: b6_ss
• Measured — Predicted
Zxx Zxy
Zyx Zyy
LOG10 [App. Resis. (ohm.m)]
LOG10 [Periods (s)]
Phase (Deg.)
LOG10 [Periods (s)]
Overview Map
Total RMS = 1.16
Zxx RMS = 0.62
Zxy RMS = 1.10
Zyx RMS = 1.54
Zyy RMS = 0.76

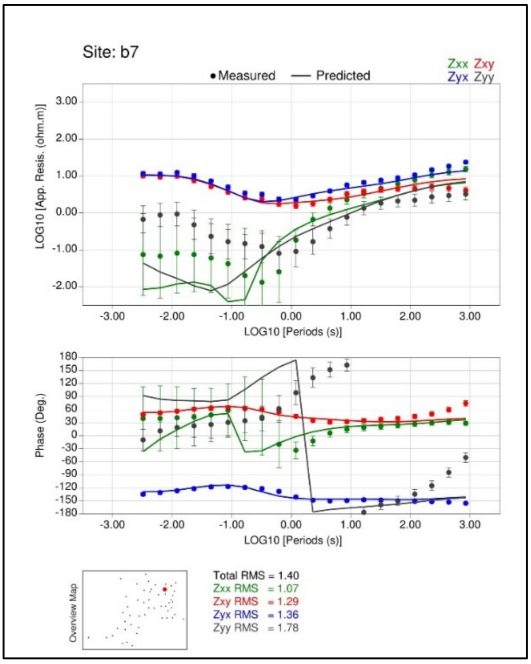
Site: b7
• Measured — Predicted
Zxx Zxy
Zyx Zyy
LOG10 [App. Resis. (ohm.m)]
LOG10 [Periods (s)]
Phase (Deg.)
LOG10 [Periods (s)]
Overview Map
Total RMS = 1.40
Zxx RMS = 1.07
Zxy RMS = 1.29
Zyx RMS = 1.36
Zyy RMS = 1.78

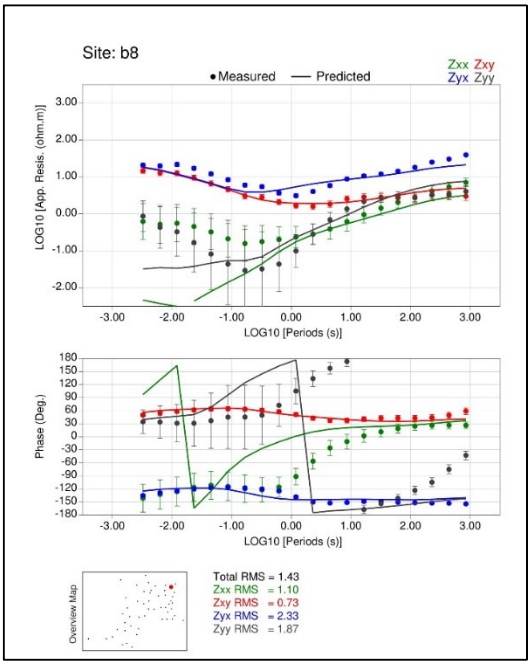
Site: b8
Zxx Zxy
Zyx Zyy
• Measured — Predicted
LOG10 [App. Resis. (ohm.m)]
3.00
2.00
1.00
0.00
-1.00
-2.00
-3.00 -2.00 -1.00 0.00 1.00 2.00 3.00
LOG10 [Periods (s)]
Phase (Deg.)
180 150 120 90 60 30 0 -30 -60 -90 -120 -150 -180
LOG10 [Periods (s)]
Overview Map
Total RMS = 1.43
Zxx RMS = 1.10
Zxy RMS = 0.73
Zyx RMS = 2.33
Zyy RMS = 1.87

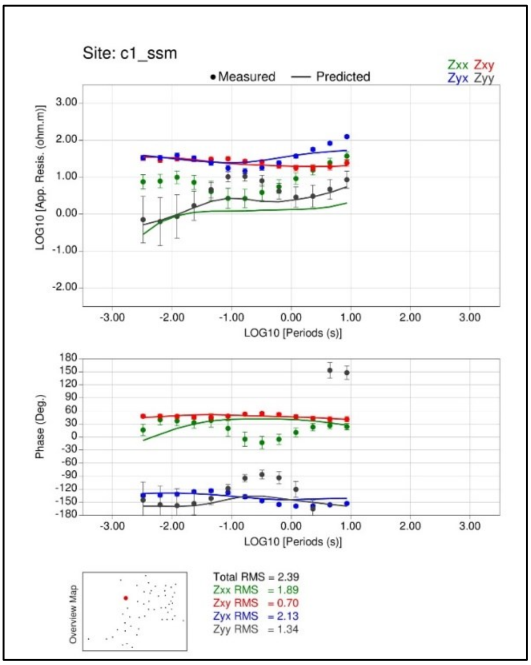
Site: c1_ssm
Zxx Zxy
Zyx Zyy
• Measured — Predicted
LOG10 [App. Resis. (ohm.m)]
3.00
2.00
1.00
0.00
-1.00
-2.00
-3.00 -2.00 -1.00 0.00 1.00 2.00 3.00
LOG10 [Periods (s)]
Phase (Deg.)
180 150 120 90 60 30 0 -30 -60 -90 -120 -150 -180
LOG10 [Periods (s)]
Overview Map
Total RMS = 2.39
Zxx RMS = 1.89
Zxy RMS = 0.70
Zyx RMS = 2.13
Zyy RMS = 1.34

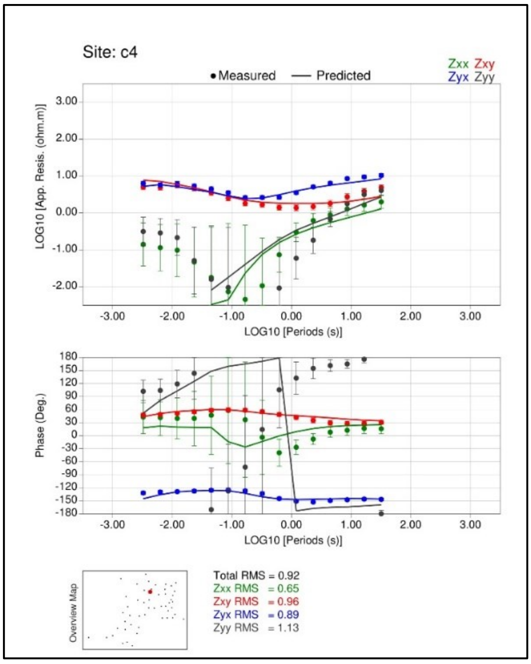
Site: c4
Zxx Zxy
Zyx Zyy
• Measured — Predicted
LOG10 [App. Resis. (ohm.m)]
3.00
2.00
1.00
0.00
-1.00
-2.00
-3.00 -2.00 -1.00 0.00 1.00 2.00 3.00
LOG10 [Periods (s)]
Phase (Deg.)
180 150 120 90 60 30 0 -30 -60 -90 -120 -150 -180
LOG10 [Periods (s)]
Overview Map
Total RMS = 0.92
Zxx RMS = 0.65
Zxy RMS = 0.96
Zyx RMS = 0.89
Zyy RMS = 1.13

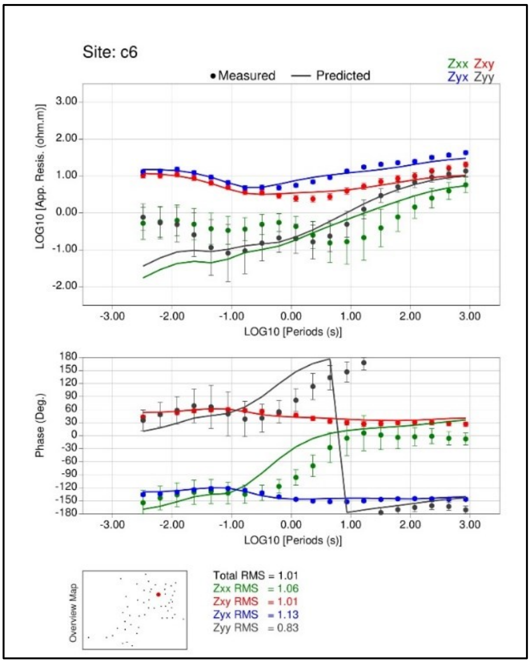
Site: c6
Zxx Zxy
Zyx Zyy
• Measured — Predicted
LOG10 [App. Resis. (ohm.m)]
3.00
2.00
1.00
0.00
-1.00
-2.00
-3.00 -2.00 -1.00 0.00 1.00 2.00 3.00
LOG10 [Periods (s)]
Phase (Deg.)
180 150 120 90 60 30 0 -30 -60 -90 -120 -150 -180
LOG10 [Periods (s)]
Overview Map
Total RMS = 1.01
Zxx RMS = 1.06
Zxy RMS = 1.01
Zyx RMS = 1.13
Zyy RMS = 0.83

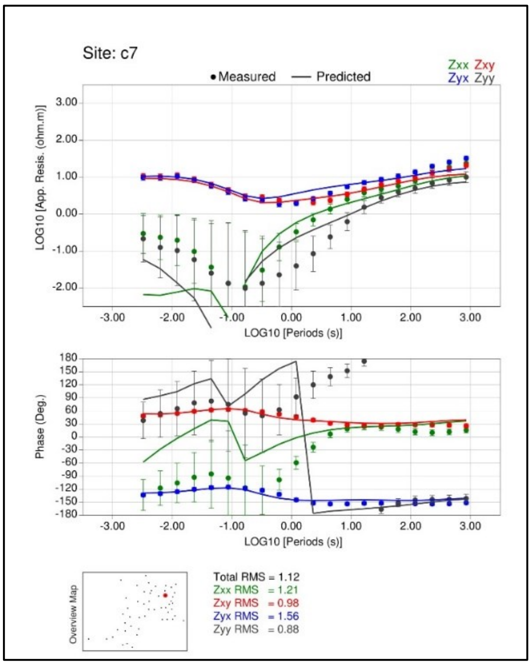
Site: c7
Measured
Predicted
Zxx Zxy
Zyx Zyy
LOG10 [App. Resis. (ohm.m)]
LOG10 [Periods (s)]
Phase (Deg.)
Overview Map
Total RMS = 1.12
Zxx RMS = 1.21
Zxy RMS = 0.98
Zyx RMS = 1.56
Zyy RMS = 0.88

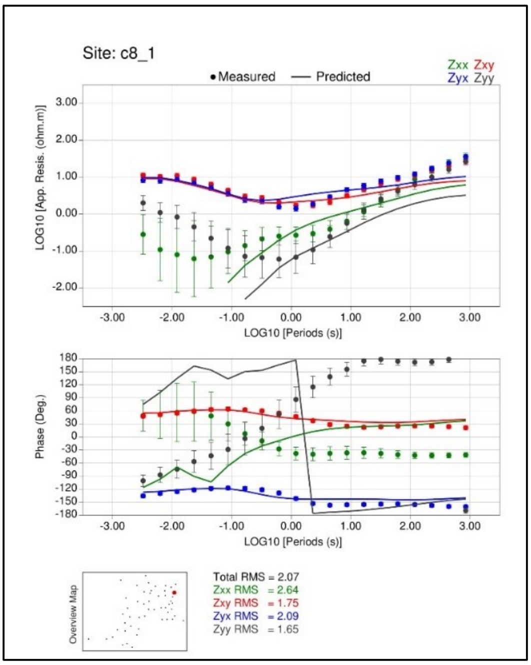
Site: c8_1
Measured
Predicted
Zxx Zxy
Zyx Zyy
LOG10 [App. Resis. (ohm.m)]
LOG10 [Periods (s)]
Phase (Deg.)
Overview Map
Total RMS = 2.07
Zxx RMS = 2.64
Zxy RMS = 1.75
Zyx RMS = 2.09
Zyy RMS = 1.65

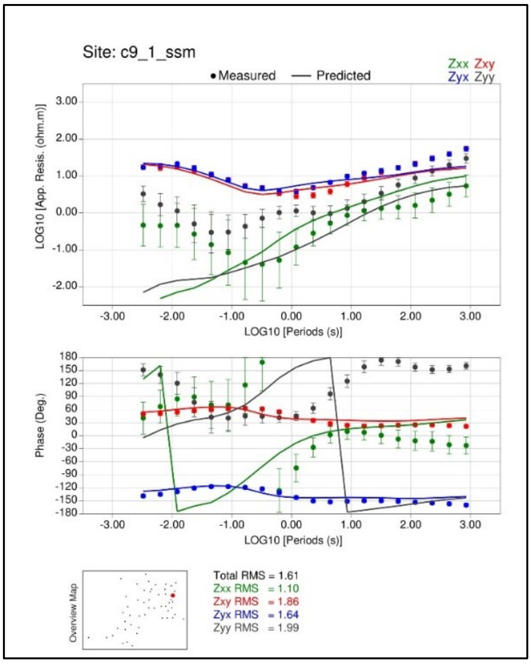
Site: c9_1_ssm
Measured
Predicted
Zxx Zxy
Zyx Zyy
LOG10 [App. Resis. (ohm.m)]
LOG10 [Periods (s)]
Phase (Deg.)
Overview Map
Total RMS = 1.61
Zxx RMS = 1.10
Zxy RMS = 1.86
Zyx RMS = 1.64
Zyy RMS = 1.99

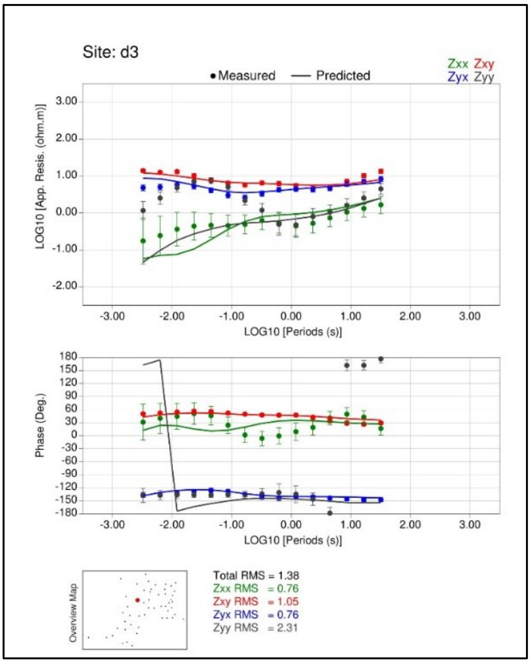
Site: d3
Measured
Predicted
Zxx Zxy
Zyx Zyy
LOG10 [App. Resis. (ohm.m)]
LOG10 [Periods (s)]
Phase (Deg.)
Overview Map
Total RMS = 1.38
Zxx RMS = 0.76
Zxy RMS = 1.05
Zyx RMS = 0.76
Zyy RMS = 2.31

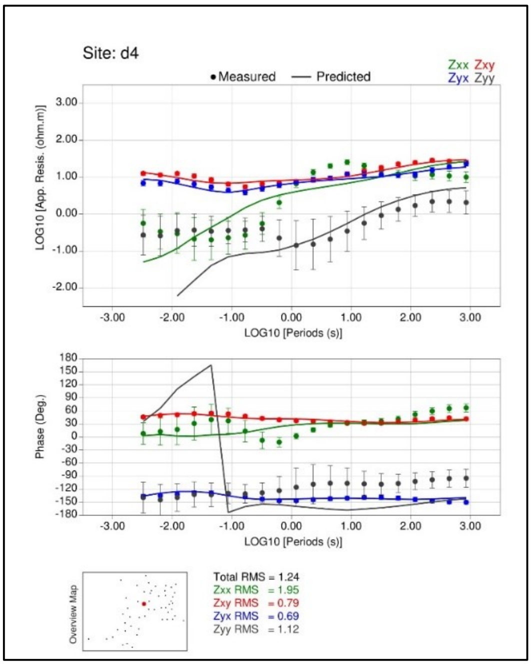
Site: d4
• Measured — Predicted
Zxx Zxy
Zyx Zyy
LOG10 [App. Resis. (ohm.m)]
LOG10 [Periods (s)]
Phase (Deg.)
Overview Map
Total RMS = 1.24
Zxx RMS = 1.95
Zxy RMS = 0.79
Zyx RMS = 0.69
Zyy RMS = 1.12

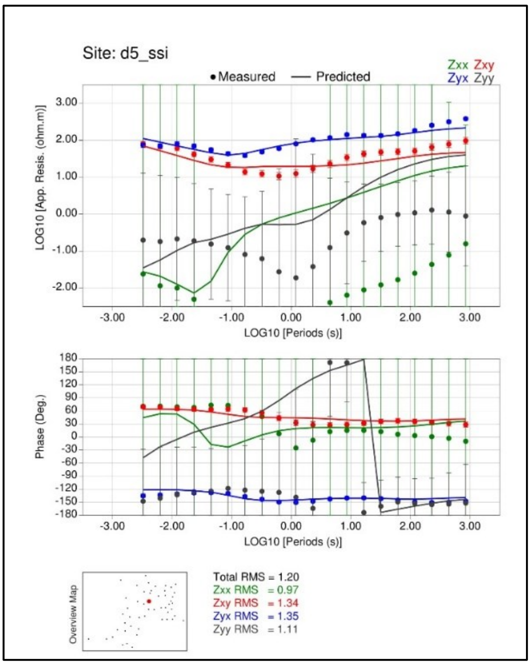
Site: d5_ssi
• Measured — Predicted
Zxx Zxy
Zyx Zyy
LOG10 [App. Resis. (ohm.m)]
LOG10 [Periods (s)]
Phase (Deg.)
Overview Map
Total RMS = 1.20
Zxx RMS = 0.97
Zxy RMS = 1.34
Zyx RMS = 1.35
Zyy RMS = 1.11

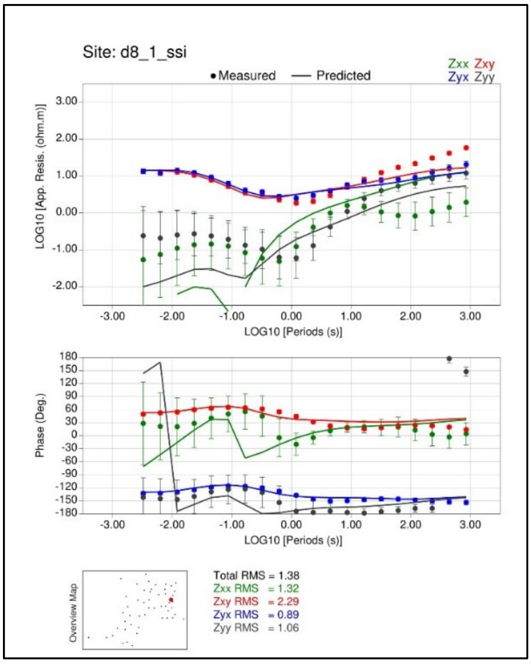
Site: d8_1_ssi
• Measured — Predicted
Zxx Zxy
Zyx Zyy
LOG10 [App. Resis. (ohm.m)]
LOG10 [Periods (s)]
Phase (Deg.)
Overview Map
Total RMS = 1.38
Zxx RMS = 1.32
Zxy RMS = 2.29
Zyx RMS = 0.89
Zyy RMS = 1.06

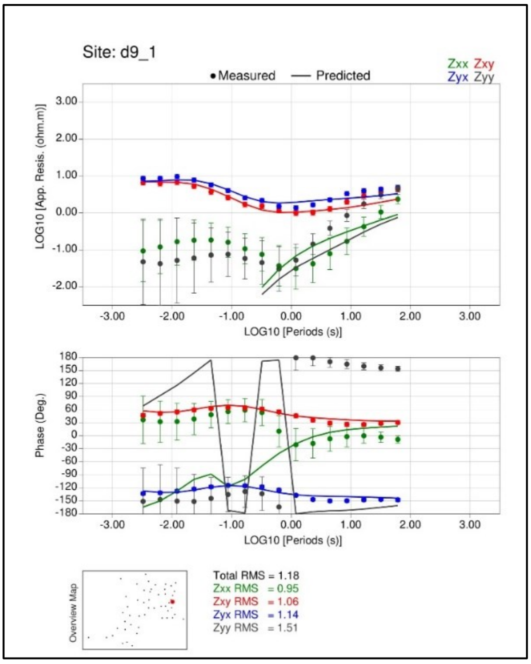
Site: d9_1
• Measured — Predicted
Zxx Zxy
Zyx Zyy
LOG10 [App. Resis. (ohm.m)]
LOG10 [Periods (s)]
Phase (Deg.)
Overview Map
Total RMS = 1.18
Zxx RMS = 0.95
Zxy RMS = 1.06
Zyx RMS = 1.14
Zyy RMS = 1.51

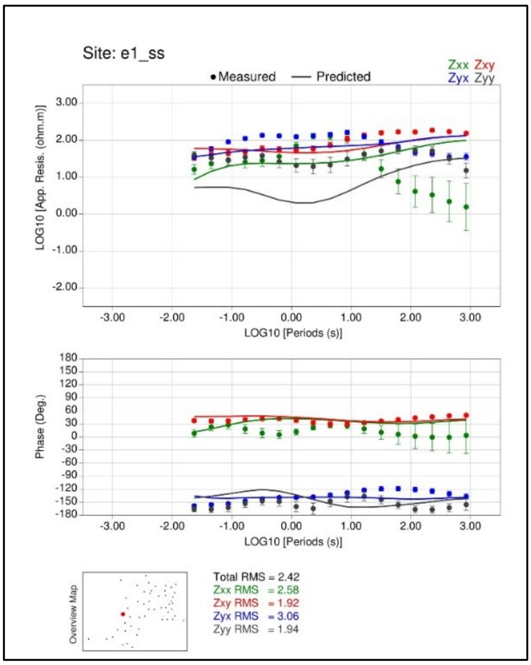
Site: e1_ss
Zxx Zxy
Zyx Zyy
• Measured — Predicted
LOG10 [App. Resis. (ohm.m)]
3.00
2.00
1.00
0.00
-1.00
-2.00
-3.00 -2.00 -1.00 0.00 1.00 2.00 3.00
LOG10 [Periods (s)]
Phase (Deg.)
180 150 120 90 60 30 0 -30 -60 -90 -120 -150 -180
-3.00 -2.00 -1.00 0.00 1.00 2.00 3.00
LOG10 [Periods (s)]
Overview Map
Total RMS = 2.42
Zxx RMS = 2.58
Zxy RMS = 1.92
Zyx RMS = 3.06
Zyy RMS = 1.94

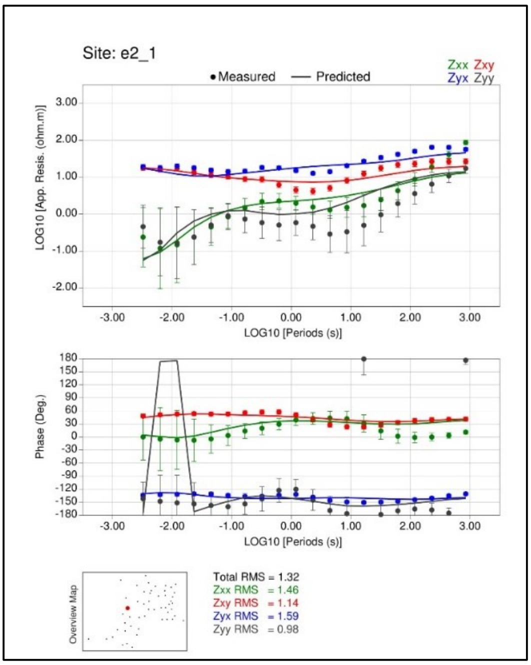
Site: e2_1
Zxx Zxy
Zyx Zyy
• Measured — Predicted
LOG10 [App. Resis. (ohm.m)]
3.00
2.00
1.00
0.00
-1.00
-2.00
-3.00 -2.00 -1.00 0.00 1.00 2.00 3.00
LOG10 [Periods (s)]
Phase (Deg.)
180 150 120 90 60 30 0 -30 -60 -90 -120 -150 -180
-3.00 -2.00 -1.00 0.00 1.00 2.00 3.00
LOG10 [Periods (s)]
Overview Map
Total RMS = 1.32
Zxx RMS = 1.46
Zxy RMS = 1.14
Zyx RMS = 1.59
Zyy RMS = 0.98

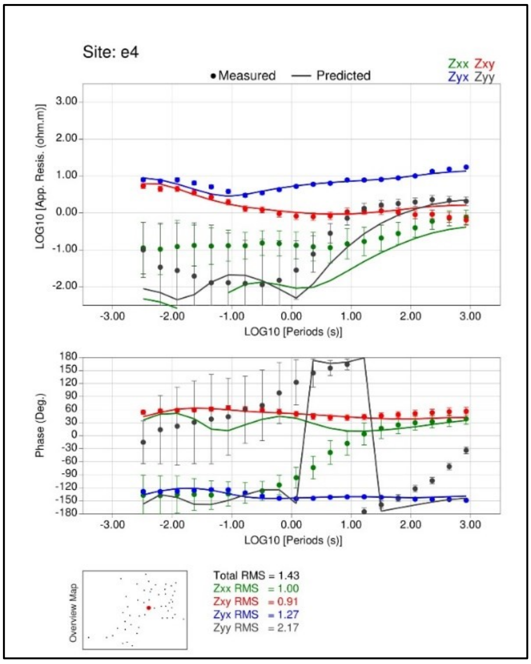
Site: e4
Zxx Zxy
Zyx Zyy
• Measured — Predicted
LOG10 [App. Resis. (ohm.m)]
3.00
2.00
1.00
0.00
-1.00
-2.00
-3.00 -2.00 -1.00 0.00 1.00 2.00 3.00
LOG10 [Periods (s)]
Phase (Deg.)
180 150 120 90 60 30 0 -30 -60 -90 -120 -150 -180
-3.00 -2.00 -1.00 0.00 1.00 2.00 3.00
LOG10 [Periods (s)]
Overview Map
Total RMS = 1.43
Zxx RMS = 1.00
Zxy RMS = 0.91
Zyx RMS = 1.27
Zyy RMS = 2.17

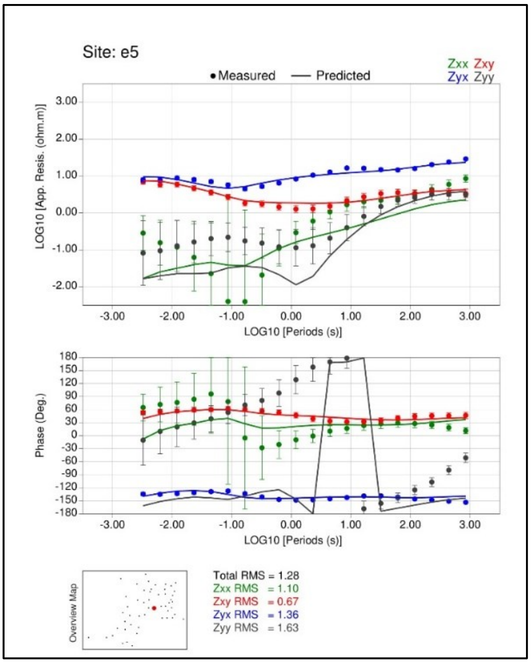
Site: e5
Zxx Zxy
Zyx Zyy
• Measured — Predicted
LOG10 [App. Resis. (ohm.m)]
3.00
2.00
1.00
0.00
-1.00
-2.00
-3.00 -2.00 -1.00 0.00 1.00 2.00 3.00
LOG10 [Periods (s)]
Phase (Deg.)
180 150 120 90 60 30 0 -30 -60 -90 -120 -150 -180
-3.00 -2.00 -1.00 0.00 1.00 2.00 3.00
LOG10 [Periods (s)]
Overview Map
Total RMS = 1.28
Zxx RMS = 1.10
Zxy RMS = 0.67
Zyx RMS = 1.36
Zyy RMS = 1.63

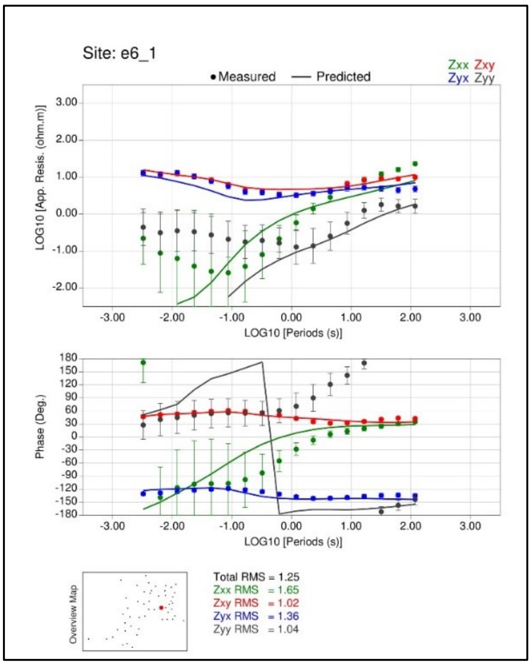
Site: e6_1
• Measured — Predicted
Zxx Zxy
Zyx Zyy
LOG10 [App. Resis. (ohm.m)]
LOG10 [Periods (s)]
Phase (Deg.)
LOG10 [Periods (s)]
Overview Map
Total RMS = 1.25
Zxx RMS = 1.65
Zxy RMS = 1.02
Zyx RMS = 1.36
Zyy RMS = 1.04

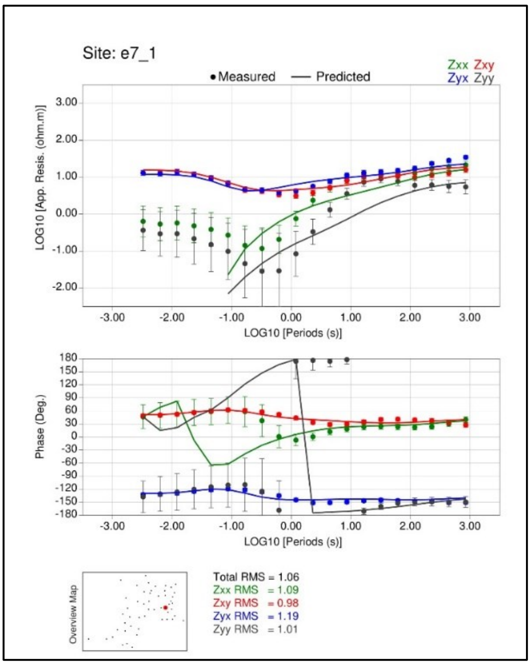
Site: e7_1
• Measured — Predicted
Zxx Zxy
Zyx Zyy
LOG10 [App. Resis. (ohm.m)]
LOG10 [Periods (s)]
Phase (Deg.)
LOG10 [Periods (s)]
Overview Map
Total RMS = 1.06
Zxx RMS = 1.09
Zxy RMS = 0.98
Zyx RMS = 1.19
Zyy RMS = 1.01

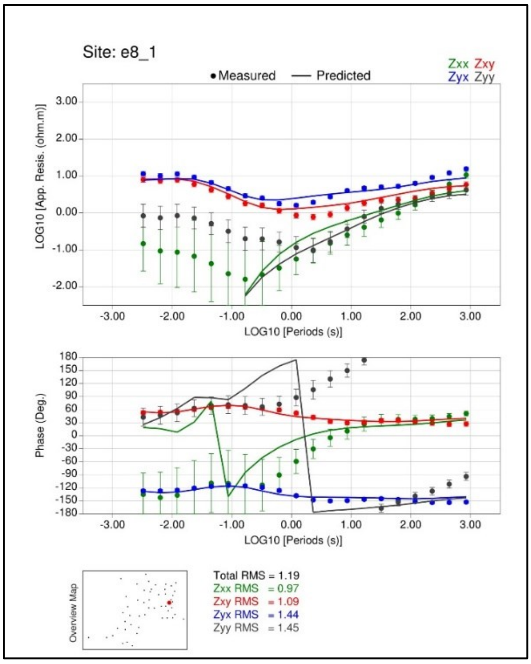
Site: e8_1
• Measured — Predicted
Zxx Zxy
Zyx Zyy
LOG10 [App. Resis. (ohm.m)]
LOG10 [Periods (s)]
Phase (Deg.)
LOG10 [Periods (s)]
Overview Map
Total RMS = 1.19
Zxx RMS = 0.97
Zxy RMS = 1.09
Zyx RMS = 1.44
Zyy RMS = 1.45

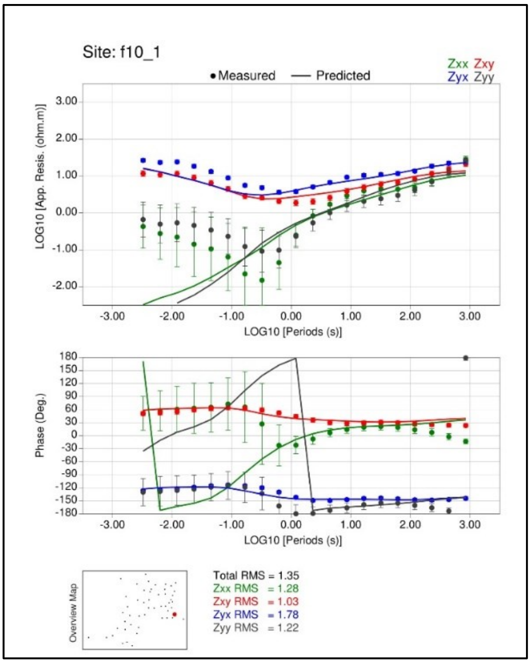
Site: f10_1
• Measured — Predicted
Zxx Zxy
Zyx Zyy
LOG10 [App. Resis. (ohm.m)]
LOG10 [Periods (s)]
Phase (Deg.)
LOG10 [Periods (s)]
Overview Map
Total RMS = 1.35
Zxx RMS = 1.28
Zxy RMS = 1.03
Zyx RMS = 1.78
Zyy RMS = 1.22

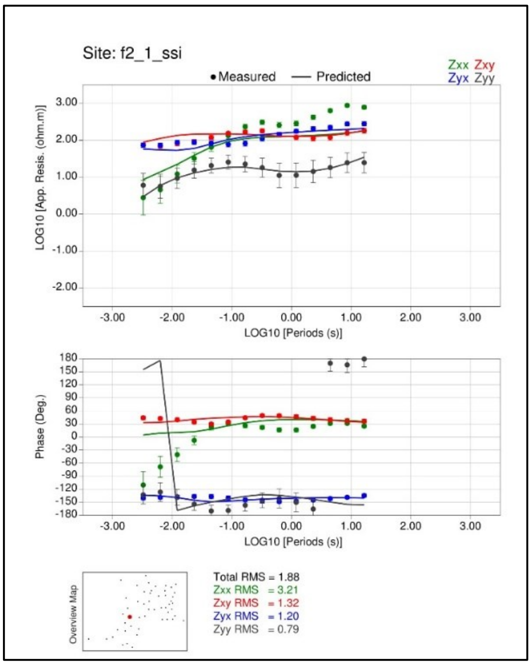
Site: f2_1_ssi
Zxx Zxy
Zyx Zyy
● Measured — Predicted
LOG10 [App. Resis. (ohm.m)]
3.00
2.00
1.00
0.00
-1.00
-2.00
-3.00
1.00
LOG10 [Periods (s)]
Phase (Deg.)
180
150
120
90
60
30
0
-30
-60
-90
-120
-150
-180
Overview Map
Total RMS = 1.88
Zxx RMS = 3.21
Zxy RMS = 1.32
Zyx RMS = 1.20
Zyy RMS = 0.79

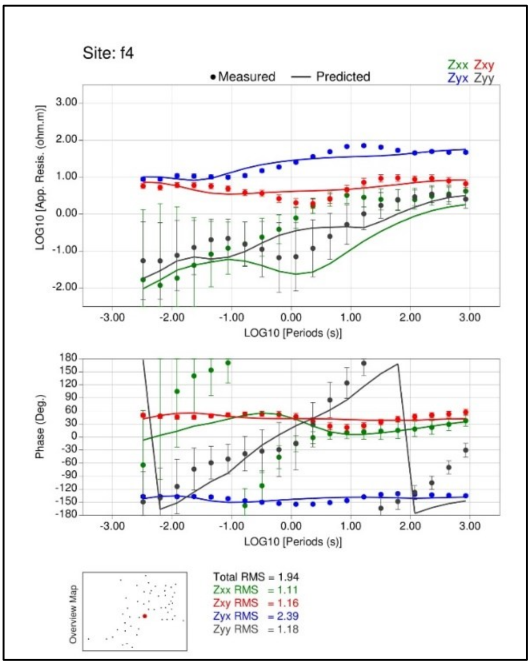
Site: f4
Zxx Zxy
Zyx Zyy
● Measured — Predicted
LOG10 [App. Resis. (ohm.m)]
LOG10 [Periods (s)]
Phase (Deg.)
Overview Map
Total RMS = 1.94
Zxx RMS = 1.11
Zxy RMS = 1.16
Zyx RMS = 2.39
Zyy RMS = 1.18

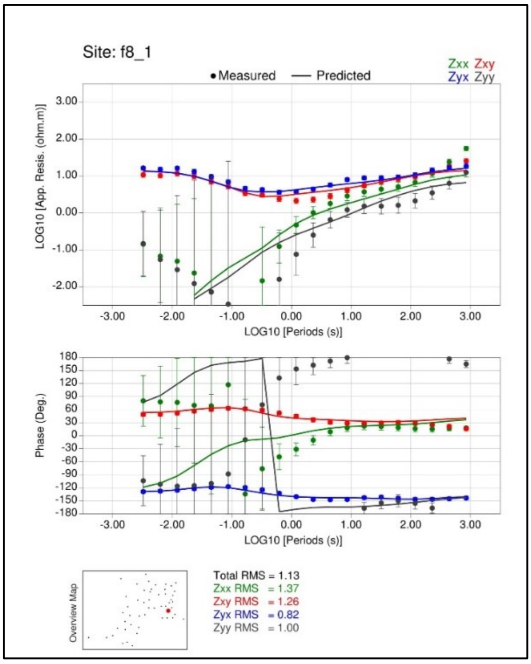
Site: f8_1
Zxx Zxy
Zyx Zyy
● Measured — Predicted
LOG10 [App. Resis. (ohm.m)]
LOG10 [Periods (s)]
Phase (Deg.)
Overview Map
Total RMS = 1.13
Zxx RMS = 1.37
Zxy RMS = 1.26
Zyx RMS = 0.82
Zyy RMS = 1.00

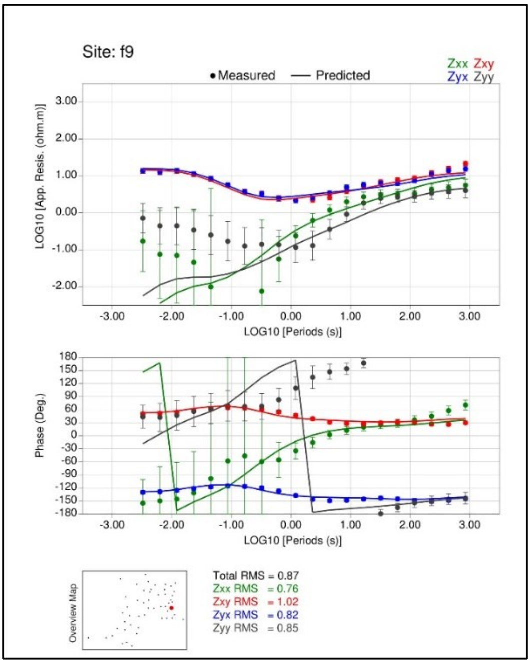
Site: f9
Zxx Zxy
Zyx Zyy
● Measured — Predicted
LOG10 [App. Resis. (ohm.m)]
LOG10 [Periods (s)]
Phase (Deg.)
Overview Map
Total RMS = 0.87
Zxx RMS = 0.76
Zxy RMS = 1.02
Zyx RMS = 0.82
Zyy RMS = 0.85

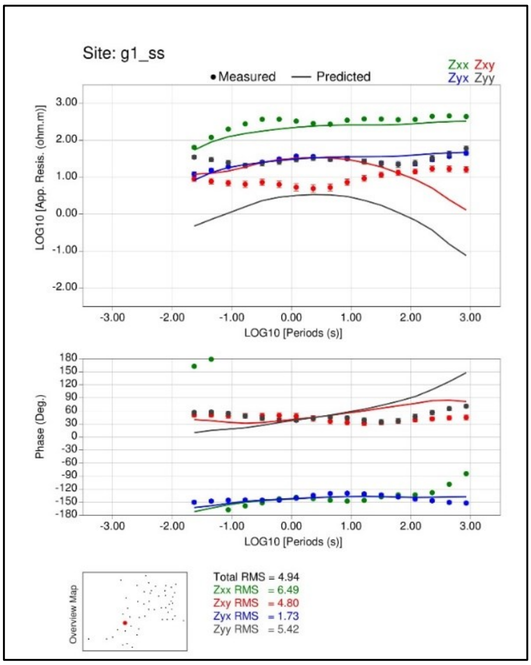
Site: g1_ss
• Measured — Predicted
Zxx Zxy
Zyx Zyy
LOG10 [App. Resis. (ohm.m)]
3.00
2.00
1.00
0.00
-1.00
-2.00
-3.00 -2.00 -1.00 0.00 1.00 2.00 3.00
LOG10 [Periods (s)]
Phase (Deg.)
180 150 120 90 60 30 0 -30 -60 -90 -120 -150 -180
-3.00 -2.00 -1.00 0.00 1.00 2.00 3.00
LOG10 [Periods (s)]
Overview Map
Total RMS = 4.94
Zxx RMS = 6.49
Zxy RMS = 4.80
Zyx RMS = 1.73
Zyy RMS = 5.42

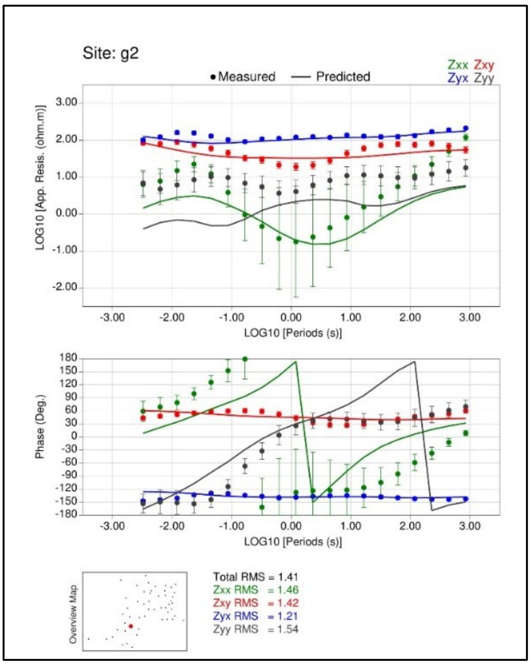
Site: g2
• Measured — Predicted
Zxx Zxy
Zyx Zyy
LOG10 [App. Resis. (ohm.m)]
3.00
2.00
1.00
0.00
-1.00
-2.00
-3.00 -2.00 -1.00 0.00 1.00 2.00 3.00
LOG10 [Periods (s)]
Phase (Deg.)
180 150 120 90 60 30 0 -30 -60 -90 -120 -150 -180
-3.00 -2.00 -1.00 0.00 1.00 2.00 3.00
LOG10 [Periods (s)]
Overview Map
Total RMS = 1.41
Zxx RMS = 1.46
Zxy RMS = 1.42
Zyx RMS = 1.21
Zyy RMS = 1.54

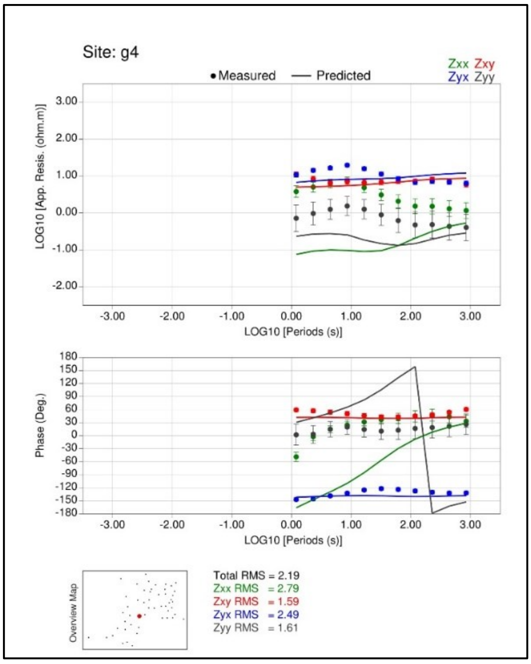
Site: g4
• Measured — Predicted
Zxx Zxy
Zyx Zyy
LOG10 [App. Resis. (ohm.m)]
3.00
2.00
1.00
0.00
-1.00
-2.00
-3.00 -2.00 -1.00 0.00 1.00 2.00 3.00
LOG10 [Periods (s)]
Phase (Deg.)
180 150 120 90 60 30 0 -30 -60 -90 -120 -150 -180
-3.00 -2.00 -1.00 0.00 1.00 2.00 3.00
LOG10 [Periods (s)]
Overview Map
Total RMS = 2.19
Zxx RMS = 2.79
Zxy RMS = 1.59
Zyx RMS = 2.49
Zyy RMS = 1.61

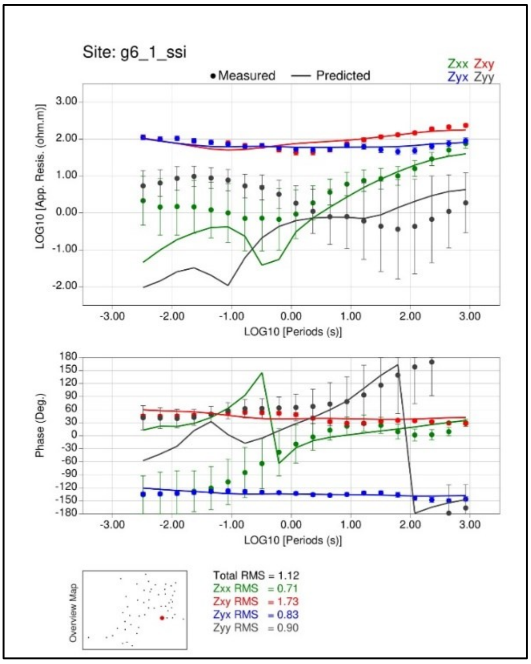
Site: g6_1_ssi
• Measured — Predicted
Zxx Zxy
Zyx Zyy
LOG10 [App. Resis. (ohm.m)]
3.00
2.00
1.00
0.00
-1.00
-2.00
-3.00 -2.00 -1.00 0.00 1.00 2.00 3.00
LOG10 [Periods (s)]
Phase (Deg.)
180 150 120 90 60 30 0 -30 -60 -90 -120 -150 -180
-3.00 -2.00 -1.00 0.00 1.00 2.00 3.00
LOG10 [Periods (s)]
Overview Map
Total RMS = 1.12
Zxx RMS = 0.71
Zxy RMS = 1.73
Zyx RMS = 0.83
Zyy RMS = 0.90

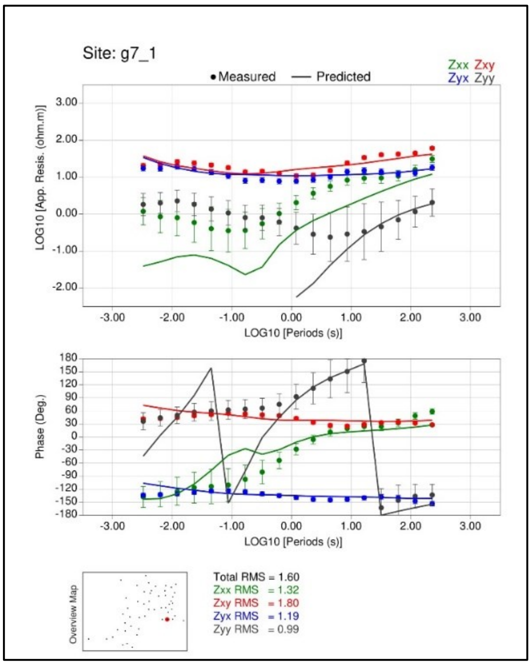
Site: g7_1
Measured
Predicted
Zxx Zxy
Zyx Zyy
LOG10 [App. Resis. (ohm.m)]
LOG10 [Periods (s)]
Phase (Deg.)
Overview Map
Total RMS = 1.60
Zxx RMS = 1.32
Zxy RMS = 1.80
Zyx RMS = 1.19
Zyy RMS = 0.99

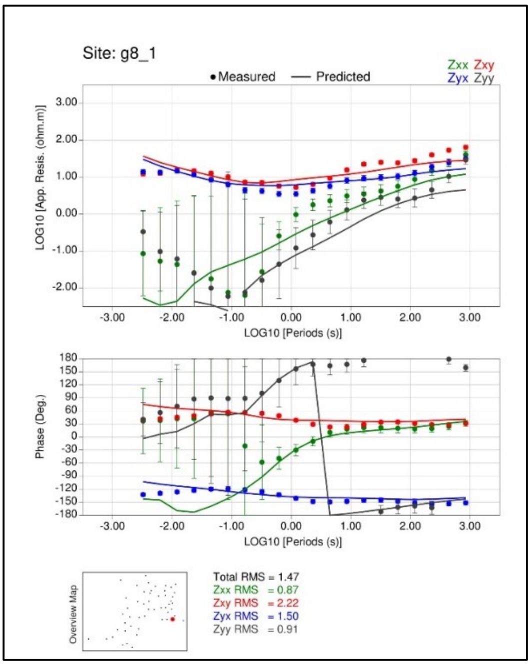
Site: g8_1
Measured
Predicted
Zxx Zxy
Zyx Zyy
LOG10 [App. Resis. (ohm.m)]
LOG10 [Periods (s)]
Phase (Deg.)
Overview Map
Total RMS = 1.47
Zxx RMS = 0.87
Zxy RMS = 2.22
Zyx RMS = 1.50
Zyy RMS = 0.91

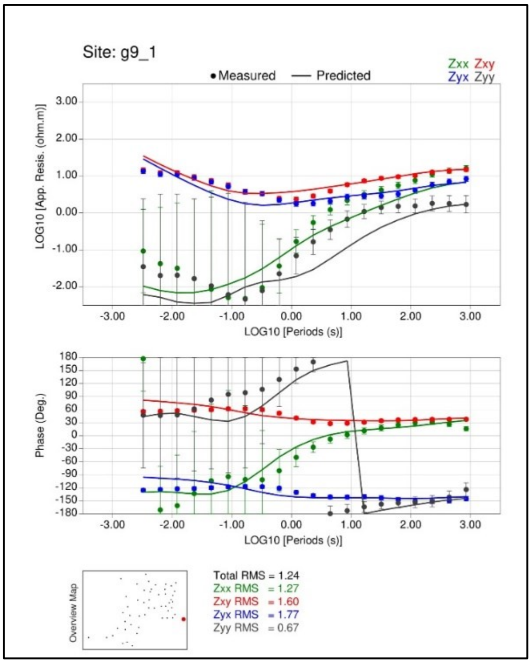
Site: g9_1
Measured
Predicted
Zxx Zxy
Zyx Zyy
LOG10 [App. Resis. (ohm.m)]
LOG10 [Periods (s)]
Phase (Deg.)
Overview Map
Total RMS = 1.24
Zxx RMS = 1.27
Zxy RMS = 1.60
Zyx RMS = 1.77
Zyy RMS = 0.67

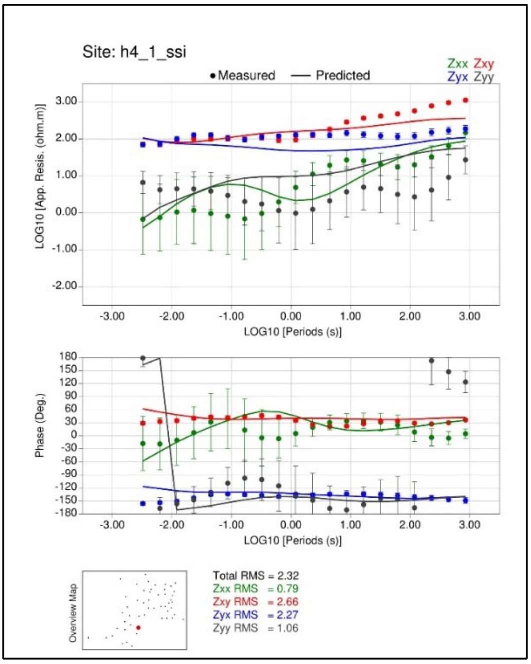
Site: h4_1_ssi
Measured
Predicted
Zxx Zxy
Zyx Zyy
LOG10 [App. Resis. (ohm.m)]
LOG10 [Periods (s)]
Phase (Deg.)
Overview Map
Total RMS = 2.32
Zxx RMS = 0.79
Zxy RMS = 2.66
Zyx RMS = 2.27
Zyy RMS = 1.06

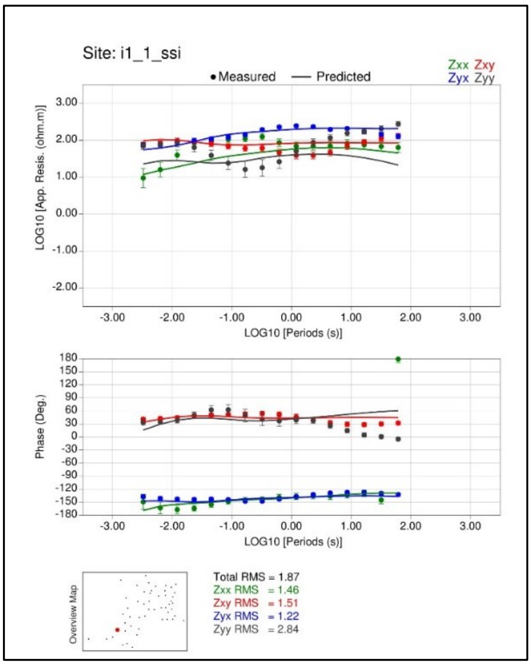
Site: i1_1_ssi
Zxx Zxy
Zyx Zyy
• Measured — Predicted
LOG10 [App. Resis. (ohm.m)]
3.00
2.00
1.00
0.00
-1.00
-2.00
-3.00 -2.00 -1.00 0.00 1.00 2.00 3.00
LOG10 [Periods (s)]
Phase (Deg.)
180 150 120 90 60 30 0 -30 -60 -90 -120 -150 -180
-3.00 -2.00 -1.00 0.00 1.00 2.00 3.00
LOG10 [Periods (s)]
Overview Map
Total RMS = 1.87
Zxx RMS = 1.46
Zxy RMS = 1.51
Zyx RMS = 1.22
Zyy RMS = 2.84

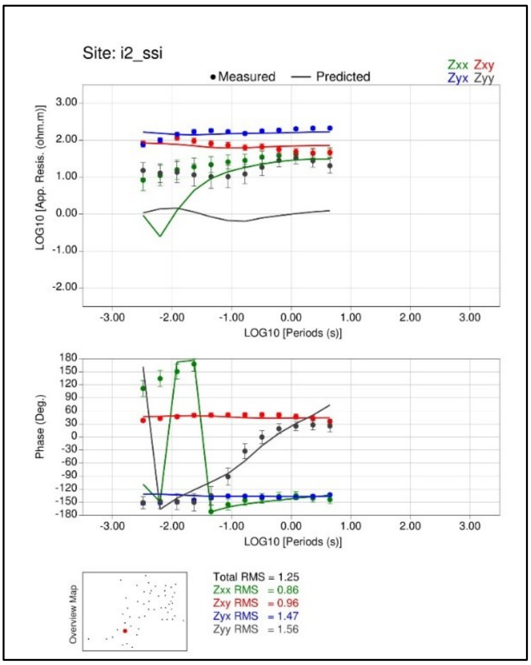
Site: i2_ssi
Zxx Zxy
Zyx Zyy
• Measured — Predicted
LOG10 [App. Resis. (ohm.m)]
3.00
2.00
1.00
0.00
-1.00
-2.00
-3.00 -2.00 -1.00 0.00 1.00 2.00 3.00
LOG10 [Periods (s)]
Phase (Deg.)
180 150 120 90 60 30 0 -30 -60 -90 -120 -150 -180
-3.00 -2.00 -1.00 0.00 1.00 2.00 3.00
LOG10 [Periods (s)]
Overview Map
Total RMS = 1.25
Zxx RMS = 0.86
Zxy RMS = 0.96
Zyx RMS = 1.47
Zyy RMS = 1.56

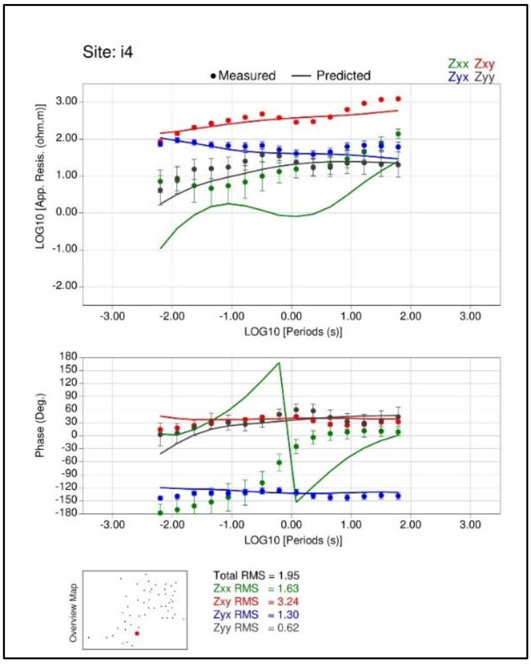
Site: i4
Zxx Zxy
Zyx Zyy
• Measured — Predicted
LOG10 [App. Resis. (ohm.m)]
3.00
2.00
1.00
0.00
-1.00
-2.00
-3.00 -2.00 -1.00 0.00 1.00 2.00 3.00
LOG10 [Periods (s)]
Phase (Deg.)
180 150 120 90 60 30 0 -30 -60 -90 -120 -150 -180
-3.00 -2.00 -1.00 0.00 1.00 2.00 3.00
LOG10 [Periods (s)]
Overview Map
Total RMS = 1.95
Zxx RMS = 1.63
Zxy RMS = 3.24
Zyx RMS = 1.30
Zyy RMS = 0.62

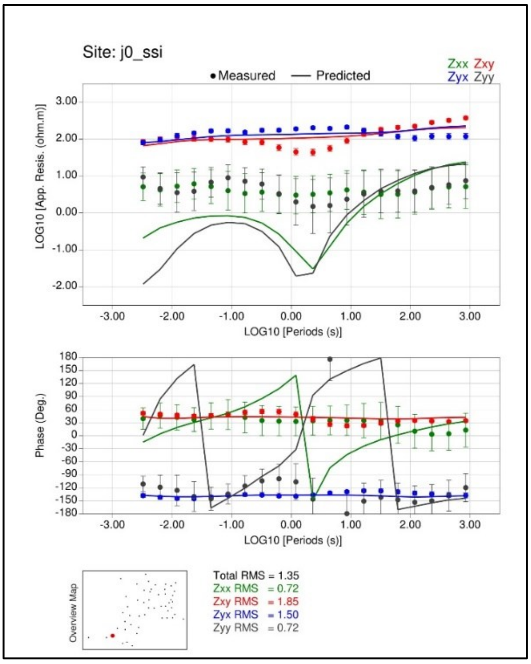
Site: j0_ssi
Zxx Zxy
Zyx Zyy
• Measured — Predicted
LOG10 [App. Resis. (ohm.m)]
3.00
2.00
1.00
0.00
-1.00
-2.00
-3.00 -2.00 -1.00 0.00 1.00 2.00 3.00
LOG10 [Periods (s)]
Phase (Deg.)
180 150 120 90 60 30 0 -30 -60 -90 -120 -150 -180
-3.00 -2.00 -1.00 0.00 1.00 2.00 3.00
LOG10 [Periods (s)]
Overview Map
Total RMS = 1.35
Zxx RMS = 0.72
Zxy RMS = 1.85
Zyx RMS = 1.50
Zyy RMS = 0.72

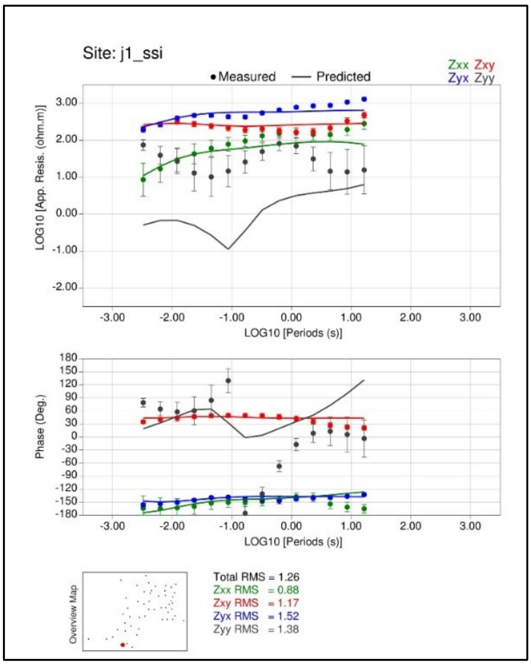
Site: j1_ssi
• Measured — Predicted
Zxx Zxy
Zyx Zyy
LOG10 [App. Resis. (ohm.m)]
LOG10 [Periods (s)]
Phase (Deg.)
Overview Map
Total RMS = 1.26
Zxx RMS = 0.88
Zxy RMS = 1.17
Zyx RMS = 1.52
Zyy RMS = 1.38

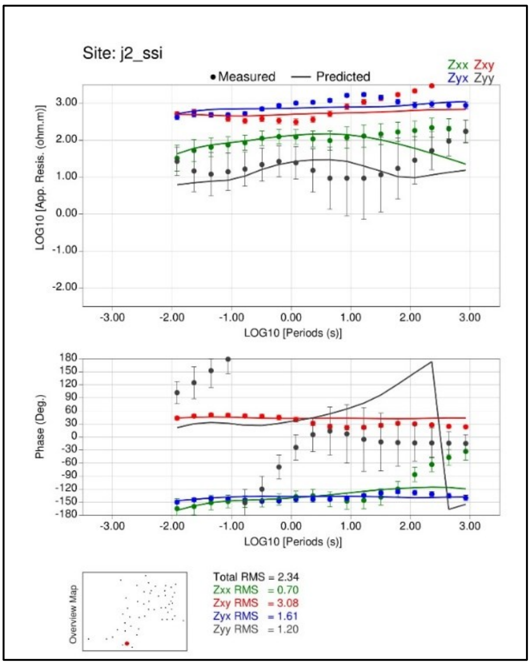
Site: j2_ssi
• Measured — Predicted
Zxx Zxy
Zyx Zyy
LOG10 [App. Resis. (ohm.m)]
LOG10 [Periods (s)]
Phase (Deg.)
Overview Map
Total RMS = 2.34
Zxx RMS = 0.70
Zxy RMS = 3.08
Zyx RMS = 1.61
Zyy RMS = 1.20

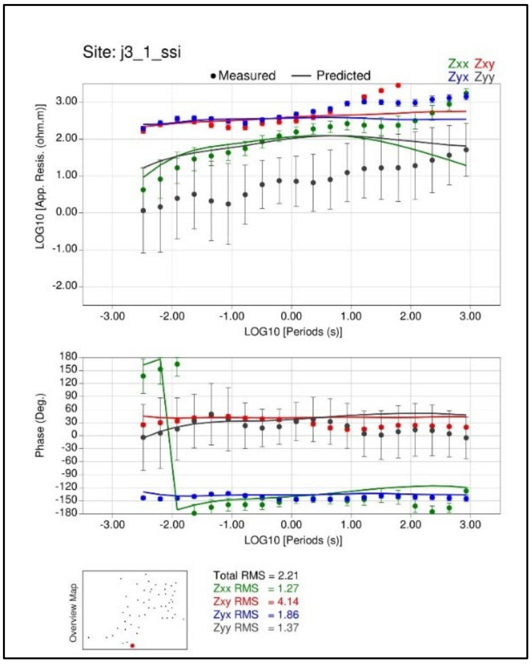
Site: j3_1_ssi
• Measured — Predicted
Zxx Zxy
Zyx Zyy
LOG10 [App. Resis. (ohm.m)]
LOG10 [Periods (s)]
Phase (Deg.)
Overview Map
Total RMS = 2.21
Zxx RMS = 1.27
Zxy RMS = 4.14
Zyx RMS = 1.86
Zyy RMS = 1.37

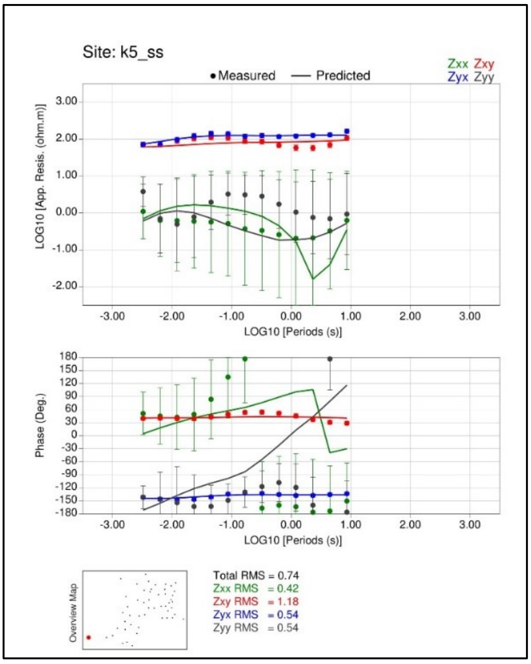
Site: k5_ss
• Measured — Predicted
Zxx Zxy
Zyx Zyy
LOG10 [App. Resis. (ohm.m)]
LOG10 [Periods (s)]
Phase (Deg.)
Overview Map
Total RMS = 0.74
Zxx RMS = 0.42
Zxy RMS = 1.18
Zyx RMS = 0.54
Zyy RMS = 0.54

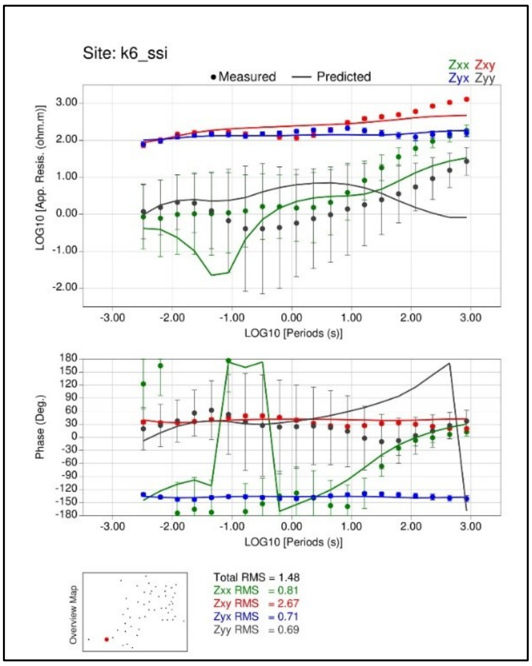
Site: k6_ssi
● Measured — Predicted
Zxx Zxy
Zyx Zyy
LOG10 [App. Resis. (ohm.m)]
3.00
2.00
1.00
0.00
-1.00
-2.00
-3.00 -2.00 -1.00 0.00 1.00 2.00 3.00
LOG10 [Periods (s)]
Phase (Deg.)
180 150 120 90 60 30 0 -30 -60 -90 -120 -150 -180
-3.00 -2.00 -1.00 0.00 1.00 2.00 3.00
LOG10 [Periods (s)]
Overview Map
Total RMS = 1.48
Zxx RMS = 0.81
Zxy RMS = 2.67
Zyx RMS = 0.71
Zyy RMS = 0.69

Appendix E
3D MT inversion tests

E.1 Inversion of full Z and T with strike-aligned grid (test B)

The inversion test B assumed a homogeneous starting model and 10% error floor for Z_{xy}, Z_{yx} and T and 15% error floor for Z_{xx},and Z_{yy}. The outcome is shown in Figures. E.1, E.2 and E.3. With respect to test A (Figures 7.2, 7.3, 7.4), the RMSE was little higher and the resistivity structures were more smoothed. In particular, the deep resistive body of Figure E.3d reached a maximum resistivity value higher than that of test A. This could be attributed to the strike-aligned rotation of the grid.

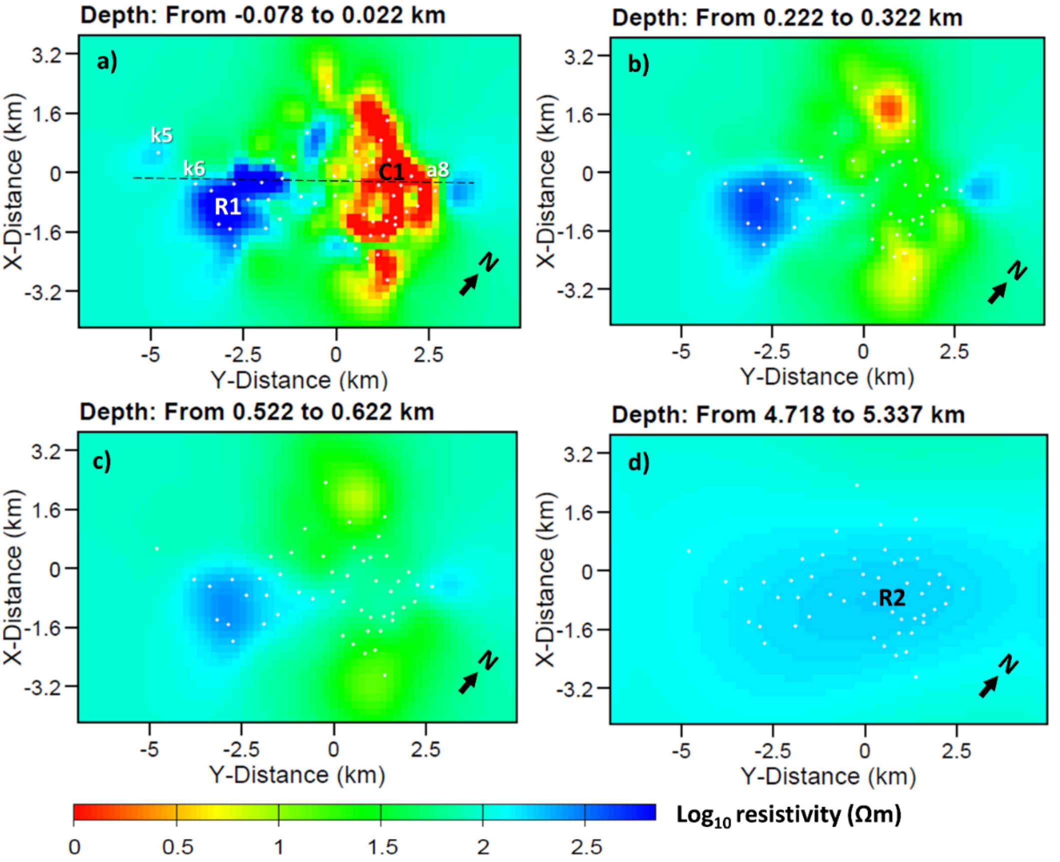

Figure E.1 Plain view of the 3D resistivity model of test B (N130°E) at different depths: **a)** 78 m a.s.l., **b)** 222 m, **c)** 522 m, **d)** 4.7 km b.s.l.. The mesh is aligned with the geoelectrical strike, that is, the North is rotated 40° clockwise and the x-axis is parallel to the strike. The black-dashed profile drawn in a (from site *k5* to *a8*) is the cross-section reported in Figure E.2

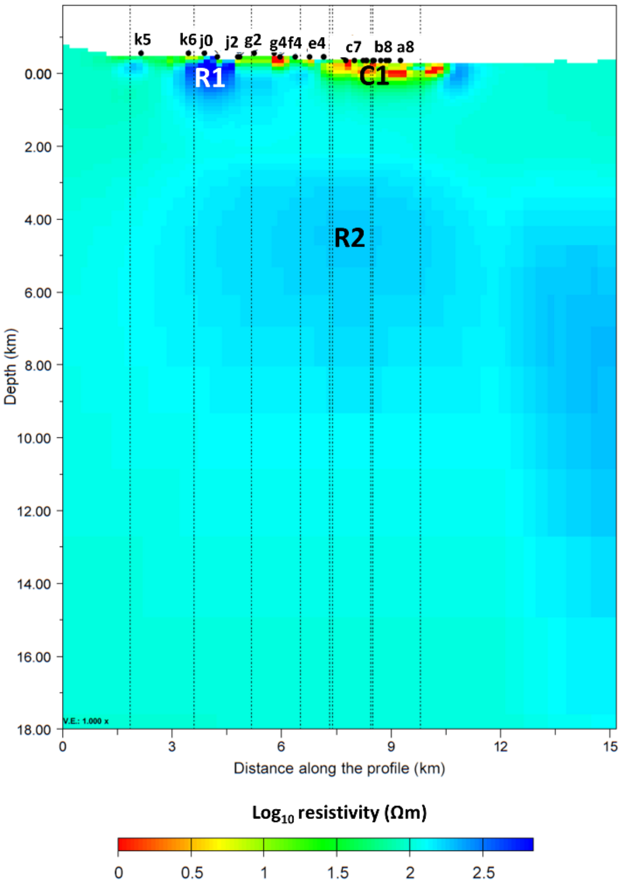

Figure E.2 Vertical cross-section of the model from test B corresponding to the MT profile investigated in Section 6.3. The profile is directed SW-NE orthogonally to the strike direction and crosses sites from *k5* to *a8* (see Figure E.1a)

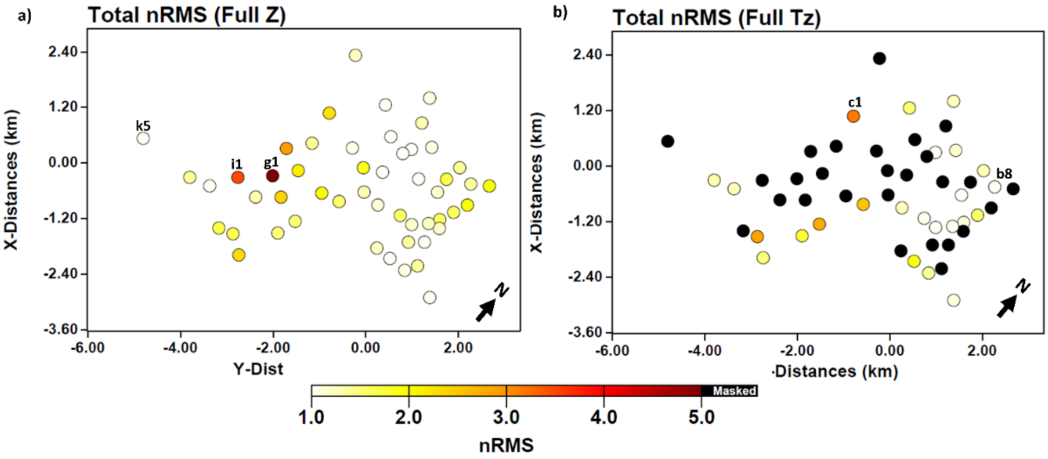

Figure E.3 Distribution of RMSE at each site for test B. **a)** Total normalized RMSE for the impedance tensor (*Z*). **b)** Total normalized RMSE for the Tipper matrix (***T***). The black dots in b mean no Tipper data. The errors are normalized for the full period range.

E.2 Inversion of full Z and T with strike-aligned grid and a priori (test C)

Inversion test C was initialized by using an a priori model derived from the 2D inversion result of Manzella et al. (2006). Although driven by prior knowledge, the final 3D model shown in Figures E.4, E.5 and E.6 was compatible with the resistivity distribution of test D (Figures 7.5, 7.6, 7.7). The deep resistive body was characterized by sharp edges, resulting from the a priori starting model and little changed after the inversion. This minimal modification of the starting model stems from the intrinsic inversion scheme of ModEM software, that solve the inverse problem for the rough transformed model parameter. The presence of the a priori structure positively influenced the data fitting. In fact, the final RMSE normalized for the full period bandwidth was 1.75 for $\underline{Z}$ and 1.42 for $\boldsymbol{T}$ (Table 7.1).

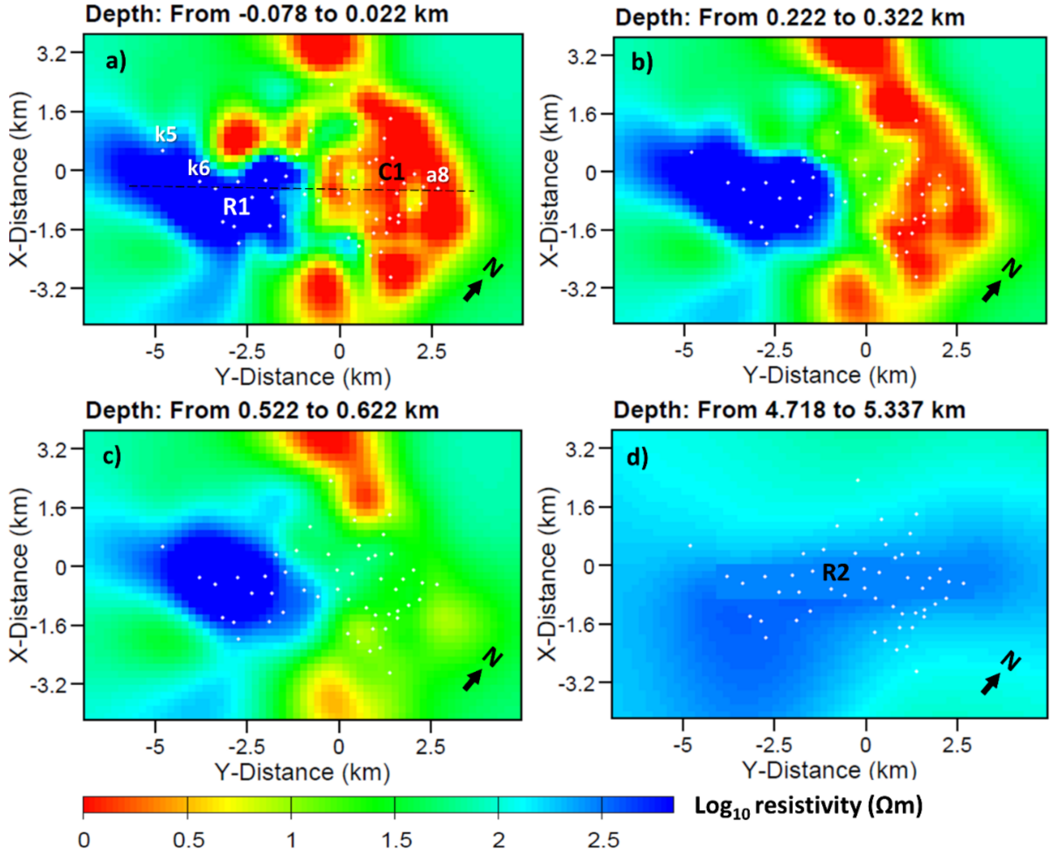

Figure E.4 Plain view of the 3D resistivity model of test C (N130°E) at different depths: **a)** 78 m a.s.l., **b)** 222 m, **c)** 522 m, **d)** 4.7 km b.s.l.. The mesh is aligned with the geoelectrical strike, that is, the North is rotated 40° clockwise and the x-axis is parallel to the strike. The black-dashed profile drawn in a (from site *k5* to *a8*) is the cross-section reported in Figure E.5

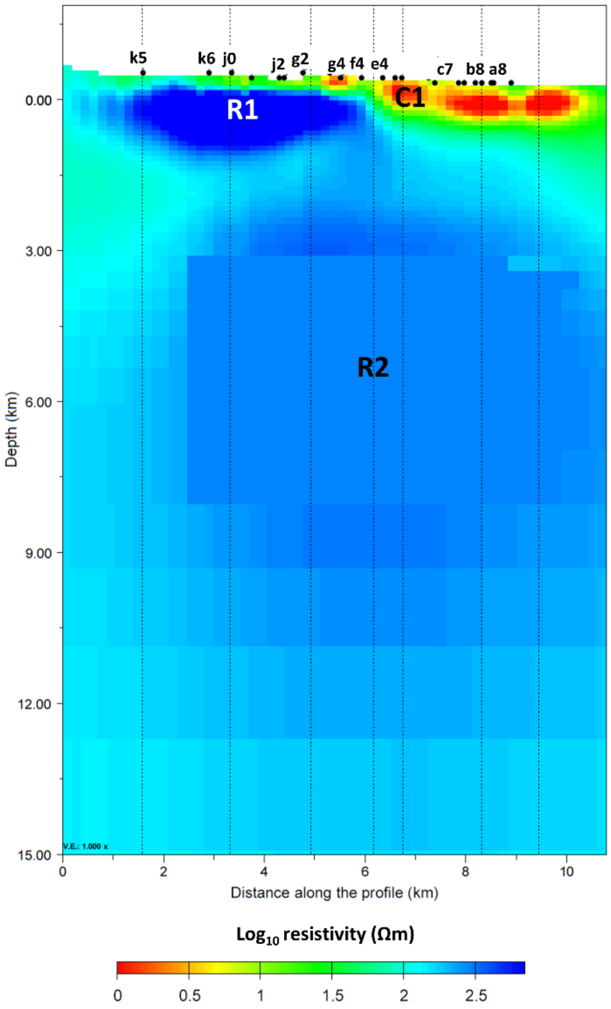

Figure E.5 Vertical cross-section of the model from test C corresponding to the MT profile investigated in Section 6.3. The profile is directed SW-NE orthogonally to the strike direction and crosses sites from *k5* to *a8* (see Figure E.4a)

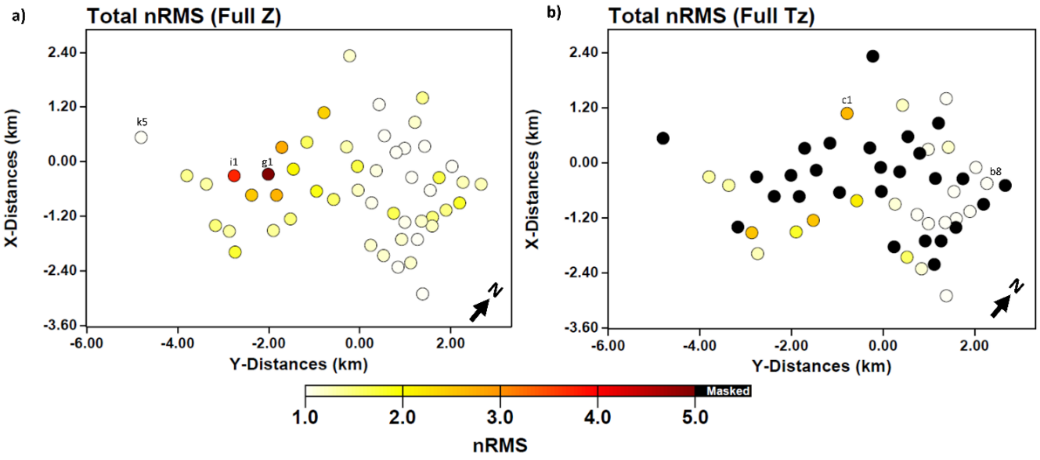

Figure E.6 Distribution of RMSE at each site for test C. **a)** Total normalized RMSE for the impedance tensor ($\underline{Z}$). **b)** Total normalized RMSE for the Tipper matrix ($\boldsymbol{T}$). The black dots in b mean no Tipper data. The errors are normalized for the full period range.

E.3 Inversion of full Z with strike-aligned grid (test E)

Inversion test E yielded the worst RMSE (Table 7.1 and Figure E.8). The superficial resistivity structures depicted in Figures E.7 and E.8 were not dissimilar to those of test D (Figures 7.5 and 7.6). From 1.5 to 3 km of depth b.s.l., the model was more homogeneous than the model of test D and the deep resistive body was less resistive than in test D.

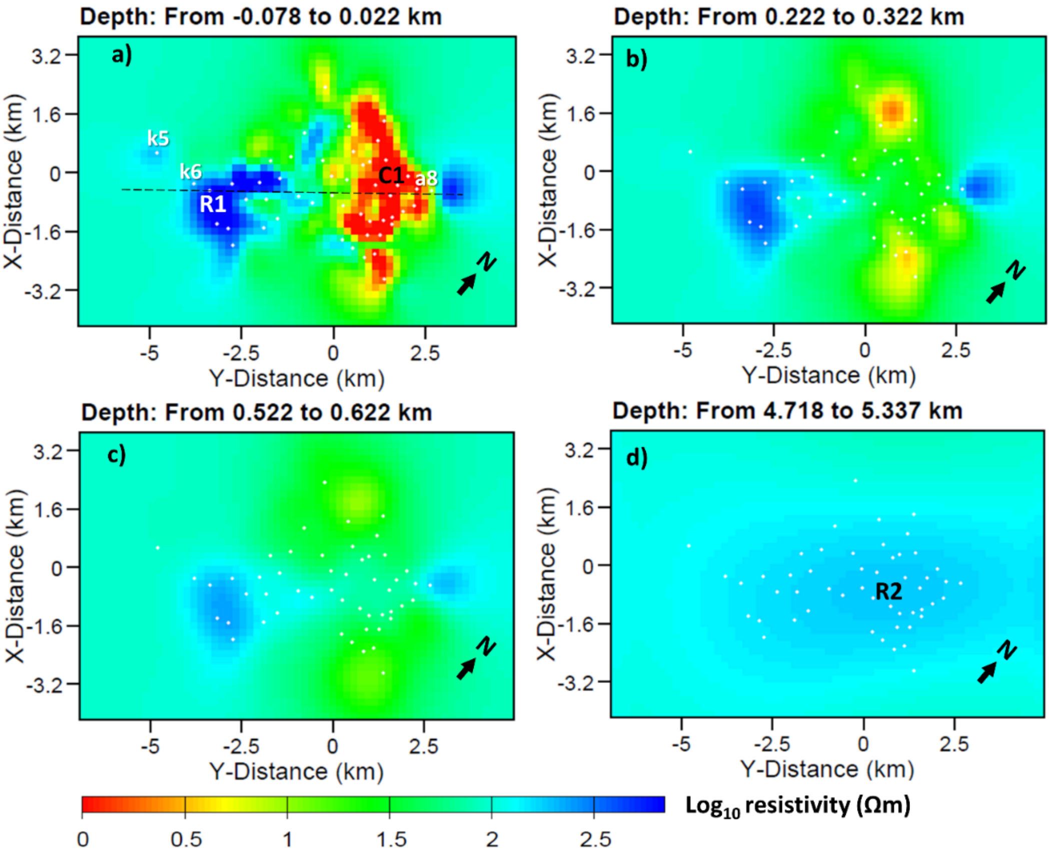

Figure E.7 Plain view of the 3D resistivity model of test E (N130°E) at different depths: **a)** 78 m a.s.l., **b)** 222 m, **c)** 522 m, **d)** 4.7 km b.s.l.. The mesh is aligned with the geoelectrical strike, that is, the North is rotated 40° clockwise and the x-axis is parallel to the strike. The black-dashed profile drawn in a (from site *k5* to *a8*) is the cross-section reported in Figure E.8

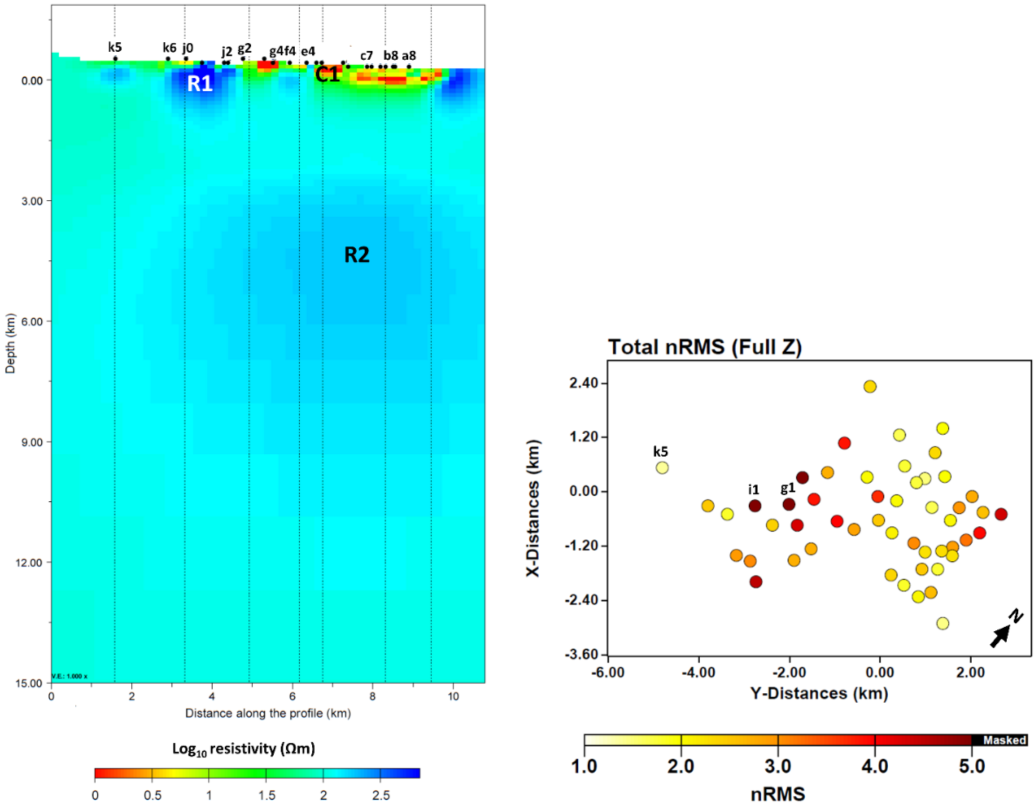

Figure E.8 left) Vertical cross-section of the model from test E corresponding to the MT profile investigated in Section 6.3. The profile is directed SW-NE orthogonally to the strike direction and crosses sites from *k5* to *a8* (see Figure E.7a); **right)** Distribution of RMSE at each site for test E. Total normalized RMSE for the impedance tensor (Z). The errors are normalized for the full period range.

E.4 Inversion of T with strike-aligned grid (test F)

Given the low error floor, inversion test F resulted in an appreciable final RMSE (Table 7.1 and Figure E.10). The importance of the inversion of only the vertical transfer function appeared from the resistivity contrasts highlighted in Figures E.9 and E.10. Similarly to all the other inversion tests, the deep resistive body was imaged between 3 and 8 km of depth b.s.l. but it resulted shifted towards west, probably due to the poor number of sites including Tipper data. the most important contribution of this test was its significant sensitivity at depth and the evidence of lateral constraints.

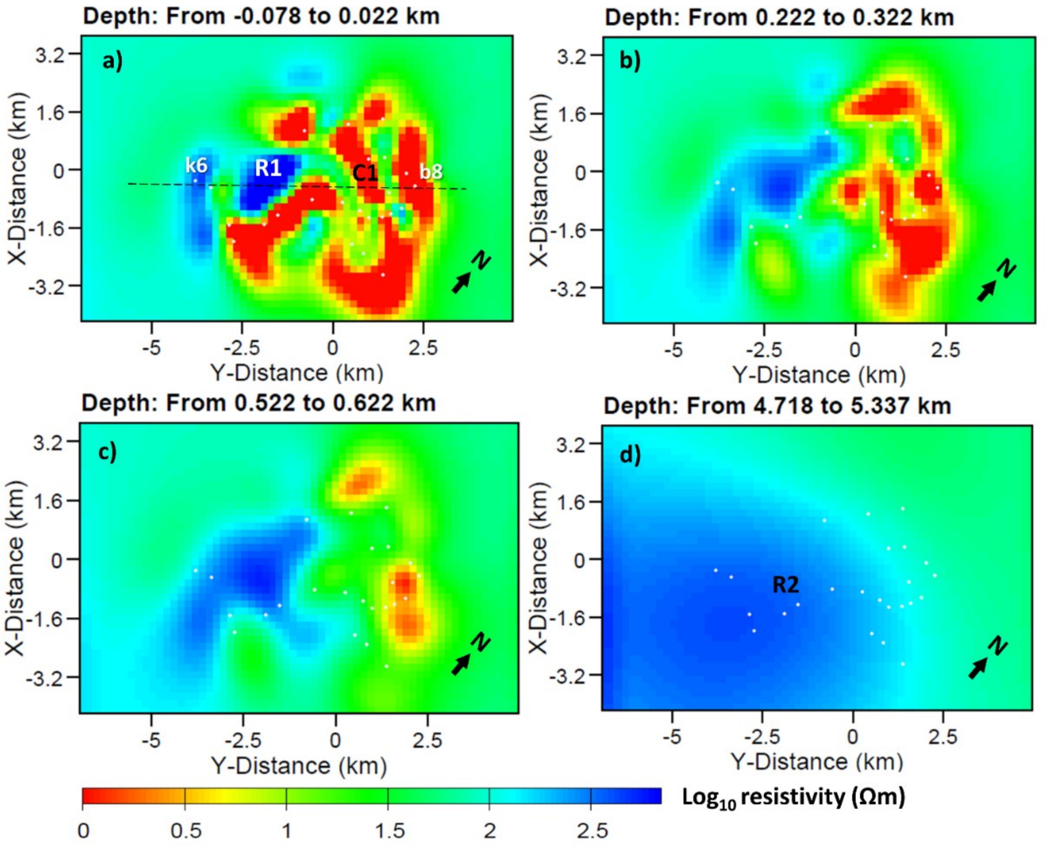

Figure E.9 Plain view of the 3D resistivity model of test F (N130°E) at different depths: **a)** 78 m a.s.l., **b)** 222 m, **c)** 522 m, **d)** 4.7 km b.s.l. The mesh is aligned with the geoelectrical strike, that is, the North is rotated 40° clockwise and the x-axis is parallel to the strike. The black-dashed profile drawn in a (from site *k6* to *b8*) is the cross-section reported in Figure E.10.

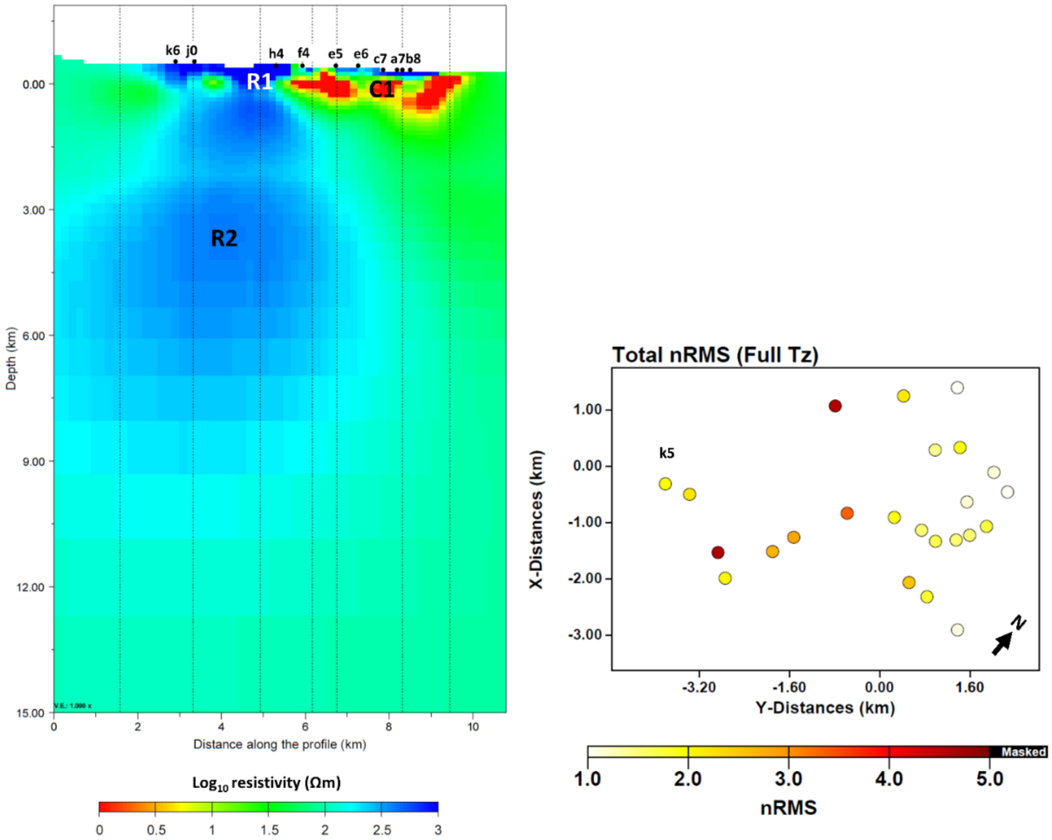

Figure E.10 left) Vertical cross-section of the model from test F corresponding to the MT profile investigated in Section 6.3. The profile is directed SW-NE orthogonally to the strike direction and crosses sites from *k5* to *a8* (see Figure E.9a); **right)** Distribution of RMSE at each site for test F. Total normalized RMSE for the Tipper matrix (***T***). The errors are normalized for the full period range.

E.5 Sensitivity test for the inversion model from test D

A sensitivity test was carried out for the 100-Ωm structure that in inversion model D was embedded between C1 and R2 below sites *k5-e4* (see Figure 7.9). From 2D modeling (Figure 5.9 and Figure 6.8), it resulted slightly more conductive (30-70 Ωm) than in the 3D-inversion model. To assess if the 100-Ωm structure was necessary to fit the data, it was replaced with a 1-Ωm body. The perturbed model is shown in Figure E.11 and is about 8 km large from 0.6 km to 2.5 km of depth.

The recalculation of the forward problem led to an overall RMSE increase of 130%, and to an RMSE increase from 116% to 280% for the sites above the body. An example of worsening of data fitting is in Figure E.12. This test confirmed that the 100-Ωm structure was required by the model in order to fit the data.

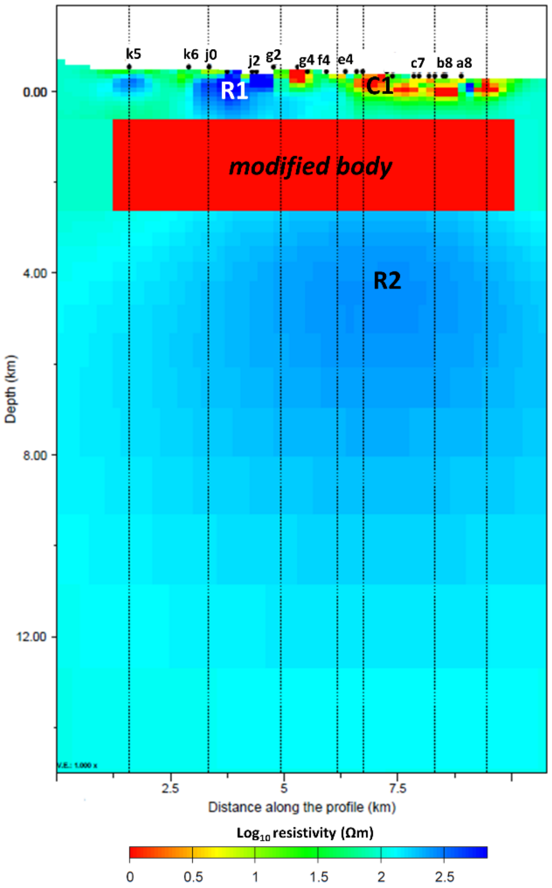

Figure E.11 Vertical cross-section of the model from test D where the 100-Ωm structure was tested and replaced with a 1-Ωm conductor (modified body). The section corresponds to the MT profile investigated in Section 6.3. The conductor is about 8 km large from 0.6 km to 2.5 km of depth.

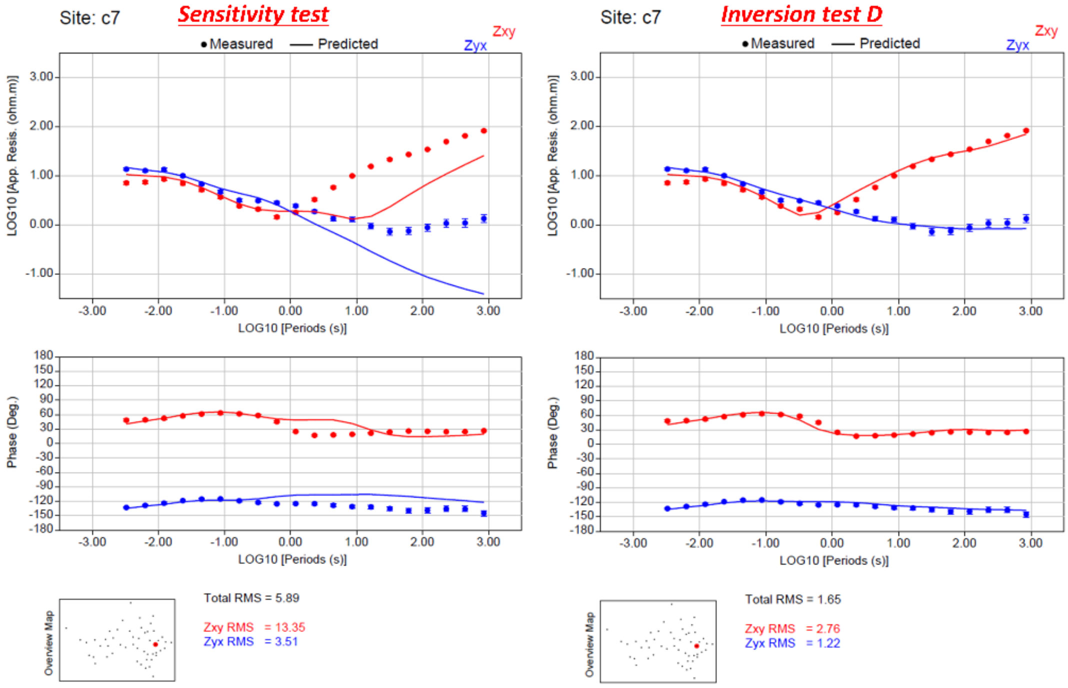

Figure E.12 For site *c7* the fitting between measured data (colored dots) and predicted response (colored lines) is plotted for apparent resistivity and phase of the off-diagonal impedance tensor components: **left)** data fitting after sensitivity test; **right)** data fitting after inversion test D.

Stochastic music

Music can explain everything.

Jonchaies for 109 musicians by Iannis Xenakis

This piece of music was written by the Greek musician and engineer Iannis Xenakis. It presents the application of complex mathematics, such as statistics, theory and geometry, to the composition of music in order to create the so called stochastic music. This cerebral and eccentric piece of music can be associated to the choreography of bird flocks and the swarming behavior of elements in a group. By using clusters of sound and almost cacophonic elements, the composer effectively depicts the hard search for the global optimum in the infinite exploration space and the need for many desperate iterations.